HZG REPORT 2015-1 // ISSN 2191-7833

Development and Implementation of a Nano-tomography Setup at the PETRA III Beamline P05

(Von der Mathematisch–Naturwissenschaftlichen Fakultät der Christian–Albrechts–Universität zu Kiel im Jahr 2014 als Dissertation angenommene Arbeit)

M. Ogurreck

wissen
schafft
nutzen

Helmholtz-Zentrum
Geesthacht
Zentrum für Material- und Küstenforschung

HZG REPORT 2015-1

Development and Implementation of a Nano-tomography Setup at the PETRA III Beamline P05

(Von der Mathematisch–Naturwissenschaftlichen Fakultät der Christian–Albrechts–Universität zu Kiel im Jahr 2014 als Dissertation angenommene Arbeit)

M. Ogurreck

Helmholtz-Zentrum Geesthacht
Zentrum für Material- und Küstenforschung GmbH | Geesthacht | 2015

Die HZG Reporte werden kostenlos abgegeben.
HZG Reports are available free of charge.

Anforderungen/Requests:

Helmholtz-Zentrum Geesthacht
Zentrum für Material- und Küstenforschung GmbH
Bibliothek/Library
Max-Planck-Straße 1
21502 Geesthacht
Germany
Tel.: +49 4152 87-1690
Fax.: +49 4152 87-1717
E-Mail: bibliothek@hzg.de

Druck: HZG-Hausdruckerei

Als Manuskript vervielfältigt.

ISSN 2191-7833

Helmholtz-Zentrum Geesthacht
Zentrum für Material- und Küstenforschung GmbH
Max-Planck-Straße 1
21502 Geesthacht

www.hzg.de

HZG REPORT 2015-1

Development and Implementation of a Nanotomography Setup at the PETRA III Beamline P05

(Von der Mathematisch-Naturwissenschaftlichen Fakultät der Christian-Albrechts-Universität zu Kiel im Jahr 2014 als Dissertation angenommene Arbeit)

Malte Ogurreck

182 pages with 112 figures and 14 tables

Abstract

X-ray nanotomography is used to analyze materials on the sub-micrometer scale. Many soft biological materials, i.e. most organic tissues, can be imaged with soft X-rays. For materials with a higher electron density, such as bone or teeth, metals, and ceramics, X-ray energies of more than 10 keV need to be used. All these setups require X-ray optics for either direct imaging of the object in question or for preparing a magnified projection.

The P05 Imaging Beamline for X-ray micro- and nanotomography is situated at the newly refurbished PETRA III 3rd generation storage ring at DESY. A dedicated experiment for X-ray nanotomography at higher energies was built in one of the two experimental hutches. An X-ray optics concept tailored for this experiment was specified and an accompanying mechanics concept was devised. Based on these concepts, the experiment was designed and installed.

In addition to testing the nanotomography experimental components, the beamline front end was commissioned and the influence of these components on the nanotomography experiment was investigated. Higher harmonics from the undulator and monochromator as well as beam position drifts caused by mechanical drifting the monochromator were investigated to analyze their influence on the nanotomography. The X-ray optics were tested in detail and an operational setup was achieved for both the X-ray microscopy and the cone-beam setup. The achieved resolution of the hard X-ray microscope is better than 100 nm line and space.

Nanotomographies were performed on a nanoporous gold sample and a photonic glass sample. Image correlation and correction allowed to perform a reconstruction of the photonic glass sample using a filtered backprojection algorithm. The packing fraction η of the photonic glass could be successfully extracted from the 3D-dataset.

Entwicklung und Aufbau eines Nanotomographie-Experiments an der PETRA III Strahlführung P05

Zusammenfassung

Nanotomographie mit Röntgenstrahlung wird genutzt, um Materialen auf der Submikrometerskala zu untersuchen. Viele weiche biologische Proben, d.h. die allermeisten organischen Gewebe, können mit weicher Röntgenstrahlung untersucht werden. Um Materialien mit einer höheren Elektronendichte, wie zum Beispiel Knochen und Zähne, Metalle oder Keramiken, untersuchen zu können, sind Energien der Röntgenstrahlung von mehr als 10 keV nötig. Für alle Experimente sind Röntgenoptiken nötig, um entweder direkte Abbildungen des Objektes zu erlauben oder um vergrößerte Projektionen zu erstellen.

Die P05 Strahlführung *Imaging Beamline* für Mikro- und Nanotomographie ist aufgebaut am erneuerten PETRA III Speicherring am DESY. Eine der zwei Experimentierhütten beherbergt ein eigenes Nanotomographie-Experiment bei höheren Röntgenstrahlungsenergien. Es wurde ein Konzept für die Röntgenoptiken dieses Experiments erstellt und ein damit einhergehendes mechanisches Konzept ausgearbeitet. Ausgehend von diesen Konzepten, wurde das Experiment entwickelt und aufgebaut.

Neben Tests der einzelnen Komponenten für das Nanotomographie-Experiment wurde außerdem das *Frontend* der Strahlführung in Betrieb genommen und der Einfluss dieser Komponenten auf das Nanotomographie-Experiment untersucht. Höhere Harmonische, welche durch Undulator und Monochromator entstehen, sowie Strahllageschwankungen — bedingt durch mechanisches Driften im Monochromator — wurden untersucht, um ihren Einfluss auf die Nanotomographie zu charakterisieren. Die Röntgenoptiken wurden detailliert überprüft. Es wurde ein erfolgreiches Experiment sowohl im Röntgenmikroskopie-Aufbau als auch im *Cone-beam*-Aufbau durchgeführt. Das Mikroskop für harte Röntgenstrahlung erreichte eine Auflösung von 200nm pro Linienpaar.

Nanotomographie-Messungen wurden an nanoporösem Gold und einem photonischen Glass durchgeführt. Bildkorrelationen und -korrekturen ermöglichten eine Rekonstruktion des photonischen Glases unter Nutzung des Prinzips der gefilterten Rückprojektion. Die Packungsdichte η des photonischen Glases konnte erfolgreich aus dem 3D-Datensatz bestimmt werden.

Manuscript received / Manuskripteingang in Druckerei: 10. Juni 2015

Contents

List of abbreviations

CT	computed tomography
DCM	double crystal monochromator
DESY	Deutsches Elektronen–Synchrotron
DMM	double multilayer monochromator
FBP	filtered backprojection
FFT	fast Fourier transform
FIB	focused ion beam
FWHM	Full width at half maximum
FZP	Fresnel zone plate
HZG	Helmholtz–Zentrum Geesthacht
IBL	Imaging Beamline
IMT	Institute of microstructure technology (at KIT Karlsruhe)
KB	Kirkpatrick–Baez
KIT	Karlsruhe Institute of Technology
LIGA	german acronym for Lithographie, Galvanik und Abformung — name used by the IMT for the X–ray lithography process
MLL	multilayer Laue lens
NA	numerical aperture
RMS	root mean square
RXPL	rolled X–ray prismatic lens
SEM	scanning electron microscopy / microscope
SFB986 M^3	Sonderforschungsbereich 986 – Tailor–Made Multi–Scale Materials Systems
TEM	transmission electron microscopy / microscope
VI–NXMM	Helmholtz Virtual Institute New X-ray analytic methods in material science

Chapter 1

Introduction

Tomography is a technique for non–destructively measuring the three–dimensional internal structure of objects. It is used worldwide to answer scientific questions in a wide range of fields such as materials science, medicine, or biology. In addition, tomography is a well–established method in industry for process control and optimization and for quality assurance of products. While the tomographic principle can be used with any probe interacting with the sample, the majority of applications use X–rays. Neutron tomography for materials science or nuclear magnetic resonance and positron emission tomography in medicine are other common probes. Sample sizes vary over several orders of magnitude, from complete motor blocks or turbine parts down to samples with a diameter of only several micrometers. Limits in sample dimensions are imposed by the probe transmission of the sample and the instrument setup and resolution. As an illustration, neutron transmission is high for high–Z materials, for example making it a good choice for large metallic samples. However, the low interaction of neutrons with matter also makes the detection difficult, requiring thick converters which limit the achievable resolution. For this reason, high spatial resolution tomography is basically limited to X–rays.

The principle of tomography was first presented by Hounsfield in 1973 [49] as a clinical application using an X–ray tube. Advances in the detection hardware and computing power have improved the resolution of medical computed tomography (CT) systems, however the general layout of the system has not changed and has even been adapted in many laboratory CT setups for scientific questions. Starting in the 1980s, first CT experiments have been performed at synchrotron radiation sources by Bonse et al. [11] and Flannery et al. [34]. In comparison to laboratory X–ray sources, storage rings offer a photon flux increase of several orders of magnitude and a highly monochromatic beam. In the last twenty years, many dedicated synchrotron micro tomography (SR–μCT) endstations have been built and the lower resolution limit is constantly being pushed. μCT routinely achieves resolutions of down to about 0.7 μm, limited by the optics/detector combination.

For even higher resolution, magnifying X–ray optics are needed, and the technique is called X–ray microscopy. Different X–ray optics allow for resolutions of below 50 nm over a large spectrum of energies. Combining X–ray microscopy with the tomographic principle allows for investigating the three–dimensional structure of matter on length scales of below 100 nm. The fabrication of high quality imaging X–ray optics for X–ray energies of up to 10 keV is easier than for higher energies. The energy range below 10 keV is well suited for biological and soft condensed matter samples but cannot be used for many materials science questions, for example with metallic or ceramic samples. The Helmholtz–Zentrum Geesthacht (HZG) and Karlsruhe Institute of Technology (KIT) are partners in the Helmholtz Virtual Institute *New X-ray Analytic Methods in Materials Science* (VI–NXMM) and one of the goals is the development of refractive X–ray optics for imaging applications at energies of up to 30 keV.

X–ray nanotomography experiments in this X–ray energy regime exist at only a few facilities worldwide, for example the ESRF nano–imaging experiment at ID22/ID16 [82, 86], the TOMCAT beamline at the SLS [127, 128] or the APS 32–ID [103, 109, 132]. At PETRA III, a holotomography experiment is installed at P10 [6, 99], in addition to the P05 nanotomography endstation presented in this work. The scientific importance of the materials science questions addressed at the P05 instrument is further underlined by the fact that existing experimental stations are being upgraded to allow nano–imaging at higher energies and most large synchrotron facilities which have no nano–imaging experiment yet plan to build dedicated nano–imaging endstations or beamlines.

The Helmholtz–Zentrum Geesthacht (HZG) has a strong interest in engineering materials science and routinely uses X–ray methods such as diffraction and tomography to complement other in–house techniques for materials science. HZG is involved at the refurbished storage ring PETRA III, operated by DESY, with a High Energy Material Science beamline and an Imaging Beamline dedicated to tomography. One of the aims of the Imaging Beamline is offering nanotomography capabilities for engineering materials science that routinely achieves resolutions of 100 nm.

The goal of this thesis was the design, installation, and commissioning of a nanotomography experiment at the new PETRA III beamline P05, starting with a letter of intent and finishing with a successful nanotomography measurement.

The Imaging Beamline P05 (IBL) is designed to house two dedicated experiments: a micro tomography experiment using the direct monochromatic beam showing resolutions down to below 1 µm and a dedicated nanotomography experiment employing X–ray optics. The global beamline layout is presented in Chapter 4.

In this work, the specifications and requirements for a nanotomography endstation at the PETRA III storage ring were worked out. It was necessary to develop an individual optics concept adapter to the beamline P05, accounting for its source parameters and spatial constraints—positions of the hutches and space in the hutches. Within the VI–NXMM mentioned above, re-

fractive X–ray optics were selected as the X–ray optics to be used in this experiment. The optics concepts for cone–beam and X–ray microscopy setups were worked out and are introduced in Section 5.1. The optics positions and alignment requirements set a framework for the mechanics. The specifications for the latter had to be worked out and an overall mechanics concept had to be developed. Design consideration and mechanical solutions are presented in Section 5.2.

Following the installation of the experiment, the nanotomography endstation has been commissioned. For a properly working nanotomography, several of the new general beamline components such as undulator and monochromator had to be tested and fully understood to best use the capabilities of these devices and to bar any possible problems from influencing the nanotomography. Chapter 6.1 discusses the front end installations and their influence on the experiment. The optics were tested in detail and these results are presented in Sections 6.2 and 6.3.

A test experiment of the cone–beam setup was performed for demonstrating the feasibility and is presented in Section 6.4. Flat resolution test patterns were used to analyze the performance of the X–ray optics in the X–ray microscopy setup and are shown in Section 6.5. The experimental setup has been used to perform first nanotomography measurements on two samples of the SFB 986 *Tailor–Made Multi–Scale Materials Systems* [115]: A nanoporous gold sample and a photonic glass. The scientific goals were the determination of the three–dimensional morphology ligament network and of the particle packing fraction, respectively. After the successful acquisition of a tomography dataset, the images needed to be corrected and correlated before a reconstruction could be performed. The nanotomography results are discussed in Section 6.6.

A short summary of the obtained results and an outlook at the next steps to further improve the performance of this experiment are given in the conclusion in Chapter 7.

Chapter 2

Overview of X–ray properties

As the instrument described in this thesis is installed in a beamline at the PETRA III storage ring and uses X–ray generated in this ring, the physical background of the X–ray generation in a synchrotron and storage ring and its interaction with matter will be reviewed in this chapter. For more information about the storage ring itself, please refer to Appendix A. Following, common optical elements for X–rays and their working principles will be discussed. A comparison of the different types of optics and their applicability for the instrument presented later on will close this chapter.

2.1 X–Ray generation in a storage ring

Electromagnetic fields can be used to change the trajectories of charged particles, e.g. electrons. The change of the particle trajectory is equivalent to the particle being accelerated. As electrodynamics show, any accelerated charged particle creates an electromagnetic field, i.e. photons.

Theoretical works about the radiation emitted by charged point sources were published as early as 1898 [76, 110]. For synchrotrons, the special case of a circular orbit has to be considered and the most important results of later theoretical investigations are: (a) for any given particle, the emitted synchrotron radiation energy per orbit is proportional to the fourth power of the particle energy, and (b) the synchrotron radiation is mainly concentrated in a forward cone with the opening half–angle θ_{rad} of

$$\theta_{rad} \approx \sqrt{1 - \frac{|\mathbf{v}|^2}{c^2}}, \tag{2.1}$$

where $\mathbf{v}$ is the velocity vector and c the speed of light [146]. Using the standard relativistic nomen-

clature of

$$\beta = \frac{|\mathbf{v}|}{c}$$
$$\gamma = \frac{1}{\sqrt{1-\beta^2}},$$

it is:

$$\theta_{rad} \approx \frac{1}{\gamma}. \tag{2.2}$$

The emitted power is further dependent on particle charge and particle rest mass, but these are obviously no variables to be controlled. The critical wavelength λ_c of the emitted radiation is defined as half of the power being emitted each below and above the critical wavelength.

$$\lambda_c = \frac{4\pi R}{3}\left(\frac{m_0 c^2}{E}\right)^3, \tag{2.3}$$

with R the radius of curvature of the path and m_0 the particle rest mass.

In a classical ring orbit, bending magnets—installed to allow a roughly circular particle orbit—emitt the power evenly over the whole plane of the ring, giving very little flux for any fixed position. To increase the available flux for specific points—in which the experiments will be set up—, periodic magnet structures can be used. These structures are inserted in straight sections of the storage ring and are called insertion devices. While these devices all have the same basic layout, they are classified as either wigglers or undulators, depending on the layout and the magnetic field strength. The dimensionless quality K is known as wiggler or undulator parameter:

$$K = \frac{\lambda_u e B_{max}}{2\pi m_e c}, \tag{2.4}$$

with λ_u length of the magnetic periods, e the electron charge, m_e the electron rest mass, c the speed of light, and B the maximum magnetic field strength in the electron beam plane. Figures 2.1 and 2.2 schematically show the layout and principle of a wiggler/undulator.

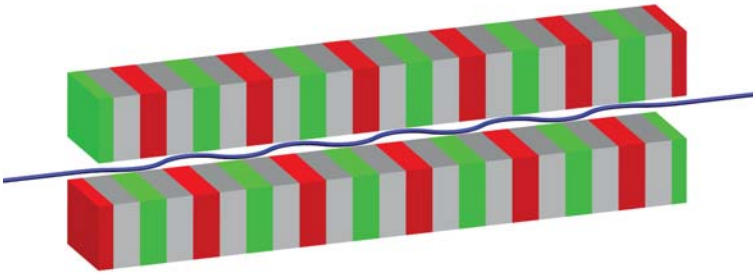

Figure 2.1: Schematic layout of an wiggler or undulator. The alternating magnet structures (colored in red and green) force the particle on an oscillating path, marked in blue.

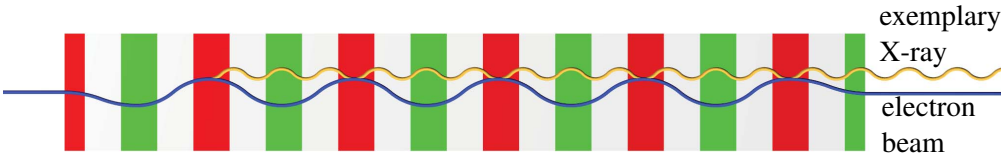

Figure 2.2: Top view of the electron trajectory in an undulator. Due to the periodic, alternating magnet field, the electron oscillates around the undisturbed trajectory. The acceleration forces the electron to emit electromagnetic radiation. If a multiple of the emitted wavelength $n\,\lambda$ matches the magnet structure period, all emissions are in phase and the distinct undulator lines appear.

The maximum angle of the particle trajectory with the orbit is given by [146]

$$\theta_{orbit} = \frac{\lambda_u e B_{max}}{2\pi m_e c \gamma} = \frac{K}{\gamma}. \tag{2.5}$$

Thus, for K = 1, the opening angle of the radiation (Equation 2.2) is equal to the angle of the particle trajectory with the orbit. The value $K = 1$ is used to separate insertion devices is undulators for $K \leq 1$ and wigglers for $K > 1$.

The details of radiation generation differ for both devices. A wiggler uses a strong magnetic field to generate a broad continuous spectrum by strongly changing the particle trajectory and thus enforcing a high emission, whereas the undulator has sharp emission lines. These lines are created through self–amplified emission. The magnetic field is designed in such a way that — as the particle moves on its trajectory through the periodic field — the particles meet their own emitted field in phase, but with n field oscillation delay and the resulting interaction increases the emission of further photons at these specific energies. For details, please refer for example to the book by Wille [146]. Examples of wiggler and undulator spectra are given in Figure 2.3. While

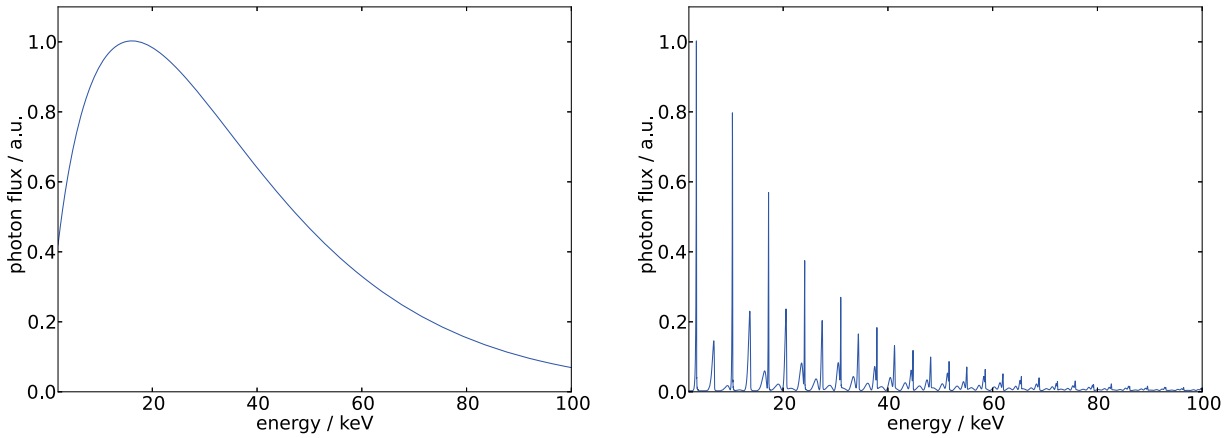

(a) wiggler **(b)** undulator

Figure 2.3: Exemplary spectra for a wiggler and an undulator. Note that the peak intensity is several orders of magnitude larger for an undulator as compared to a wiggler operating under similar conditions. Simulations were performed using Xop and the XUS and XWIGGLER packages [18–21].

all undulators also feature an underlying wiggler spectrum, the peak intensity of the undulator radiation lines is stronger by several orders of magnitude.

2.2 X–Ray interaction with matter

The interaction of X–ray with matter is similar to any other electromagnetic wave and all optical laws and concepts apply. A short overview of the basic physical interaction processes is given in Appendix B. This section concentrates on the processes and concepts that are important for X–ray imaging and X–ray optics.

For a more detailed description, please refer to the book by Als–Nielsen and McMorrow [2] or similar works.

2.2.1 Complex refractive index

In the X–ray energy regime, the complex index of refraction is commonly written as

$$n = 1 - \delta + i\beta. \tag{2.6}$$

This is due to the fact that the real part of the refractive index is close to 1 ($\delta \approx 10^{-5}$ for solids down to $\delta \approx 10^{-8}$ for gases) and the imaginary part is typically in the range of $10^{-5} - 10^{-6}$ for hard X–rays. The real part of n is responsible for reflection and refraction phenomena as well as for phase shifts whereas the imaginary part of n leads to an absorption of the wave. The parts δ and β of the refractive index are linked to the forward scattering atomic form factor (compare Equation B.2) [2]:

$$\delta(\omega) = \frac{2\,\pi\,c^2\,n_a\,r_e}{\omega^2} f_1^0(\omega) \tag{2.7}$$

$$\beta(\omega) = \frac{2\,\pi\,c^2\,n_a\,r_e}{\omega^2} f_2^0(\omega), \tag{2.8}$$

with the classical electron radius r_e, atomic number density n_a and atomic form factor parts f_1^0, f_2^0. The atomic form factor f and its parts are explained in more detail in Appendix B.2.

2.2.2 Attenuation

The quantitative attenuation, commonly referred to as absorption, in a sample of thickness z is given by Beer's law:

$$I(z) = I_0\,\exp\left(-\mu z\right) \tag{2.9}$$

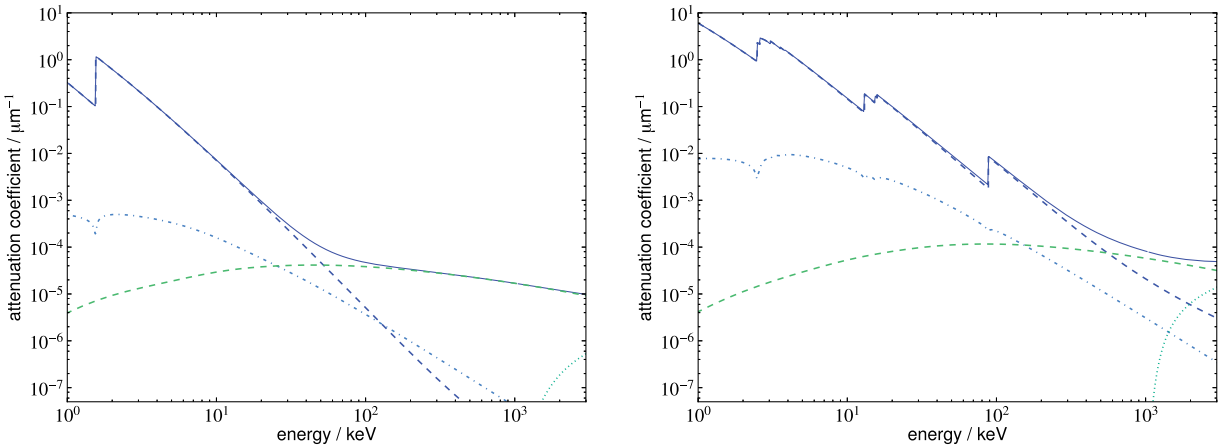

(a) X–ray interaction cross section of aluminum **(b)** X–ray interaction cross section of lead

Figure 2.4: The interaction cross sections of aluminum and lead as exemplary light and heavy elements. The blue solid line is the sum of all contributions. All contributions are also shown separately: photoelectric absorption (blue dashed line), Compton scattering (green dashed line), elastic scattering (light blue dashed/dotted line), and pair production (green dotted line). Cross–sections adapted from EPDL97 [17].

with μ, I, and I_0 the linear absorption coefficient, the transmitted intensity, and the starting intensity, respectively. For a more detailed derivation, please refer for example to [2].

In case of a varying attenuation coefficient, the transmission can be described by the integral of the local attenuation coefficient μ_{local} over the beam path in the sample:

$$I(z) = I_0 \exp\left(-\int_0^z \mu(y)dy\right). \tag{2.10}$$

The total attenuation μ_{total} is a combination of the following effects: Rayleigh scattering, Compton scattering, photoelectric absorption, and pair production. The attenuation coefficient μ_{total} is linked to the interaction cross–section σ_{total}:

$$\mu_{total} = \sigma_{total}\, n \tag{2.11}$$

with the atom number density n. The total cross section σ_{total} is the sum of the individual interaction cross–sections:

$$\sigma_{total} = \sigma_{PE} + \sigma_R + \sigma_C + \sigma_{PP} \tag{2.12}$$

and thus:

$$\mu_{total} = \mu_{PE} + \mu_R + \mu_C + \mu_{PP} \tag{2.13}$$

The individual contributions vary strongly with energy, as well as the relative strength of the effects with respect to each other. Examples are given in Figure 2.4 for some materials. For best statistics

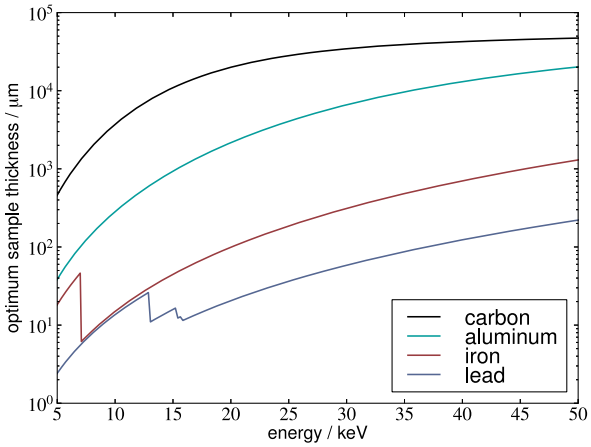

Figure 2.5: Relationship between X–ray energy and the sample thickness for highest imaging statistics ($d = 2/\mu$). Typical sample diameters are 50-500 µm for the nanotomography; the x-axis covers the accessible energy range at the Imaging Beamline. Cross–sections adapted from EPDL97 [17].

Element	Thickness / µm	Optimum energy / keV	$\sigma_{coh}/\sigma_{total}$	$\sigma_{inc}/\sigma_{total}$	$\sigma_{pho}/\sigma_{total}$
Carbon	200	3.8	1.14%	0.18%	98.6%
Carbon	500	5.1	2.0%	0.58%	97.4%
Aluminum	200	8.8	1.80%	0.26%	97.9%
Aluminum	500	12.2	3.0%	0.80%	96.2%
Iron	200	25.8	3.0%	1.0%	96.0%
Iron	500	35.5	4.4%	2.6%	93.0%
Lead	200	48.2	7.4%	1.1%	91.5%
Lead	500	120.4	4.1%	2.8%	93.1%

Table 2.1: Comparison of total attenuation cross–section contributions of the different physical processes. As most samples will be around or even below 200 µm in diameter, the contribution of the photoelectric absorption will become even higher. As pair production does not occur below 1.024 MeV, it is omitted in this table. Cross–sections adapted from EPDL97 [17].

in imaging, the energy should be selected such that the minimum sample transmission is e^{-2} [42], i.e. that the ideal sample thickness is $d = 2/\mu$. As the linear attenuation coefficient is a function of the X–ray energy, it is possible to find a corresponding energy for every sample composition and thickness. Figure 2.5 shows that the X–ray energy range of 8—25 keV and sample thicknesses of 100—500 µm are ideally suited for the investigation of many materials investigated in advanced material sciences, e.g. light–weight materials such as aluminum or titanium or implant materials such as magnesium. Table 2.1 shows the corresponding energies for certain elements and the contributions of the different effects to the total interaction cross section. For sample diameters well below 1mm, the photoelectric effect is dominating. Considering imaging applications, it is important that interaction is limited to a single process. Double scattering, for example, can lead to intensity being scattered back in the beam direction, yielding misleading results.

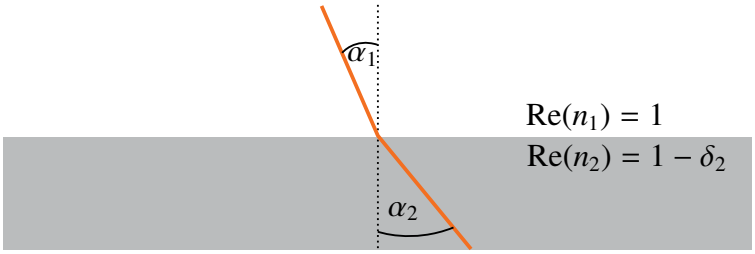

Figure 2.6: Schematic of X-ray beam refraction at an interface. Only the real part of the complex refractive index is written.

2.2.3 Refraction

The real part of the complex refractive index is responsible for refraction of the beam if it crosses a boundary. This is due to the different group velocity in a medium as compared to vacuum. Snell's law,

$$\frac{\sin\alpha_1}{\sin\alpha_2} = \frac{\mathrm{Re}\, n_2}{\mathrm{Re}\, n_1} \tag{2.14}$$

is also applicable for the X–ray energy regime. Using the nomenclature from Equation 2.6, it is

$$\frac{\sin\alpha_1}{\sin\alpha_2} = \frac{1-\delta_2}{1-\delta_1}. \tag{2.15}$$

The main difference when compared to the visible light energy range is that the real part of n is smaller for materials with a higher electron density (i.e. optically denser materials), meaning that—unlike with visible light—the beam will be refracted towards the surface normal when passing from a denser to a less dense medium. Figure 2.6 shows a sketch of a refracted X-ray beam. The change of the electromagnetic waves in materials can be used both for imaging techniques (see for example [7, 48]) and for X–ray optical elements (see Section 2.3.5).

2.3 X–Ray optics

Long after the discovery and the use of X–rays for imaging applications and diffraction experiments, optical elements for X–rays were still largely unknown. This is mainly due to the fact that absorption is prominent compared to other effects and that the necessary precision in the fabrication of optics has been a limiting factor for a long time. First experiments with focusing mirrors came up in the 1940s [27] and very soon, Kirkpatrick and Baez published their proposed setup for X–ray focusing using a combination of mirrors [59], nowadays known as Kirkbatrick–Baez mirrors (or short KB-mirrors). The use of lenses was also mentioned by Kirkpatrick and Baez but dismissed as being unfeasible [59]. Advances were also made with regard to other reflective optics such as capillaries and in diffractive optics such as Fresnel zone plates. The latter is mostly limited to soft X–rays due to the difficulties of fabricating thicker zone planes necessary for higher

energies.

Serious consideration of lenses for X–ray focusing started not before the early 1990s [131] and were soon seriously disputed [83]. First successful tests with X–ray lenses have been made by the mid-1990s using the concept of compound lenses [28, 29, 75, 123, 124] to overcome the limited focusing abilities of single lenses.

The different concepts for X–ray optics and their advantages and disadvantages will be discussed in detail below. Note that only the most prominent and relevant concepts are presented and no claim of completeness is made.

2.3.1 Reflective mirror optics

All reflective optics is based on the fact that electromagnetic waves can be totally reflected in the optically denser material at the boundary between two materials. As the real part of the complex reflective index is less than 1, vacuum is the densest optical material for X–rays, followed by gases. I.e. total reflection can occur at any surface separating vacuum or air from a solid body. The critical angle for total reflection is, however, very small and typically in the range below 1°.

Considering the case of the reflected beam running parallel to the reflecting surface ($n_1 = 1$, $\alpha_2 = 90°$) and substituting these values in Snell's law (Equation 2.15), it is

$$\frac{\sin\alpha_1}{\sin 90°} = \sin\alpha_1 = \frac{\mathrm{Re}\, n_2}{\mathrm{Re}\, n_1} = 1 - \delta_2. \tag{2.16}$$

As α is measured from the normal to the surface, substituting α with the angle θ measured from the surface, it is $\theta = 90° - \alpha$ and

$$\sin\alpha = \cos\theta.$$

Thus, we have

$$\cos\theta = 1 - \delta \tag{2.17}$$

Using the second–order Taylor expansion for the cosine:

$$\cos\theta \approx 1 - \frac{\theta^2}{2} \tag{2.18}$$

and substituting in 2.17

$$\sin\theta = \sqrt{2\delta}. \tag{2.19}$$

θ is the critical angle at which total reflection occurs. This angle is often also termed α_c. For lower incidence angles, the beam is reflected almost totally. Surface roughnesses and contaminations

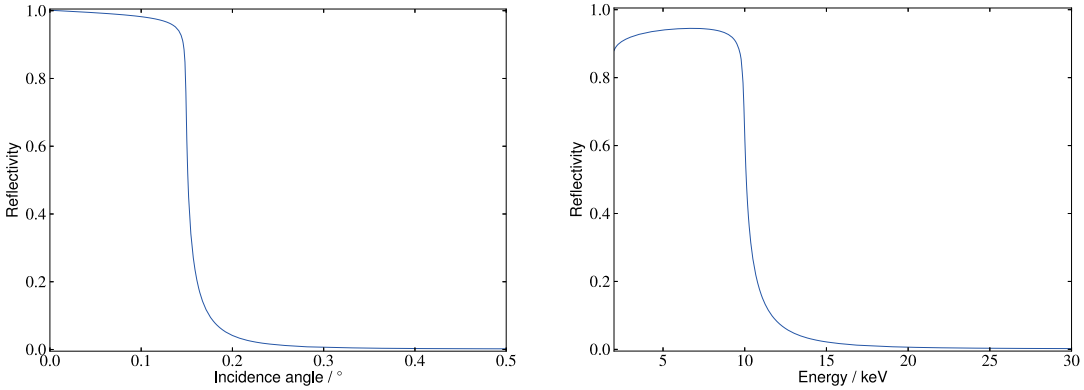

(a) Reflectivity for X–rays of $E = 12$ keV **(b)** Reflectivity at a fixed angle of incidence $\theta = 0.18°$

Figure 2.7: Reflectivity plot for a silicon mirror with a surface roughness of 0.2 nm (RMS). The data in (a) shows a plot of a fixed energy and shows the fast drop in reflectivity at the critical angle. (b) shows the reflectivity data of different X–ray energies at a fixed angle. (data from [45])

(e.g. dust) as well as the absorption in the reflecting medium all reduce the reflectivity to a value < 1. An example of a reflectivity curve is given in Figure 2.7.

Higher order suppressing mirrors

For an undulator synchrotron radiation source, X–ray energies always appear in harmonics, the strong peaks being the odd harmonics. If an energy E_0 is selected as the fundamental, 3 E_0, 5 E_0,7 E_0, ... will be present as well (see Chapter 2.1 and Figure 2.3b). If a mirror is aligned in such a way that the angle of incidence for E_0 is just a little below the critical angle, higher harmonics can be suppressed as the reflectivity for these energies is near zero (compare Figure 2.7).

Focusing mirrors

Historically, mirrors were first used as direct X-ray microscopes, creating magnified object images. Nowadays, mirrors are primarily used as focusing devices and not for direct imaging applications. For focusing, a curved mirror surface is used. As the incoming and outgoing beam have the same angle with respect to the mirror surface and the local incidence angle changes over the mirror position, the incoming rays are diverted from their paths towards a common point. This is exemplarily shown in Figure 2.8.

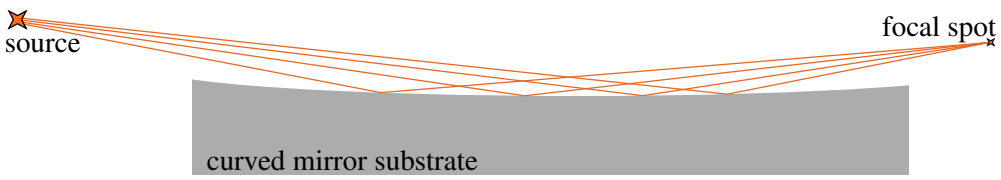

Figure 2.8: Schematic drawing of a X–ray reflection from a curved mirror surface.

A mirror with an elliptical surface and the X–ray source in the first and the X–ray focus in the ellipse's second focal point would gather all rays emitted from the source in the focus. Depending on the detailed form of the ellipse (eccentricity and curvatures), the distances between the ray's point of incidence and the focal points can vary and allow a magnification or demagnification. If an object is set in one focal point of the source, the (magnified) image can be found in the second focal point. If, however, the X–ray source is put in the ellipse's first focal point, a (demagnified) image of the source is found in the second focal point. If the dimensions are chosen properly, this allows source demagnifications of more than a factor of 1000, creating nanometer sized X–ray spots.

As the rays' angles with the surface must remain sufficiently small for total reflection ($<< 1°$), the ellipse has to be very eccentric. This poses severe problems in the design and fabrication of such devices so that generally spherical surfaces are the preferred option. While non–elliptical mirrors are feasible, these forms raise the problem of spherical aberrations. The problem increases with larger (de)magnifications but decreases with a larger incidence angle [59]. Materials with higher electron densities allow larger incidence angles, making them more suited for X–ray mirrors. Because of this fact, X–ray mirrors are typically coated with a dense metal like platinum.

As the radius of curvature is very large, the ellipse can be locally well approximated by a circle. Furthermore, a spherical surface can be slightly mechanically deformed to approximate an ellipse even better. This is the state–of–the–art setup as used in synchrotrons. The optical distances of such a spherical mirror are given by the following equation [59]:

$$\frac{1}{f\left(1+\frac{a}{2}\right)} = \frac{1}{q+2\,a\,f\,g} + \frac{1}{p-2\,a\,f}\left(\frac{2-a}{2+a}\right), \tag{2.20}$$

$$f = \frac{R\sin\theta}{2}, \tag{2.21}$$

$$a = \frac{\alpha}{\theta}. \tag{2.22}$$

q and p are the distances source–mirror and mirror–focus, respectively. The radius of curvature is denoted R; the opening angle of the mirror surface from the mirror's center is named α, with the angle of incidence of the X–ray beam θ. Typical curvature radii R are $\gg$ 1km with mirror surface lengths $\approx$ 20 cm, thus $\alpha \approx 0$. Under this premise, Equation 2.20 simplifies to

$$\frac{1}{q} + \frac{1}{p} = \frac{1}{f}. \tag{2.23}$$

The focal length f (compare Equation 2.21) depends only on the angle of incidence θ and the mirror curvature. As long as the X–ray energy is low enough, i.e. the incidence angle θ is smaller than the critical angle α_c: $\theta < \alpha_c(E)$, the focal length does not depend on the X–ray energy. The effect of a fixed focusing distance independent of the wavelength is called achromaticity and it is

one of the major advantages of mirrors for X–ray focusing.

For two–dimensional focusing, there are in principle two options. First, a single mirror can be designed with a two–dimensional surface contour. While this allows an optics setup with only one component, preparation and production of such a mirror is technically very difficult. Both the form accuracy and surface smoothness pose very high demands of the fabrication and the achieved quality is not yet sufficient for nanofocus application. Furthermore, it would be very difficult to bend such a mirror in both dimensions independently for best performance, i.e. the correction of minor form errors is very difficult. The second option consists of two crossed mirrors, each focusing in one dimension. This setup, known as Kirkpatrick–Baez mirrors (short KB mirrors) was already introduced in 1948 [59] and is the standard setup for mirrors. As the mirrors are placed behind one another, the system has inherently different focusing lengths for the horizontal and vertical plane. This has to be compensated by a different curvature of the mirrors and finetuning can be performed by altering the curvature radii through bending the mirrors.

2.3.2 Capillary optics

While not commonly used at synchrotrons, capillary optics are an option for micrometer–sized focal spots. Based on total reflection at the capillary walls, they allow for spot sizes down to a few micrometer [3, 133]. There are two general types of capillary optics. Monocapillaries with tapered cross–sections and a single reflection and bundles of capillaries — called polycapillaries— in which the beam is reflected more than once on the walls.

Polycapillaries offer an increased gain, i.e. they collect more photons in the focus, but with the drawback of an increased focal spot size [10].

Monocapillaries

Tapered monocapillaries are used to reach the goal of a small focal spot. The cross–section constantly shrinks over the length of the capillary, leading to a smaller beam. In addition, the wall profile is designed for all reflected beams to be focused on one point. Figure 2.9 schematically shows the working principle of a mono–capillary. The advantage of these elements is that they act as imaging optics for points near the optical axis, i.e. they are suited for microscopy applications.

The attainable spot sizes are limited due to the size of X–ray sources—even in a storage ring—, the technical difficulties of a smooth surface, and the errors in the processing. To overcome these limitations, it has been proposed to use single–bounce capillaries that use only one reflection in combination with other condenser optics that yield a demagnified image of the source. In combination with advanced production techniques to control the precise form of the capillaries [61], this allows for focal spots of down to 250 nm [120, 121].

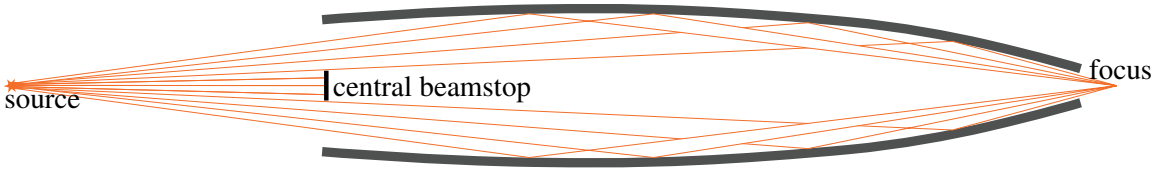

Figure 2.9: Sketch of a mono–capillary focusing optic. Total reflection on the capillary walls and the tapering of the cross–section lead to a focused X–ray beam.

Polycapillaries

For a larger acceptance angle, polycapillaries are a suitable choice [9]. In these, a large bundle of up to millions of single capillaries is arranged in such a way as to guide the X–rays through several total reflections on the capillary walls on a single spot. The layout of the capillaries is optimized for the reflection angle to stay below the critical angle, thus allowing a transmission efficiency close to 1.

The achievable focal spots are larger than those of monocapillaries, but as the acceptance angle is larger, the focal flux is increased as well. Since the beam is reflected several times on the capillary walls, these focusing elements are not suitable for imaging applications. Figure 2.10 shows the working principle of a polycapillary.

2.3.3 Waveguides

X–ray waveguides are elements that trap the electromagnetic radiation field inside a core medium and thus allows to guide the wavefield [8, 32].

One–dimensional waveguides consist of layers with different complex refractive indices. Figure 2.11 shows the layout in detail. As the real part of the refractive index is less than 1, refraction occurs away from the surface normal if $n_0 > n_i$ and again for $n_i > n_g$. If the incidence angle and the materials are chosen properly, the double refraction at the two top interfaces allows the beam to couple into the guiding layer but total reflection traps it inside. Suitable material choices are a low–Z material for the guiding layer and a higher–Z material for the interlayer. By changing the layer thicknesses of the interlayer d_i and of the guiding layer d_g, it is possible to trap only specific

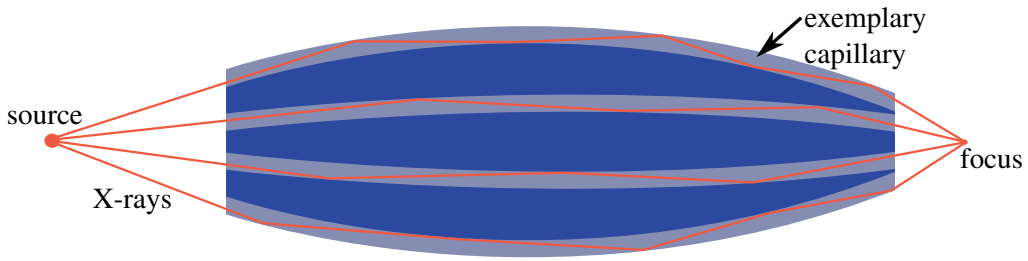

Figure 2.10: Schematic of a polycapillary focusing optics. The capillary bundle is marked in blue, four exemplary capillaries are shown in light grey–blue. The X-rays are reflected several times in each capillary until they are all guided towards the focal spot.

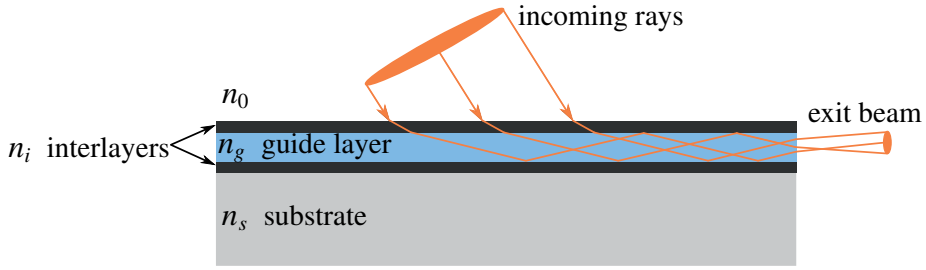

Figure 2.11: Schematic drawing of a waveguide. The beam is transmitted through the top interlayer into the guiding layer and propagates in this layer. The exit beam diameter is (in first approximation) defined by the width of the guide layer but strongly divergent.

modes of the electro–magnetic wavefield and thus to control the propagation and divergence of the focused beam [8, 32, 102].

While the theoretical transmission T of a waveguide can reach close to 1, early experimental values were often below $T = 0.1$ [62], but advances in fabrication and design have pushed experimental values up to above $T = 0.5$ [63]. Using a pre-focusing device, for example a KB mirror, the total gain of a system can be increased significantly while keeping the small spot size from a waveguide. As both KB mirrors and waveguides are principally non–energy–dispersive, this combination allows very small foci with a large energy bandpass. The increase in energy acceptance can easily balance the absorption losses inside a waveguide. Note that this last point is only of interest for applications that are insensitive to a large energy bandwidth, e.g. tomography or some diffraction experiments.

The exit spot size behind the waveguide is limited indirectly by the guiding layer thickness as this selects the captured wave mode. While the beam divergence still enlarges the focus size, beam sizes below 15 nm have already been reached for a photon energy of $E = 17.5$ keV in a setup with the sample very close to the waveguide [62, 63]. With increasing distance of the working point from the waveguide exit, the beam size strongly increases, as the divergence of the exit beam is increased with respect to the incoming beam.

2.3.4 Diffractive optics

This type of optics is based on the principle of diffraction as it occurs for example on gratings. For focusing applications, the most prominent member of this group is the Fresnel zone plate (FZP). They are routinely used for soft X–rays, but efficiency drops with higher energies so that the use for energies above approximately 10 keV is very scarce.

Multilayer mirrors can be used to monochromatize a spectrum or—in special geometries—also for focusing.

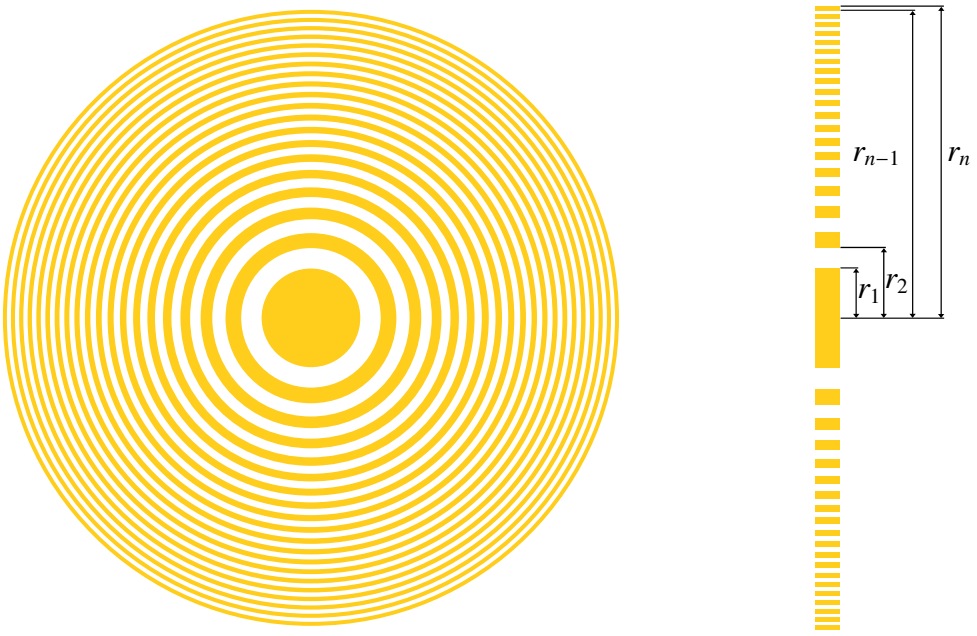

(a) Schematic top view on a zone plate. **(b)** Schematic side view on a zone plate.

Figure 2.12: Sketch of a zone plate. The radii for the different orders are marked in (b).

Fresnel zone plate

The zone plate—first described by Fresnel [35]—is binary system of ring–shaped gratings to focus the X–ray beam. These gratings can work either through absorption, i.e. the transmission is modulated or it can work as phase grating, generating a phase shift of π between adjacent regions.

A sketch of a zone plate is given in Figure 2.12. Assuming a complete absorption in one of the zone plate's regions, constructive interference in the image point is found if the optical path difference of adjacent zones is $\lambda/2$. Using the nomenclature given in Figure 2.13, it must hold that

$$p_{n+1} + q_{n+1} = p_n + q_n + \frac{\lambda}{2}. \tag{2.24}$$

Considering the total optical pathway for each zone, it is:

$$\sqrt{q^2 + r_n^2} + \sqrt{p^2 + r_n^2} = p + q + \frac{n\,\lambda}{2} \tag{2.25}$$

Solving this equation for r_n^2 yields

$$r_n^2 = \frac{n\,\lambda\,p\,q\,(p+q) + \frac{1}{4}n^2\,\lambda^2(p^2+q^2+\frac{3}{4}pq) + \frac{1}{8}n^3\,\lambda^3(p+q) + \frac{1}{64}n^4\,\lambda^4}{(p+q+\frac{n\lambda}{2})^2} \tag{2.26}$$

The radius of the zone plate increases with higher n, but $\Delta r_{n,n+1} = r_{n+1} - r_n$ diminishes with higher n. Zone plates with a large number of rings ($n \gtrapprox 100$) behave in an optically analogous way to

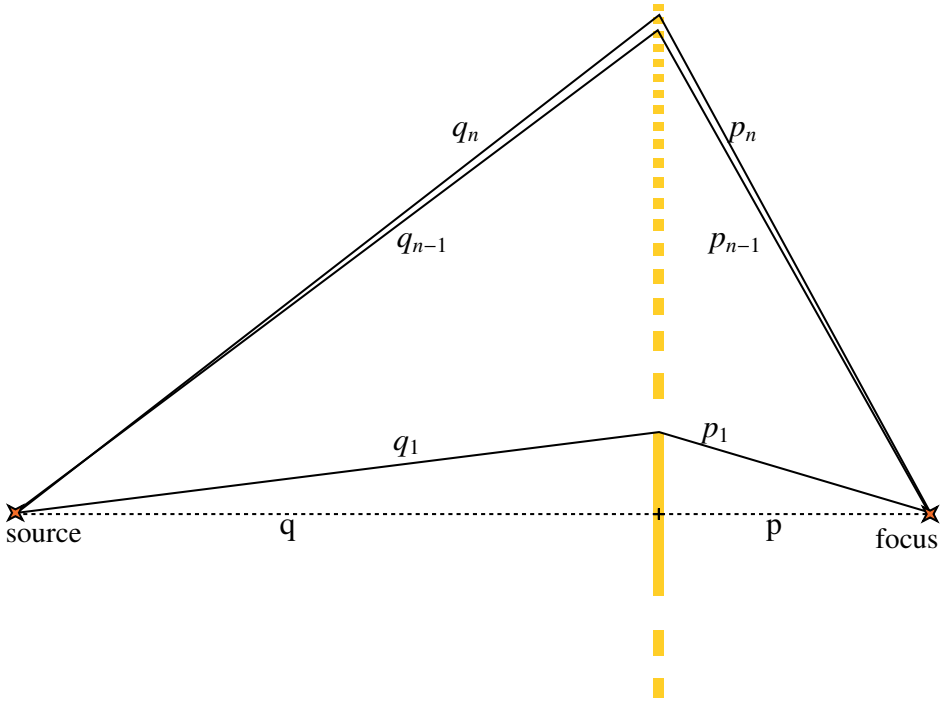

Figure 2.13: Zone plate and optical pathways.

classical lenses, i.e. it is

$$\frac{1}{f} = \frac{1}{q} + \frac{1}{p}. \tag{2.27}$$

For focusing applications it is $q \gg p$ and thus $f \approx p$. Furthermore, with focal distances in the range of mm and zone widths $\ll$ 1 µm, considering only first order terms of $n\,\lambda$, Equation 2.26 simplifies to

$$r_n^2 = n\,\lambda\,f. \tag{2.28}$$

Note that this is only valid for the first order of diffraction. As all diffractive optics, higher orders of diffraction are present. For these foci f_m of the m^{th} order of diffraction, it is

$$r_n^2 = m\,n\,\lambda\,f_m. \tag{2.29}$$

Equations 2.28 and 2.29 directly yield

$$f_m = \frac{1}{m} f. \tag{2.30}$$

The achievable resolution of a zone plate is directly linked with the numerical aperture (NA). The Rayleigh criterion [12] gives the smallest feature size Λ that can be separated to be

$$\Lambda = 1.22 \frac{\lambda}{2\mathrm{NA}}. \tag{2.31}$$

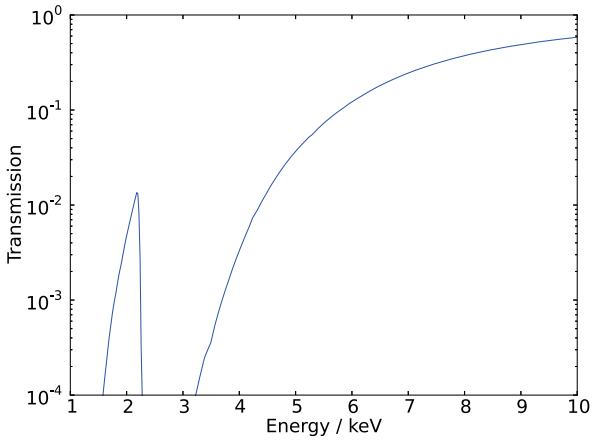

Figure 2.14: Plot of the X–ray transmission of a 2.5 µm thick gold foil. The transmission should stay well below 10%, thus limiting the energy range to below roughly 5 keV.

For zone plates, it is [143]

$$\mathrm{NA} = \frac{m\,\lambda}{2\Delta r_{n,n+1}}. \tag{2.32}$$

Substituting Equation 2.32 in Equation 2.31 gives

$$\Lambda = 1.22\frac{\Delta r_{n,n+1}}{m}. \tag{2.33}$$

As $\Delta r_{n,n+1}$ decreases with larger n, it follows that a high resolution can be achieved by using zone plates with a high number of rings n or by using high diffraction orders m. However, the intensity in each order decreases approximately with m^{-2}. This leads to only the first order being used in normal circumstances. For the first order, the achievable resolution is thus roughly equal to the smallest structure size.

For zone plates to be used effectively, the layers need to be thick enough to absorb the incoming X–rays. Assuming a smallest feasible feature size of 25 nm and an attainable aspect ratio of 100, this limits the maximum thickness to 2.5 µm. Figure 2.14 shows the transmission curve of a 2.5 µm thick gold foil. The energy range is limited to below 5 keV, as the gold foil becomes too transparent above this value. While it is possible to fabricate thicker zone plates, this also increases the minimum feature size and thus decreases the smallest focal spots. For this reason, Fresnel zone plates are commonly only used in the energy range of up to approximately 10 keV.

Multilayer mirrors

Multilayer mirrors are often used as monochromators in synchrotron beamlines. They are based on the same principle as crystal diffraction. In crystals, Bragg peak radiation occurs when the reflections from the different lattice planes interfere constructively. Not using crystal lattice planes but alternating layers of two substances yields the same result.

Figure 2.15 shows the schematic layout of a multilayer mirror. Typically, 50 – 200 layers are used with a bilayer thickness $d \approx 3$ nm. A classical material combination is platinum and silicon, but any material combination with a large difference in n is suitable; the aforementioned thickness corresponds to 5 – 6 atoms (Pt) and 6 – 7 atoms (Si). Fabrication is done by sputtering atoms on a substrate.

The theoretical description of multilayer mirrors is also done with Bragg's law

$$n\,\lambda = 2d \sin\theta \tag{2.34}$$

but with d being the layer period and not the crystal cell spacing. Typical angles for multilayer reflections are in the range of $0.5° - 5°$ (for X–ray energies 5 – 50 keV). The main advantage of these layers is the large energy bandpass they offer. Whereas silicon single crystals allow $\Delta E/E \approx 4 \cdot 10^{-4}$, multilayers can reach up to $\Delta E/E \approx 10^{-2}$. Since the undulator harmonics have a much larger energy spread, this increased energy bandwidth leads to an increase in photon flux directly proportional to the rise in $\Delta E/E$.

Plane mirrors only deflect the beam but do not act as focusing elements. If, however, the multilayer mirror surface is curved, this element can both focus the beam and monochromatize it. This combined use of a single optical element is especially interesting in imaging applications, where the total number of optical elements in the beam is to be kept small, because each element generates errors in the beam profile due to imperfections and defects.

2.3.5 Refractive optics

As the name implies, refractive optics rely on refraction at material interfaces. A typical application is focusing lenses. In contrast to optics for the visible spectrum, the real part of the complex index of refraction is smaller than one for X–rays. Thus, the resulting lens shape is different: A form that would act as a focusing lens for visible light (e.g. a biconvex lens) would enlarge the divergence of a X–ray beam and vice versa.

In addition, the differences in the (real part of the) refractive index are very small (see Section

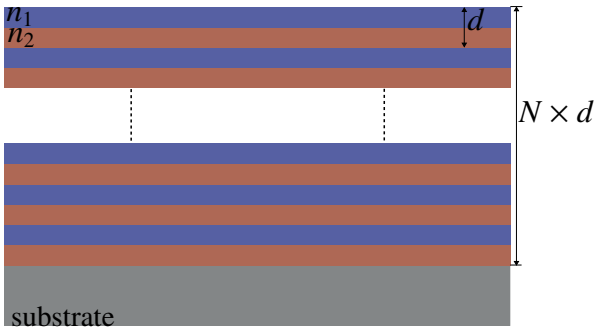

Figure 2.15: Schematic sketch of a multilayer. Alternating layers are sputtered on a substrate.

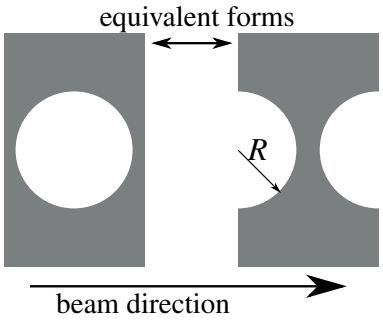

Figure 2.16: Schematic diagram of a single lens element. Optically, the biconcave lens (right) is similar to the hole (left) used as lens element. The radius of curvature is denoted R.

2.2.1) and thus only very little refraction occurs. This is countered by not using single lenses but so–called compound refractive lenses (CRLs), which are essentially an array of lenses that act as a single optical element.

Kirkpatrick and Baez already mentioned the principle of an X–ray lens in 1948 [59] but discarded the idea because of material requirements and large focal lengths. Large advances in this field did not happen until the end of the 1990s.

The first lenses produced were simple aluminum or beryllium blocks in which a number of holes have been drilled [119, 122, 123]. Because of the fabrication process, i.e. drilling, the lens shape was limited to circular holes. Light elements are used as material since the ratio δ/β is higher for low–Z materials, i.e. the amount of refraction per absorption is larger for low–Z materials.

Geometrical optics yield the resulting focal length for each lens element with a hole radius R:

$$f = \frac{R}{2\delta}. \tag{2.35}$$

Figure 2.16 shows a sketch of a single lens element and how a hole corresponds to a biconcave lens element.

The same considerations yield for an array of N lenses

$$f = \frac{R}{2\,N\,\delta} \tag{2.36}$$

and the corresponding compound refractive lens is depicted in Figure 2.17.

Due to the fabrication through drilling, these lenses are necessarily one–dimensional in focusing. To overcome this limitation, two sets of holes, rotated by 90° around the beam can be used.

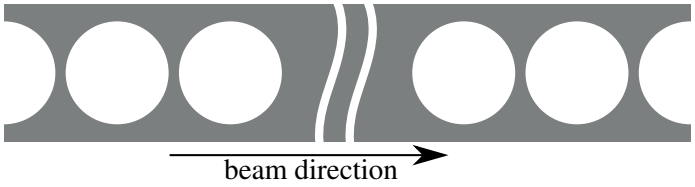

Figure 2.17: Sketch of a compound refractive lens with holes.

(a) 1d-focusing lenses

(b) 2d-focusing lenses in block layout

(c) 2d-focusing lenses with alternating structures

Figure 2.18: Schematic sketch of the first drilled compound refractive lenses.

The result is no real 2D–focusing but a set of perpendicular 1D–foci. However, as the optical properties of a system of crossed one–dimensionally focusing lenses and two–dimensional focusing lenses do not differ, this is only of interest as the two one–dimensional foci need to fall in the same transversal plane.

The first two–dimensionally focusing lenses were arranged in a row [28, 122, 124]; creating a point focus thus needs slightly different focal distances for the horizontal and vertical direction. This focal offset can be calculated and the lenses can be designed for the foci to fall into the same point but as the index of refraction is energy–dependent $n = n(E)$, or $\delta = \delta(E)$ respectively, this focal match is typically only valid for one distinct energy. Very soon, the idea of alternating single lens elements came up. These lenses inherently create a point focus and can be used for different energies[1]. Figure 2.18 shows a model of these lens forms.

The problem of the lens shape occurs in the same way as in visible light optics. First publications about an optimized lens form appeared very soon after the first lenses themselves [28, 124]. Parabolically shaped holes offer a better performance (that is mostly an increased transmission) and they reduce spherical aberrations, meaning that larger lens apertures can be used and that the size of the focal spot can be further reduced.

Let y be the offset from the lens center perpendicular to the beam propagation direction. The

[1]The focal distance still varies with the energy, but the horizontal and vertical focal lengths change synchronously

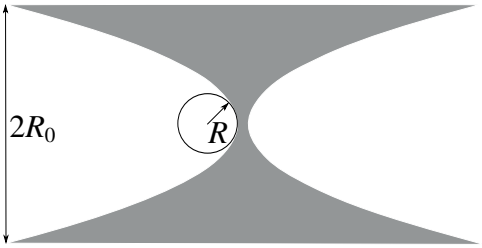

Figure 2.19: Schematic drawing of a parabolic lens profile and the radius of curvature R and the opening aperture $2R_0$.

focal length of a spherical lens is

$$f(y) = \frac{R}{2\,N\,\delta}\sqrt{1-\frac{y^2}{R^2}}. \tag{2.37}$$

It is obvious that the focal distance is roughly constant only when $y \ll R$. Thus, the useable aperture of spherical lenses is much smaller than the hole diameter.

To increase the useable aperture, a parabolic lens shape can be used. This design is practically free of spherical aberrations and it is not inherently limited in its size. A sketch of a parabolic lens shape is given in Figure 2.19. For a parabolic lens with the profile

$$y = \frac{x^2}{2R} \tag{2.38}$$

—which corresponds to the radius of curvature R in the lens center—the focal length (excluding corrections for a thick lens, see below) is given by [75]

$$f = \frac{R}{2\,N\,\delta}\left(1 - N\,\delta\left(1-\frac{u^2}{2R^2}\right)\right) \tag{2.39}$$

where u is the offset from the lens center as measured for the first lens. The correction term is typically negligible and of the order of 10^{-4} or less. The correction term for the lens thickness is [114]

$$f = f_0\frac{1}{1-\frac{1}{6}\frac{l}{f_0}} + O\left(\frac{\Delta l^2}{f_s^2}\right) \approx f_0 + \frac{L}{6} \tag{2.40}$$

where f_0 is the focal length of a similar thin CRL, f_s the focal length of a single length element, L the overall length of the CRL, and Δl the displacement of any two single lens elements.

The approximated focal length of a thick parabolic CRL is thus

$$f = \frac{R}{2\,N\,\delta} + \frac{L}{6} \tag{2.41}$$

with the radius of curvature R at the apex, N lens elements, and the total length lens L. Note that the focal distance is measured from the principal planes of the lens, located at $\pm L^2/(24 f_0)$ relative

to the center of the lens. For all practical intents and purposes, this deviation from the lens center is negligible, because the exact position of the focus distance has to be re–calibrated for every change in the optical setup. For example, a CRL of 50mm length with $f = 40$mm would have a working distance of 15mm from the lens side.

Fabrication of two–dimensional focusing lenses

The most straightforward way is using three–dimensional lenses that produce a 2d focus. These lenses can be manufactured from beryllium or aluminum using pressing techniques [73–75]. Because of the inherent symmetry around the optical axis, these lenses are easier to align and only one set is needed. Furthermore, the tool shape is very freely choosable, thus allowing e.g. parabolic lens profiles. As these lenses are pressed, however, the achievable focus quality is somewhat limited with typical values for spot sizes around 1μm. Another problem is the lens material. Because 3rd generation synchrotron radiation sources have a high portion of coherent radiation, so–called speckles can appear if the material is poly–crystalline. Single crystal or completely amorphous lenses are a solution to this problem but incompatible with pressing fabrication methods.

The most common technique in microprocessing is form generation via photo-lithography and etching of the lens forms in a substrate, e.g. silicon [13, 66, 125]. As the etching process only allows processing in one dimension, these lenses are only capable of generating a line focus. For two dimensional focusing, crossed lens packages have to be mounted in a row and thus, the horizontal and vertical foci differ.

Alternating horizontal and vertical single lens elements on one substrate are not possible using etching techniques. One way to solve the fabrication problem is using other production methods, for example deep X–ray lithography. Advantages of this technique are high structure aspect ratios, low tolerances, low surface roughnesses, and the ability to create structures with different orientations on one substrate [90–93, 107]. For crossed lenses, structures can be grown under +45° and −45° on a single substrate. Figure 2.20 exemplarily shows a schematic of the layout and the resulting X–ray lens.

Advanced lens forms

The largest problem of X–ray lenses is the high absorption. While the gain value—defined as the ratio of focused flux in the focus and the flux through a pinhole of equal size—can easily reach 10^4, the overall transmission of the lens, i.e. the flux behind the lens divided by the flux in front of the lens, is of the order of $10^{-2} - 10^{-1}$. In addition, the transmission is highest in the thin lens center and drops towards the lens sides with increasing thickness.

For most nanofocus experiments, the flux in the focal spot is the relevant parameter; however

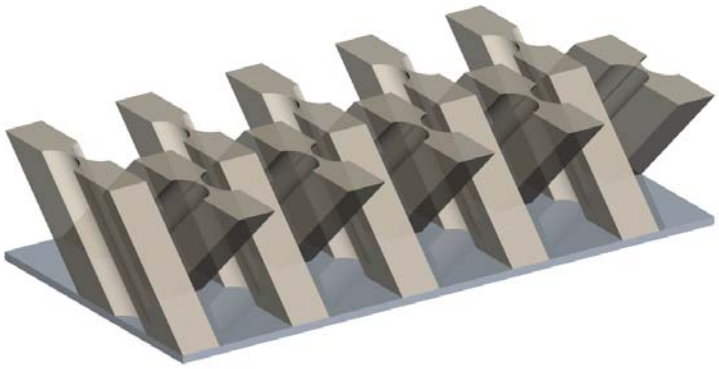

(a) Schematic sketch of crossed CRLs on a joint substrate.

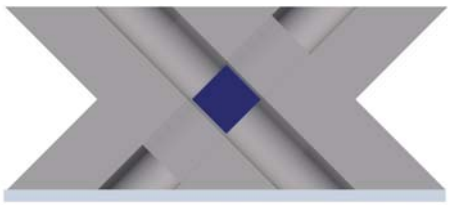

(b) Front view of the lens package. The usable X-ray aperture is marked by the blue square.

Figure 2.20: Schematic sketch of crossed CRLs on a joint substrate. (a) shows the general layout, while (b) shows which part of the structures is used for X-ray focusing.

imaging applications need an evenly illuminated field of view and thus, the overall transmission is of high importance.

While lenses with a large aperture can be produced rather easily, the limiting factor in performance is the increasing thickness. As the transmission drops in the outer, thicker regions, these parts do not play any role for the optical characteristics of the lens. The effective lens aperture is given by [75, 113, 114]

$$D_{eff} = 2R_0 \sqrt{\frac{1}{a_p}\left(1 - \exp(-a_p)\right)}, \quad a_p = \frac{\mu N R_0^2}{2R} + \frac{N \delta^2 k_i^2 \sigma^2 R_0^2}{R^2} \tag{2.42}$$

with the geometric aperture R_0, apex radius of curvature R, linear attenuation coefficient μ, incoming wave number k_i, average (RMS) roughness of the lens surface σ, number of lens elements N, and index of refraction decrement δ.

As the effective aperture is dependent on the material choice, X–ray energy, and fabrication quality (surface roughness), D_{eff} poses the real limit in lens size and forms. Figure 2.21 exemplarily shows the calculation results for a polymer CRL. In this case, the effective aperture in the energy range 5–50 keV is limited to around $80 - 100\,\mu m$.

To increase the useable aperture, the absorption has to be reduced. The easiest way to achieve this result is to alter the lens form. Lenses work by refraction at the interfaces and by phase–shifting

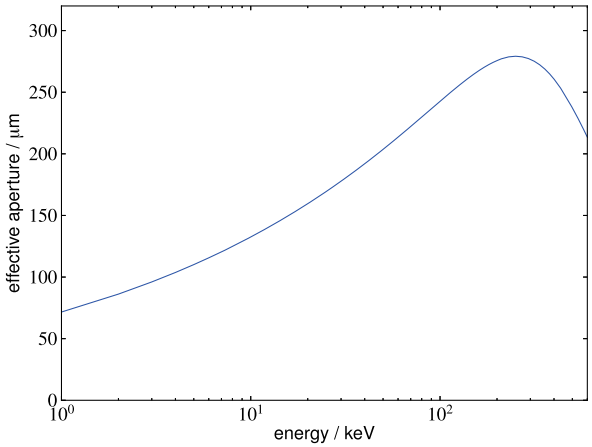

Figure 2.21: Calculation of the effective aperture of a SU8 polymer CRL. The effective aperture d_{eff} is significantly smaller than the geometric aperture $2R_0 = 600\mu m$ (calculation parameters: $N = 5$, $f = 0.25\,mm$, $\sigma = 3nm$, radius of curvature R dynamically adapted for each energy).

the wave in the lens material due to the difference in the complex refractive index. Consider the propagation of the wave in vacuum and in the material. After a certain length, the vacuum wave and the wave in the lens material are in phase again, having made m_1 and m_2 oscillations ($m_1, m_2 \in \mathbb{N}$). This length is given to be [54]

$$L = \frac{2\pi\lambda}{\delta(\lambda)} \tag{2.43}$$

or in the energy formulation

$$L = \frac{2\pi c h}{\delta(E) E} \tag{2.44}$$

with the speed of light c, Planck constant h, refractive index decrement δ (compare Equation 2.6) and photon energy E. With the wave field being in phase again after the length L, this is also true at $n \cdot L$, with $n = 1, 2, 3, \ldots$. Removing material packages of the length $n \cdot L$ does not alter the wave phase but reduces the X–ray absorption. Lenses with material packages of thicknesses $m \cdot L$ removed are known as Fresnel lenses. In the X–ray community, these lens designs are often also referred to as kinoform lenses. Figure 2.22 shows this process and how the final lens looks like. The use of Fresnel lenses for X–rays has already been suggested at the beginning of the 1990s [131, 148] but fabrication difficulties delay the widespread use of these optical elements as the achieved focal spot sizes have long been in the range of micrometer [52, 54, 126] and spots well below a micrometer have just recently been achieved [1]. One major problem of Fresnel lenses is the illumination. To avoid scattering and reflection on the long straight sides, the illuminating beam has to be very parallel with nearly zero divergence. For example, Alianelli et al. use one lens with the source in its focal point in front of the Fresnel lens to achieve parallel illumination [1]. The parallel illumination requirement makes low–absorbing Fresnel lenses a great tool for

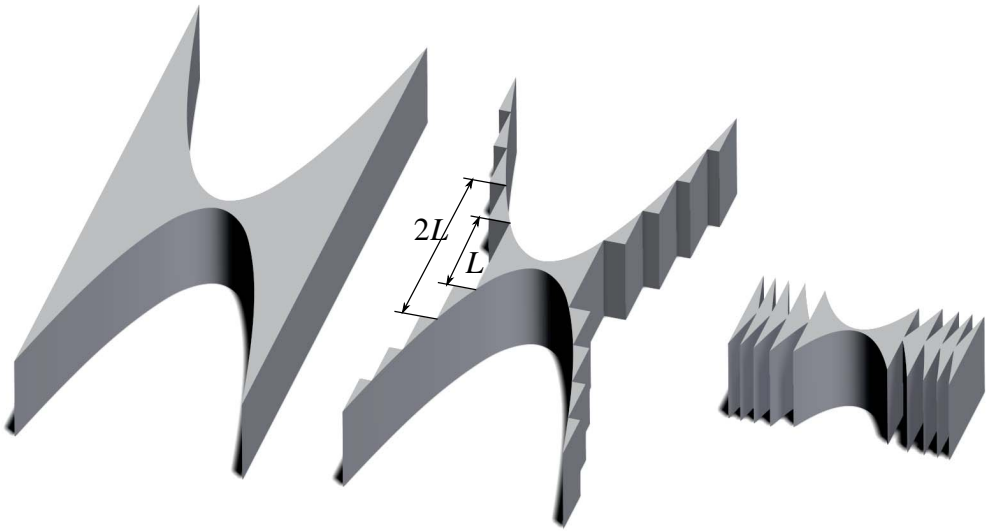

Figure 2.22: Sketch of a classical refractive lens (left) and material packages of length $m\,L$ removed (middle). If this form is compacted, it acquires the shape of a Fresnel lens (right).

creating intense focal spots but severely limits their use as imaging optics because microscopic imaging requires divergent illumination of the sample.

Prismatic lenses

Apart from the classical lens forms, lenses made from other shapes are also under development, most prominent of which are prismatic lenses, also referred to as *clessidra lenses*. The piecewise design with small prisms does not allow these lenses to be used for imaging, but they are well suited for illumination and focusing applications that do not require nanometer–sized spots.

Because refraction of X–rays is very small at each interface, each prismatic lens consists of a multitude of single elements. The adept placement of these elements allows the creation of X-ray lenses with a large aperture and (comparably) low absorption [15, 54, 55, 117, 137].

Each prism refracts the beam and the total refraction for each incoming ray can be adjusted by the number of elements. Figure 2.23 gives a schematic sketch of this scheme. The achievable minimal spot size is limited by the prism size: Because each prism of height h gives a parallel beam of height h, the overall spot size cannot be smaller than h. The structure sizes are typically in the range of a few micrometers which is why these optics cannot be used for creating nanofocal spots.

The great advantage of this optics is the adjustable focal size and divergence. While the divergence is given by the focal length and the distance of the outermost lens elements from the optical axis, the spot size can be tailored by the size of the prismatic elements. Increasing the height h of each element also increases the focal spot size. The drawback is the increasing lens length and absorption in the optics. Alternatively, instead of one element with height h, n elements with a

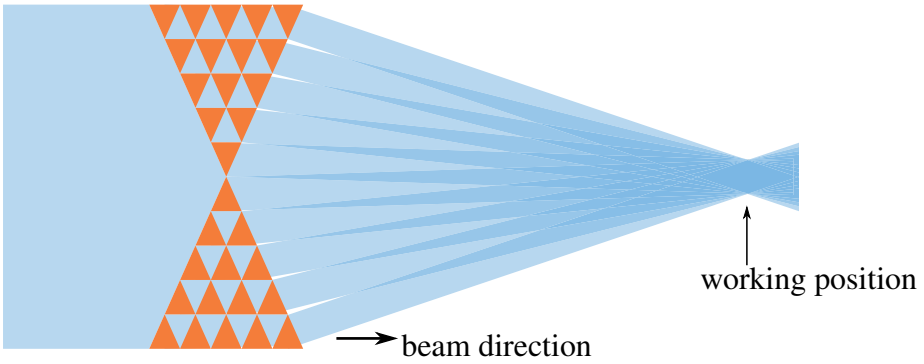

Figure 2.23: Schematic scheme of a prism X–ray lens. The beam refraction is dependent on the number of prismatic elements. Varying the number and positions of the individual elements, all rays can be concentrated in one spot. The spot size is similar to the element dimensions, which is why only microfoci can be achieved with this kind of optics.

height h/n can be used. i.e. the number of lens elements stays constant over several rows. This scheme allows a flexible design of different optical elements from a single prismatic template.

For X–ray microscopy and its need of divergent illumination (see Chapter 3.2.4), prismatic condenser lenses have great advantages. The optical properties of such lenses can be altered to suit the experimental needs perfectly. The drawback of this optimized placement of each prism element is that this optics are chromatic and only work properly at one design energy.

For two–dimensional focusing, two of these structures can be mounted under 90°, similar to CRLs. A more simple way to achieve 2D–focusing is rolling a 1–D focusing lens to achieve a rotationally symmetric version which creates a point spot. These rolled X–ray prismatic lenses (RXPLs) are fabricated from a microstructured foil: Rows of prisms are imprinted on a foil. The geometry and number of elements is determined by cutting the foil to te required shape before rolling the foil around a core, for example a thin glass fibre [117, 137].

2.3.6 Comparison of optics and conclusion

All optics are based on one of the three basic principles: reflection, refraction, and diffraction. The weak interaction strength of X–rays with matter makes the design of optical elements a challenge, but with large advances in the last decade. Due to the small angles involved, optics and optical lengths are rather large, as compared to other parts of the spectrum.

While most of the optics presented above allow the creation of a X–ray nanofocus, either as stand–alone devices or in a tiered arrangement, the imaging capabilities of the optics differ enormously. For microscopy and other imaging applications, not the spot size of the optics is important but whether the optics allow undistorted optical imaging of objects. Table 2.2 shows the key data for the distinct types of optics to allow their comparison.

For imaging applications, the choice of optics is basically limited to Fresnel zone plates and

Type of optics	energy range / keV	allows imaging	smallest focus / nm
KB mirrors	< 20	no	25 (line) [85]
Monocapillaries	< 30	no	250 (point) [121]
Polycapillaries	< 30	no	> 1000
Waveguides	< 20	no	10 (point) [63]
Fresnel zone plates	< 10	yes	15 (point) [106]
Compound refractive lenses	5 – 200	yes	50 (point) [112]

Table 2.2: Comparison of some key features for different kinds of optics. The field 'energy range' gives the ideal energy for these elements. Most optics can also be used above this threshold, but with less efficiency and/or increased spot sizes. The 'allows imaging' shows whether the optics complies with Abbe's sine condition for imaging; and the 'smallest focus' field gives the smallest reported focal spot size from the literature.

CRLs. While Fresnel zone plates can achieve a higher resolution and a larger aperture, they are limited to the lower energy range if trying to achieve the optimum quality. With increasing energy, CRLs gain the upper hand, the tradeoff point being somewhere around 10 keV.

The quality of X–ray optics and the achievable spot sizes have strongly increased in the last decade. Nowadays, spot sizes below one micron are routinely generated at synchrotrons and can be achieved even at X–ray tubes. For most applications, the type of optics used is freely choosable. Depending on the detailed experimental requirements, KB mirrors, CRLs, and Fresnel zone plates are all widespread at synchrotron radiation sources. Capillaries are not as widespread but are a suitable choice for X–ray tubes because they are in principle free of chromatic aberration[2]. While waveguides promise a very small source, the high divergence and low photon flux limit the use of this optics to the creation of point foci.

[2]The useable energy range of capillaries is only limited by the design: The angle of total reflection is energy–dependent and the reflectivity drops heavily above the critical angle, making capillaries unsuitable for higher energies.

Chapter 3

X–Ray Imaging

3.1 Introduction

The use of X–rays for imaging applications is widespread and a routine technique. Starting in medicine, radiographies and tomographies with X–rays are common because of the high penetration depth of the X–rays. In industry, the same techniques are used for quality and process control. While the plain amount of usage is probably higher in medicine and industry, the most diverse applications are in the scientific area. For example, biologists seek knowledge about animal and plant parts; environmental scientists are looking at the porosity and water transport in soils; material scientists are looking at joining connections, e.g. welds; archeologist are interested in fossils without having to cut their unique samples. The wide range of X–ray energies and penetration depths makes all these different questions answerable. For most scientific applications, the use of radiography, i.e. two–dimensional projections, is not sufficient and tomographic methods are employed. The basics of tomography are well described in the literature (for example, in the books of Herman [46], Kak and Slaneys [57], or Natterer [88]) and a short introduction is also provided in Section 3.3.

The required spatial resolution for each specific question determines, whether the question can be answered using X–ray imaging or not. Synchrotron radiation X–ray computed tomography routinely allows resolutions down to roughly 1μm but many problems require higher resolutions. The feature sizes in the semiconductor industry are often below 100 nm. For visualizing the two–dimensional circuitry, the use of X–ray microscopes is mandatory as only they offer the required spatial resolution and the penetration depth to see the circuits buried in the wavers. This technique is explained in Section 3.2.

In those cases, where both the high spatial resolution of a X–ray microscope and three–dimension information of the sample are required, X–ray nanotomography is the technique of choice. Tomographic reconstruction methods work independently of the image formation process.

This fact allows the use of X–ray microscopy images as input, yielding a magnified tomographic 3D reconstruction.

In the first part of this chapter, X–ray microscopy techniques will be presented, followed by tomographic reconstruction methods. The merging of both for the X–ray nanotomography will be included in Chapter 5.

3.2 X–ray microscopy

3.2.1 Introduction

For many industrial and scientific applications, it is necessary to control and evaluate small structures. Optical microscopy[1] is limited by the high absorption coefficient in hard condensed matter (e.g. metals, electronic parts), and often only the surface is accessible. Furthermore, the resolution is limited by the wavelength and numerical aperture of the microscope. State–of–the–art commercial microscopes achieve a resolution about 200 nm for visible light. While there are ways to lower this number using advanced techniques, these techniques are not routinely available.

Scanning electron microscopy (SEM) allows the imaging of features with nanometer–resolution but it is also limited to surface analysis. Different contrast mechanisms allow the acquisition of a very detailed overview of the surface and its structures with a high spatial resolution, but this technique is insensitive to bulk features.

The use of transmission electron microscopes (TEM) allows penetrating samples and acquire transmission measurements. The drawback, however, is that sample thicknesses are limited to some hundred nanometers and that samples have to be measured in vacuum, making sample preparation a very extensive procedure. With tilting the samples, it is possible to calculate real three–dimensional absorption images of the samples, but due to the very thin samples, the depth information is very limited. In addition, the preparation techniques cannot be used on all sample types, making this technique unavailable to these samples.

For the visualization of small, embedded features like electronic circuits on a wafer, probes with a higher penetration depth and a high resolution are needed. Hard X–rays offer the required penetration and modern synchrotron radiation sources offer enough flux for usage as an X–ray microscope, using X–ray optics.

There are three basic ways to acquire magnified images with X–rays. First, a magnified projection of the sample is possible, as depicted in Figure 3.1. The second way is scanning. For this setup, a focused spot is generated and the sample is scanned point–wise using this spot and acquiring images. While this is technically not a microscope, this setup is commonly called scan-

[1] For reasons of simplicity, optical microscopy refers to microscopy using the wavelength regime of visible light.

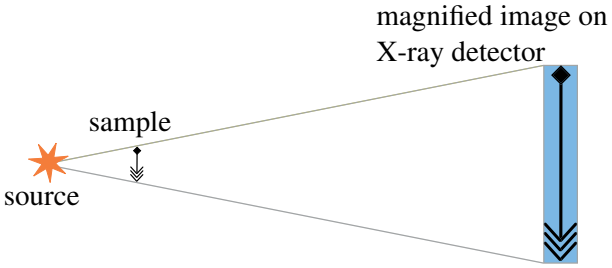

Figure 3.1: Schematic sketch of a X–ray magnified projection. Divergent rays from a small source pass through the sample and are analyzed by a detector. Due to the shape of the X–ray envelope, this setup is often referred to as cone beam setup.

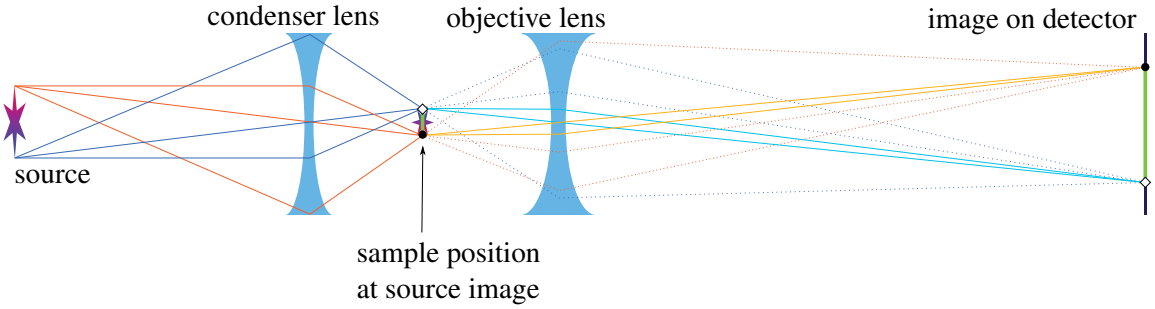

Figure 3.2: Schematic sketch of a X–ray microscope. The condenser gives a demagnified image of the source which coincides with the sample position. The objective lens projects a magnified, upside–down image of the sample on the detector.

ning transmission X–ray microscope. Last, it is possible to create a real microscopic image of the sample with X–ray optics. Figure 3.2 shows a sketch of this setup, called transmission X–ray microscope.

3.2.2 Cone beam projection setup

While the optical projection in the conebeam setup is very simple, the difficulties lie in the generation of a highly intense small source. The small source is necessary for achieving a high resolution. Figure 3.3 shows a sketch of the projection. The distances necessary for an estimation of the resolution are given and the achievable resolution will be discussed here. Consider two sample features of a sample—depicted as rhombus and triangle in Figure 3.3—at a distance of d. The intercept theorem yields that the features are projected on the detector at an image distance i, given by

$$i = \frac{p+q}{q} d. \tag{3.1}$$

Furthermore, the finite source size blurs each infinitely small feature to a size of u (compare Figure 3.3):

$$u = \frac{p}{q} s. \tag{3.2}$$

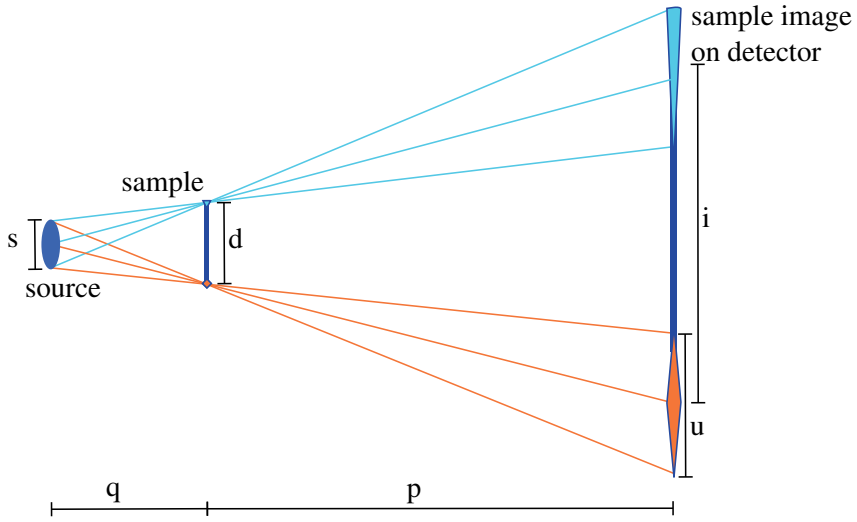

Figure 3.3: Cone beam distances.

Ideally, each infinitely small feature should yield an infinitely small image, i.e. $u \to 0$. But for two points to be distinguished on the detector image, it must be

$$i > u.$$

Using Equations 3.1 and 3.2:

$$\frac{p+q}{q} d > \frac{p}{q} s \tag{3.3}$$

$$\Leftrightarrow \quad (p+q)\, d > p\, s \tag{3.4}$$

$$\Leftrightarrow \quad d > \frac{p}{p+q} s \tag{3.5}$$

The magnification M is

$$M = \frac{i}{d} = \frac{p+q}{q} \tag{3.6}$$

As the aim is a large M, it follows that $p \gg q$. Using this, it is

$$\frac{p}{p+q} \approx \frac{p}{p} = 1 \tag{3.7}$$

and thus Equation 3.5 simplifies to

$$d \gtrapprox s. \tag{3.8}$$

The minimal sample feature size that can be resolved is thus roughly equivalent to the source size. While the resolution can be further limited by the other components in the setup, the source is the lower limit of what is achievable. Modern X–ray optics with source sizes below 50 nm make this

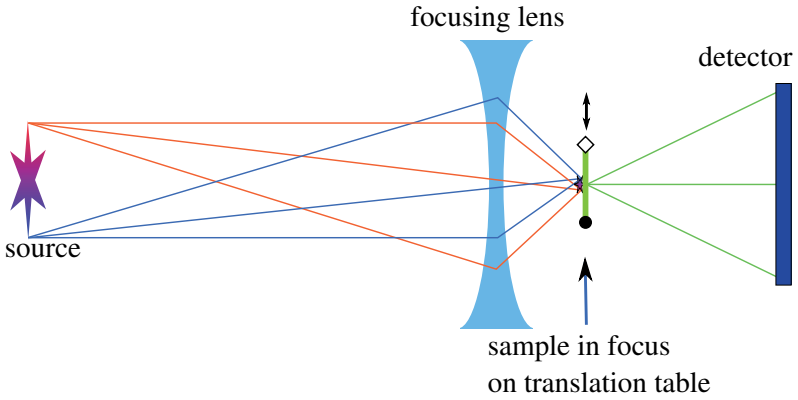

Figure 3.4: Schematic sketch of a scanning X–ray microscope. The sample is scanned through the nanofocused spot and the individual information is later combined in one image.

setup a feasible possibility.

3.2.3 Scanning transmission X–ray microscopy setup

The scanning transmission X–ray microscope also relies on a nanofocused source. It is, however, not necessary to use optics that fulfills Abbe's sine condition, i.e. all X–ray optics including KB mirrors or waveguides can be used.

The sample has to be positioned in the focused spot and scanned. It is critical that the sample positioning stability and positioning accuracy are high enough to allow precise measurements. The stability and accuracy need to be below the size of a virtual pixel, i.e. typically below the X–ray spot size. The performance of both X–ray optics and mechanics limits the achievable resolution to around 50 nm.

Figure 3.4 shows the schematic setup. As already mentioned, any kind of X–ray optics can be used. The spot size, spot stability and sample positioning have to be precise enough to allow the measurement for each point before the sample is moved and the next point is scanned. Note that in principle, also the optics could be scanned, but positioning errors, especially in angular positioning, are much more critical for the optics than for the sample.

The main advantage of this setup is, that many kinds of information can be collected from the sample. For pure absorption measurements, a photo diode that counts the transmitted X–ray intensity suffices as detector; if additional information like scattering shall be collected, a larger space–resolving detector is needed. An energy–dispersive fluorescence detector allows to measure the elemental composition in each point.

An individual map of all scanned points can be created for each piece of information acquired; for example each elemental channel in a fluorescence measurement can be visualized [111].

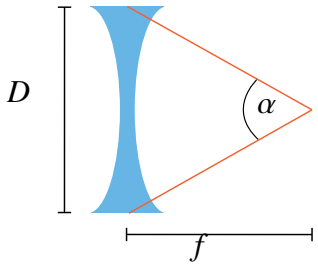

Figure 3.5: The numerical aperture is half the opening angle of the maximum light cone with the lens. This maximum angle is achieved for parallel illumination, which focuses all light at the distance f. D is the opening aperture of the lens.

3.2.4 Full–field transmission X–ray microscopy

Cone beam projections give a geometrical projection of the sample and scanning transmission X–ray microscopy only yield single points that can be stitched together; only a full–field transmission X–ray microscopy gives true magnified images of the sample. First microscopes with resolutions below 200 nm were already demonstrated in 1999, although at much lower energies [58].

The resolving power of a microscope is determined by the resolving power of the objective lens. Optical systems are characterized by the numerical aperture (NA), defined as

$$NA = n \sin\theta, \tag{3.9}$$

with the refractive index n and the angle θ being half the opening angle of the maximum light cone with the lens (compare Figure 3.5, $\theta = \alpha/2$). For X–rays, it is $n \approx 1$. In addition, the respective angles are very small, so that it is $\sin\theta \approx \tan\theta \approx \theta$. Equation 3.9 thus simplifies to

$$NA \approx \frac{D}{2f} \tag{3.10}$$

For two points to be resolved, they must be separated by a distance larger than the resolution R [12]:

$$R = 0.61\frac{\lambda}{NA} \tag{3.11}$$

where λ is the wavelength of the probing X–rays and NA is the numerical aperture. Using Equation 3.10, the resolution is thus

$$R = \frac{1.22\,\lambda\,f}{D}. \tag{3.12}$$

Therefore, the imaging objective should have the largest possible aperture and the focal distance should be as short as possible. Note that this formula is only valid, if the complete angular acceptance of the objective lens is illuminated. For synchrotron radiation sources with long distances between source and experiments and small sources with a very low divergence, it is necessary to

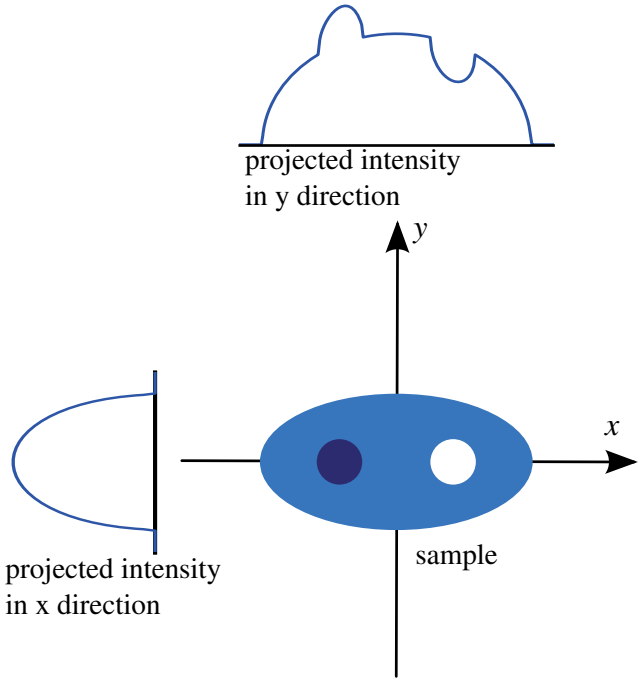

Figure 3.6: Sketch to demonstrate the tomographic principle. When looking at the body from different directions, the projected thickness differs. The color codes the absorption intensity: White has an absorption value of 0, light corresponds to a value of 1 and the dark blue to a value of 2. When looking in y–direction, the body cannot be distinguished from a normal ellipse with an overall absorption value of 1. Using many such projections, the original form of the body can be reconstructed.

include condenser optics which enlarges the beam divergence.

3.3 Tomography

The name tomography is derived from the old Greek *tome* for a cut and the verb *graphein*, to write. By taking X–ray projections of an object from different directions, it is possible to reconstruct the three–dimensional inner structure of an object. The first successfully performed and published tomography was a medical tomography of a human head by Hounsfield in 1973 [49]. Oldendorf already carried out similar experiments in 1961 [98], but without applying the mathematics for a three–dimensional reconstruction.

Figure 3.6 schematically demonstrates how the projections of an object differ, depending on the viewing direction.

3.3.1 Mathematical description of tomography

The mathematical basics for tomography were laid down by Radon [104] and later refined by Cormack [16]. They describe how a function can be described by its line integrals.

In tomography, let $\mu(x, y)$ be the local absorption coefficient in the point (x, y). The experimental projection yields the integral of values in direction of the beam. The problem now is finding a function from values for its line integrals, i.e. the inverse problem with respect to Radon and Cormack.

Assume a sample in the (x, y) plane and let the function to be reconstructed be $f(x, y)$. If the X–ray beam direction is parallel to the y–axis, the signal p measured in the point x_0 is

$$p(x_0) = \int_{-\infty}^{\infty} f(x_0, y)\, dy. \tag{3.13}$$

For a projection from any angle θ with respect to the x, y–coordinate system, i.e. for a signal in a direction

$$t = x\cos\theta + y\sin\theta, \tag{3.14}$$

the integration has to be performed along lines u perpendicular to t, with

$$u = -x\sin\theta + y\cos\theta. \tag{3.15}$$

The projection of f at points t can be written as an integral over the path $u = \text{const}$

$$p_\theta(t) = \int_{u=\text{const}} f(x, y)\, du. \tag{3.16}$$

Using Equations 3.14 and 3.15, x and y can be expressed with u and t:

$$x = -u\sin\theta + t\cos\theta \tag{3.17}$$

$$y = u\cos\theta + t\sin\theta. \tag{3.18}$$

Substituting for x, y in Equation 3.16, it transforms to

$$p_\theta(t) = \int_{-\infty}^{\infty} f(-u\sin\theta + t\cos\theta, u\cos\theta + t\sin\theta)\, du. \tag{3.19}$$

Another way of expressing the function from Equation 3.16 is using Dirac's delta function:

$$p_\theta(t) = \int_{-\infty}^{\infty}\int_{-\infty}^{\infty} f(x, y)\, \delta(x\cos\theta + y\sin\theta - t)\, dx\, dy. \tag{3.20}$$

The function $p_\theta(t)$ is also called the Radon transform of the function $f(x, y)$.

Figure 3.7 shows the function values of a $p_\theta(t)$ example. As each point in the projection follows a sine–line curve with the variation of θ, this data is often also called sinogram. For the analysis

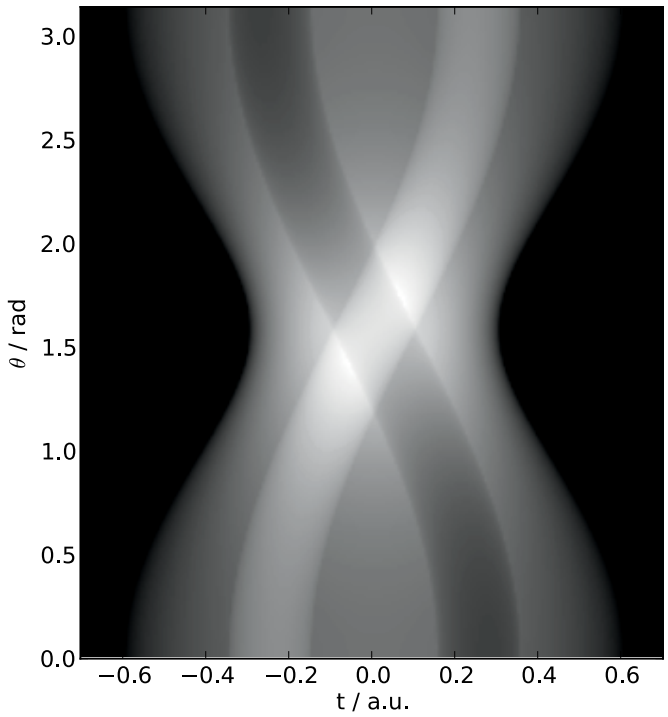

Figure 3.7: Sketch of the values of $p_\theta(t)$. The raw data used is the same as depicted in Figure 3.6.

and reconstruction, the Fourier transforms of $f(x, y)$ and $p_\theta(t)$ are needed:

$$F(X, Y) = \int_{-\infty}^{\infty} \int_{-\infty}^{\infty} f(x, y)\, e^{-2\pi i (x X + y Y)} dx\, dy \tag{3.21}$$

$$P_\theta(T) = \int_{-\infty}^{\infty} p_\theta(t)\, e^{-2\pi i t T} dt \tag{3.22}$$

The Fourier transforms of $p_\theta(t)$ and $f(x, y)$ are linked by

$$P_\theta(T) = F(T \cos\theta, T \sin\theta). \tag{3.23}$$

The Fourier transform of the measured value $p_\theta(t)$ corresponds to the Fourier transform of the function $f(x, y)$ along lines through the origin and rotated by the angle θ. Equation 3.23 and its interpretation are often referred to as Fourier Slice Theorem.

If the angles θ cover the whole range $[0, \pi)$ or any other interval with the width π, $f(x, y)$ can be recovered from the projection data.

3.3.2 Reconstruction algorithms

For a detailed derivation of the various reconstruction techniques, please refer to the already mentioned literature [46, 57, 64, 88]. Here, only the outlines and ideas will be presented. The algorithms have to be separated into two groups. The first group is composed of algorithms for the illumination with parallel light—the standard case at synchrotrons—and the second group of al-

gorithms covers the case of divergent illumination as in conebeam microscopy. For the latter case, the reconstruction is more complex, as the projection of each sample point lies not in a plane but follows a three–dimensional trajectory. Consequently, also the reconstruction requires a three–dimensional approach.

Filtered backprojection

The most common reconstruction technique is the filtered backprojection algorithm (FBP). The function $f(x, y)$ can be written as the inverse Fourier transform of $F(X, Y)$:

$$f(x,y) = \int_{-\infty}^{\infty}\int_{-\infty}^{\infty} F(X,Y)\, e^{2\pi i\,(x\,X + y\,Y)} dX\, dY. \tag{3.24}$$

If using polar coordinates (T, θ) for F, Equation 3.24 changes to

$$\begin{aligned} f(x,y) &= \int_{0}^{\pi}\int_{-\infty}^{\infty} F(X(T,\theta), Y(T,\theta))\,|T|\, e^{2\pi i\,(x\,X(T,\theta) + y\,Y(T,\theta))} dT\, d\theta && (3.25)\\ &= \int_{0}^{\pi}\int_{-\infty}^{\infty} F(T\cos\theta, T\sin\theta)\,|T|\, e^{2\pi i\,(x\,T\cos\theta + y\,T\sin\theta)} dT\, d\theta && (3.26)\\ &= \int_{0}^{\pi}\int_{-\infty}^{\infty} P_\theta(T)\,|T|\, e^{2\pi i\,T\,(x\cos\theta + y\sin\theta)} dT\, d\theta && (3.27) \end{aligned}$$

where the Fourier Slice Theorem (see Equation 3.23) has been used in the last step. Because of the term $|T|$—introduced in the coordination transformation from Cartesian to polar coordinates—, the integral is referred to as filtered projection.

In addition to the mandatory filter $|T|$, additional filter functions can be included. These filters can reduce the noise at higher frequencies in the spectra, but this leads to a drop in spatial resolution of the reconstructed data. Let $g(T)$ be any kind of filter with

$$H(T) = |T|\, g(T). \tag{3.28}$$

Inserting $H(T)$ for $|T|$, and using Equation 3.14 as well as the convolution theorem in Equation 3.27, it is

$$\begin{aligned} f(x,y) &= \int_{0}^{\pi}\int_{-\infty}^{\infty} H(T)\, P_\theta(T)\, e^{2\pi i\,T\,(x\cos\theta + y\sin\theta)} dT\, d\theta && (3.29)\\ &= \int_{0}^{\pi} \underbrace{\left(\int_{-\infty}^{\infty} H(T)\, e^{2\pi i\,T\,(x\cos\theta + y\sin\theta)} dT\right)}_{h(t)} * \underbrace{\left(\int_{-\infty}^{\infty} P_\theta(T)\, e^{2\pi i\,T\,(x\cos\theta + y\sin\theta)} dT\right)}_{p_\theta(t)} d\theta && (3.30)\\ &= \int_{0}^{\infty} h(t) * p_\theta(t)\, d\theta && (3.31) \end{aligned}$$

The angular integral of the inverse Fourier transform of $H(T)$, $h(t)$ convolved with $p_\theta(t)$ is thus equivalent to $f(x, y)$.

Algorithms are either based on Equation 3.29 or Equation 3.31. While both forms are mathematically identical, the implementation of the filtering in the frequency space or as a convolution in real space require a different implementation. The usage of the fast Fourier transform (FFT) allows a fast implementation of the FBP algorithm in both implementations. For a reconstruction with a minimum of artifacts, the knowledge of the exact position of the center of rotation, i.e. $t = 0$, is needed. However, this position can be extracted from the data by iteratively reconstructing with different t values and optimizing image metric parameters. For the detailed discussion of these metrics, refer to Donath [25, 26].

Maximum likelihood method

Apart from the filtered backprojection, other mathematical methods exists that try to reconstruct the data using algebraic (see e.g. [40, 87]) or statistical algorithms (see for example [105]). To give a short insight, one such method—the Maximum likelihood method—is presented here.

While not commonly used in synchrotron radiation tomography because of high computational requirements, this method nevertheless allows a reconstruction from much noisier data and very few projections [105].

For this method, the data to be reconstructed is split into small cells (corresponding to the voxels). The signal of the detector pixel i is the result of the attenuation along its path, the ray $\overrightarrow{r_i}$:

$$I_i = I_{0,i} \exp\left(-\int_{\vec{r}} \mu(x,y)\, d\vec{r}\right). \tag{3.32}$$

In case of a discrete distribution, this transforms to

$$I_i = I_{0,i} \exp\left(\sum_{k=1}^{N} \mu_k\, c_{k,i}\right) \tag{3.33}$$

with the local attenuation coefficient μ_k and the path length of ray i through the cell k given by $c_{k,i}$. The sum is performed over all cells along the ray. Figure 3.8 shows a sketch with all the aforementioned variables.

With N_i the number of photons in the ray i, the likelihood function is defines as:

$$L(\mu) = \prod_i \frac{I_i^{I_{0,i}} \exp(-I_i)}{I_{0,i}!} \tag{3.34}$$

For the reconstruction, this function has to be maximized:

$$L(\mu) \longrightarrow \max \tag{3.35}$$

The variables of this function are the attenuation coefficients μ_k, but as these are all dependent (each

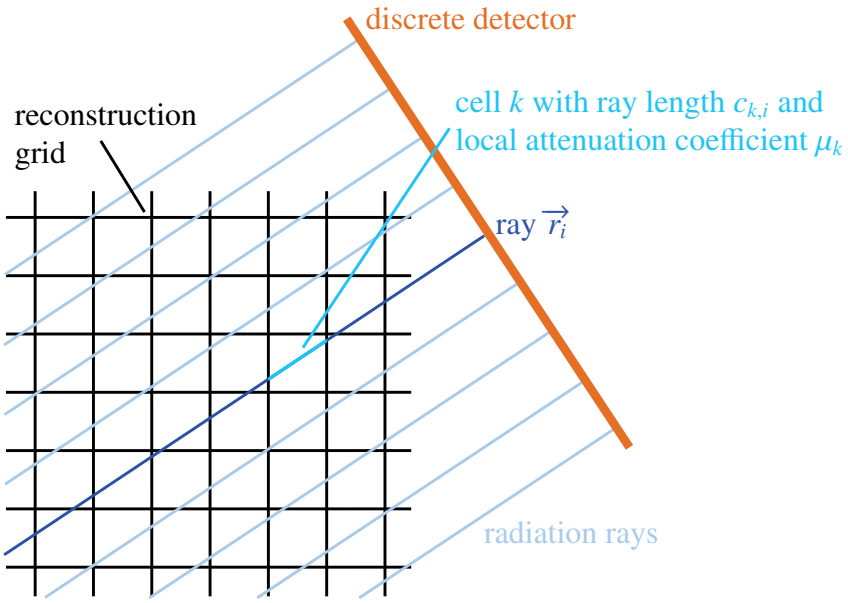

Figure 3.8: Sketch of the nomenclature. The data to be reconstructed is segmented into cells k. The rays—corresponding to the pixel positions on the discrete detector—pass through the sample. Exemplarily, the ray r_i travels a length of $c_{k,i}$ in the cell k.

ray i must fullfill Equation 3.33), maximizing the likelihood function is a numerically demanding project. For datasets with many projection angles and large reconstruction grids, this technique is not competitive with its computational needs but for smaller datasets with limited projection angles, the reconstruction quality is significantly superior to the filtered backprojection.

3.3.3 Cone-beam tomography

All the reconstruction techniques mentioned earlier are based on parallel illumination of the sample. In the case of cone beam geometry, this is no longer the case. First, consider a plane. If illuminated from a single spot, the intensity in the detector pixels is no longer the sum of parallel rays, but depends of the rotation angle θ as well as the fan angle β. The problem is divided in two parts. First, the two–dimensional problem will be discussed and later extended to include all three dimensions.

Using Feldkamp's notation [31], let the detector be in the center or rotation. This simplifies the following equations and does not limit the deduction. With the source distance from the center of rotation d and the real detector distance d_d from the center of rotation, a simple scaling of the detector data by $d/(d + d_d)$ converts the true data to this system. Figure 3.9 shows the setup and the variables.

The perpendicular distance l between coordinate origin and the ray from the source to the

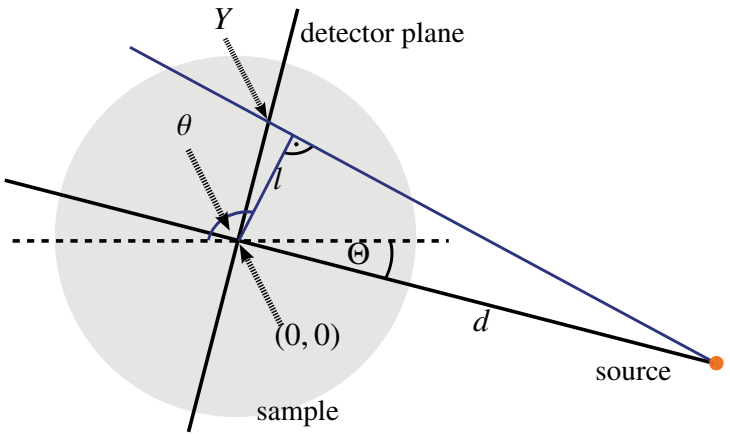

Figure 3.9: Sketch of the fan beam geometry. The labels will be explained in the text.

detector point Y can be expressed by Y and d:

$$l = \frac{Y\,d}{\sqrt{d^2 + Y^2}}. \tag{3.36}$$

For the axis rotation angle Θ, the angle θ is given by

$$\theta = \Theta + \frac{\pi}{2} + \alpha, \tag{3.37}$$

where

$$\alpha = \arctan\left(\frac{l}{\sqrt{d^2 - l^2}}\right). \tag{3.38}$$

Data is acquired on the detector at rotational angles Θ, i.e. in the form $P_\Theta(Y)$. Using cylindrical coordinates (l, θ), the projections can be described in cylindrical coordinates as well. For $|l| < d$, it is $p(l, \theta) = P_\Theta(Y)$. In analogy to Equation 3.20 for parallel illumination, the projected data is given by

$$p(l, \theta) = \int_0^d \int_0^{2\pi} f(r, \phi)\, \delta(l - r\, \cos(\theta - \phi))\, r\, d\phi\, dr. \tag{3.39}$$

The data $f(r, \phi)$ can be reconstructed using the Radon transform [47]:

$$f(r, \phi) = \frac{1}{4\,\pi^2} \fint_0^{2\pi} \fint_{-\infty}^{\infty} \frac{1}{r\, \cos(\theta - \phi) - l}\, \frac{\partial}{\partial l}\, (p(l, \theta))\; dl\, d\theta \tag{3.40}$$

Here, $\fint$ is the Cauchy principal value of the integral for θ and l, i.e. the point $r\, \cos(\theta - \phi) - l = 0$ is excluded in the integration.

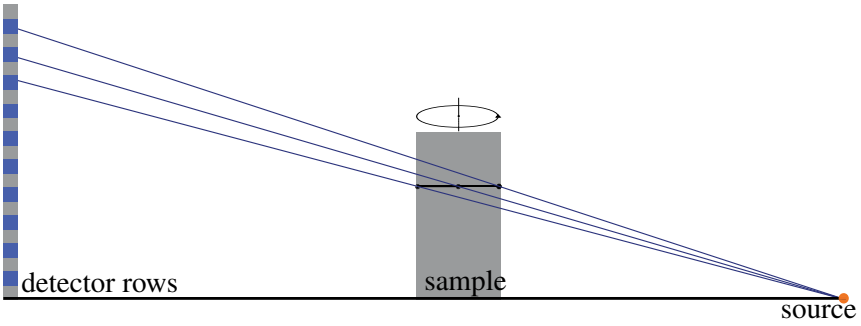

Figure 3.10: Schematic drawing for the cone beam geometry. Consider the grey sample cylinder. As a sample rotates, the point on its surface wanders. 90 degree steps are marked by the black dots and it is obvious, that the projection of each position does fall on a different detector row.

For the detector center plane, this is the solution. For all other planes, the problem is further complicated by the 3rd dimension. As the sample rotates, each point of the sample wanders on an ellipse on the detector. The important point is that the point does not stay in one detector row. Figure 3.10 demonstrates this behavior.

By extending the fan–beam mathematics to the third dimension, the problem is easily solvable, although a lot more complicated than for parallel illumination. Depending on the implementation, the derivation changes slightly. For further information, please refer to, for example, Herman [47] or Feldkamp [31].

A large issue for all algorithms is the accuracy. Reconstruction quality is dependent on the sample position relative to the center of rotation and source position and, more importantly, the reconstruction quality changes throughout the sample [39, 141]. This is due to the fact that discrete sampling is necessary. The farther away from the central plane, the larger the errors.

These errors can be kept small if the cone angle is small, but in return this corresponds to a limited field of view, i.e. a small sample. Other improvements are done by using more complex scanning geometries. The simplest deviation is the helical scanning mode, where the sample is rotated and simultaneously shifted in the height [141]. Related ideas are approaches with changing the source–sample distance while rotating and z–shifting the sample. Another approach is made by moving the source on a complex three–dimensional itinerary [141] relative to the sample and detector.

These approaches are all tailored to X-ray tube applications where changing the source–sample distances is rather easy. Using a storage ring, the source is fixed and the implementation of complicated curves for the sample to move on is difficult because of the requirements for the mechanics: As the sample size and exact position may vary from measurement to measurement, such movements along a precise path can only be implemented with six–axis kinematics of the rotational axis. The size of the rotational axis combined with the requirements for speed and precision prohibit such an implementation.

In addition, the resolution requirements differ strongly between medical tube system with precision needs in the range of several hundred micrometers or high–resolution synchrotron radiation experiments that need micrometer precision. For X–ray microscopy and nanotomography, the requirements are increased again, down to the range of some tens of nanometers. Only helical scanning modes or the simple standard approach are really feasible.

Chapter 4

The Imaging Beamline

This chapter is dedicated to describing the Imaging Beamline (IBL / P05) at which the nanotomography experiment is installed. Many of the components are general purpose and used for both the nano and microtomography, e.g. the monochromators. A brief description of the microtomography experiment is included, as its detector unit can be used. The nanotomography experimental hutch will be described as well, whereas the nanotomography experiment itself is described in Chapter 5.

4.1 Beamline Layout

The beamline is situated on a shared sector of the newly refurbished PETRA III storage ring. The sector is divided between the *Hard X-ray Micro/Nano-Probe beamline* (P06) and the Imaging Beamline (IBL).

Both beamlines share a common front end in the ring, but separated vacuum systems downstream of the source. In the following, only the P05 part of the sector will be discussed.

An overview of the PETRA III sector 4 is given in Figure 4.1. Due to the small beam divergence and consequently the small beam size, the micro tomography experiment has to be installed as far downstream of the source as possible, leaving the first experimental hutch for the nanotomography experiment. While creating smaller focal spots is easier further down from the source (the geometric demagnification is larger), one can gather more intensity with the same optical aperture closer to the source. In addition, this experimental arrangement allows very long optics–to–detector distances, as the nanotomography experiment in the first hutch can be used in combination with the micro tomography camera unit in the second experimental hutch.

An automated beam pipe changer is installed in the first hutch, allowing a continuous vacuum system from source to experimental hutch 2.

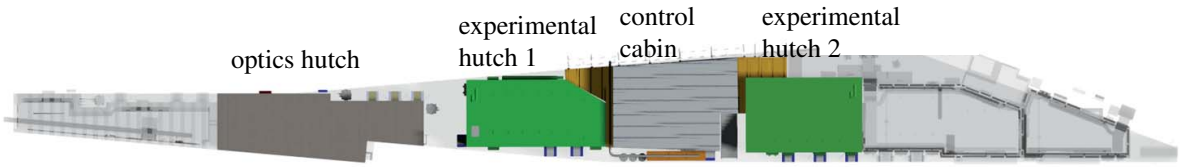

Figure 4.1: Schematic drawing of the PETRA III sector 4, excluding the front end. The hutches and space reserved for beamline P06 is partly blanked out, whereas P05 hutches are shown solid. The optics hutch is marked grey; the experimental hutches are colored in green. The first hutch is dedicated to the nanotomography experiment, the second one to the micro tomography. The control hutch is situated in between the experimental hutches.

4.2 Front end and optics

X-ray source

The PETRA III storage ring is the source for the P05 beamline. An undulator at a low–β section generates the X–rays for the experiment. The electron beam shape leads to a X–ray source size of roughly 95×15 µm^2 (horizontal × vertical, FWHM) with a divergence of 70×13µrad^2 (h × v, FWHM). For more details, see Appendix A.

The X-ray source is a 2m long PETRA III standard undulator [4], manufactured by Accel Instruments GmbH. Key parameters are given in Table 4.1. At the smallest gap, the 1^{st} harmonic is found at $E = 3450$eV. The K–range of the undulator is large enough for an overlap in energies when switching between the harmonics, i.e. the full energy spectrum is easily accessible.

Additional front end components

The front end houses a fixed carbon filter as well as optional additional carbon or copper filters. These are used to absorb the low energies in the spectrum to decrease the thermal load on the additional components. Water–cooled primary slits with a fixed vertical opening of 1.2 mm are used for screening stray radiation. A second slit system with four brackets, also water–cooled, allows the fine control of the beam size and the corresponding thermal load. A beam shutter in the storage ring space terminates the front end. Although the vacuum system is connected, front end and experimental area are separated by a water–cooled diamond window. All these front end components are custom–designed and built in–house by DESY.

Minimum magnetic gap	9.5 mm
Period length λ_U	29 mm
Length L	2 m
Peak field B_0	0.81 T
Deflection parameter $K_{\max}$	2.2
On–axis power density	30 µW / µrad^2

Table 4.1: Key parameters for the PETRA III standard undulator [4].

Beamline optics

In this section, the beamline optics will be presented, with the exclusion of focusing X–ray optics, described in the nanotomography experiment section in Chapter 5.

The major components are the two monochromators: A double crystal monochromator (DCM) with silicon crystals in Bragg geometry and a double multilayer monochromator (DMM). The beamline layout requires a vertical offset of 22 mm between white and monochromatic beam. This value is defined by the beam stop, which has only a small opening around 22 mm offset for the monochromatic beam.

While not yet installed, the DMM—designed and fabricated by Bruker ASC GmbH—will be the first element in the optics hutch. The main advantage of multilayers is their large energy bandpass, yielding a much higher flux [130]. As the undulator harmonics are much broader than the crystal acceptance, the monochromatic flux is limited by the crystals. Multilayers allow $\Delta E/E$ of up to 10^{-2}, an increase of almost two orders of magnitude when compared to silicon crystals in 111 geometry, yielding a similar increase in the flux. Due to the small reflection angles of multilayers combined with the fixed offset, the distances between the two multilayer crystals is rather large, leading to a massive design of the substructure, vacuum chamber and mechanics. For example, at an energy of 50 keV, the beam deflection is only 0.5°. To achieve a vertical offset of 22 mm, the crystals have to be separated by more than 2.4 m.

The substrates will be coated in–house at the HZG [129], and different coatings are planned to cover the complete energy range of $5 - 50$ keV with a high reflection efficiency.

The double DCM is the standard DESY monochromator design for PETRA III, manufactured by Oxford Instruments. Two sets of crystals are installed, using the silicon 111 and silicon 311 reflections, respectively. Both sets work in Bragg geometry and the small bandwidth $\Delta E/E \approx 10^{-4}$ allows very precise energy settings which are needed, for example, for absorption edge tomography.

For diagnostics, thin diamond screens, mounted under 45° and joined with cameras, as well as thin metal foils with electronic current counters are installed. These allow monitoring and evaluating the beam position, profile, and intensity. A water–cooled set of apertures is also included behind the monochromator for tailoring the beam size to the experimental needs.

4.3 Micro tomography experiment

The micro tomography experiment is installed in the second hutch. It consists of a granite substructure that is mounted on a tripod for height and tip/tilt alignment and linear mounts for translations perpendicular to the beam. These components are custom–designed and built in–house at the HZG

workshop.

On this platform, two units are mounted: the sample unit and the detector unit.

The complete sample unit is constructed by Aerotech Inc and is supported on three points, each motorized. Again, this setup allows for height and tip/tilt adjustment of the rotational axis. An air–bearing linear stage for transverse displacement of the rotational stage is mounted under the latter to position the rotation stage relative to the beam. For sample positioning, a stack of five piezo actuators is installed inside the aperture of the rotational axis. They allow x, y, z translations and rotations Rx, Ry. This is essential for centering the sample on the rotational stage.

The detector unit was manufactured by PI miCos GmbH. It is installed on a second granite substructure. The complete unit is mounted on three pods for tip/tilt corrections and height adjustments. A long polished granite acts as base for a horizontal translation of the camera station in beam direction. Using an air–bearing granite slider, the camera unit can be positioned in beam direction with micrometer precision. The station itself consists of microscope optics and a light–tight housing for up to two cameras and the necessary mechanics for camera adjustment. The optics are custom made by Präzisionsoptik Gera and are calculated for fixed magnifications $M = 5\times,\ 10\times,\ 20\times,\ 40\times$ with a numerical aperture of $NA = 0.25$. This high value for the NA allows both a high resolution and a large solid angle of light gathering. The scintillator crystals are mounted in a motorized changer, allowing the choice between several thicknesses for optimum depth resolution. The optics magnifies the scintillator image on a camera of up to 60×60 mm^2 area, corresponding to modern 4096×4096 pixel CCDs. A removable mirror on a fast and accurate translation stage allows switching between the two cameras. A heavy duty translation is used for changing the cameras position, because each magnification has a different working distance. The fine optical adjustment is done by moving the first lens of the objective. Its motorization allows changing the distance to the scintillator while keeping a fixed focal distance. At last, an aperture and absorbers are installed to select the wavelength bandpass for the scintillator emissions and for controlling the amount of light gathered.

4.4 Nanotomography hutch

The experimental hutch is situated at 63.5 – 72.5 m distance from the source. Because of permanently installed vacuum components (valves for venting and closing, vacuum pumps, and beam windows) and safety installations like the beam shutter, the useable length in the hutch is limited to approximately 7 meters. In addition, a vacuum pipe over the complete length of the hutch needs to be installed for the micro tomography experiment. A last constraint is the vacuum pipe for the beamline P06, which runs at about 280 mm distance from the beam, practically parallel to the latter. Considering the size of flanges, brackets etc., the useable width at beam height is limited to

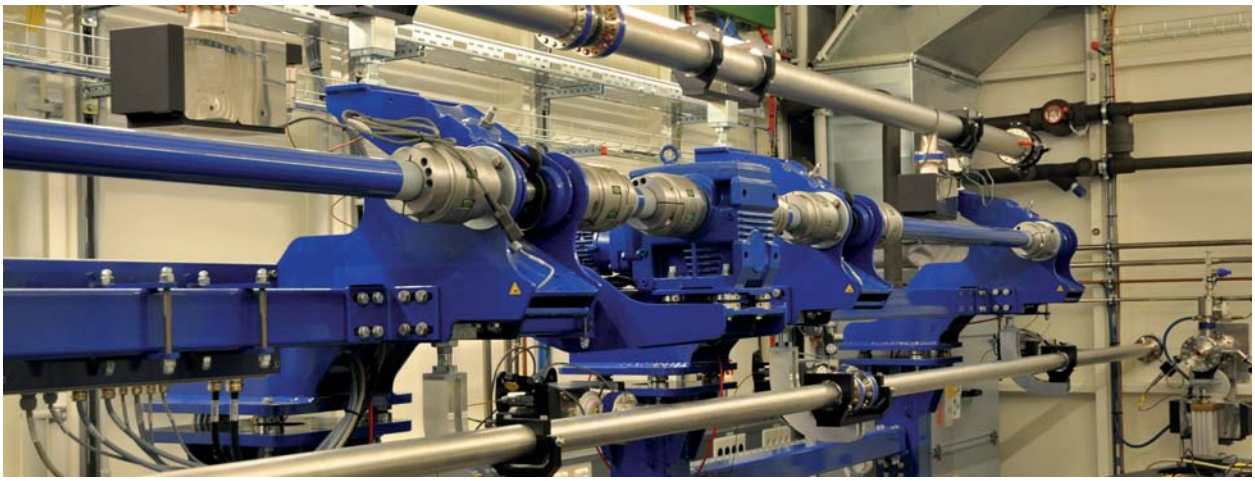

Figure 4.2: Image of the beam pipe robot. The P06 vacuum pipe is seen in the bottom, the blue coated machine is the holder for the pipes and the rotation mechanism. The P05 beam pipe is currently removed for experiments in EH1 and held by the robot. It is visible at the top of the image. At the very right is the diamond window, which separates the experimental area from the front end and optics vacuum. The limits imposed by the P06 beam pipe on the room for experimental installations are clearly visible.

about 200 mm in direction of the P06 beam pipe.

For easy switching between the micro and nanotomography setups, the P05 beam pipe is mounted on a robot for moving it in beam and storage positions. The robot was engineered and built in-house at the HZG workshop. Figure 4.2 shows the resulting installation in EH1. Apart from the easy usage, the main advantage of the robot is the fact that it is not necessary to manually install and uninstall the beampipe in the vicinity of the nanotomography experiment. Considering how heavy and bulky the vacuum pipes are and how sensitive the experimental equipment is, this minimizes the chances of damage done during installation works.

The experiment itself is installed on a 6.8 m long granite slab. This 10 ton substructure acts as a vibrational dampener and as optical bench to position the single components with respect to each other. Figure 4.3 shows a photo of the substructure. While the nanotomography experiment will only be used with the vacuum pipe removed, the components itself block the same room required for the vacuum pipe. To eliminate the need of permanent installation and uninstallation, the substructure is mounted on a pivot bearing, set about 2 m from one end. The complete structure and can be rotated around that point so that the opposite end is removed from the beam path. The experimental installations can be parked here, to avoid uninstalling them.

To achieve pivoting, the far end of the granite is mounted on four airpads of 200 mm diameter. If these pads are supplied with pressurized air, they lift the granite some micrometers so that it can be moved on the polished granite ground plate. A pneumatic cylinder is used for positioning the granite substructure.

The detailed experimental setup for the nanotomography experiment is given in Chapter 5, together with the design considerations, based on the constraints described in this section.

Figure 4.3: The granite substructure for the experiment. A 6.8 m long granite slab acts as optical bench for the experimental installations. On the right side in the background is the granite ground plate for a horizontal translation of the complete substructure on air pads. This is necessary for removing the experiment from the beam path to install the vacuum pipe.

Chapter 5

The nanotomography experimental setup

This chapter is dedicated to describing the final design and setup of the nanotomography experiment. A large part of this thesis was devoted to develop an optics concept and specifications for the optics and mechanics. Both the constraints and design considerations for the optics will be discussed as well as their solutions. While the implementation of the mechanics was not part of this work, the required design specifications and design parameters to achieve both the required precision and a high degree of flexibility had to be worked out and are described as well.

5.1 Layout of experimental X–ray optics

The concept for the X–ray optics of the P05 nanotomography endstation had to be developed from scratch. There already exist some X–ray microscopes scattered over the world, but the intended X–ray energy range, access to X–ray optics, experimentally available space for propagation distances, and—most importantly—source parameters make each instrument unique, thus requiring a detailed, individual concept for the X–ray optics.

For the case of P05, the challenge lay in designing an optical and mechanical concept that allows both cone beam and full field microscopy setups (see Section 3.2) over a broad energy range while respecting the constraints imposed by the layout of the sector. In the following, the requirements for the two different setups will be presented and it will be described how these requirements are met.

5.1.1 Cone beam setup

As described in Section 3.2.2, the resolution in the cone beam setup is limited by the X–ray spot size. The photon source has a size (FWHM) of $87 \times 14\ \mu m^2$ (see Section A). For a target spot size

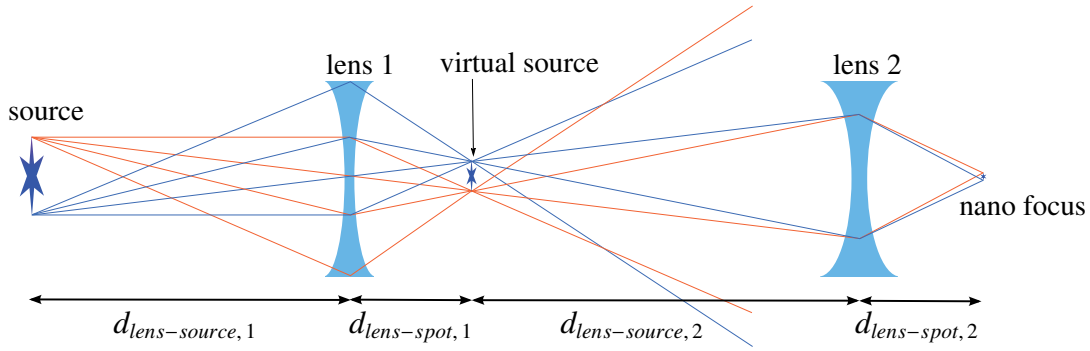

Figure 5.1: Sketch of the cone–beam setup and its distances. The distances for the two lenses are not to scale, those of lens 1 being much larger than for lens 2.

of 50 nm, this requires a horizontal demagnification of

$$M \approx \frac{90\,\mu\text{m}}{50\,\text{nm}} = 1800.$$

In addition, the focal distance also determines the beam divergence and the beam profile. A homogeneous beam profile is only achieved in the central region, where the absorption of the lens does not dominate the beam shape. For practical reasons, the divergence should be kept moderate, because it determines the distance of the sample. The following example shall demonstrate the situation: Assuming a sample with the same diameter as the lens aperture, the sample needs to be placed in a distance of $2\,f$ for a tight but complete illumination. For very small f, the distance between sample and spot size can go down to some millimeter, which significantly complicates sample handling and the installation of apertures between optics and sample to reduce stray illumination.

The requirements are thus a spot size of below 50 nm, a moderate divergence, and a large working distance. This can only be achieved by a two–tiered approach: The demagnified image spot of the first lens is further demagnified by a second lens. A sketch of this scheme is given in Figure 5.1. The overall source demagnification is

$$M_{total} = M_1 \times M_2. \tag{5.1}$$

For both systems, the geometric demagnification is given by

$$M_i = \frac{d_{\text{lens-source},\,i}}{d_{\text{lens-spot},\,i}} \tag{5.2}$$

where $d_{\text{lens-source}}$ and $d_{\text{lens-spot}}$ give the distances between the source and the lens and between lens and spot, respectively. Because of the large distance from the photon source to the optics hutch, M_1 needs to be larger than M_2, with $M_1 \times M_2 \approx 1800$.

Following the beam from the source, the first possibility for installing focusing elements is at

the end of the optics hutch, at about 58 m distance from the source. A length of 1.5 m is accessible for the installation of optics, apertures and diagnostic equipment. The subsequent space is occupied by a beam shutter, a permanently installed vacuum transfer pipe between the optics hutch and EH1 and vacuum components at the beginning of EH1. The next accessible free space is at about 64.5 m distance from the source, in the experimental hutch. A distance of at least 6.5 m between the two sets of lenses needs to be covered, the design constraint is thus

$$d_{\text{lens–spot, 1}} + d_{\text{lens–source, 2}} \geq 6.5\,\text{m}. \tag{5.3}$$

In addition, $d_{\text{lens–spot, 1}}$ should be as large as possible, to gather as many photons as possible. The aperture of the second lens is of the same order of magnitude as the first lens. The geometric enlargement of the beam leads thus to a loss in intensity of

$$I_1 \approx I_0 \left(\frac{d_{\text{lens–spot, 1}}}{d_{\text{lens–source, 2}}} \right)^2 . \tag{5.4}$$

Absorption in the lens and the beam shape and divergence lead to the central part of the cone being more intense than the flanks, i.e. the intensity loss as given by Equation 5.4 is overrated. For example, distances of $d_{\text{lens–spot, 1}} = 1.2\,\text{m}$ and $d_{\text{lens–source, 2}} = 5.3\,\text{m}$ would lead to $I_1 = 0.05\,I_0$. The actual values are slightly higher, but about one order of magnitude is lost.

Furthermore, the projected magnification of the sample should reach at least $M = 25$, i.e. with a propagation distance of approximately 4.5 m, this leads to

$$d_{\text{lens–spot, 2}} \leq \frac{4.5\,\text{m}}{25} = 0.18\,\text{m}. \tag{5.5}$$

The constraints given by Equations 5.3, 5.4, and 5.5 restrict the choice of parameters, but still leave room for some optimization. The necessary boundaries are accounted for by the following choice of geometry:

The first lenses are designed with a nominal focal distance of 1 m. The lens parameters (compare Figure 2.19)

$$\begin{aligned} R &= 35.0\,\mu\text{m}, \\ R_0 &= 160.0\,\mu\text{m}, \\ N &= 5, \ldots, 22 \end{aligned}$$

for the energy range of 10 to 20 keV allow keeping the focal distance constant at 1200 ± 105 mm. Figure 5.2 shows the results of the calculation. The properties of the lens materials change slightly with energy and a sudden change of the properties always occurs at a change of the number of lens elements. As a result, the function of the focal distance resembles a sawtooth in its shape.

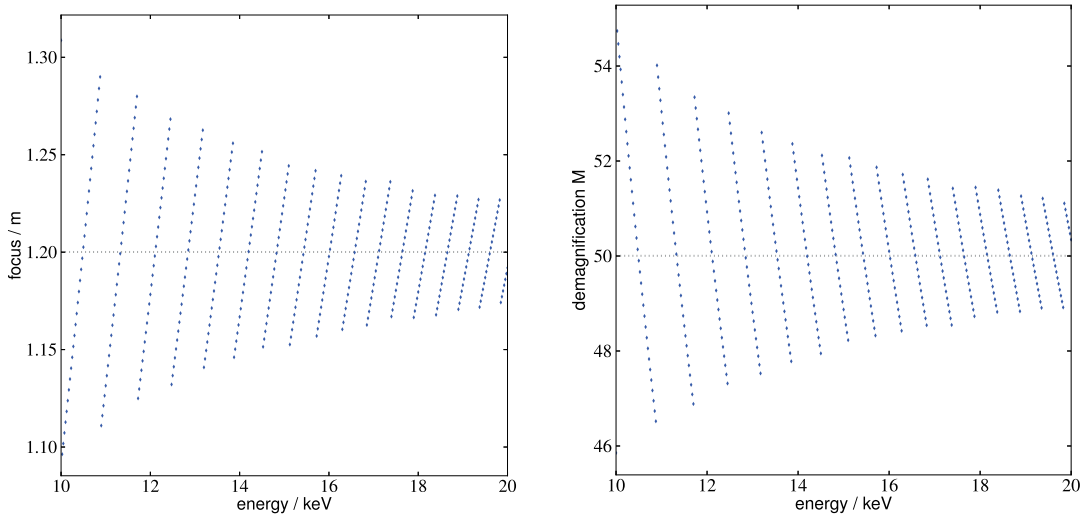

(a) focal distance **(b)** source demagnification

Figure 5.2: Calculations of focal distances and resulting geometrical source demagnifications for the lens set no. 1. The dotted gray line is the target, the blue dots are the best matches, calculated in 25 eV steps. Because the number of lens elements can only change in steps of one lens element, there are jumps around the best fit. The target demagnification can be reached using the aforementioned parameters for the lenses.

As the actual source demagnification varies between $M = 46$ and $M = 54.5$, the required demagnification for the second lens also varies around $M = 30$. The target if thus not a flat line any more, but a second sawtooth to compensate the energy–dependent behavior of the first set of lenses. Lenses with the following parameters

$$\begin{aligned} R &= 6.0\mu\text{m}, \\ R_0 &= 50.0\mu\text{m}, \\ N &= 10,\ 11,\ \ldots,\ 40 \end{aligned} \tag{5.6}$$

allow a good approximation of the target values. Figure 5.3 shows the results of the calculation for the second lens. The achieved overall demagnification values are given in Figure 5.4. The setup allows to achieve the target demagnification with only slight variations over the energy range of 10 to 20 keV.

The working distance of 150 mm allows sufficient room for sample adjustment. For example, a sample with width and height similar to the aperture—which is around 100 µm—needs to be positioned at around 150 mm behind the focus, i.e. around 300 mm behind the lens. For smaller samples and higher magnifications, the sample can be positioned closer to the X–ray spot. However, the achievable resolution is limited to the spot size, regardless of higher magnifications.

The calculations presented here are for the aforementioned target resolution of 50 nm. The geometry does not allow smaller spot sizes, but larger spot sizes can be easily accomplished by

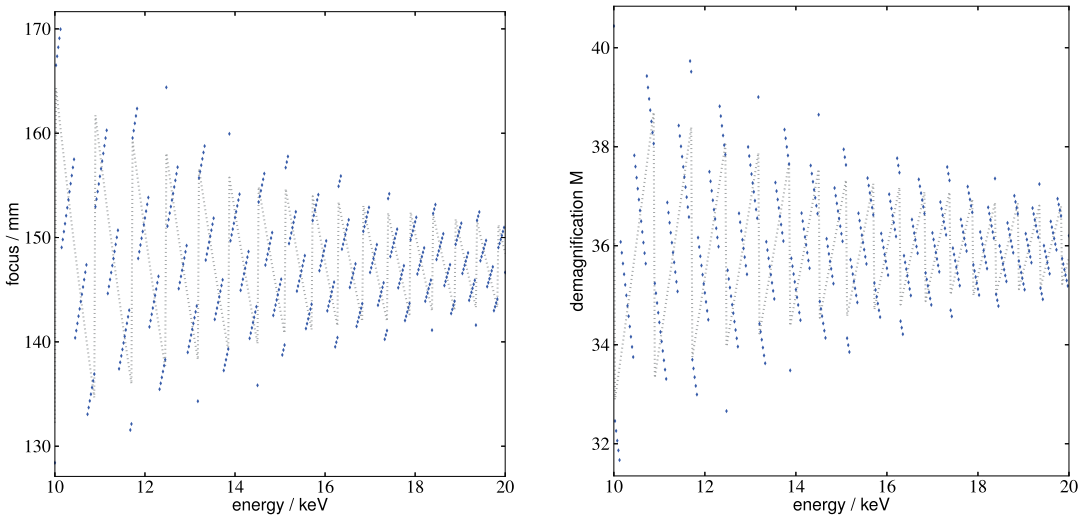

(a) focal distance **(b)** source demagnification

Figure 5.3: Calculations of focal distances and resulting geometrical source demagnifications for lens set no. 2. The dotted gray line is the target, determined by M_1 and $M_{target} = 1800$. The blue dots are the best matches, calculated in 25 eV steps. Because the number of lens elements can only change in steps of one lens element, there are jumps around the best fit.

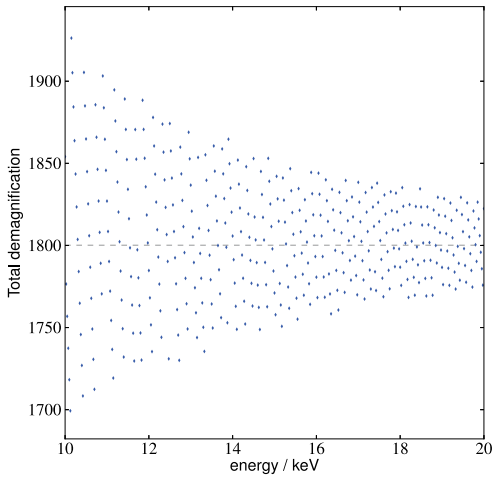

Figure 5.4: The overall source demagnification M, calculated with the lens parameters described in the text. The optics allow demagnification values very close to the target value of 1800 throughout the energy range from 10 to 20 keV.

varying the distances $d_{\text{lens-spot, 1}}$ and $d_{\text{lens-source, 2}}$. The geometric enlargement given in Equation 5.4 can be smaller, if a lower source demagnification is required. While larger spots lead to a deterioration of the achievable resolution, they offer a direct increase in photon flux.

5.1.2 X-ray microscopy setup

Imaging lens

The basics of a full field X–ray microscopy setup are given in section 3.2.4. For this setup, the resolution is limited by the optics, according to Equation 3.12:

$$A = \frac{1.22\,\lambda\,f}{D}.$$

To avoid confusion with the lens radius of curvature R, the resolution is abbreviated by A in this section. While the wavelength λ is defined by the experimental needs of the sample absorption, the parameters of focal length f and lens effective aperture D are freely selectable within limits. The lens aperture is limited by the effective aperture (see Equation 2.42). As both f and D_{eff} depend on the lens parameters N, R, R_0:

$$\begin{aligned} f &= f(N,\, R,\, R_0) \\ D_{eff} &= D_{eff}(N,\, R,\, R_0), \end{aligned}$$

it is

$$R = R(\lambda, N,\, R,\, R_0). \tag{5.7}$$

Consider a geometry with R = const and R_0 = const. To increase the resolution, the focal distance has to be decreased. This is done by increasing the refractive power, i.e. by increasing the number of lens elements. However, a higher N directly decreases both the effective aperture and the lens transmission.

Furthermore, the resolution in the full field microscope should be constant throughout the complete field of view. The angular acceptance of the lens decreases with the distance of the sample to the optical axis, and correspondingly the numerical aperture as well. This results in a lower resolution for these points, i.e. the resolution is not constant throughout the complete field of view. The effect gets stronger with decreasing focal distances, limiting the focal distance. The criterion of whatever deterioration of resolution is still acceptable limits the field of view because points lying further out of the optical axis suffer from a stronger decrease in the angle of acceptance. For tomographic applications, the requirement of a homogeneous resolution throughout the complete image is much stronger than for purely two–dimensional microscopy applications where the ef-

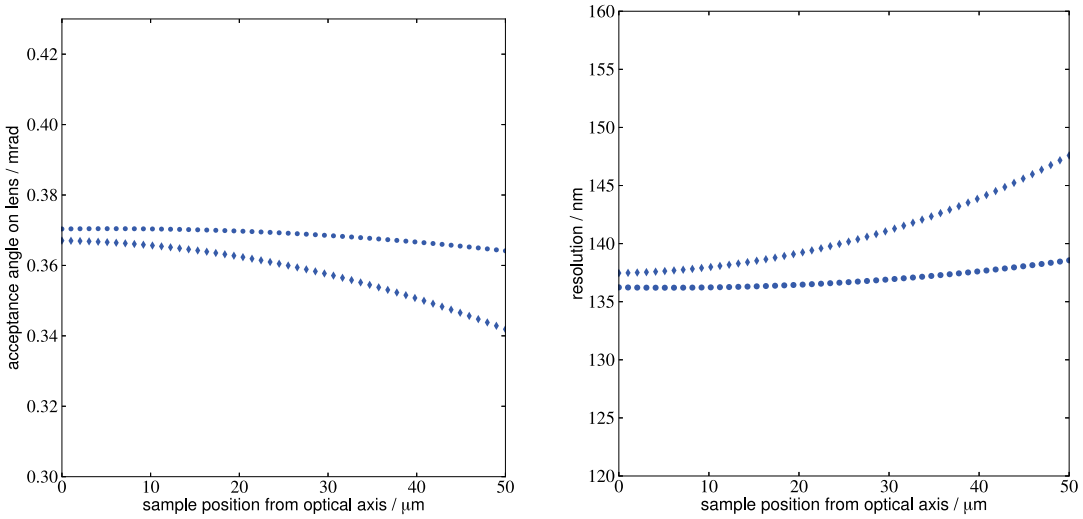

(a) angular acceptance **(b)** image resolution

Figure 5.5: Ray-tracing simulation results of the lens' angular acceptance for points off the optical axis. Points in the horizontal plane are marked with dots, points with a vertical offset are marked by diamonds. Simulation parameters: $E = 15\,\mathrm{keV}$, $f = 110\,\mathrm{mm}$, $M = 15$, effective aperture $D = 68\,\mu\mathrm{m}$. Simulation courtesy of Felix Marschall [79].

fects can be directly accessed in the image. Figure 5.5 shows the decreasing angular acceptance towards the edges of the field of view. The trend of decreasing resolution off the optical axis gets stronger with decreasing focal length.

For tomographic applications, it is also important that the microscope gives a sharp image throughout the complete sample depth. This corresponds to a sufficiently large depth of field of the X–ray optics. The near and far depth of field D_n and D_f, respectively, for imaging optics can be calculated from geometric considerations [41]:

$$D_n = \frac{s\,f^2}{f^2 + \frac{f\,c}{D}(s-f)} \tag{5.8}$$

$$D_f = \frac{s\,f^2}{f^2 - \frac{f\,c}{D}(s-f)}. \tag{5.9}$$

Here, f is the focal width of the lens, s is the sample distance, D is the lens aperture, and c the circle of confusion, i.e. the acceptable spot size that a point source would create. Demanding that sample features are blurred no more than 20 nm in size, and assuming a magnification $M = 25$, the acceptable circle of confusion is $c = 500\,\mathrm{nm}$. The depth of field Δs in which a point source would give an extended image of less than 500 nm is $\Delta s = D_f - D_n$. Figure 5.6 shows the depth of field for different focal distances, with an otherwise constant geometry. The depth of field should be larger than the sample size to minimize optical errors. Thus, the sample size ultimately defines the minimal focal distance of the optics. For the nanotomography experiment, sample sizes of

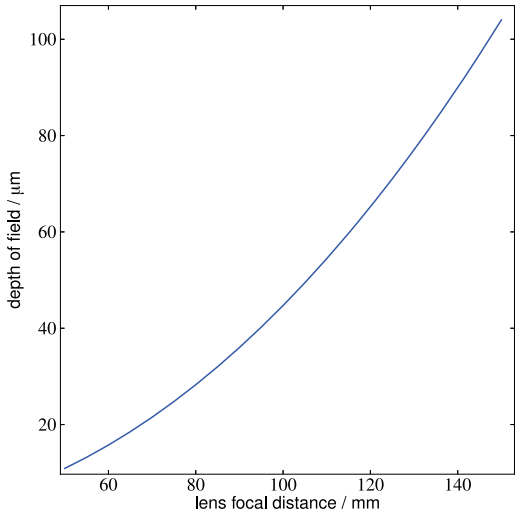

Figure 5.6: Calculations of the depth of field for a lens with variable focal distance f. The sample distance s varies accordingly, with a fixed distance to the detector. Parameters for the calculations are: circle of confusion $c = 500$ nm, lens aperture $D = 80\,\mu$m

$60\times60\times60\,\mu m^3$ are expected and are in accordance with the field of view for full field microscopy (see below). Correspondingly, the focal length should be larger than approximately 120 mm.

A compromise value for the working distance has to be found, meaning that the optimum focal distance is not $f \to 0$. Here, a value of $f = 0.12$ m was chosen based on sufficient depth of focus, resolution and uniform resolution over the field of view. Using the same lens parameters as for the cone beam geometry (Equation 5.6), the chosen working distance can be achieved with less than 5% deviation, using between 10 and 40 lens elements. Figure 5.7 shows that the deviation from the design value is smaller for higher energies. As the refractive decrement of each lens element decreases with increasing energy, the change between N and $N + 1$ lens elements becomes less pronounced.

With focal distance and the effective lens aperture known, the resolution limit of the setup can be calculated. Figure 5.8 shows both the effective aperture and the resolution limit. While the decreased absorption at higher energies leads to a slight increase in the effective lens aperture, the dominating effect is the decrease in the X–ray wavelength for increased photon energies. If the angular acceptance of the objective lens is fully illuminated, resolutions below 200 nm are achievable with this setup.

Condenser optics

The imaging lens can only achieve its theoretical resolution if the illumination covers the full angular acceptance. Due to the very high parallelism in the PETRA III X–ray beam with a divergence below 30 µrad (RMS), a condenser optics has to be included to enhance the beam divergence.

A divergent illumination has to be provided over the complete imaging field of view. This

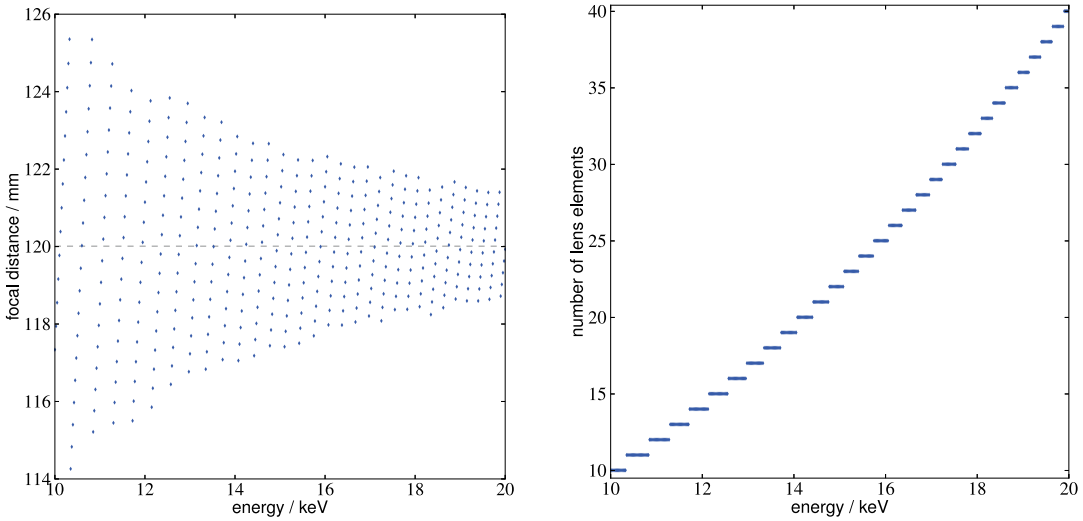

(a) focal distance **(b)** number of required lens elements

Figure 5.7: Calculations of working distance and the number of required lens elements for the objective lens. The dots are the values calculated in 25 eV steps. Because the number of lens elements can only change in steps of one lens element, there are jumps around the best fit.

defines the size of the illuminated spot and the required divergence in this point. The divergence angle in the illumination has to be larger than twice the numerical aperture. For an imaging lens with

$$f = 120\,\text{mm}$$
$$D = 100\,\mu\text{m},$$

this yields a required illumination angle of

$$\alpha = 2\,\text{NA} = 8.333 \cdot 10^{-3}. \tag{5.10}$$

In addition, the illuminated field of view should be larger than 60 µm. These two demands define the condenser diameter D and the working distance f. The working distance scales proportionally with the diameter, as

$$\tan\alpha \approx \alpha = \left(\frac{D - D_0}{f}\right), \tag{5.11}$$

where D_0 is the illuminated field of view. For optimal light gathering capabilities, the aperture should be as large as possible. Practical limitations are both the beam size and the condenser fabrication.

Classical lenses produce an image of the source, demagnified by the ratio of source distance d_{source} to $d_{\text{working distance}}$. At PETRA III, the vertical source size of only about 10 µm (FWHM) and

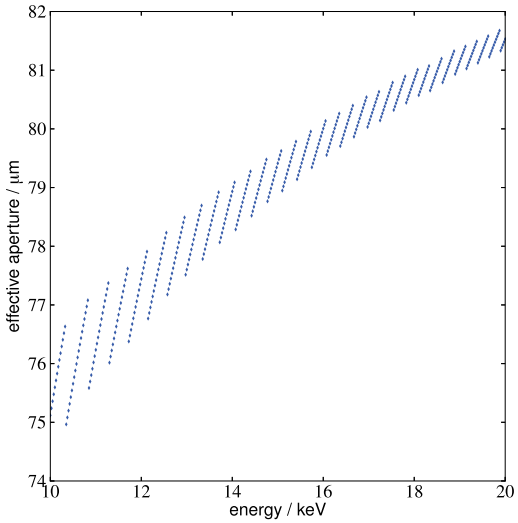

(a) effective aperture

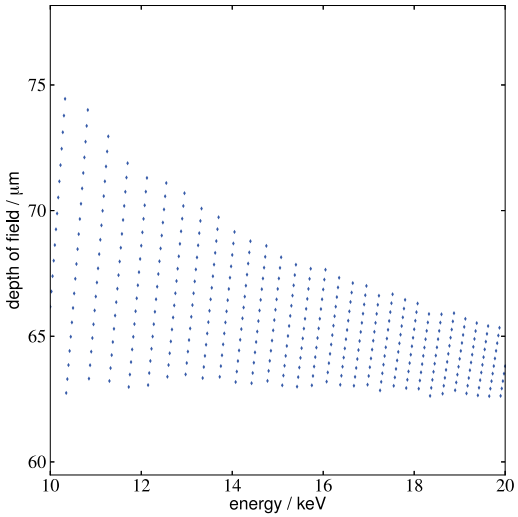

(b) depth of field

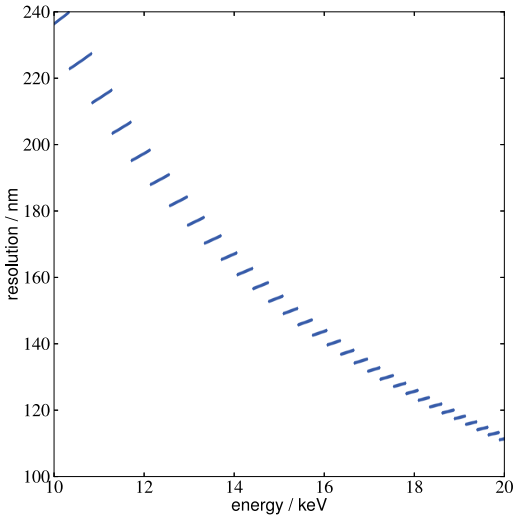

(c) resolution limit

Figure 5.8: (a) Calculations of effective lens aperture and (b) depth of field. (c) In combination with the focal distance (Figure 5.7(a)), the resolution limit can be calculated. Note that the enhanced resolution with increasing photon energy, is due to the decreasing photon wavelength, the other parameters being similar. Values are calculated in 25 eV steps.

an expected image size of 60 µm are not compatible with a large opening angle α.

X-ray lenses composed of prisms or similar structures [117] allow tailoring the required spot size and working distance. Note that it is not required to acquire a well–defined image of the source but only to provide divergent illumination.

For a condenser diameter of $D = 600\,\mu\text{m}$, an illuminated field of view $d_{illum} = 60\,\mu\text{m}$ and the required divergence angle α from Equation 5.10, Equation 5.11 can be solved for the working distance

$$f = 0.65\,\text{m}. \tag{5.12}$$

This working distance fully illuminates the opening aperture of the objective lens with divergent illumination. A further increase in beam divergence would not lead to any improvements in the microscopy image quality while decreasing the total photon flux. Increasing the photon angle with respect to the optical axis only leads to an increase in photons that do not match the angular acceptance of the objective lens, i.e. which are lost.

5.2 Experimental implementation

This section describes the requirements in positioning mechanics, stability, and flexibility for the different parts of the experiment. Following the requirements, the corresponding solutions are presented as well.

5.2.1 Optics hutch equipment

For the cone beam setup, the first lens creating the virtual source has to be positioned in the optics hutch. The X–ray lens has to be adjusted in position (x, z) and orientation (Rx, Rz) with respect to the X–ray beam. The position in beam direction (y) only changes the focal position relative to the source; the rotation around the beam axis (Ry) does not change the virtual source at all, because the lens is two–dimensional. Thus, both these degrees of freedom are not needed for alignment.

The KIT lithographic fabrication process allows structures of up to 20 mm width, i.e. several X–ray lenses can be created on one substrate. In addition, the installation and change of lens wafers in the vacuum is a rather time–consuming endeavor. Correspondingly, the design shall be capable of installing several wafers in parallel.

The requirements for positioning accuracy are given in Table 5.1. The difficulties lie in the combination of the mechanics. Standard high–quality translation stages have pitch and yaw errors of ±50 µrad each. Goniometer stages are precise in one direction but wobble errors for the other directions are above ±125 µrad [38, 84].

positioning direction	required movement range	minimum required precision
x translation	15 mm	3 µm
z translation	15 mm	3 µm
rotation around x–axis (Rx)	3 °	35 µrad
rotation around z–axis (Rz)	3 °	35 µrad

Table 5.1: Required adjustment mechanics and necessary precision for the alignment of KIT X–ray lenses. Data taken from [69]

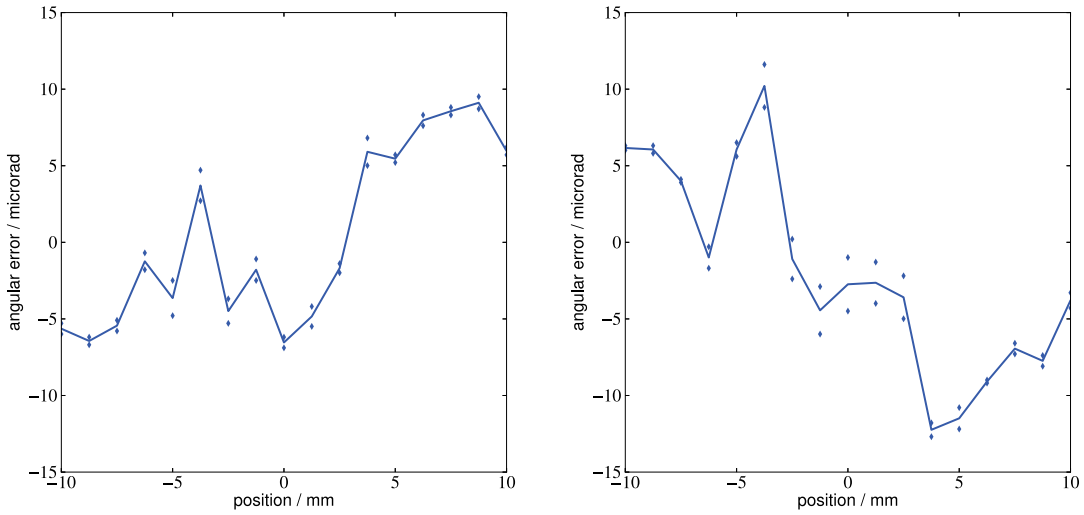

(a) error in Rx **(b)** error in Rz

Figure 5.9: Measurement of the angular errors for a linear movement in x. The kinematics is stable even over large linear displacements, the errors are well below the requirements for the X–ray lenses.

Two linear stages and two goniometer stages are necessary to cover all four directions (x, z, Rx, Rz). Assuming all the errors from these stages to be independent, the overall angular error (two translation plus one goniometer stage, as the other goniometer stage is precise in the required direction) adds up to

$$\Delta\alpha = \pm\sqrt{50^2 + 50^2 + 125^2}\,\mu\text{rad} \approx \pm 145\,\mu\text{rad}. \tag{5.13}$$

This is unacceptably large as compared to even the minimum required precision of the mechanics. A stacking of axes is not suitable, but an integrated approach has to be chosen. A customized PI miCos GmbH SpaceFab offers all the necessary translations and rotations. It consists of three sets of crossed axes, upon which a platform with three legs is mounted, connected through bearings. Apart from the smaller spatial requirements for an integrated mechanics, the overall stability of the setup is greatly improved. Figure 5.9 shows measurement results from an interferometric test of the mechanics. The angular error is well within the acceptable range.

The lens positioning unit is mounted in a large vacuum chamber of 1.5 m length, allowing

an uninterrupted vacuum from the beamline front end up to the experimental station. In addition to the lens positioning mechanics, 1.2 m length are still available in the vacuum tank. A PI miCos custom–built linear translation stage with 500 mm travel range is installed in beam direction, allowing diagnostics or apertures to be installed later on. Cabling, vacuum cable feedthroughs, and motor power amplifiers are already installed to allow an easy integration of these systems. A beamline slit system is mounted about 1.5 m upstream of the X–ray optics positioning mechanics and can be used to tailor the beam position, width, and height to the requirements of the X–ray optics.

Two retractable photo diodes are installed at beam entrance and exit tubes in the vacuum chamber because no camera system can be installed in the vacuum chamber. They allow monitoring the beam intensity in front and behind the lenses. In combination with a precise in–vacuum slit system, this setup allows for a complete characterization of the lens performance and properties.

The complete setup is depicted in Figure 5.10. The flexibility and stability of the mechanics allow the precise positioning of lithographic X–ray lenses as well as other optical components. The only constraint for optics is the fixed position of 59 m downstream from the source and the travel range of the linear axis reserved for diagnostics. Distances of 0.6 – 1.3 m between X–ray optical elements and diagnostic position are feasible and define the working distance of the optics—if diagnostics or slits are necessary. If the diagnostics can be ignored, any distance between zero and the next lens is feasible.

5.2.2 Experimental hutch – substructure

Depending on the type of setup (microscopy, cone beam) and target magnifications, the distances between the components vary and need to be adjusted. This requires a precise and reproducible translation of the individual components.

A second requirement is stable positioning over short and long timescales. The main issues for short and long term stability are vibrations and thermal drifts, respectively. Vibrations can be damped by a high mass of the structure. In addition, the larger the mass, the more energy is needed for a defined temperature change. This makes larger masses preferable, because they react more slowly to changes in ambient conditions. The air conditioning in the experimental hutch guarantees a climatic stability to within 0.1° C and in combination with a slowly reacting body allows a thermally stable substructure. Furthermore, minimizing thermal effects requires a low coefficient of thermal expansion.

Granite unites the requirements of stiffness, high density, low thermal expansion, and high specific heat. It was thus the material of choice for the experimental substructure.

A single granite slab of 6.8 m length, 0.6 m width, 0.9 m height, and a weight of 10.2 metric

Figure 5.10: View of the in–vacuum lens positioning mechanics, as mounted in the vacuum chamber. The base plate is visible at the bottom inside the chamber. The mechanics are mounted on this plate to prevent bending due to the bending of the chamber walls if evacuated. To the right, the kinematics for lens positioning are visible; to the left in the background, the long translation in beam direction for slits or diagnostics. The retractable photo diodes are not visible, they are mounted directly on the chamber walls next to the entrance and exit pipes. To the very right, the adapter for the lens and two lenses are mounted on the kinematics.

Figure 5.11: Mounting schema for the granite substructure. The positions of the setup points are marked with the orange circles. The orientation is defined because of mounting the structure in three points only. To minimize bending of the granite, the points are placed in the Bessel distances of the long axis.

tons acts as experimental substructure. The comparably large height is necessary for a planar surface, as the bending is inversely proportional to the third power of the thickness. The structure is mounted on three points only to guarantee a defined position. Figure 5.11 sketches the mounting. Using the Bessel points for the support minimizes the overall bending of the granite in direction of the long axis.

The surface of the substructure is polished and acts as slide face for four air–bearing slabs on which the individual experimental components are installed. The preparation of the granite surfaces and the installation of the air–bearing system was performed by LT Ultra. A channel in the surface is used for horizontal guidance of the four slabs and is fitted with permanent magnets for propelling the slabs via a linear induction motor. A schematic view is given in Figure 5.12. Usage of the channel side faces allows a high precision of the position alignment in the horizontal plane,

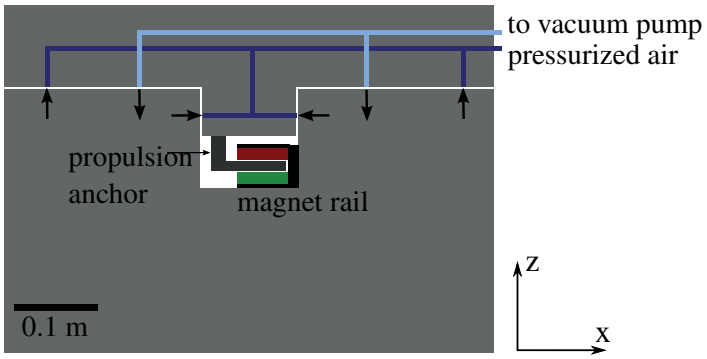

Figure 5.12: Schematic cross–sectional view of granite substructure. A combination of pressurized air and partial vacuum is used to hold the sliders in a defined position. The horizontal stability is created by using the channel side faces as supporting surface. The resulting forces on the slider are indicated by arrows. A magnet rail mounted in the channel is used to propel the sliders with a linear induction motor.

perpendicular to the beam. The motor control is responsible for the stability in beam direction. A Renishaw linear encoder guarantees a resolution in beam direction of below 2 µm. For highest position stability during measurements, the pressurized air can be switched off, settling the slider on the substructure.

Each slider is $600 \times 600\,\mathrm{mm}^2$ in size. Tubes for partial vacuum, pressurized air, sensor cabling, and security bumpers require a minimal distance of 80 mm between two sliders, i.e. the minimal distance of points at the centers of two adjacent sliders is 680 mm. As the four sliders share the overall travel range of 6.1 m, each slider has a remaining travel range of 4.06 m. A cable track ensures that the components on the sliders can be used in any position along the travel range, posing no constraints on the positioning of the individual components. One slider is reserved for the installation of the sample positioning, one for the detector. The remaining two are destined for X–ray optics. Of these two, one slider is set in front of the sample stage and one behind it, as seen if looking with the beam. This design allows performing both cone beam and X–ray microscopy experiments with the same experimental setup and with only a minimum of modifications.

5.2.3 Experimental hutch – sample stage

The sample stage includes the rotational axis as well as positioning stages. The mechanical stability has to be well below the target resolution for the sample, setting the requirements for the mechanics to be more stable than 100 nm.

Sample stage substructure

There are three reasons that require a motorized substructure for the sample stage. First, the beam position can change with respect to the experimental installation. This movement has to be compensated. Second, the installation of sample environment or any other reason for the sample posi-

positioning direction	minimum required precision
x translation	100 nm
z translation	100 nm
rotation around x–axis (Rx)	1 µrad
rotation around y–axis (Rz)	1 µrad

Table 5.2: Required accuracy for the directions of travel for the sample stage.

tion on the rotational axis to change needs to be balanced. Last, the sample has to be moved in and out of the beam to acquire reference images.

While the first two points do not need a high precision (better than 1 µm), they do need a very high temporal stability. Any position drift during the measurement would lead to reconstruction artifacts. The same is true for any changes in the sample position. Hence, the axis that moves the sample stage out for reference images needs to have a very high reproducibility better than 100 nm.

As not only the beam position but also the beam direction can vary, for example by changing the angle of the second monochromator crystal, the sample stage needs also to be aligned angularly. The pitch alignment shall be as good as possible. Assume a sample diameter of 100 µm and a virtual detector pixel size of $10 \times 10\,\mathrm{nm}^2$. For best quality reconstruction, any tipping of the sample should not change the position on the detector significantly. Calculating with 10 nm vertical offset, the corresponding angle is

$$\Delta = \arctan\left(\frac{10 \cdot 10^{-9}}{100 \cdot 10^{-6}}\right) = 100.0\,\mu\mathrm{rad}. \tag{5.14}$$

This value is an upper limit. Because modern stages can reach values in the range of 1 µrad, this lower value shall be taken for the required position accuracy. While this seems an exceedingly stern requirement, angular errors are not correctable in the tomographic reconstruction. Linear displacement errors can be handled and corrected, whereas angular errors cannot. In order not to exclude further use of the stage, these strict error tolerances will be used. The error in tilting is similar to the tipping error and also the corresponding positioning requirements. An overview of all requirements for the axes are given in Table 5.2.

This leads to a total of 4 degrees of freedom: x, z, Rx, Rz. Two reasons argue against a stacking of axes: To avoid the summation of errors and to define the position of the sample rotational axis freely.

While there are still 4 motors necessary for achieving all desired degrees of freedom, a smart combination of the former leads to a higher stability. One motor is required for the x translation, the other three are used for independent motorized elevation stages. A synchronous movement acts as a z motor, asynchronous moves can be used for tipping and tilting. The motor stages used for these movements are customized stages from PI miCos GmbH.

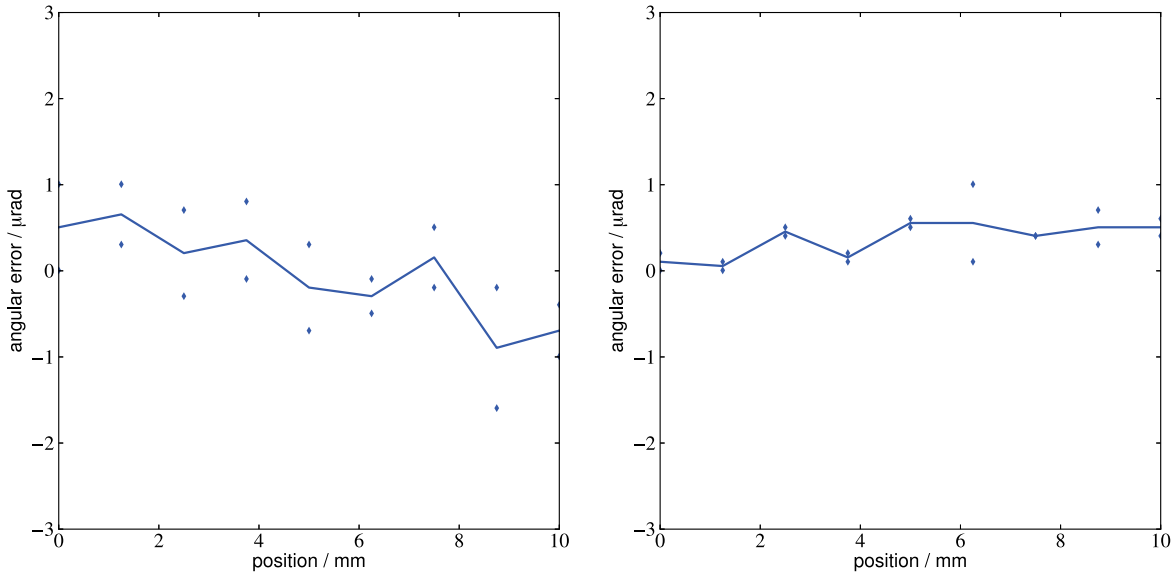

(a) pitch error **(b)** yaw error

Figure 5.13: Errors of the sample stage X–axis. The measurements were performed at the sample position, i.e. 460 mm above the axis, which has been loaded with 110 kg to simulate the weight of the rotational axis.

With a distance of 300 mm between two elevation stages, an angle of 1 µrad tilt corresponds to $\Delta z = 300\,\text{nm}$. A stage with a high gear reduction can achieve a resolution of better than 100 nm, clearly sufficient for this application. Three stages, mounted in a triangular arrangement are thus sufficiently precise for elevation, tipping, and tilting while minimizing errors.

The x translation has two functions. First, the center of rotation has to be aligned with respect to the beam. This task requires a travel range of 10 mm, an accuracy in the range of some micrometer, but combined with a stability better than 50 nm. Second, the complete sample stage has to be moved out of the beam to acquire reference images. The travel range is about the sample size, i.e. 500 µm are sufficient. But the position reproducibility of the sample has to be better than 50 nm, including pitch and yaw errors below 1 µrad to allow the sample projections to be properly processed in a tomographic measurement.

Both requirements are fulfilled by one massive linear axis, equipped with an encoder for higher positioning precision. Pitch and yaw errors are below 1 µrad (RMS) and the straightness and flatness are better than 50 nm (RMS) each. Figure 5.13 shows the angular error profile. During a measurement, only a limited section of the available translation will be used. If using a section of the axis which is very flat, the actual accuracy is even better than the average values which are given.

Sample stage

The sample stage consists of two components. First and most importantly, the rotational axis for tomographic measurements. Second, the sample positioning mechanics. As the sample needs to

be positioned exactly in the center of rotation, an alignment stage is necessary. The complete stage is manufactured by PI miCos GmbH.

The requirements on the stability of the rotational axis are the same as for the sample stage positioning in the previous paragraphs. There are four different errors to be considered:

- Rotational error: Errors in the sample stage rotation value.
- Radial error: Movement of the center of the axis of rotation.
- Axial error: Movements of the plane of rotation along the axis of rotation.
- Wobble error: Errors in the angular orientation of the axis of rotation.

The accuracy requirements for the *rotational error* are the least strict. Using an encoder on the rotation axis, the rotational error can be reduced to around $10^{-5}\,^{\circ}$. Considering that typical angular step sizes for a tomography are $\Delta\theta = 0.2^{\circ}$, an uncertainty of below 0.002° is sufficient. The *radial error* is a parallel movement of the axis of rotation. As the movement in direction of the beam is negligible, only the component perpendicular to the beam is of interest. This error leads to shifts of the sample on the detector image. As it is only a translation, it can be easily correted using image processing, for example by tracking the sample outline or center of mass. Similarly to the radial error, the *axial error* is a linear translation. It corresponds to the sample moving up and down on the detector. Uncorrected, this error would causes severe reconstruction artifacts. Tracking distinct sample features, all projections can be aligned before sinograms are created, making this error correctable using image processing. The *wobble error*, i.e. the angular position stability of the axis of rotation, is the most critical error. Throughout turning the axis, the angular orientation of the axis of rotation has to be kept constant. A pitching of the axis of rotation in the beam direction cannot be corrected and leads to sample features moving over several detector rows.

The estimation of tolerable errors for the sample position from Equation 5.14 applies to the rotation axis as well. Because of the rotation, pitch and yaw errors are combined in the wobble error, which has to be kept below 2 µrad. The axial error has to be kept below the detector pixel size, and the same is true for the radial error. For best resolutions, the errors shall be smaller than 50 nm each. Table 5.3 given an overview of the measurement results for the rotational axis. Although the measurement quality would benefit from even smaller error values, the achieved values reflect the current technical limit.

Sample stage error analysis

To assess the influence of these errors on the obtainable measurement quality, a phantom simulation was performed. The projections of nine cylinders were simulated and reconstructed. Three cylinders of 50 nm, 100 nm, and 200 nm height and radius each with linear attenuation values of

type of error	error σ
axial error	16.92 nm
radial error	21.43 nm
tilt Rx	0.223 µrad
tilt Ry	0.190 µrad

Table 5.3: Results of error measurement for the rotational stage. The errors were measured at the nominal sample position of 20 mm above the surface of the axis.

	no error	statistical error	statistical, radial, and axial error
attenuation I	$1.800\,\mu m^{-1}$	$1.8\,\mu m^{-1}$	$1.8\,\mu m^{-1}$
variance I	$0.696\,mm^{-1}$	$4.03\,mm^{-1}$	$7.935\,mm^{-1}$
attenuation II	$1.400\,\mu m^{-1}$	$1.400\,\mu m^{-1}$	$1.423\,\mu m^{-1}$
variance II	$1.723\,mm^{-1}$	$4.766\,mm^{-1}$	$16.766\,mm^{-1}$
attenuation III	$1.000\,\mu m^{-1}$	$0.999\,\mu m^{-1}$	$1.012\,\mu m^{-1}$
variance III	$1.302\,mm^{-1}$	$4.287\,mm^{-1}$	$15.567\,mm^{-1}$

Table 5.4: Analysis of the reconstruction for the simulation of rotational errors. The values were obtained by a rectangle of 10×10 pixel in the center of each of the largest cylinders. The attenuation values are normalized to the values of 0 and 1.8 for the lowest and highest attenuation values, respectively.

$1.0\,\mu m^{-1}$, $1.4\,\mu m^{-1}$, and $1.8\,\mu m^{-1}$ made up the phantom to be investigated. The radial and axial displacement error were each randomly determined for each projection, with a Gaussian error distribution and the variance σ as given by Table 5.3. Radial errors shift the projected image on the detector while axial errors influence the transmission: If the axial error moves the sample up or down, only part of the detector row is attenuated and the overall intensity is the normalized sum of direct transmitted beam and attenuated part. The statistical error varies the photon flux on the detector according to a Poisson distribution around the mean value. The reference image is statistically modulated as well.

The results of these errors on the reconstruction quality are given in Figure 5.14 and Table 5.4. They show that the statistical error only has a minor impact on the reconstruction. While the variation in attenuation increases, the absolute values are still precise. Figure 5.14a and 5.14b visualize the influence of the statistical error on the reconstruction quality. The color coding highlights artifacts with linear attenuation $\mu < 0$; these values are physically impossible and they can all be attributed to reconstruction artifacts.

Adding radial and axial errors introduces slight variations in the average attenuation values and larger variations of these (compare Table 5.4), but the overall quality still remains very good. Artifacts with $\mu < 0$ become more pronounced with the introduction of radial and axial errors in Figure 5.14c. If a lower threshold of 0 is used in the reconstructed image, the artifacts disappear (compare Figure 5.14d), but it has to be kept in mind that the overall attenuation is constant, i.e. for every pixel with an attenuation error of $-\delta$, the value $+\delta$ is distributed as an error in the remaining

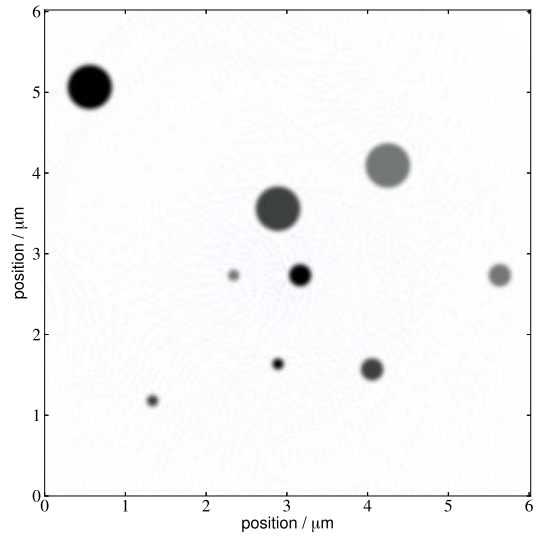

(a) reconstruction with no errors (full scaling)

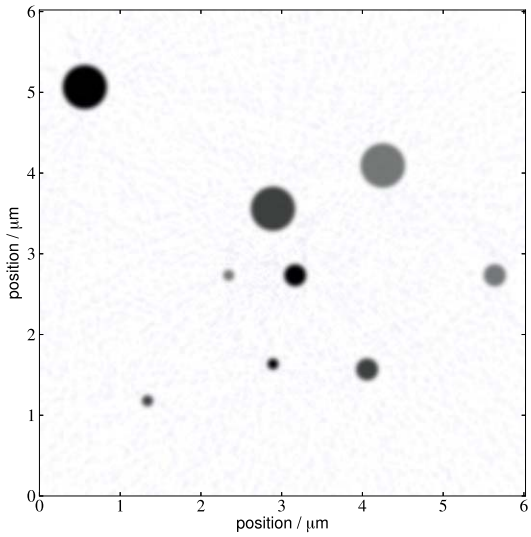

(b) reconstruction with statistical error only (full scaling)

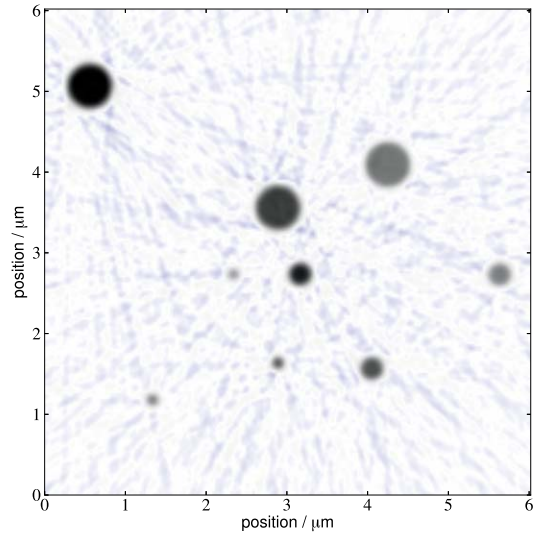

(c) reconstruction with statistical, axial and radial errors (full scaling)

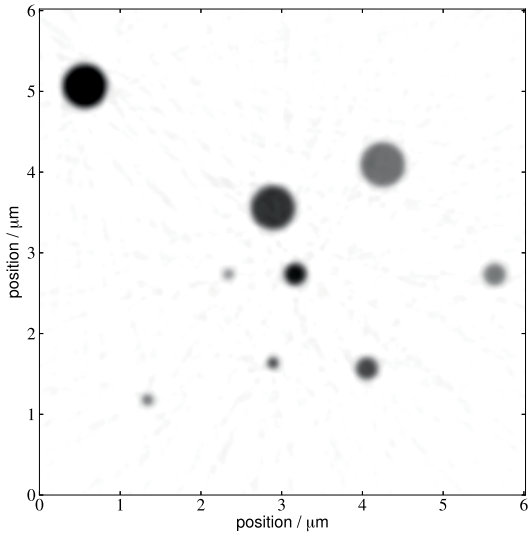

(d) reconstruction with statistical, axial, and radial errors (lower threshold 0)

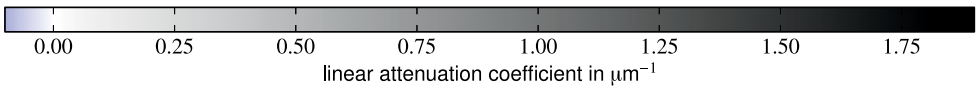

(e) color scaling for reconstructions above

Figure 5.14: Reconstruction of a phantom to evaluate the influence of errors on the reconstruction quality. Three cylinders of 50 nm, 100 nm, and 200 nm radius and height, each with linear attenuation coefficients of $1.0\,\mu m^{-1}$, $1.4\,\mu m^{-1}$, $1.8\,\mu m^{-1}$ were reconstructed with and without errors. For the statistical error, the full number of counts N was set to $N = 30000$ with a Poisson distribution. The grid size is 301×301 pixels and 901 rotation steps were simulated.
Note that the color coding (blue values for negative attenuation coefficients) is set to pronounce these errors for an error evaluation.

pixels.

The edge blurring is more difficult to compensate due to the radial and axial errors. Filtering can be used to enhance feature borders, but the tradeoff is a deterioration in the attenuation value precision. Nevertheless, even 100 nm sized–objects are still discernable, along with their respective attenuation values.

5.2.4 Experimental hutch – optics positioning stage

The optics positioning stage includes kinematics for the alignment of X–ray optics, positioning stages for X–ray apertures, and retractable photo diodes.

Depending on the chosen setup (cone beam or X–ray microscopy), the optics positioning must be useable on the first or third slider. In addition, the orientation changes with the setup, i.e. the configuration of lens and apertures is reversed.

The latter demand requires the complete stage to be very compact: Because of the close–by P06 beam pipe, construction space is very limited in one direction. Demanding the stage to fit after reversing its orientation, the spatial constraints have to be fulfilled at both sides of the beam.

The working distances of the X–ray optics define the distances between the optics and the sample. Mounting the sample centered on its slider and considering that working distances can be as low as some 10 mm, the optics need to be positioned potentially hanging over the sample stage. The same holds for the apertures, which need to be positioned between sample and optics.

Translation requirements for the optics are the same as for the installation in the optics hutch, presented in Section 5.2.1. Table 5.1 in Section 5.2.1 lists the required precision. To allow for a higher flexibility with future developments and to allow the installation of several lenses simultaneously, travel ranges have been defined more generously. For x and z, ranges of 20 mm and 50 mm, respectively, were selected. In beam direction, large translations can be conducted with the linear motors of the respective sliders; the optics positions is only required for fine adjustments of sample–optics distances. Two directions with large travel ranges, one direction with a limited range and three rotations are points that favor a miCos SpaceFab kinematics, mounted with the main travel plane perpendicular to the beam path. Since the mechanics is approximately (three–fold) symmetric around the X–ray beam, there is no possibility to install it above the rotational axis' surface. An installation next to the sample stage and a cantilever for the installation of the optics solve the spatial constraints.

Figure 5.15 shows the installed optics station with the kinematics for the X–ray optic positioning.

The apertures are installed hanging on a *xyz* stage for alignment in the beam and for parking them outside the beam. Since this stage can only move the complete set of apertures, additional

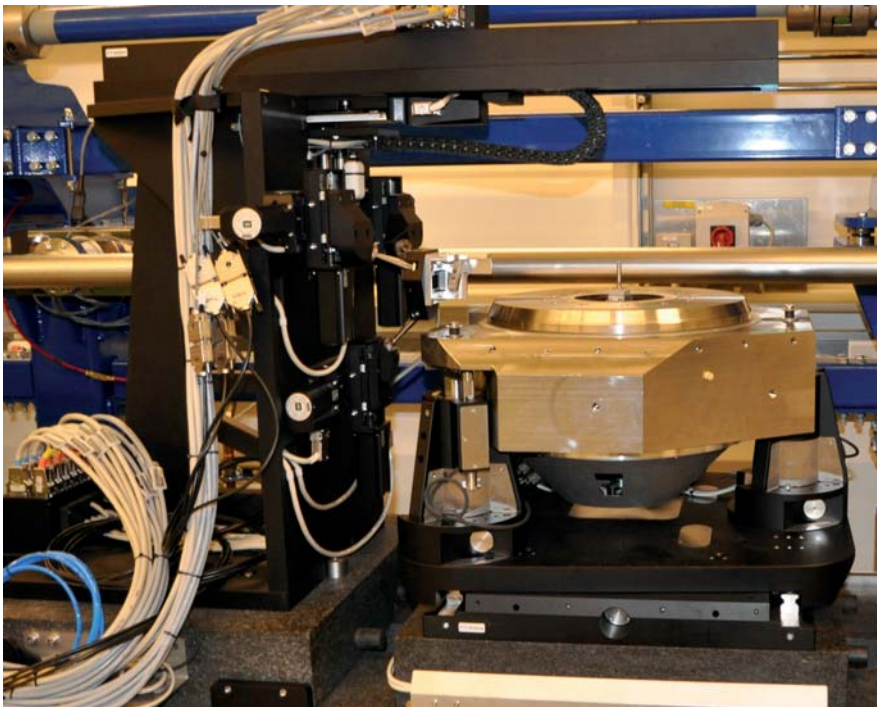

Figure 5.15: Photograph of the optics station, mounted in the X–ray microscopy orientation. The optics station is shown to the left and top of the image. The SpaceFab kinematics is mounted on the central support and the X–ray lenses are mounted on the flyer (center of the image). The cross bar is visible at the top and is used for installing the apertures and photo diodes (hidden from view).

motors for at least two of the four aperture sides are needed to control both the aperture position and aperture size. Motorizing all four brackets has the advantage that each bracket can be moved individually without affecting the other brackets or the slit position. Two *xy* piezo stages are installed for fine alignment of the slit brackets. This allows to change the aperture opening from zero to 350 µm and to scan it with a resolution of 10 nm. The global position can be adjusted independently of the opening with the *xyz* stage.

Scanning the apertures can be used to characterize the X–ray focus size using the slit as a knife edge. To ensure a proper quality of the edges, they have been polished with a focused ion beam (FIB) to a surface roughness of below 10 nm.

A view of the installation with apertures and photo diode is given in Figure 5.16. The photograph gives a good impression of the hanging, compact installation of all the aforementioned components.

5.2.5 Experimental hutch — detector positioning and detector

Detector positioning mechanics

The fourth slider is reserved for the detector and underlying positioning mechanics. The mechanics are needed to adjust the detector field of view to the position of the direct X–ray beam for alignment

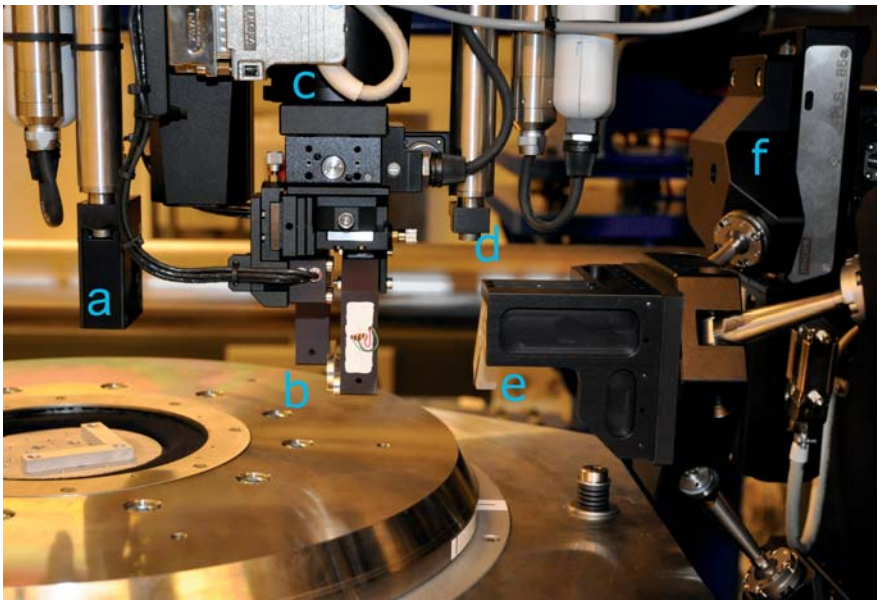

Figure 5.16: Photograph of the optics station, mounted in cone–beam geometry. The X–ray source is to the right of the image, the sample position at the center of the rotational axis to the left. The following components of the optics station are visible: (a) a photo diode on a retractable axis, currently in parking position. (b) X–ray apertures, installed on two crossed piezo stages and (c) mounted on a motorized *xyz* stage. (d) A second pusher motor for a photo diode in inverse orientation, currently uninstalled. The X–ray lenses (e) are mounted on the kinematics (f).

and X–ray microscopy image for imaging, respectively. Three degrees of freedom are necessary for detector positioning: translations in the plane perpendicular to the X–ray beam (x, z) and rotation of the CCD around the X–ray beam axis (Ry). The mechanics is designed to accommodate the same detector system as used for the micro tomography (compare Section 4.3). Because a rotation of the CCD is already included in the detector system, the mechanics only consists of a x translation and a z elevation stage. Travel ranges are 50 mm and 20 mm for x and z, respectively.

Due to technical complications, the micro tomography detector system could not yet be used for the first experiments. This required to install an additional cradle for the CCD to align its pixel columns with respect to the rotational axis. A gear box with a conversion of 10 makes the axis self–locking and allows a precision of better than 15 µrad.

Camera system

The camera system used for the nanotomography commissioning experiments is the same that was in operation at the micro tomography endstation of the HARWI II beamline at the DORIS III storage ring. It consists of a cooled CCD chip, a motorized adapter for focusing, a photo objective as optics and a scintillator. All components are connected with blackened, light–tight tubes. Figure 5.17 shows an image of the detector system, mounted on the detector mechanics and on the cradle.

The X–ray photons are converted in a cadmium tungstate ($CdWO_4$) scintillator crystal with

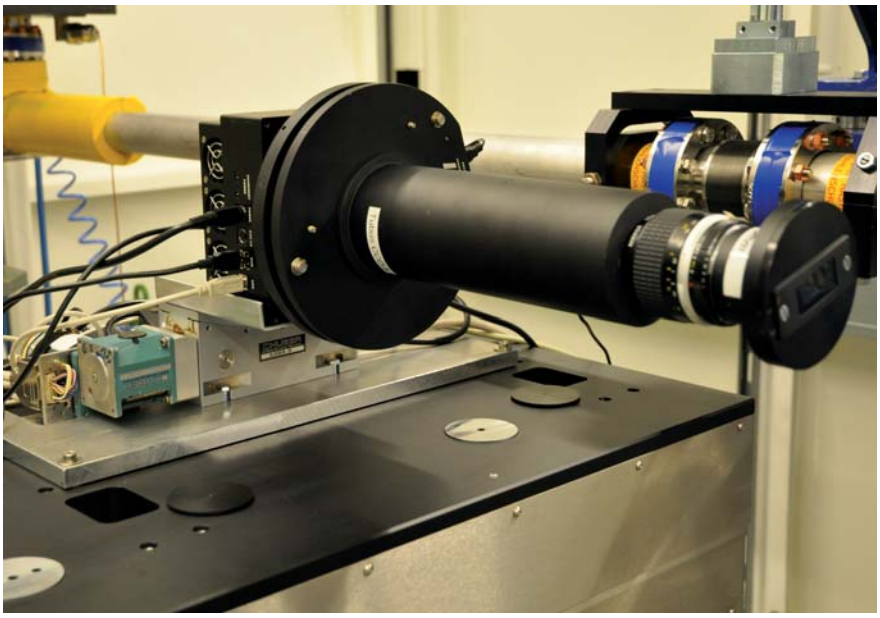

Figure 5.17: Image of the temporary detector on a cradle and the positioning mechanics. The camera system consists of a cooled CCD chip, a motorized adapter for focusing, a photo objective as optics and a scintillator crystal.

a thickness t of $t = 100\,\mu m$. $CdWO_4$ has an emission maximum at 475 nm and an emission bandwidth of roughly 100 nm (FWHM). Luminescence decay time is given with 14 µs [50], which is unsuitable for ultra–fast measurements, but well suited for nanotomography with exposure times in the range of seconds.

A commercial NIKKOR 35mm f/1.4 camera lens is used for magnifying the scintillator image. The lens is mounted in reverse orientation, i.e. the scintillator is set up in the classical camera film plane. In this orientation, the camera acts as a magnifying optics and projects a magnified sharp image on the CCD at a distance of about 300 mm. A typical magnification value for the nanotomography setup is $M \approx 10$. The resolution as determined with a modulation transfer function (MTF) edge measurement [14] is about 2 µm with an effective pixel size of 1.2 µm. In combination with an X–ray magnification of $M = 20$, this yields an overall resolution of 100 nm. For better resolutions, the micro tomography detector system would have to be used. This system is designed for a resolution of 700 nm for the visible light optics only. Using the same X–ray magnification, the resolution could be as good as 35 nm, but this would still be constricted by the X–ray optics as the limiting factor.

The motorized adapter is needed to focus the magnified image from the objective lens onto the CCD. The mechanics achieve a positioning accuracy of 1.5 µm between CCD and lens. As the scintillator screen is mounted very close to the focal length of the objective, the system is very sensitive to the correct distance of the CCD.

The camera is a Finger Lake Instruments model PLO9000, equipped with a Peltier cooling element to operate the camera at −15 °C. The CCD chip area is 3056×3056 pixels of $12 \times 12\,\mu m^2$

size. Analog–digital conversion bandwidth is 16 bit, with a digitalization speed of 10 MHz. The true dynamic range of the camera is 13 bit [48], i.e. $2^{13} = 8192$ different levels of information can be distinguished with a statistical significance. The camera is equipped with an iris shutter to regulate the exposure times. Because of finite opening and closing times, exposures are limited to times larger than 80 ms.

The efficiency of the detection system can be estimated as follows: The scintillation photon yield is 12 – 15 / keV [50]. These photons are emitted in the complete 4π solid angle, whereas the objective covers 0.33 sr (distance to scintillator $l = 48$ mm, lens diameter $d = 33$ mm). Because of refraction at the crystal surface, the effective solid angle is smaller by approximately $n^2_{CdWO_4} = 2.2^2 = 4.84$ [14]. The effective solid angle is 0.07 sr. The optics capture only the fraction $\frac{0.07}{4\pi} = 0.0056$ of all photons emitted. The lens aperture light transmission is variable from $T = 0.1$ (for $f/1.4$) to $T = 8 \cdot 10^{-4}$ (for $f/16$). Because the image resolution also suffers from a large lens aperture, a realistic working value is $f/4$ and $T = 0.0125$.

Transmission efficiency of lenses and optics and the detector quantum efficiency can be calculated and for this camera system, an overall efficiency of $\epsilon \approx 0.22$ [25] has been determined.

Combining these effects yields the overall efficiency, calculated exemplarily for 13 keV X–ray photon energy:

$$\begin{aligned} 1\,\gamma_{X-ray} &\xrightarrow{\text{scintillator}} 170\,\gamma_{vis} \xrightarrow{\text{camera solid angle: } \times 0.0056} 0.95\,\gamma_{vis} \\ &\xrightarrow{\text{lens aperture: } \times 0.0125} 0.012\,\gamma_{vis} \xrightarrow{\text{transmission efficiency: } \times 0.22} 0.0026\,\gamma_{vis} \\ \Rightarrow 1\,\gamma_{X-ray} &\rightarrow 0.0026\,\gamma_{vis} \end{aligned} \tag{5.15}$$

A measurement of the absolute flux of X–ray photons at the nanotomography experiment showed a flux of $4 \cdot 10^{12}$ photons/second/mm^2. The condenser optics has an opening aperture diameter of 1.8 mm, i.e. an opening area of 2.5 mm^2. Calculating with a transmission efficiency of $T \approx 0.5$ for condenser and objective X–ray lens each and considering the air path of $l \approx 4$ m with a transmission $T \approx 0.35$ yields a total X–ray photon flux of

$$4 \cdot 10^{12} \gamma_{X-ray} \mathrm{s}^{-1} \times 2.5 \times 0.5 \times 0.5 \times 0.35 = 8.75 \cdot 10^{11} \gamma_{X-ray} \mathrm{s}^{-1}. \tag{5.16}$$

Assume that the X–ray microscopy image has a size of 1500×1500 pixels on the detector and using 10000 counts / pixel, a total of $2.25 \cdot 10^{10}$ counts are needed. As the detector quantum efficiency is already included in Equation 5.15, this number corresponds to a number of $8.65 \cdot 10^{12}$ X–ray photons, or to an exposure time of

$$t = \frac{8.65 \cdot 10^{12}\,\gamma_{X-ray}}{8.75 \cdot 10^{11} \gamma_{X-ray}\,\mathrm{s}^{-1}} = 9.9\,\mathrm{s}. \tag{5.17}$$

This value is compatible with actual measurement times in the full field microscopy setup, as described in Chapter 6.

5.2.6 Thermal stability

Drifts of the positioning mechanics caused by relaxation of mechanics, joints or bearings are not expected. The expertise that the manufactures acquired over the years allows them to guarantee a position stability in the range of some ten nanometers. In addition, encoders are used to achieve a reproducibility of the same order of magnitude.

However, the stability of the components is also dependent on the environmental conditions. Thermal drifts can occur and need to be accounted for. The PETRA III experimental hall is air–conditioned to $T = 21 \pm 1\,^{\circ}C$ to create relatively stable conditions. Each experimental hutch has an individual air–conditioning system which stabilizes the hutch temperature to $T = 22 \pm 0.1^{\circ}C$. The temperature difference between experimental hall and experimental hutches is a technical necessity for the hutch air–conditioning systems. These systems need a set–point offset from the ambient conditions (in this case: the experimental hall). The air–conditions control parameters are not accessible.

For testing the stability—both the thermal and mechanical stability—, measurements with an interferometer have been performed on key mechanical components. The interferometer also includes sensors for temperature and air pressure to eliminate the influences of the air path on the measurement results. The sensor data are also independently available and they show that the temperature is stable to within $\pm 0.1\,^{\circ}C$, but that the temperature target value varies from time to time. The data show several occasions, at which the temperature changes by more $0.1\,^{\circ}C$ and then stays stable at the new value. For all intents and purposes, the hutch has been sealed during these experiments. No one entered the hutch or opened doors, only a slight air exchange through the cable chicanes occurred. Figure 5.18 shows an exemplary measurement during which a temperature jump occurred. The logs of the air–conditioning systems in the experimental hall and hutch show no events that can explain this behavior.

A temperature stability of $0.1\,^{\circ}C$ can be assumed in the experimental hutch. The experimental substructure is made of granite and the energy required to heat this structure by $\Delta T = 0.01^{\circ}C$ is $E = 79\,\mathrm{kJ}$. Heat can only be transported by air and the heat transfer coefficient of air is $U \approx 2\,\mathrm{W/m^2/K}$. Considering the very small temperature differences and the granite surface area of $A \approx 20\,\mathrm{m^2}$, the variations in the local air temperature are much too small to have a significant impact on the substructure. The mechanics, however, are made of steel and aluminum with much lower masses. Furthermore, these components have a much larger surface–to–volume ratio. All these factors allow the mechanics to equilibrate their temperature much faster to the ambient conditions, i.e.

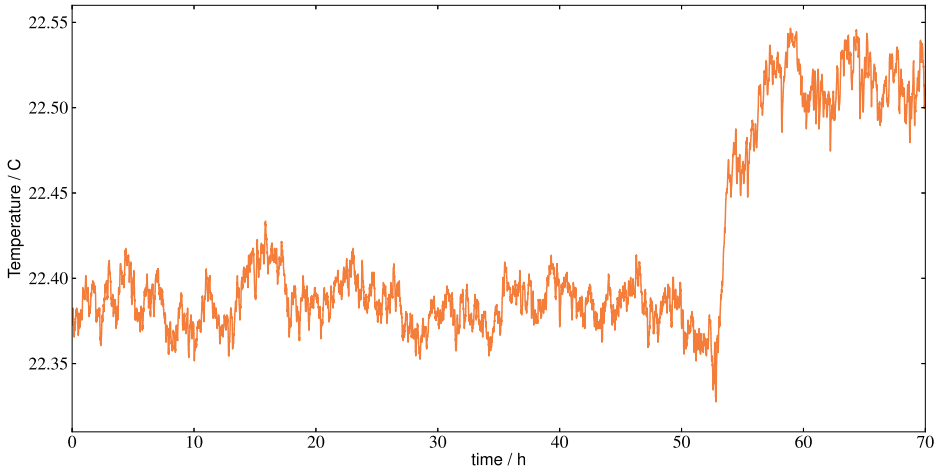

Figure 5.18: Temperature measurement in the experimental hutch EH1, at the optics position. While the temperature variations are in the range of 0.05 °C, unexplainable temperature jumps occur occasionally, during this measurement around $t \approx 53$ h. Note that no one entered the hutch during the measurements and the doors have been closed during the full measurement time.

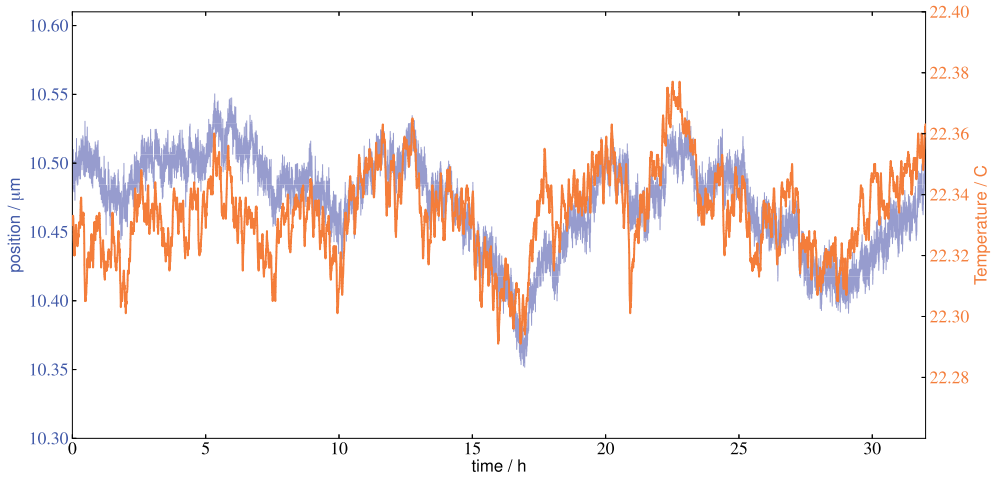

Figure 5.19: Measurements of temperature and optics position on SpaceFab kinematics with an interferometer. The temperature (orange) scale is left, the position (blue) scale is to the right. The position qualitatively follows the temperature drift, albeit with a slight time delay.

the air temperature. Figure 5.19 shows one position stability measurement. Position changes in the mechanics can be well correlated with temperature changes. Although the absolute position variations of $\Delta l \approx 200$ nm seem low, similar variations can be observed for all components. A relative movement of optics and sample can be larger and needs to be considered.

The ambient condition in the experimental hutch are very stable, but even temperature variations of $\Delta T = 0.05\,°C$ are sufficient to induce thermal drifts of several hundred nanometers that need to be corrected. The drift timescale, however, is long and for each individual image, the conditions can be assumed to be stationary.

Chapter 6

Results

6.1 Beamline front end

The performance of the beamline front end and optics is critical for a successful nanotomography, as it strongly depends on a stable and well–defined beam. The most critical components are the monochromator and undulator. These two components define the available flux, beam size and shape and beam stability.
Because the nanotomography end–station was installed shortly after the front end and micro tomography end–station, the beamline optics were not yet understood and characterized. A significant part of the experimental work was dedicated to understand the beamline components and verify that they work in the expected stability and performance regime. The following section presents the results of the beamline optics commissioning and discusses the consequences for the nanotomography experiment.

6.1.1 Monochromator stability

The monochromator performance is very critical because it creates not only a parallel beam offset but also—to a certain degree—changes the angle at which the beam hits the experiment. While these angular changes are very small, the long lever of the beamline transforms these small angles into strong vertical displacements. Furthermore, the required alignment precision of the X–ray optical components of about 10 µrad requires an angular stability of the beam of the same order of magnitude.

Bragg axis stability and drift

First and foremost, the monochromator has to be stable over long periods of time, at the very least over the duration of a single tomographic scan. The stability of the main Bragg axis can be eval-

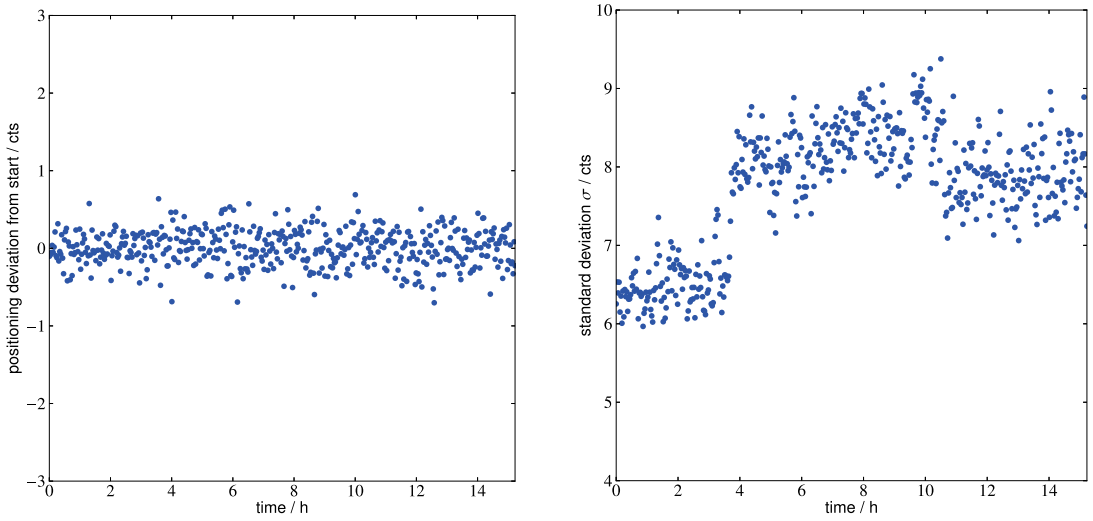

(a) position stability **(b)** position noise

Figure 6.1: Measurement of the monochromator Bragg axis position stability. **(a)** shows the absolute encoder position, with only every 1000th data point shown. The Points were acquired with a measurement frequency of 4 Hz. The feedback keeps the position very stable with only very little jitter. **(b)** shows the standard deviation for each set of 1000 data points. The global standard deviation for the measurement is $\sigma = 0.139\,\mu\text{rad}$. The jump in the position noise seen around $t = 3.5\,\text{h}$ is probably caused by changes in the closed–loop feedback circle and not understood. These jumps occur occasionally but have no measurable effect on the beam position and beam vibrations.

uated by using the encoder position values of the axis. A Renishaw encoder system with 920,000 counts per degree is installed. This corresponds to $1\,\text{count} \equiv 1.0870 \cdot 10^{-6}\,^\circ \equiv 0.01897\,\mu\text{rad}$. Figure 6.1 shows the stability of the Bragg axis. Because the axis is equipped with a direct drive, a closed loop feedback system is necessary for keeping a stable position. A total of 250, 000 position data points have been taken over a time of $t = 13.5\,\text{h}$. The peak–to–peak differences in the encoder positions are $\Delta = 71.8125\,\text{counts} = 1.3623\,\mu\text{rad}$ with a standard variation of $\sigma = 7.319\,\text{counts} = 0.139\,\mu\text{rad}$.

Because both crystals of the double crystal monochromator are mounted on the same base plate, any difference in the angular position corresponds to a shift in the X–ray energy. The silicon 111 monochromator crystals have a d–spacing of $d_{111} = 3.1355\,\text{Å}$. Using $E = h\nu = hc/\lambda$ and substituting λ according to Bragg's law, the energy and its derivative are given as:

$$E = \frac{hc}{2d}\frac{1}{\sin\theta} \tag{6.1}$$

$$\frac{dE}{d\theta} = -\frac{hc}{2d}\frac{\cos\theta}{\sin^2\theta} \tag{6.2}$$

$$\Rightarrow dE = -\frac{hc}{2d}\frac{\cos\theta}{\sin^2\theta}\,d\theta \tag{6.3}$$

Assuming an energy of $E = 20\,\text{keV}$ with a corresponding Bragg angle $\theta = 9.14628°$, and a

jitter of $d\theta = 0.139\,\mu\text{rad}$, the numerical value is

$$dE = 77.25\,\text{keV} \times d\theta = 77.25\,\text{keV} \times 0.139\,\mu\text{rad} = 1.074 \cdot 10^{-5}\,\text{keV} \tag{6.4}$$

The relative change in energy dE/E is about 10^{-6}, whereas the energy bandwidth of the monochromator is already about $1.35 \cdot 10^{-4}$.

Concluding, the change in energy from the monochromator movement is completely negligible for any nanotomography or X–ray microscopy application, even at target resolutions of some nanometers.

2nd crystal pitch stability

Of more influence than the Bragg drive is the pitch position of the second Bragg crystal. To fine–tune the relative position of the second crystal with respect to the first crystal, the second crystal is mounted on a flexure hinge and driven by a linear stage equipped with a gear box.
Both crystals are cooled down to about 78 K using liquid nitrogen which is fed through the piping with a pump operated around 25 Hz. Cryogenic cooling is necessary because of the high heat load of the white X–ray beam on the first crystal. To minimize the lattice mismatch between the two crystals, the second crystal is as well. The drawback, however, is the system stability: The combination of delicate mounting using a flexure hinge and cryogenic pumping with a pulsed throughput of about 3 liters min^{-1} creates two severe problems.

First, high frequency vibrations of the crystal shift the beam position and orientation randomly. Currently, there is no concept to counter these. A frequency analysis of the vibration yielded no clear result as to where these vibrations originate.

Second, there is a severe beam drift. While some drift is expected in case of changing thermal load, e.g. when changing the crystal angle with respect to the beam, thermal equilibrium should be reached fast. The filtered white X-ray beam has a heat input of about 50 W on the monochromator, whereas the cryo–cooler has a capability of about 300 W, more than enough to keep the crystal temperature stable with and without beam. The thermal conductance of the silicon crystals in the specific monochromator geometry is $5.96\,\text{W}\,\text{K}^{-1}$. Switching the beam on and off results in a thermal load change of about 50 W and a resulting temperature change of about $50\,\text{W}/5.96\,\text{W/K} = 8.4\,\text{K}$ at the surface position hit by the beam, with respect to the basic temperature of 79.5 K. This moderate temperature change gives no indication that changes in the heat load should be responsible for beam drifts on the timescale of one day. Figure 6.2 shows that there is a severe drift over long times that has to be countered. The data also show that the maximum intensity correlates with the position on the CCD, indicating that there is indeed a mechanical drift of the crystal. Aligning the crystals for maximum intensity yields the same beam position, regardless of

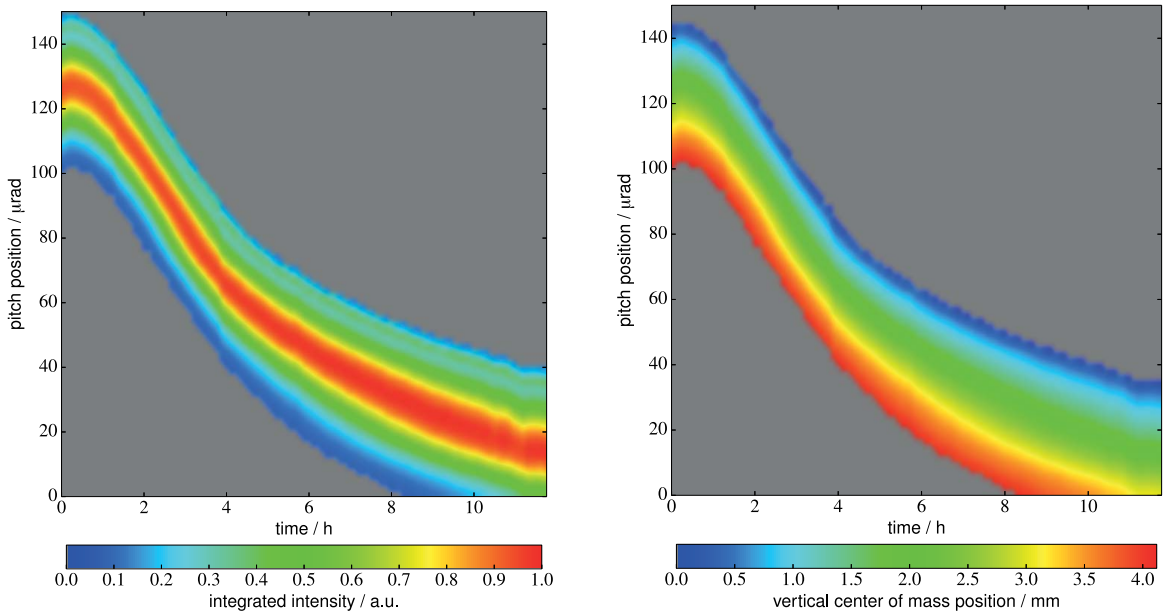

(a) intensity **(b)** position

Figure 6.2: Measurement of the pitch position stability. The pitch position has been scanned repeatedly for 12 hours. The beam intensity (i.e. average count rate on a CCD) and the beam position (i.e. vertical position of the center of mass of the beam) have been calculated from the data. It is obvious that both the intensity and the detector position vary with the time, whereas both these values are linked. The gray areas correspond to scans where the intensity maximum wandered off the CCD.

the mechanical position of the 2^{nd} crystal.

Figure 6.3 shows the position of the beam center of mass at each pitch position of maximum intensity. Because the pitch steps in the scan were selected large to cover a sufficiently large position width, the resulting position accuracy is very low. The step width of $\Delta = 0.0001° = 1.75\,\mu\text{rad}$ is an order of magnitude larger than typical step widths selected for pitch optimization, hence the large error bars. A fit of the data yields a beam position of

$$y_{beam}(t) = (-8.64 \pm 0.84)\,\frac{\mu\text{m}}{\text{h}} \cdot t\,[\text{h}] + (1649.95 \pm 5.69)\,\mu\text{m} \tag{6.5}$$

$$\frac{dy}{dt} = (-8.64 \pm 0.84)\,\frac{\mu\text{m}}{\text{h}} \tag{6.6}$$

While there is a remaining apparent drift of the beam position over time, the covariance matrix of the fit is

$$cov = \begin{pmatrix} 3.236\,10^{-5} & -4.618\,10^{-6} \\ -4.618\,10^{-6} & 7.081\,10^{-7} \end{pmatrix}. \tag{6.7}$$

The fact that the non–diagonal elements of the matrix are of the same order of magnitude as the diagonal elements shows that the quality of the fit is not good because the two parameters are not independent. The data does not support a statement of a significant pitch drift over time if the

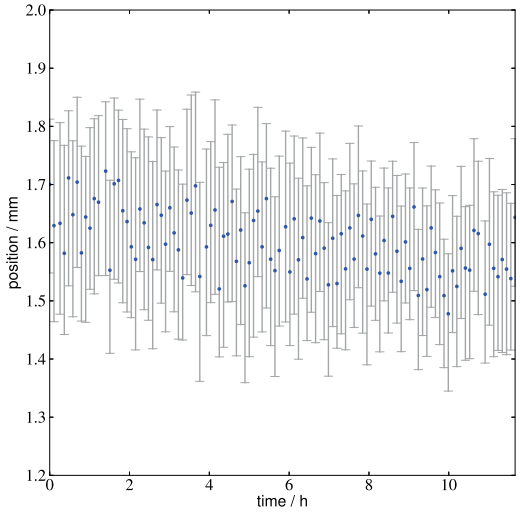

Figure 6.3: Position of the beam center of mass on the CCD at the position of maximum beam intensity. Because of the coarse steps in pitch, the position is not ideally defined and the errors are comparably large.

beam is aligned by means of maximum intensity. For estimating the influence of beam drifts, the fit results can be used as upper error bounds.

The measurements were performed in the micro tomography hutch, i.e. the distance between the monochromator and the detector was $d = 32\,\mathrm{m}$. The nanotomography experiment is set up at a distance of $d \approx 11\,\mathrm{m}$ from the monochromator and the smaller distance reduces the absolute nominal drift values by the ratio of the two distances. The corresponding beam position and beam direction drifts at the nanotomography position are thus:

$$\frac{dy_{beam}}{dt} = \frac{11}{32}(-8.64 \pm 0.84)\,\mu\mathrm{m\,h^{-1}} = (-2.97 \pm 0.289)\,\mu\mathrm{m\,h^{-1}} \tag{6.8}$$

$$\frac{dy'_{beam}}{dt} = \frac{(-8.64 \pm 0.84)\,10^{-6}}{32}\mathrm{h^{-1}} = (-0.27 \pm 0.026)\,\mu\mathrm{rad\,h^{-1}} \tag{6.9}$$

Critical for the X–ray optics is the angular alignment relative to the beam and the positioning accuracy of the lenses is in the range of several µrad. The calculated angular drift is negligible for all nanotomography experiments planned, even at highest resolutions. The global drift has to be corrected by using the beam intensity and this feedback keeps the beam position stable enough for all applications. General experience from the numerous beamtimes also shows that the beam position can be kept very stable by scanning the pitch and moving it to the position of maximum intensity.

6.1.2 Higher harmonics

As already mentioned in Chapter 2.1 and shown in Figure 2.3, the spectrum of the undulator not only includes the fundamental energy but also higher harmonics. The same is true for the monochromator reflections. If the double crystals are in reflection geometry for the silicon 111

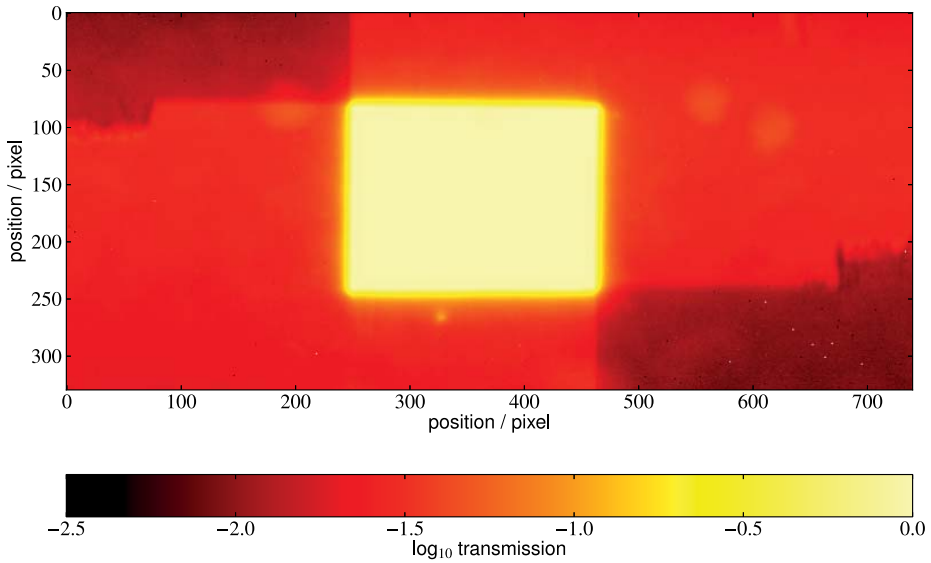

Figure 6.4: Transmission image of a set of twin L–shaped apertures with a thickness $t = 50\,\mu\text{m}$. The darker regions in the top left and bottom right corners correspond to the area where the two aperture foils overlap, i.e. where the projected thickness is $t = 100\,\mu\text{m}$. The ragged edges are due to the fabrication process. The shape has been cut with a wire eroding machine and the high quality surface smoothness has been achieved by polishing with a focused ion beam.

reflection at an energy E_0, the same geometry also permits the 333 reflection of $3\,E_0$ to pass. The 222 reflection is theoretically forbidden, but occurs due to asymmetries in bonding and thermal vibrations [30]. Thus, the system of undulator and monochromator generates and transmits not only the target energy E_0 but also energies $n\,E_0$ with $n = 2, 3, \ldots$. Due to their increased energy, these higher harmonics have a higher transmission through X–ray optical elements, increasing their relative contribution. Furthermore, these higher energies can penetrate thin aperture foils, creating image errors.

Because most of the early commissioning experiments described here were performed at $E = 13\,\text{keV}$, all performance calculations were exemplarily computed at this energy as well. The effects that are responsible for higher harmonics are general and valid at all energies.

Figure 6.4 shows an X–ray transmission map of twin gold apertures. Table 6.1 gives the experimental transmission values for different aperture thicknesses. The theoretical transmission through a gold foil with a thickness of $t = 50\,\mu\text{m}$ at $E = 13\,\text{keV}$ is $T_{theo} = 8.7 \cdot 10^{-7}$ whereas the measured value of $T_{exp} = 2.76 \cdot 10^{-2}$ is about 5 orders of magnitude larger than expected. These high transmission values can only be caused by a strong contribution of higher energies in the spectrum. For example, the transmission values of a gold foil with a thickness of $t = 50\,\mu\text{m}$ for the 3^{rd} and 5^{th} harmonic are $T_{39\,\text{keV}} = 0.26$ and $T_{65,\,\text{keV}} = 0.70$, respectively. A relative fraction of the higher harmonics of only a few percent is sufficient to explain these values.

aperture thickness t / µm	aperture transmission
0 (direct beam)	1.0
50	0.0276
100	0.0167

Table 6.1: Experimental transmissions through gold aperture foils, fundamental energy = 13 keV.

Influence of higher harmonic on imaging

Higher harmonics in X–ray microscopy imaging lead to three fundamental problems. First, they can penetrate apertures and optical elements and lead to a photon background in the detector image. Second, the scintillator absorbs the X–ray photons and emits light in the visible spectrum. In first approximation and full absorption in the scintillator, the light yield is proportional to the energy of the incoming photon. High energy photons create a disproportionally high visible light yield, thereby even enhancing their effect on the camera image. The last point to consider is the X–ray optics. This optics focus the higher harmonics at completely different distances. The focal distance of the lenses is inversely proportional to the part δ of the complex refractive index and in turn, δ is proportional to the square of the photon energy:

$$\begin{aligned} f &\sim \frac{1}{\delta} \\ \text{and } \delta &\sim \frac{1}{E^2} \\ \Rightarrow f &\sim E^2 \end{aligned}$$

The installation of thicker aperture foils can be used to block stray high–energetic transmissions, but higher harmonics in the direct beam cannot be filtered out and additional measures have to be taken. For X–ray microscopy, the condenser lens can be used as an energy filter. This scheme is exemplarily shown in Figure 6.5. Crucial for this scheme is a condenser lens that blocks the direct illumination of the guard aperture and only uses refracted X–rays for illumination.

While this principle is a very convenient way for getting rid of higher harmonics in an X–ray microscopy setup, it cannot be used for the cone–beam setup because the CRLs for creating the focal spot require a direct illumination.

Using a two–tiered cone beam setup (compare Section 5.1.1), the effects of higher harmonics become even more pronounced due to the different focal positions between the two X–ray optics. The absolute intensity of the target energy drops significantly, as a large fraction is lost due to the geometry (compare Section 5.1.1). However, the focal distances for higher harmonics are significantly larger and correspondingly, a much smaller fraction of the higher harmonic intensity is lost. This leads to an increased fraction of higher harmonics at the second tier of optics. Again, these higher harmonics are focused at a much longer distance from the optics.

Consider the following example: The objective lens is designed with $f = 150\,\text{mm}$ at $E =$

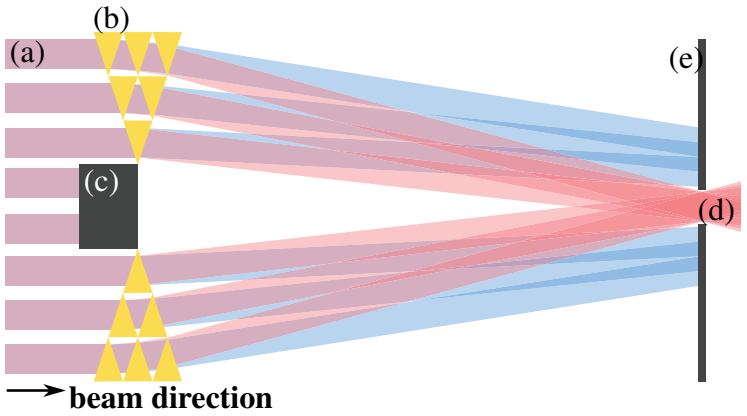

Figure 6.5: Schematic setup of higher harmonics suppression with a condenser lens. The multi–energy photon beam (a, colored in violet red) propagates from the left to the right and hits the prismatic condenser lens (b, colored in golden yellow) with a central beam stop (c). Only the desired energy (marked in light red) is focused in the working position (d) whereas the higher energies (exemplary, marked in light blue) are absorbed by a guard aperture because the refractive power of the optics is significantly less for higher energies.

13 keV and an image distance of $d = 3.0\,\mathrm{m}$. The corresponding magnification is $M = 3.0/0.15 = 20$, i.e. the incident intensity will be distributed over an area of $A = 20^2\, A_{lens\,aperture} = 400\, A_{lens\,aperture}$. The intensity in each pixel would be $I = 1/400\, I_0 = 0.0025\, I_0$. A higher harmonic with $E = 39\,\mathrm{keV}$ would be focused at $f_{39} = 1.36\,\mathrm{m}$. At the image distance of $d = 3\,\mathrm{m}$, the beam would be enlarged by a factor 2.213 and the resulting intensity were $I_{39} = 2.213^{-2}\, I_{0,39} = 0.204\, I_{0,39}$. If the overall intensity of the higher harmonic were $I_{0,39} = 0.02\, I_0$, an area of about 2.2×2.2 lens apertures were subject to twice as many photons of the higher harmonics as compared to the desired fundamental. Obviously, this is no desired state.

Figure 6.6 shows an exemplary image of this effect. Not only is the central region strongly affected by the higher harmonics but an additional cross–shaped feature appears as well. These structures are caused by the crossed structures of the lenses for horizontal and vertical focusing. They are due to the higher harmonics, as can be proven by a reference image with suppressed higher harmonics (compare Figure 6.6(b)). The overall background structure of the illuminated field of view is due to the parallel illumination of the optics (no condenser in use) and the beam coherence and disappears in the case of divergent illumination.

Because of the points presented in this section, it is necessary to quantify the influence of higher harmonics at the beamline P05 and to determine which steps can be taken to minimize the effects.

Pitch detune

One solution to the problem described above is in detuning the pitch. Because the monochromator rocking curves for the fundamental and higher harmonics are shifted with respect to each other and because the rocking curve for the higher order reflections (e.g. Si 333 instead of Si 111)

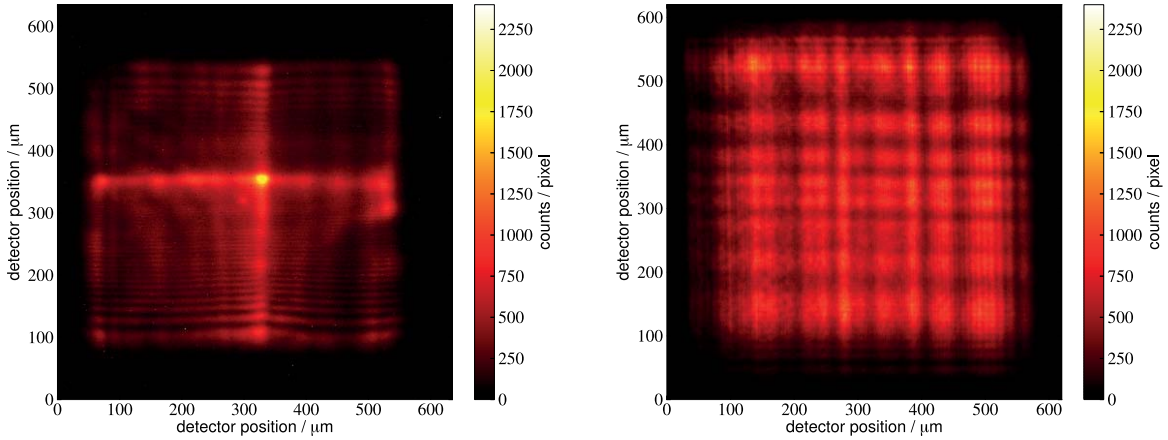

(a) CCD image of the magnified X–ray beam with higher harmonics present

(b) CCD image of the magnified X–ray beam with suppressed higher harmonics

Figure 6.6: Two CCD images of the magnified X–ray beam with and without higher harmonics present. The background structure in the illuminated field of view resembles an interference pattern. It is an effect of the direct parallel illumination with the partly coherent beam.

X–ray energy / keV	scattering cross section / 10^{-30} m^2
13	3.799
39	3.464
65	3.187

Table 6.2: Scattering cross sections of free electrons for different X–ray energies.

has a smaller angular width, it is possible to detune the position of the second crystal in such a way that the higher order reflections do not match. Figure 6.7 shows Darwin reflectivity plots to demonstrate the principle. However, the non–negligible source divergence leads to a broadening of the reflectivity curves. This effect has a significant impact for higher order reflections because the limited angular acceptance is increased. Due to this effect, the source characteristics have to be considered and experimentally characterized. For more information about crystal reflections and reflectivity, please refer to Als–Nielsen and McMorrow [2] or similar books.

Energy–resolved photon intensity measurements were performed with an energy–dispersive Germanium detector. This type of detector allows to count single photons and to determine their energy. The detector is mounted under 90° relative to the beam to avoid oversaturation. The detection efficiency of the detector is close to 100% over the complete energy range, but the detection rate is also influenced by the scattering statistics. In first approximation, the scattering cross–sections of free electrons were calculated to estimate the scattering probabilities for the different energies [60]. Table 6.2 gives some values for comparison. While the scattering cross–section decreases with increasing energy, this effect is small and all values are of the same order of magnitude. The complete energy range of 13 keV to 65 keV can be detected at a detector orientation of 90° to the X–ray beam and the detector counting statistics are normalized to the scattering cross–section.

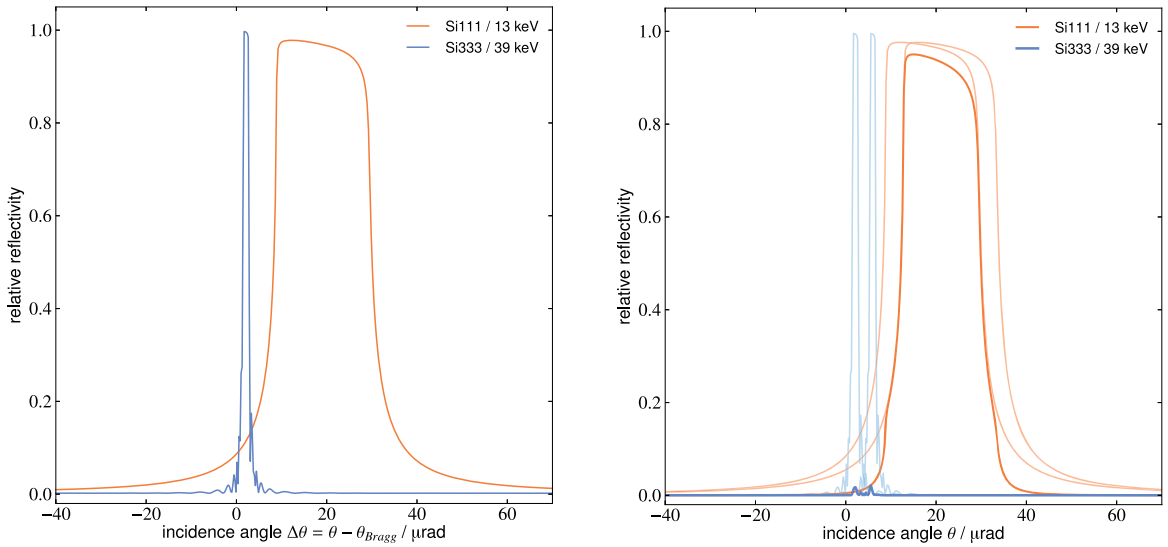

(a) Reflectivity for a single reflection

(b) Overall reflectivity of two detuned crystals (detune $\delta\theta = 4\,\mu\text{rad}$).

Figure 6.7: Darwin reflectivity curves for the fundamental energy and the 3^{rd} harmonic, calculated for the silicon 111 reflection at $E = 13\,\text{keV}$. **(a)** shows the reflectivity curve of a single reflection. Note that the maxima of the curves do not coincide. **(b)** shows the effective reflectivity of two detuned crystals, calculated by multiplying original the reflectivity curves (marked in light colors). Shifting one curve relative to the other yields a strong suppression of the 3^{rd} harmonic whereas the fundamental energy is only slightly dampened. Simulation is performed using the Xop package Xcrystal [18–22].

Figure 6.8 shows a map of a spectral measurement at different pitch positions. The effect of pitch detuning on the intensity of the higher harmonics is obvious. The relative decrease in intensity is smaller for the fundamental than the loss of intensity for the higher harmonics. This yields a net suppression of the higher harmonics. Numerical data for the influence of the pitch position on the energy–dependent intensities is given in Figure 6.9. Detuning is necessary to minimize the effects of the higher harmonics and allows the suppression of, for example, the 3^{rd} harmonic from $I_{rel} = 0.111$ to $I_{rel} = 0.0028$, i.e. by a factor of 39.6 while keeping 80.4% of the intensity at 13 keV.

Undulator curves

Detuning the pitch allows the suppression of higher harmonics propagation, whereas varying the gap opening allows suppressing the formation of these harmonics at the source. The energy width of each harmonic peak and of the corresponding higher harmonics is constant. Changing the undulator gap results in a shift of the energy of maximum emission $\Delta E_{I_{max}}$. For a higher harmonic of the order n, the maximum emission is shifted by $n \cdot \Delta E_{I_{max}}$. Figure 6.10 (a) shows a simulation of the photon flux through a pinhole in the nanotomography hutch. The best theoretical position for the undulator gap to minimize higher harmonics is a little larger than the position of maximum flux,

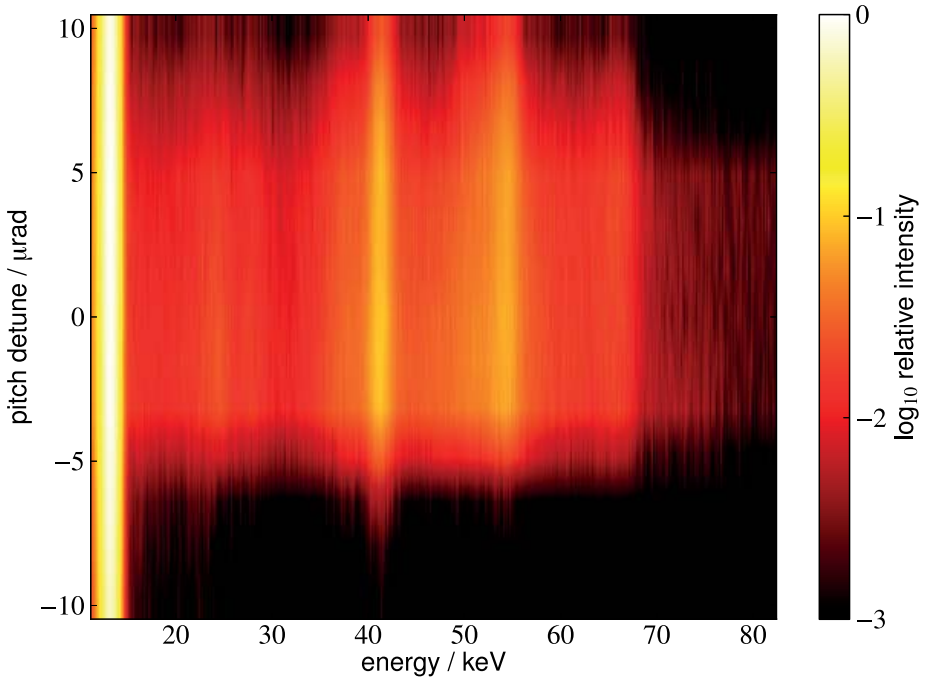

Figure 6.8: Map of the photon intensity at different energies and pitch detune positions. The fundamental at 13 keV is dominant, but the higher harmonics are clearly visible, as well as their variation with varying pitch.

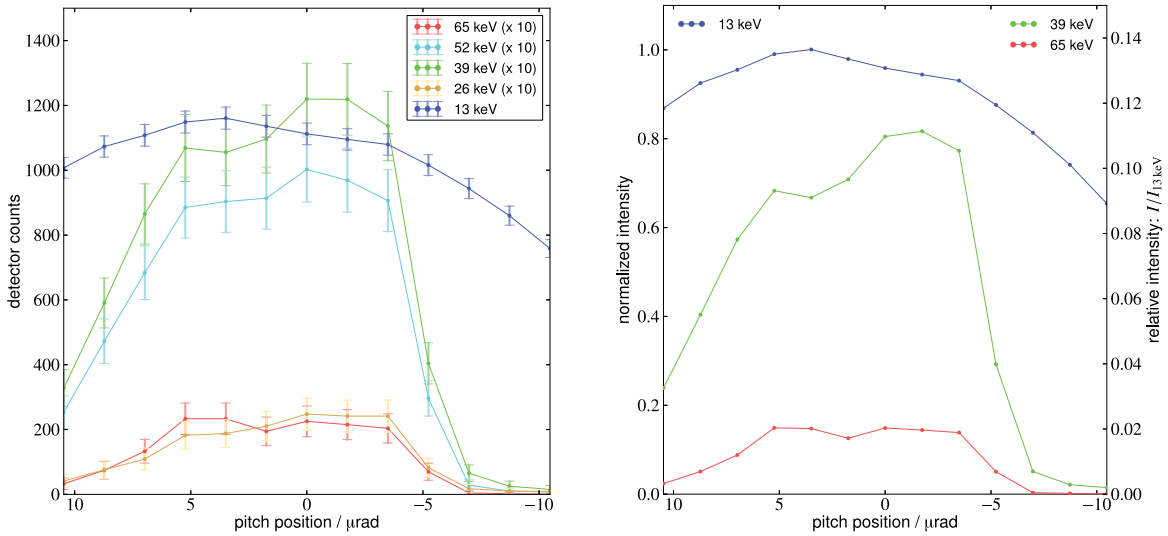

(a) Absolute counting intensities

(b) Relative intensity of higher harmonics

Figure 6.9: Intensity measurement of the energy spectrum in the experimental hutch using a Germanium detector. (a) shows the overall intensities, corrected for the cross–section variations. The 3^{rd} and 4^{th} harmonics are the most dominant ones. The overall reflection width of the fundamental energy ($E = 13$ keV) is much larger than for the higher harmonics. Note that the maximum intensity is expected at a detune of zero. The shift in the maximum position is due to the arbitrarily selected starting point for the 0 value which might be shifted relative to the previous position because of the system drift. (b) shows the relative intensities (in photons) of the 3^{rd} and 5^{th} harmonic and in comparison the normalized intensity at 13 keV. A detune of approximately $\Delta\theta = -7$ µrad is a good compromise between eliminating the higher harmonics and a high flux at $E = 13$ keV.

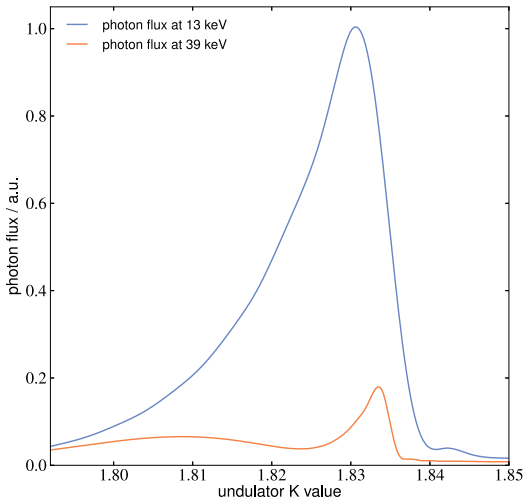

(a) Photon flux for 13 keV and 39 keV.

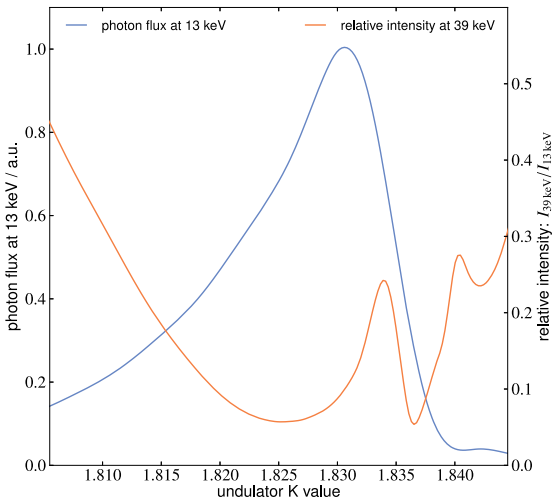

(b) Fraction of higher harmonics relative to desired energy.

Figure 6.10: Calculations for the IBL undulator for 13 keV and 39 keV (3^{rd} and 9^{th} harmonics, respectively) through a centered pinhole of $1 \times 1\,\mathrm{mm}^2$ at 64 m source distance (i.e. in the nanotomography hutch). (a) shows the positions of the maxima and their size. The width of the 39 keV line is much smaller and its maximum is shifted a little to larger K values. This effect can also be observed in the relative intensity in (b). For a compromise of minimal influence of higher harmonics and highest photon flux at 13 keV, the ideal K value is a little smaller than at maximum intensity. A smaller K value corresponds to a larger gap. Simulations performed using the Xop package XUS [18–21].

as shown in Figure 6.10 (b). A measurement of the gap curve gave a slightly different result and is presented in Figure 6.11. The best position coincides with the gap position of maximum intensity at $E = 13\,\mathrm{keV}$. However, these measurements were performed with the full beam profile and not with an on–axis pinhole. Because of the shape of the undulator emission cones, the energetic spectrum is dependent on the position in the cone. A slight change of the emission characteristics is expected for a comparison of pinhole and complete beam profile.

Higher harmonics summary

Higher harmonics can be a severe problem for imaging using X–ray optics. The necessity of a condenser in the X–ray microscopy setup can be exploited by cleverly designing the condenser to absorb the direct beam and using the chromaticity of the X–ray diffraction. A corresponding scheme for the cone–beam setup does not exist. In this case, it is necessary to suppress higher harmonics in the beamline frontend, i.e. undulator and monochromator.

The necessary parameters for suppressing higher harmonics in the monochromator have been determined. By shifting the undulator gap slightly off the optimal position, it is further possible to inhibit the creation of higher harmonic photons in the undulator. Combining these two effects, it is possible to reduce the higher harmonic photon flux to values which can be handled in the experiment.

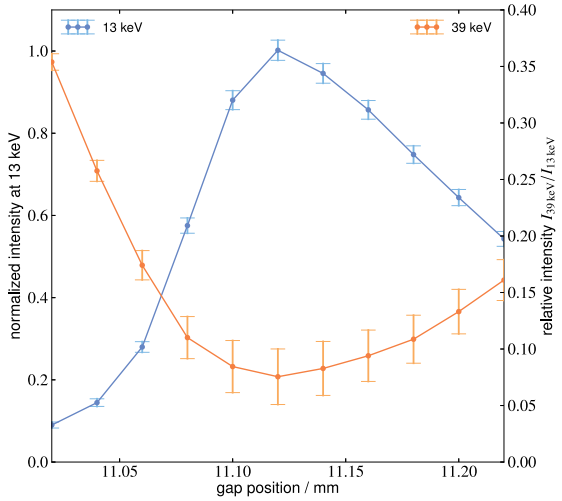

Figure 6.11: Measurement of the flux in dependence of the gap position and the relative intensity of the 3^{rd} harmonic. The overall shape agrees well with the simulation in Figure 6.10, except for the missing shift between intensity maximum and minimum of the higher harmonics relative intensity curve. This is expected because this measurement was performed with the complete beam profile and not with an on–axis pinhole. Note that the graphs appear to be flipped if compared with Figure 6.10 because in this figure, the x–axis is marked with the measured gap position.

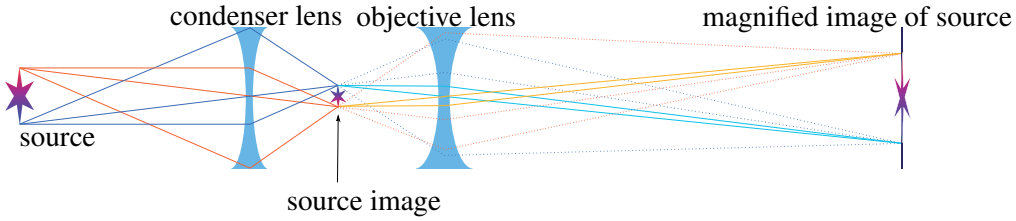

Figure 6.12: Test setup for characterizing the position stability of the storage ring and beamline optics. The setup allows imaging a magnified image of the focus of the first lens.

6.1.3 Short time fluctuations

The overall stability and quality of the beam can be ensured using methods like detuning and repeated pitch optimizing against drifts. However, these affect only the long term stability of the beam. For magnified imaging, the correct beam position is crucial. A test was performed with a two–tiered lens setup to visualize the focus position of the first lens. Figure 6.12 gives a sketch of the setup. The magnification has been characterized by using a test pattern with defined structure sizes. This allows for an absolute scaling of the position changes.

While the setup with a CCD camera has a low frame rate, random fluctuations in the position can still be recorded by a large set of samples. The estimation of high frequency fluctuations is more difficult. A proper analysis of these would require a fast camera with a time resolution well below one second (i.e. $t_{exposure} + t_{readout} << 1$ s) and a spatial resolution in the range of 1 µm—the additional, required spatial resolution is provided by the magnifying X–ray optics. Unfortunately, such a camera system was not available at the beamline at the time of these tests. Fast imaging systems are necessarily equipped with direct electronics for each pixel or with a fast analog–digital

converter. In the first case, the pixel electronics limits the pixel spacing to some ten micrometers and in the second case, the necessity of a fast analog–digital conversion introduces a lot of electronic noise.
High frequency disturbances are expected from two major sources. One is the storage ring. The continuous fast orbit feedback system works with sampling and feedback rates of about 100 Hz, and any effects of the orbit feedback systems would be seen only on timescales of $t = 1/f \approx 10$ ms. As the typical exposure time is in the range of seconds, the fast orbit feedback system should not have a major influence on image–to–image variations. A drift in the storage ring, however, can have a long–term impact, but should not induce short–term position variations. The second source is the monochromator. The liquid nitrogen for the cryo–cooling is pumped through the monochromator by an external pump from the liquid nitrogen dewar. While the inner diameters of the nitrogen pipes are all kept to the same diameter, couplings and bends may still induce turbulences in the pipe system which is critical because they can cause vibrations. The second monochromator crystal is mounted on crossed solid state hinges which can easily react on external stimuli like vibrations. To minimize resonances, the operating frequency of the pump can be adjusted in the range of $20 - 50$ Hz but must never be shut down completely. In a system with two crossed flexure hinges, potential turbulence and external forced pumping is complex and the behavior can be chaotic. As the monochromator used at the IBL beamline is identical to those at most other PETRA III beamlines, a DESY task force investigates these vibrations which occur at all monochromators. A test measurement of the monochromator yielded vibration frequencies of $f = 50$ Hz, $f = 100$ Hz and in the band of $F = 220 - 280$ Hz.

Beam position fluctuations in the range of seconds can be resolved with a CCD camera. A measurement with 1000 images has been performed at the maximum possible speed, i.e. limited by the CCD readout speed. The achieved frame rate was $f = 0.74$ Hz. Each focal spot has been characterized by determining integral intensity, horizontal and vertical positions and widths (FWHM), respectively. Figure 6.13 shows a plot of the horizontal and vertical positions. The horizontal position stability of about 300 nm is significantly better than the vertical one with only 1.2 µm. In addition, the change with time of the horizontal position is dominated by a random drift, which can be explained by mechanical relaxation or thermal drift. The time–dependence of the vertical position, however, is a well–modulated periodic behavior on short time scales. The offset and amplitude of the periodic modulation vary over time, but the effect stays the same. Considering that the magnified detector pixel size was $d = 139$ nm, this is a position spread of several pixels and not compatible with a target resolution of 100 nm.
A Fourier analysis of the time dependence of the position data is shown in Figure 6.14 and confirms this fact: The spectrum of the horizontal position does not include any distinct peaks, whereas the vertical position spectrum shows peaks at $f = 0.15$ Hz, $f = 0.30$ Hz, and $f = 0.45$ Hz. Figure

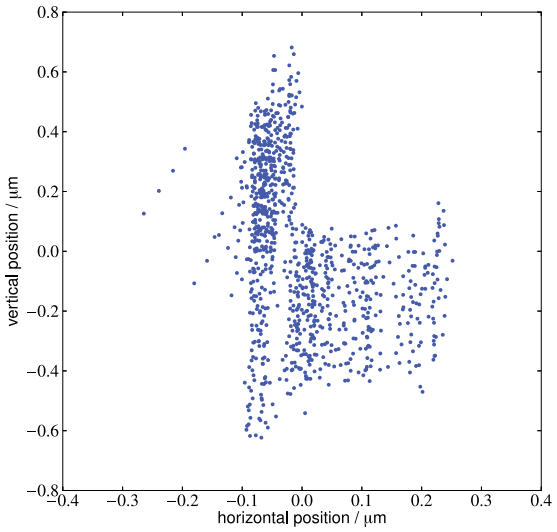

(a) Position deviation from the average position, both horizontal and vertical

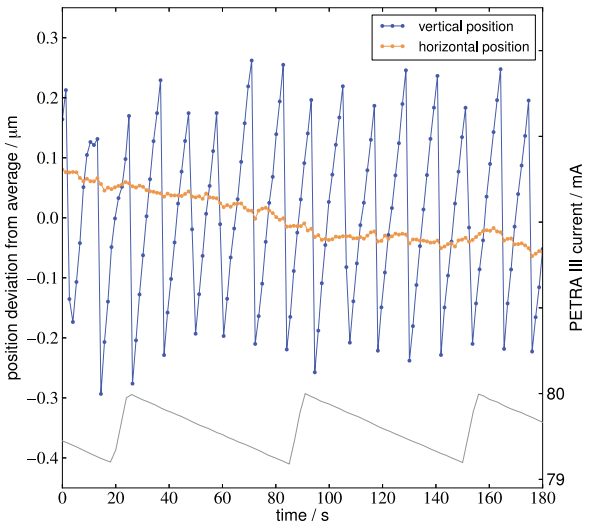

(b) Timeline of the position deviation from the average (time range limited for better time resolution in plot). The PETRA III current is shown in gray.

Figure 6.13: Results from a stability measurement with 1000 points. The position stability deviates significantly from the average position on the scale of sub–micrometer precision. (b) shows a timeline of 140 data points and it shows that the horizontal position deviation is dominated by a drift with small short–time fluctuations whereas the vertical position suffers a very periodic modulation but on a different timescale than the top-up modus. Note that the offset and amplitude of the vertical modulation varies over time (compare **(a)**).

6.14(c) shows the spectrum of the time variation of the PETRA beam current due to beam losses and injections. While it is still reasonable to assume the ring to be the source of these disturbances, they cannot be directly due to the variations in the PETRA current but have to arise from other effects. The frequency of these variations is very distinct, suggesting that it is not due to the monochromator cooling ($f \approx 20 - 50\,\mathrm{Hz}$) or mechanical jitter.

In addition to the position stability, there are also issues with focus size and intensity. An overview of the results is shown in Figure 6.15. The FWHM spread of the focal spot size in horizontal direction is below 20 nm whereas the vertical spread is of the order of 200 nm, which is a whole order of magnitude worse. Considering that the position spread is also significantly larger in the vertical direction, the FWHM size variation is probably an artifact created by vertical position variations within individual images. The vertical movement of the beam, as seen in Figure 6.13(b), is expected to distort the circular focal spot over time and this effect shows as a wider beam profile in the vertical direction. Most problematic of all is the variation in intensity shown in Figure 6.15(b). The peak intensity in the images is about 10,000 photons per pixel. Due to the Poisson photon statistics, the expected counting variations of a measurement with n counts is given by $VAR(n) = \sqrt{n}$. The relative error is $1/\sqrt{n}$. For the numbers given above, this yields a relative error of $VAR(10,000)_{rel} = 0.01$. The measured relative variance $VAR_{rel,\,meas} = 0.041$ is much larger

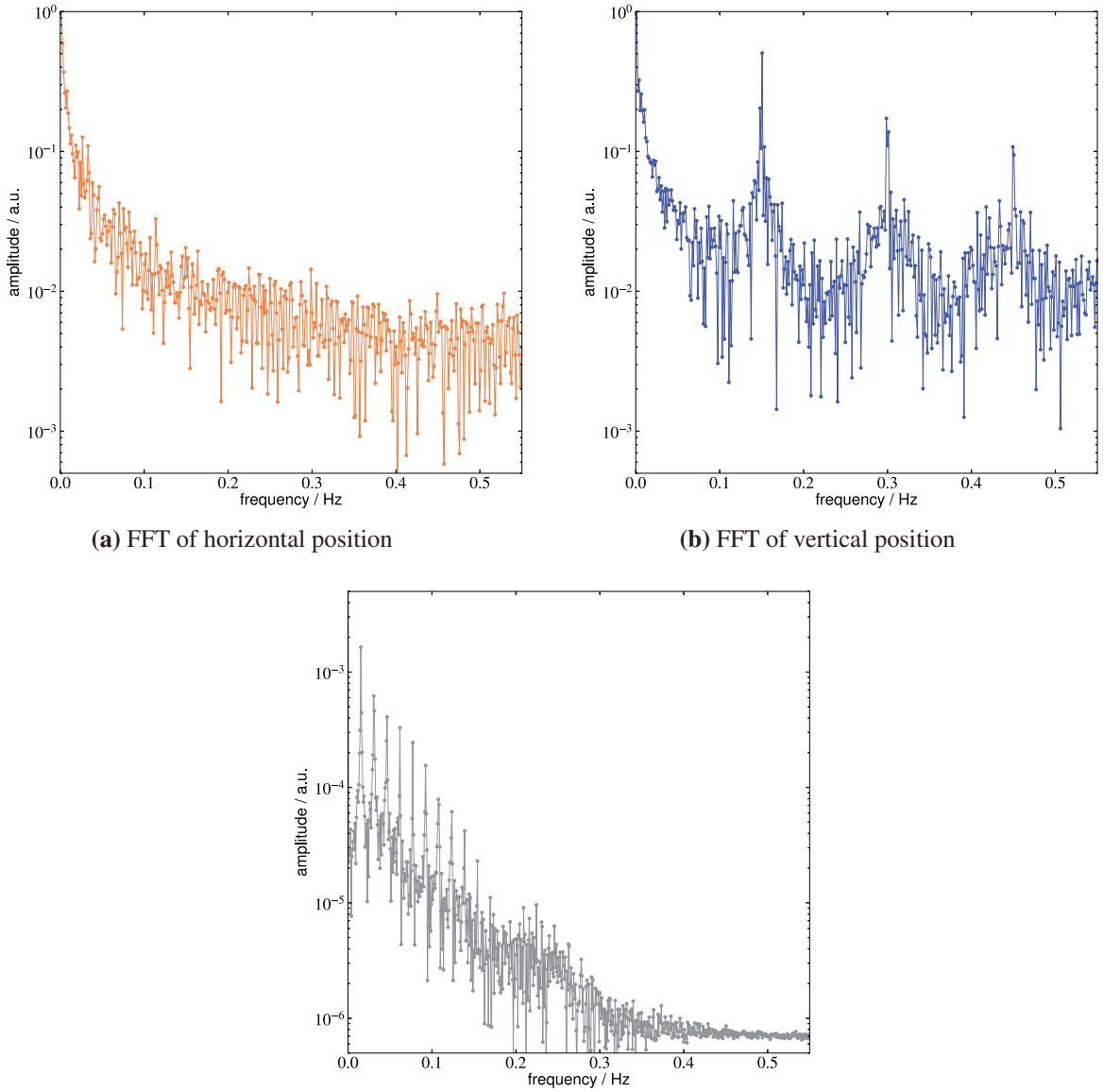

(a) FFT of horizontal position

(b) FFT of vertical position

(c) FFT of PETRA beam current

Figure 6.14: Fast–Fourier transforms of the chronological horizontal and vertical beam positions and the PETRA III ring current. While the horizontal spectrum consists of only the noise, both the vertical position and ring current spectrum have distinct peaks. However, the spectra do not match, i.e. the vertical movement is not synchronous with the PETRA III injections and must originate from some other source.

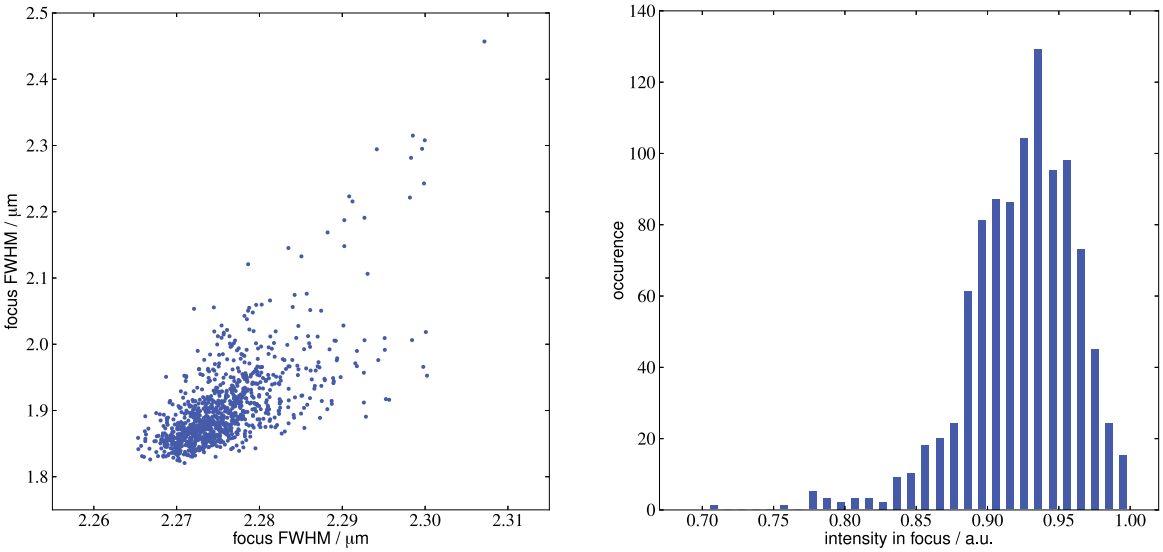

(a) Full width at half maximum of the focal spot (determined by Gaussian fit). Note the different scaling in horizontal and vertical directions.

(b) Histogram of the focal intensity distribution.

Figure 6.15: Results from a stability measurement with 1000 points. The focus size (FWHM) deviates significantly on the scale of sub–micrometer precision. (b) shows a histogram of the intensity variation (bins correspond to bands of 1% intensity of maximum intensity). The intensity in the focus varies by more than ±5% around the maximum of occurrence.

than the expected statistical error. The intensity fluctuations do not coincide with fluctuations in the PETRA III ring current and are also by an order of magnitude larger than the variations in the beam current. Also, there is no clear correlation between the intensity variations and either the time or the horizontal focus position, as shown in Figure 6.16. The beam intensity shows a slight dependence on the vertical beam position, albeit with a large error. A linear fit is shown in Figure 6.16(c) and while the fit reproduces the trend, the remaining relative error (RMS) is still $VAR_{rel} = 0.0297$, i.e. the fit is typically off by 2.97%. This value is only slightly better than the relative variance of the raw data $VAR_{rel,\,meas} = 0.041$.

Typical images have a dynamic range of $14 - 16$ bit, i.e. between $16,384$ and $65,536$ counts per pixel. For the numbers given above, the photon Poisson statistics yields relative variances of

$$VAR(16,384)_{rel} = 0.0078 \text{ and}$$
$$VAR(65,536)_{rel} = 0.0039.$$

These values are by a factor of 5 to 10 smaller than the errors calculated above, which are the expected variation from a uniform photon flux. Even though the absolute counts in this experiment are sufficiently high to allow a good counting statistics, the exposure time of $t_{exp} = 0.1$ s is very short. Intensity fluctuations that originate in the ring or the front end optics cannot be reduced but need to be compensated. Short term fluctuations can either be compensated by fast and precise

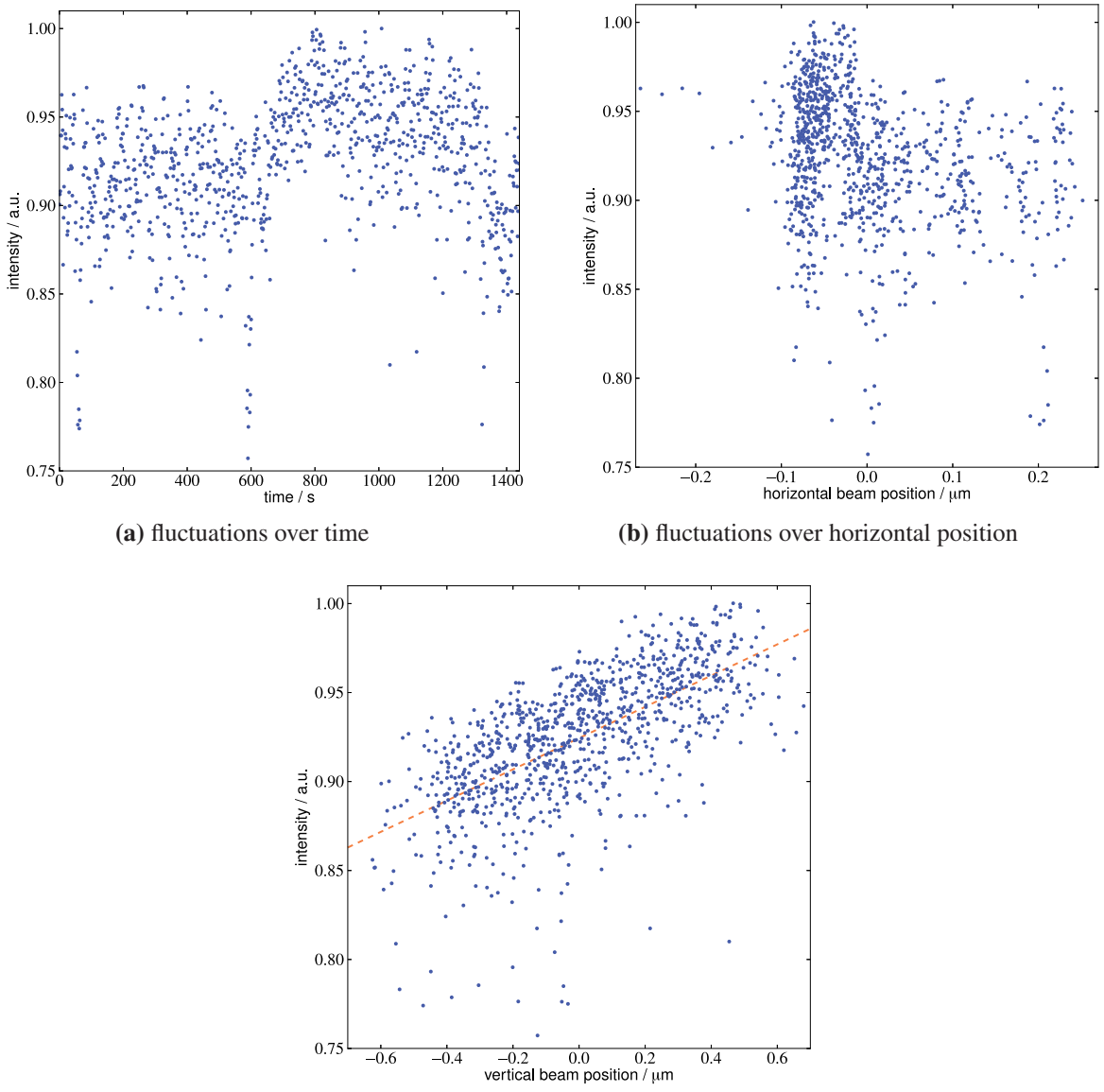

(a) fluctuations over time

(b) fluctuations over horizontal position

(c) fluctuations over vertical position

Figure 6.16: Plots of the intensity fluctuations over (a) time, (b) horizontal, and (c) vertical beam positions. There is no clear correlation in either of the plots (a) and (b). A fit of the position dependency is given for (c), but the resulting errors are still much larger than for example the PETRA III beam current variations.

beam monitors that allow a continuous measurement of the photon intensity on a short timescale or by integrating over these fluctuations. Integration is performed by using longer exposure times in the range of several seconds. Because no fast and precise beam position monitors are installed and because the typical exposure time for an X–ray microscopy image is in the range of $5-30$ seconds, the long exposure times are used to integrate over these short term fluctuations. Concerning the cone–beam setup, the same argument holds: Because the sample is mounted in the divergent beam, the intensity per time and per pixel on the detector is much smaller than in this test experiment, leading to longer exposure times.

Conclusions

The beam stability suffers vertical periodic drifts with frequency bands at $f = 0.15\,\text{Hz}$, $f = 0.3\,\text{Hz}$, $f = 50\,\text{Hz}$, $f = 100\,\text{Hz}$, and $f = 220-280\,\text{Hz}$ whereas the horizontal position is affected by long–term drifts in the storage ring and to a lesser extent by random noise. The position of the focal spot is not stable on short timescales. On short time scales, the intensity pulses with a variance of $VAR \approx 4\%$. Beam intensity monitors could be installed and used to observe the beam intensity fluctuations and store the respective data for later correlation with the images. However, longer exposure times also integrate over these fluctuations and yield a sufficiently homogeneous intensity.

A solution to the position fluctuations is the design and installation of an illuminating optics with a large field of view and a homogeneous illumination function. These two demands are also the basic requirements of the condenser lens in the X–ray microscopy setup. Correspondingly, using a well–designed condenser can eliminate the problem for the X–ray microscopy setup. Experimental results shown in Sections 6.6 and 6.5 confirm that short term fluctuations have no limiting effect on the X–ray microscopy setup.

For measurements in the cone–beam setup, position fluctuations need to be corrected by a fast feedback system, for example using piezo actuators and tilting the 2^{nd} monochromator crystal. The required hardware is already installed at the beamline, with the exception of a fast position sensor. Longer exposure times can be used to cancel the fluctuations in the cone–beam setup as well. The main disadvantage for this method is that the effective focal spot size will be enlarged, leading to a slight reduction in the resolution (compare Section 3.2.2).

The results shown in Sections 6.6 and 6.5 show that the long term beam stability is sufficiently good to cancel out the effects of fast fluctuations.

6.2 Illumination optics

The illumination of the sample is very important. For acquiring a radiograph, it is feasible to scan the sample through a small beam profile to acquire an image of a larger sample area and stitch

the individual images. For tomography, however, the complete sample cross–section needs to be illuminated in a single exposure, limiting sample size to the beam cross-section. The illumination optics are important as they may limit the field of view and the achievable resolution (compare Section 5.1.2).

In X–ray microscopy, the resolution is limited by the numerical aperture of the optics. However, this is only valid if the angular divergence of the radiation is at least as large as the angular acceptance of the objective lens. If the divergence of the incoming radiation is smaller, this lower value of the angular divergence has to be used in calculating the NA, yielding an inferior resolution. This fact and the requirement of a large illuminated area make the illumination optics a critical component.

6.2.1 CRL as illumination

Compound refractive lenses can be used for illumination, but only for scanning radiography applications. The achievable spot size is limited by the focusing characteristics of the lens and the beamline geometry. It is not possible to create a spot size larger than some micrometers using a CRL at the P05 beamline.

As discussed in Section 6.1.3, the position stability of the spot is limited by the beamline performance and not satisfactory yet. While the problem can be neglected for most cases, using a CRL as illumination generates a small and intense spot. This leads to short exposure times and in turn to the aforementioned short term fluctuations. Due to the shape of the spot—approximately a two–dimensional Gaussian—even small variations in the position have a significant impact in the intensity for each pixel, especially on the flanks of the distribution. The problem becomes more pronounced with steeper slopes. Figure 6.17 shows an illumination spot achieved with a CRL. It is about $2 \times 2\,\mu m^2$ (FWHM) and can be well approximated by a two–dimensional Gaussian. The problem arises when this spot is shifted by beam instabilities, as shown in Figure 6.17(c).

A scan with $\Delta x = \Delta y = 272\,\text{nm}$, corresponding to $\Delta x = \Delta y = 2.0\,\text{pixels}$, was performed and the resulting data stitched for a composite image. Figure 6.18 shows the resulting stitched image. Except for the text at the top and two lines at the side, the scan field show be devoid of structures, i.e. the field should be of homogeneous transmission intensity of $T = 1$. The result shows very nicely that the beam is not stable and larger errors occur. Also, the errors in x–direction seem more to be due to random noise whereas structured artifacts appear in y–direction. The overall normalized error is $\sigma = 0.0785$ (RMS).

A similar test measurement of a field of 500 nm lines and spaces reveals that some structure can be seen. While the test pattern itself shows some damage effects in the respective field which appear more pronounced in the horizontal structures, the image itself seems to suffer from

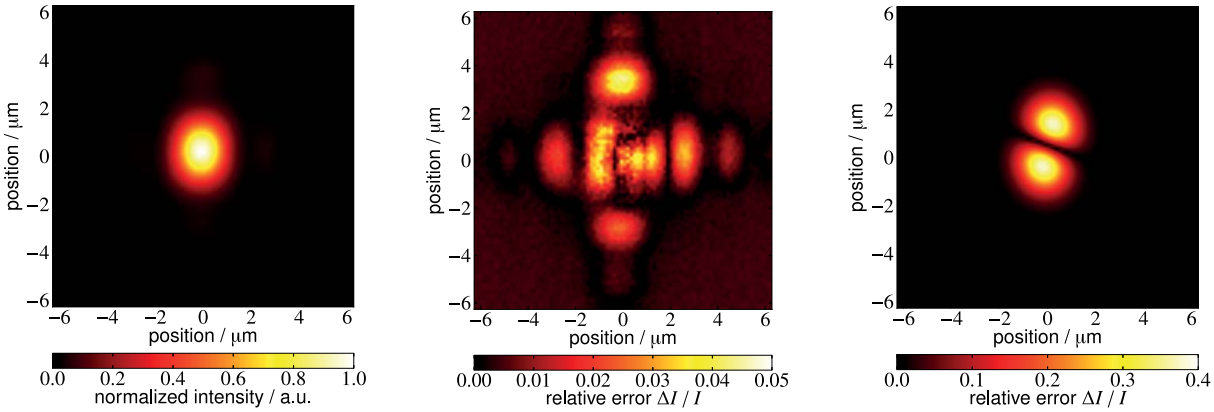

(a) **(b)** Deviation of fit from data **(c)** Difference of two shifted images

Figure 6.17: **(a)** Image of the focal spot generated by the CRL used as condenser. The spot is about $2\times2\mu m^2$ in size (FWHM) and can be well approximated by a two–dimensional Gaussian (compare **(b)**). **(c)** If this spot is shifted by a typical displacement (horizontal 100 nm and vertical 500 nm), the relative errors become very pronounced and dominate the image. Note the different color scaling for subfigures (b) and (c).

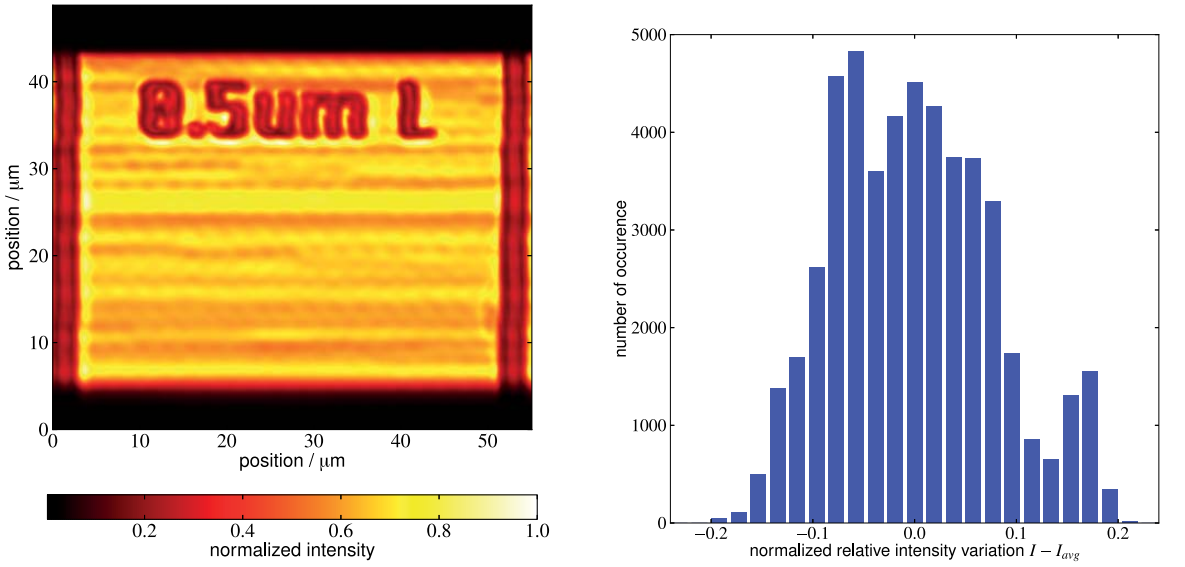

(a) **(b)**

Figure 6.18: **(a)** Stitched image composed by summing up the contributions of the individual images created by a small focal spot. The sample is part of a test pattern. The text is clearly visible, but the region below it is empty of structure and should appear as uniform. **(b)** Histogram of the intensities in the plain region. Because of small step width, each pixel is illuminated several times, increasing the statistics and reducing the overall error. However, the normalized intensity still varies over ±10%, showing that stability issues persist in this setup.

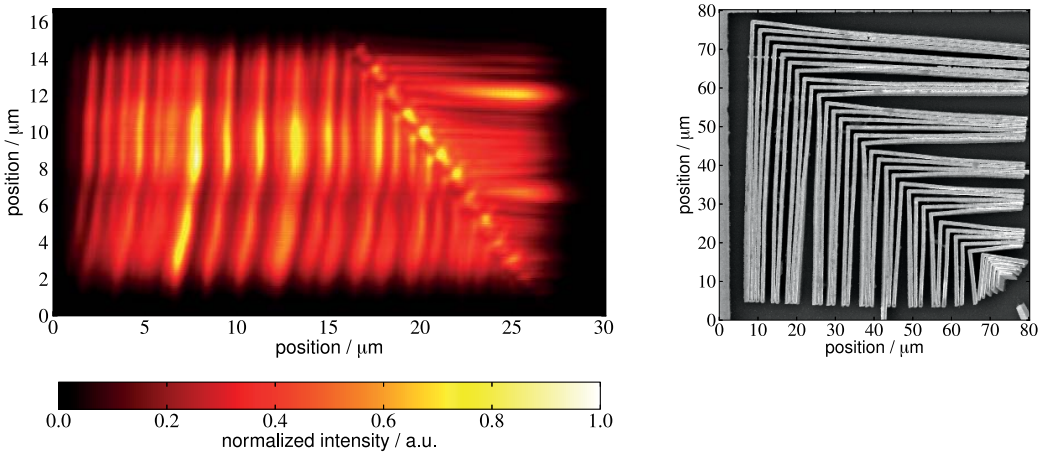

(a) X-ray radiography **(b)** SEM image [67]

Figure 6.19: Images from the same region of the test pattern: (a) composite image stitched from individual focused X–ray beam images and (b) SEM image. The SEM image clearly shows that the supposedly periodic line–and–space–arrangement is no longer periodic. Vertical lines can be seen in the X–ray radiograph but these structures are nevertheless distorted by errors.

energy	13 keV
illuminated field of view	60 µm
working distance	1.25 m
beam divergence at working distance	640 µrad
source distance	64 m
lens diameter	800 µm

Table 6.3: Nominal parameters of the rolled condenser lenses used in tests [136].

the aforementioned vertical beam movement, making qualitative statements difficult. Figure 6.19 shows the corresponding X–ray radiograph and an SEM image for comparison.

6.2.2 Rolled condenser lenses

Rolled condenser lenses consisting of small prisms [117] (rolled X–ray prismatic lens, RXPL) are much better suited for usage as a condenser than classical CRLs. They offer both a large aperture and a large illuminated field of view. Furthermore, they are designed for a tailored constant divergence throughout the complete field of view, enabling the same theoretical resolution for the complete sample.

The fabrication of these rolled condenser lenses is still in the process of optimization, i.e. the effective lens parameters still differ significantly from the theoretical design parameters.

For testing purposes, a set of two rolled condenser optimized for $E = 13\,\mathrm{keV}$ was used. The relevant parameters are given in Table 6.3. The lens diameter is very large compared to the typical aperture of a CRL. This is necessary for achieving the target divergence and also allows gathering a much larger portion of the incoming beam, greatly increasing the photon flux. Figure 6.20 shows

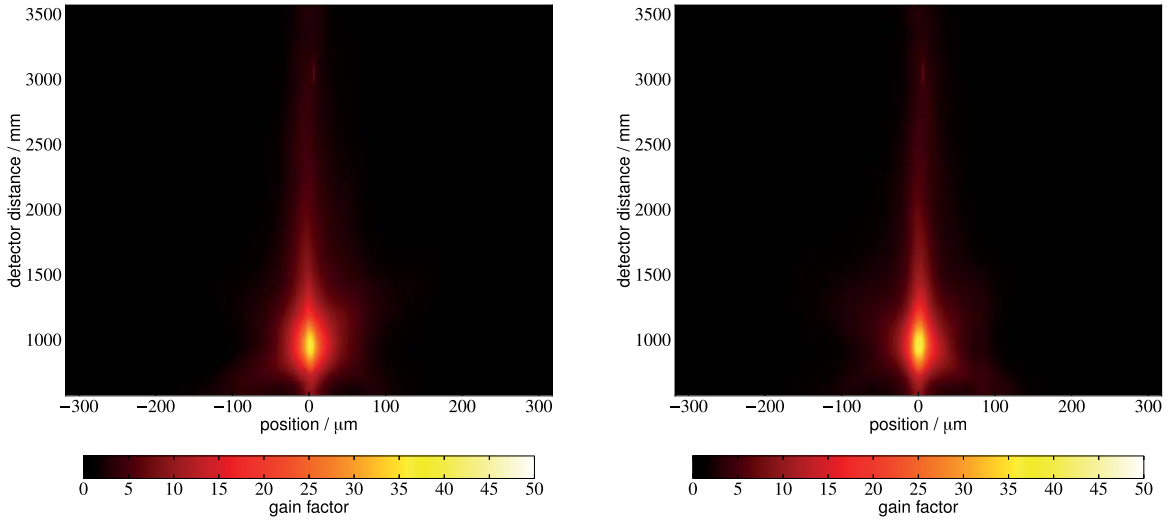

(a) vertical **(b)** horizontal

Figure 6.20: Gain measurement for rolled X–ray prismatic lenses used as condenser. The horizontal and vertical gain is very similar, as is expected due to the rotational geometry.

the measured intensity profiles with varying detector distance. Figure 6.21 shows slices of these data for easier interpretation. The highest gain—measured at the center of the spot—is not found at the target working distance of $t = 1.25\,\mathrm{m}$ but at $t_{vert} = 0.924\,\mathrm{m}$ and $t_{hor} = 0.902\,\mathrm{m}$. The deviation of 35% from the design value is already a clear indication that there are still optical errors in the rolled condenser lenses, probably due to problems with the fabrication. Problems also manifest in the profile of the spot: While designed to deliver a spherical flat illumination, the resulting form is more Lorentzian with FWHM values of $d_{vert} = 34.2\,\mu\mathrm{m}$ and $d_{hor} = 31.4\,\mu\mathrm{m}$, whereas the expected spot shape is a disk with $50\,\mu\mathrm{m}$ diameter.

A magnified look at the spot through an objective lens allows for a further characterization of the spot's shape. Figure 6.22 shows a sample image. In larger magnification, the shape of the spot differs significantly from a smooth circular shape. Note that the ring shaped structures in the outer regions are very problematic as they generate pronounced structures in the background illumination which shift in case of beam variations from the same stability problem that has been discussed in Section 6.1.3.

For X-ray microscopy applications, not only the shape and size of the illuminated field of view are important but even more so is the divergent illumination of the sample. The achievable resolution of the objective lens is heavily dependent on the degree of divergence in the sample illumination. A detailed investigation concerning the effect of the differences between calculated and effective working distances on the divergence properties of the lenses has been performed by H. Vogt (IMT, KIT) to improve the performances of these illumination optics and are part of his PhD thesis [137].

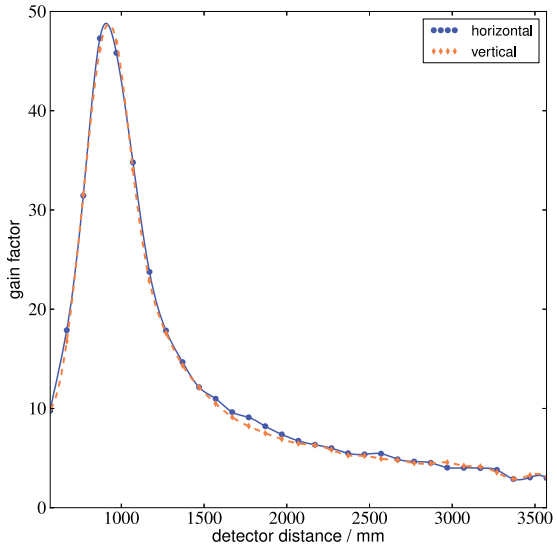

(a) gain with varying detector distance

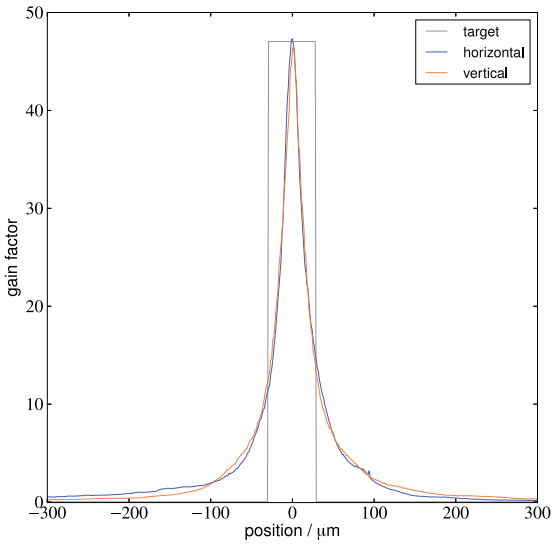

(b) position dependant gain profile at the distance with the maximum average gain

Figure 6.21: **(a)** Plot of the central gain over the detector distance (i.e. a slice at position 0). The measurement points are denoted with the symbols, the lines represent a cubic interpolation. **(b)** Plot of the beam profile at the detector distance $d = 0.82\,\mathrm{m}$.

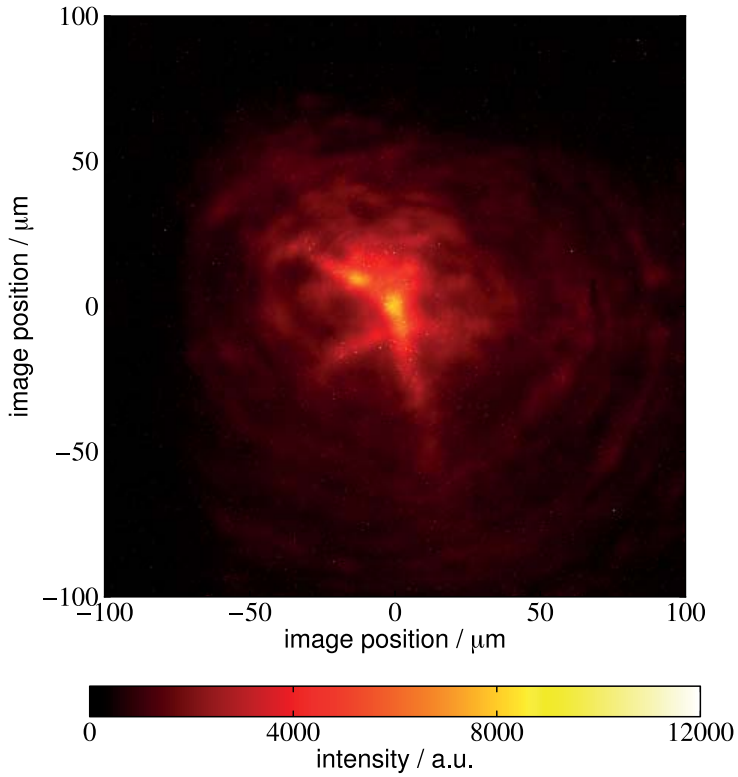

Figure 6.22: Magnified image of the spot as seen through the objective lens. The inhomogeneous illumination is obvious and can lead to severe artifacts in case of beam instabilities.

Conclusion

It has been demonstrated that CRLs can be used for illuminating the sample in an X–ray microscopy setup. The illuminated area is very small, however, and beam instabilities have a significant impact on the image quality because small position variations lead to large intensity fluctuations. Furthermore, the angular spread of the illumination is not constant throughout the focal spot.

Optics that has been designed to act as dedicated condensers has strong advantages. They allow tailoring both the angular variation in the illumination and the illuminated field of view. While other condenser concepts exist as well [56], RXPL have been used for these experiments. Illuminated field of view and angular acceptance have been tailored for the setup at P05 and while there are still deviations from the design values, the lenses can still be used as condenser lenses. Imaging with a resolution of better than 100 nm was possible with the use of these kind of illumination optics.

6.3 Objective optics

CRLs (compare Section 2.3.5) have been used as objective optics for all imaging experiments. All lenses used for these experiments have been fabricated at the IMT, KIT. Different designs that differ in lens number, parabola curvature and aperture have been used and their parameters are given in Table 6.4. HZG is a partner in the Helmholtz Virtual Institute *New X-ray analytic methods in material science* (VI-NXMM) and has access to newly developed lenses with varying apertures [80, 81], which have been used in some experiments as well. These lenses are developed to achieve an improved resolution through the complete field of view.

The respective resolution limits of the various lens designs (compare Table 6.4) differ significantly, but all are well suited for tests with the nano test pattern with its structures in the range from 50 nm to 800 nm. First tests have been performed with the lens layouts 05_505P and 08_762P at $E = 13\,\mathrm{keV}$, whereas new lenses with an improved layout have been used for later tests, commissioning and first experiments. These results will be presented in detail in Section 6.5.

6.3.1 Alignment

The alignment of lens structures has to be performed in two steps. The first step is the rough alignment based on the projected shape of the lens. If ideally aligned, all the lens elements are in a row and only one clear structure is visible in transmission. Figure 6.23 shows some steps of the first alignment. The fine–tuning of the alignment exploits the imaging capabilities of the lens.

design name	05_505P	08_762P	1277_00_A0	1231_00_A0
energy	13 keV	13 keV	17.4 keV	30 keV
radius of curvature	5.9 µm	10.125 µm	7.0 µm	6.0 µm
number of elements	12	38	81	249
opening aperture	60 µm	100 µm	78 µm	100 µm
focal distance	156 mm	91 mm	105 mm	106 mm
working distance	149 mm	80.5 mm	97.9 mm	97.8 mm
numerical aperture	$1.9\,10^{-4}$	$5.49\,10^{-4}$	$4.70\,10^{-4}$	$2.35\,10^{-4}$
resolution limit	306 nm	106 nm	75 nm	86 nm

Table 6.4: Parameters of the compound refractive lenses used as objective lenses. [79, 89].

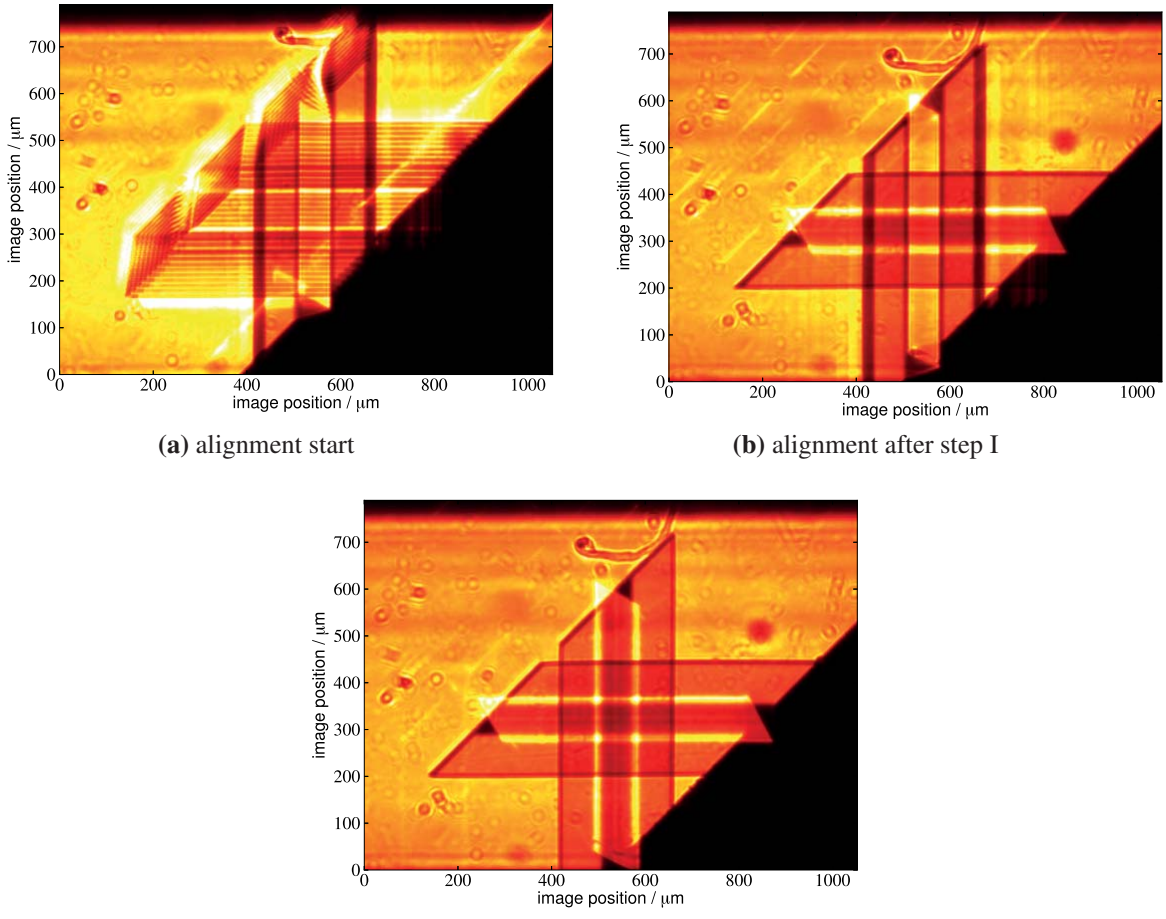

(a) alignment start

(b) alignment after step I

(c) alignment after step II

Figure 6.23: X–ray radiograms of the objective lens (design 05_505P) at various stages of the alignment. **(a)** Starting orientation. A severe misalignment around the horizontal axis is visible through repeating, slightly shifted structures. The vertical axis is slightly misaligned, as shown by the wide dark streaks at the sides and reflections on the side. **(b)** The horizontal axis is aligned, only the slight misalignment of the vertical axis persists. **(c)** Both axes are aligned. Because the detector is not setup in the focal plane but in the image plane, the focus and line foci are not points/lines but show up as lighter lines at the edges of the lens.

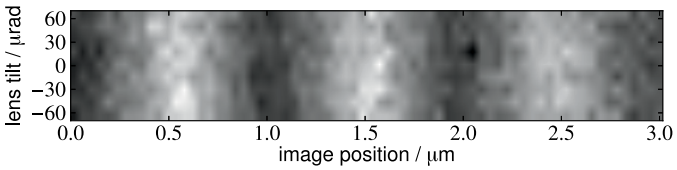

(a) rotation around Rx

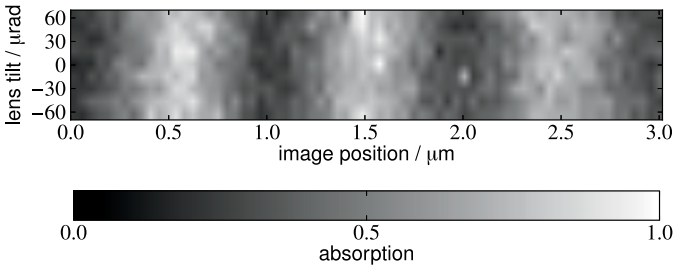

(b) rotation around Rz

Figure 6.24: Composite image of slices from radiographies of an X–ray resolution test pattern. The rows correspond to the different rotational positions. To exclude sample orientation effects, only one detector line has been investigated. There is strong noise in the signal but no clear trend is apparent.

Using a test pattern, further fine rotations of the lens result in changes of the image quality. This can be used to find the optimum lens orientation.

For best performance, all individual parabolic lens elements (compare Section 2.3.5) shall have a vertical offset of below 2 µm. This corresponds to an angular misalignment of 33.3 µrad or 0.002°, respectively, for a 60 mm long lens. For shorter lenses, the acceptable angular misalignment is correspondingly larger. While these values seem arbitrarily selected, the reasonable limit of the required alignment precision is the linearity of the supporting silicon waver and the lens elements. The flatness of the silicon wafer on which the lenses are mounted is typically about 2 µm. Measurements with a light microscope show that the deviation of the lens form a straight line is as high as 5 µm (for designs 05_505P and 08_762P). This result in mind, there should be a large angular range in which the image quality does not alter significantly.

Tests with lens 08_762P confirm this effect. The lens length is $l = 24$ mm, i.e. a rotation of $\Delta\phi = 0.001° = 17.45$ µrad corresponds to a lateral displacement between entrance and exit aperture of $d = 0.42$ µm. The lens was tilted for a total of 0.008°, i.e. the exit aperture was shifted by up to 3.35 µm with respect to the entrance aperture. Rectangular structures on a test pattern which should also show a rectangular absorption pattern were used to determine the image quality with respect to the tilting angle. A better lens alignment results in a better image quality, i.e. the deviation of the profile from the rectangular shape should be smaller. Figure 6.24 gives the raw measurement data for tilting the lens about the two axis' perpendicular to the beam direction.

The measurement showed no significant trend for tilting both around the $x-$ and the $z-$axis.

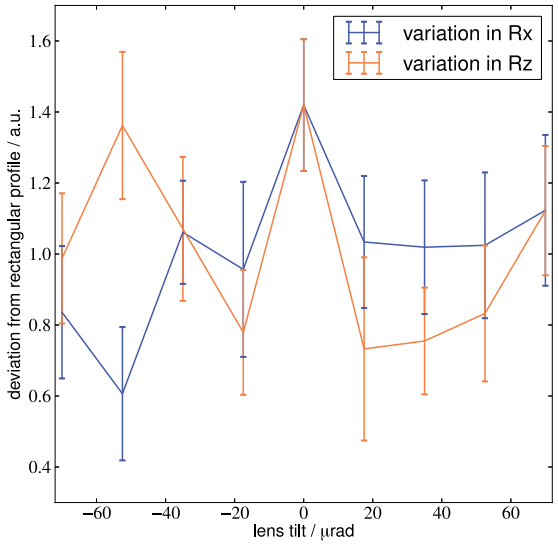

Figure 6.25: Deviation of radiographic profiles from the rectangular profile of the test pattern, plotted in dependence of the lens tilt in *Rx* and *Rz*. No significant influence of the tilt on the image quality can be established. The apparent trends with the lens tilt are negligible, as described in the text in detail. The zero position was established by aligning the lens as shown in Figure 6.23.

Figure 6.25 gives a plot of the results. Linear fitting of the measured values yields

$$f_{Rx} = 1.008 \pm 0.333 + (0.00228 \pm 0.00738)\, x\,[\mu\text{rad}]\,, \tag{6.10}$$

$$f_{Rz} = 1.006 \pm 0.333 - (0.00164 \pm 0.00768)\, x\,[\mu\text{rad}]\,. \tag{6.11}$$

Apparently, the slope values are very small and much smaller than the errors in the slope. Taking this into account, no trend can be detected and the lens behaves as expected with a large angular range in which the image quality is very similar.

6.3.2 Image errors

For tomographic applications, it is important that the X–ray optics yield magnified images with a linear scaling of the sample without any distortions. As distortions due to lens errors always occur at the same image positions, a sample volume would rotate in and out of the distorted region. Severe ring artefacts would be the result in the reconstruction. According to optics theory, the theoretical lens layout does not induce any image errors; thus, all image errors are induced by deviations of the X–ray lens from its norm parameters.

Some image errors and non–linearities appear in imaging in both tested lens designs (05_505P and 08_762P). The exact source of these errors is still not clear, but there is an agreement that these image errors are due to lens imperfections introduced in the fabrication [70, 79]. A known problem is the linearity of the lens elements. Ideally, the center of all lens elements should be found on a straight line. In reality, deviations of up to some 10 µm can exist for a bad LIGA exposure. In

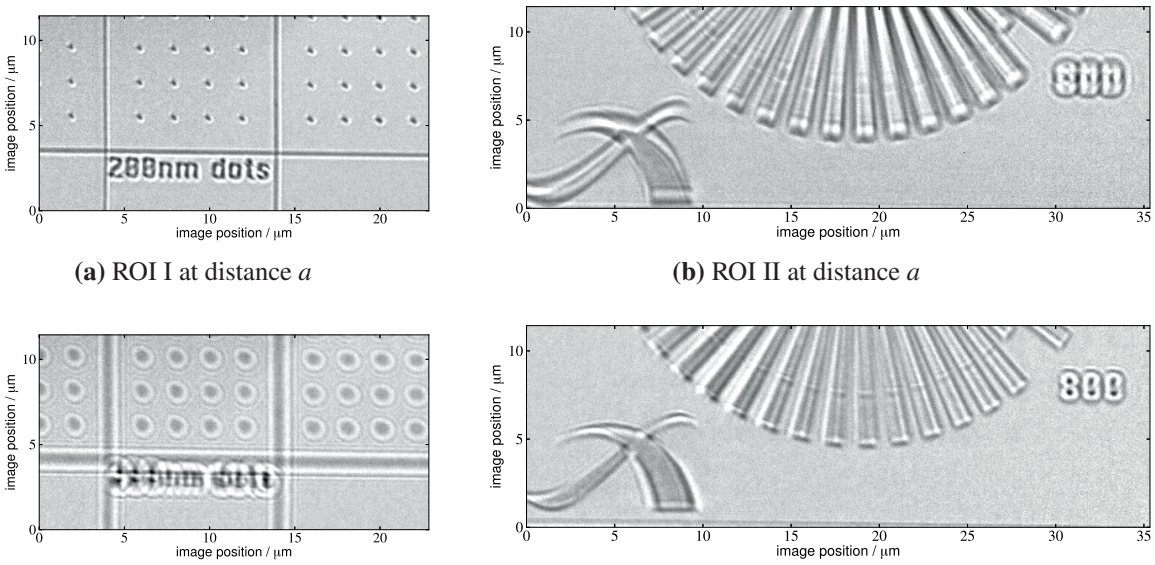

(a) ROI I at distance a

(b) ROI II at distance a

(c) ROI I at distance b

(d) ROI II at distance b

Figure 6.26: Results of parallel illumination imaging. **(a)** and **(b)** show different regions of interest from the full field of view at distance a. While the dots are well defined, the Siemens star region is out of focus. In **(c)** and **(d)**, the effects are reversed: Now, the dots are completely defocused whereas the Siemens star region is sharp. The distance $b - a = 3\,\text{mm}$ is very large, compared to an expected depth of focus of about 0.2 mm. Because of the focus position stepping width of $\delta d = 1\,\text{mm}$, ROI II is not complete focused at distance b. It still appears a little defocused, although significantly improved as compared to distance a.

combination with lens sizes (i.e. lens apertures) of only around 100 µm, this is a severe problem.

However, due to the complex light paths in the lens and the large amount of lens elements, it is difficult to trace an image error back to a specific part of the lens. A detailed analysis of this problem can be performed using wave propagation simulations. Such tools were not readily available to me and go beyond the scope of this work. But the problem can also be tracked using parallel illumination. Because the ray paths in the lens are well defined for parallel illumination, image errors can be traced to different regions of the CRL. Figure 6.26 shows an example case where the working distances do not fit over the field of view. A deviation of the working distance of $\Delta d = 3\,\text{mm}$ for different regions of the field of view is very large.

Errors can be minimized by reducing the lens aperture opening. Figure 6.27 shows how closing the apertures in front of the objective lens can alter the field of view. While the overall field of view is diminished, image errors in the center are significantly reduced. This effect points towards non–linear lens elements being responsible for at least part of the errors.

As mentioned above, these errors are due to the fabrication process and not completely understood yet. At the moment, the only solution is trying out different lenses until a suitable one is found. Once identified, these defect–free lenses can be used for X–ray microscopy and nanotomography applications.

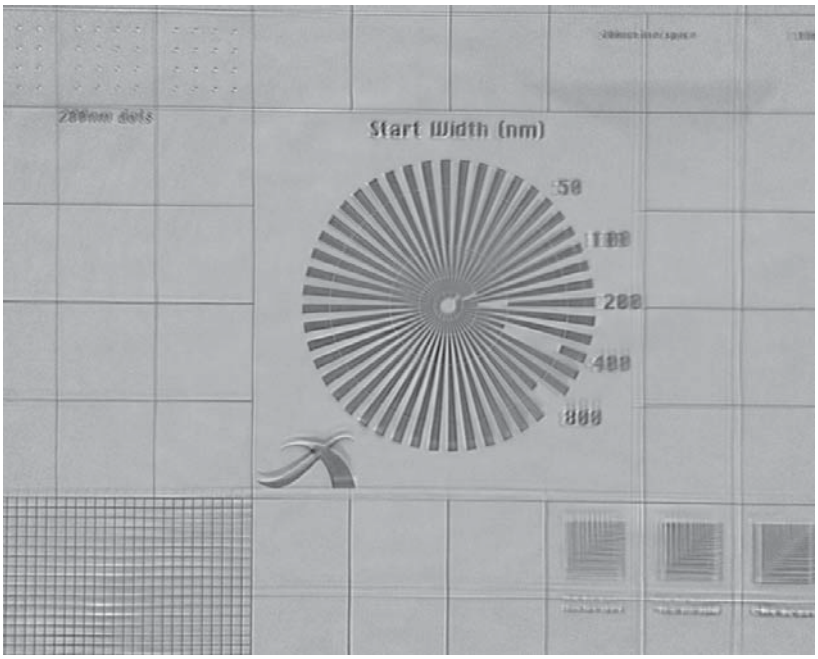

(a) aperture adjusted to lens opening

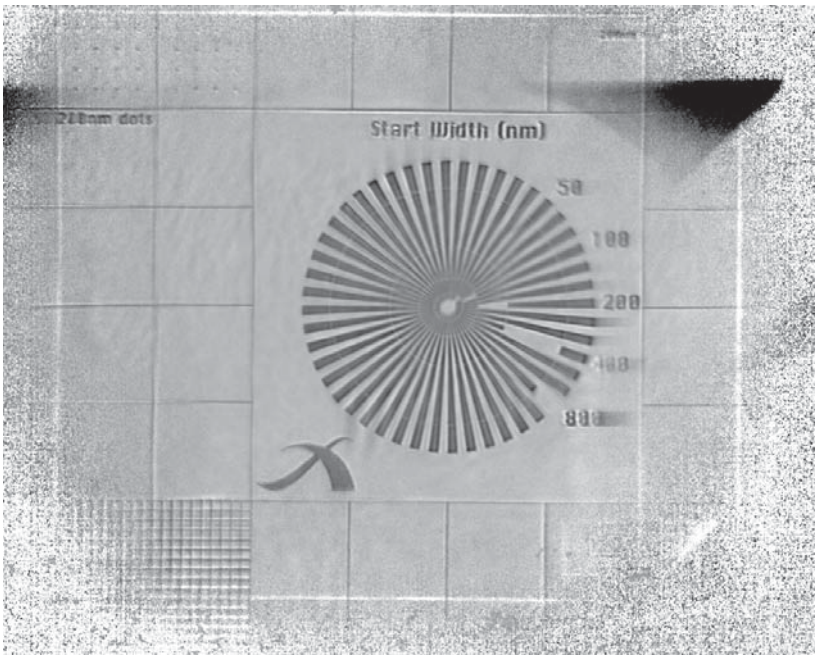

(b) aperture closed by 66 µm

Figure 6.27: Influence of the aperture opening on image quality: Comparison of two absorption images taken at otherwise identical conditions. In **(a)**, the beam aperture in front of the lens has been adjusted to fit the lens opening aperture. There are some image errors like twin images visible. **(b)** shows the same image with the apertures closed by 66 µm. The field of view is significantly reduced due to the smaller lens aperture. However, most image errors disappear. On the right side, there appear some new smeared stripes, but the overall image quality is significantly enhanced. Because of the reduced angular acceptance at the borders of the field of view, a quality reduction in these regions is expected as well as a deterioration of the overall resolution.

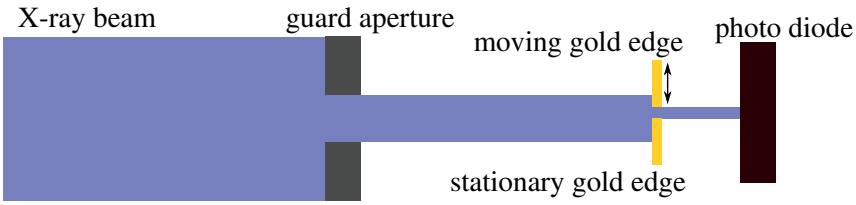

Figure 6.28: Schematic drawing of the measurement scheme for determining the focal spot size. The gold edges are moved in the confined beam and the resulting beam intensity is monitored for calculating the response function of the edges. Note that the setup for the $x-$ and $z-$directions is similar and only one dimension is depicted here.

6.4 Cone–beam setup

The cone–beam setup relies on the creation of a nanofocus for imaging, as the focal spot size limits the resolution (compare Section 3.2.2). Spot sizes can be measured by knife edge scans with defined absorbers. For this procedure, a gold edge has been prepared by focused ion beam milling from a 50 µm thick foil. Using the FIB allows surface qualities of about 20 nm over a large distance. The foils used in the experiment have polished side lengths of between 500 µm and 800 µm.

6.4.1 Focus characterization

Characterizing the focal spot size, the measured profile ideally corresponds to the focal spot width. However, this requires the scan to be performed without any influence of the guard slits. Because reflections or orientation errors might influence the result, the response function of the measurement system has been characterized by testing the performance of the slit system used in this experiment. A pair of guard slits limits the overall beam size and the gold edges have been scanned through the beam using a Piezosystem Jena PXY200 D12 system. Figure 6.28 shows the general measurement scheme. Ideally, the integrated intensity should decrease linearly while there is still beam transmitted through the edges and remain at zero for the overlap. Figure 6.29 shows the results of these measurements.

The overall results agree well with the expectations of a linear decrease for a decreasing opening area and a flat line for a zero gap, but there is a clear deviation around very small openings. Using these deviations as the system response kernel in a deconvolution of the raw data allows to separate the lens' focal spot size from the influence of the measurement system. The response functions have a full width at half maximum of

$$FWHM_x = 0.88\,\mu\text{m}, \tag{6.12}$$

$$FWHM_z = 0.77\,\mu\text{m}. \tag{6.13}$$

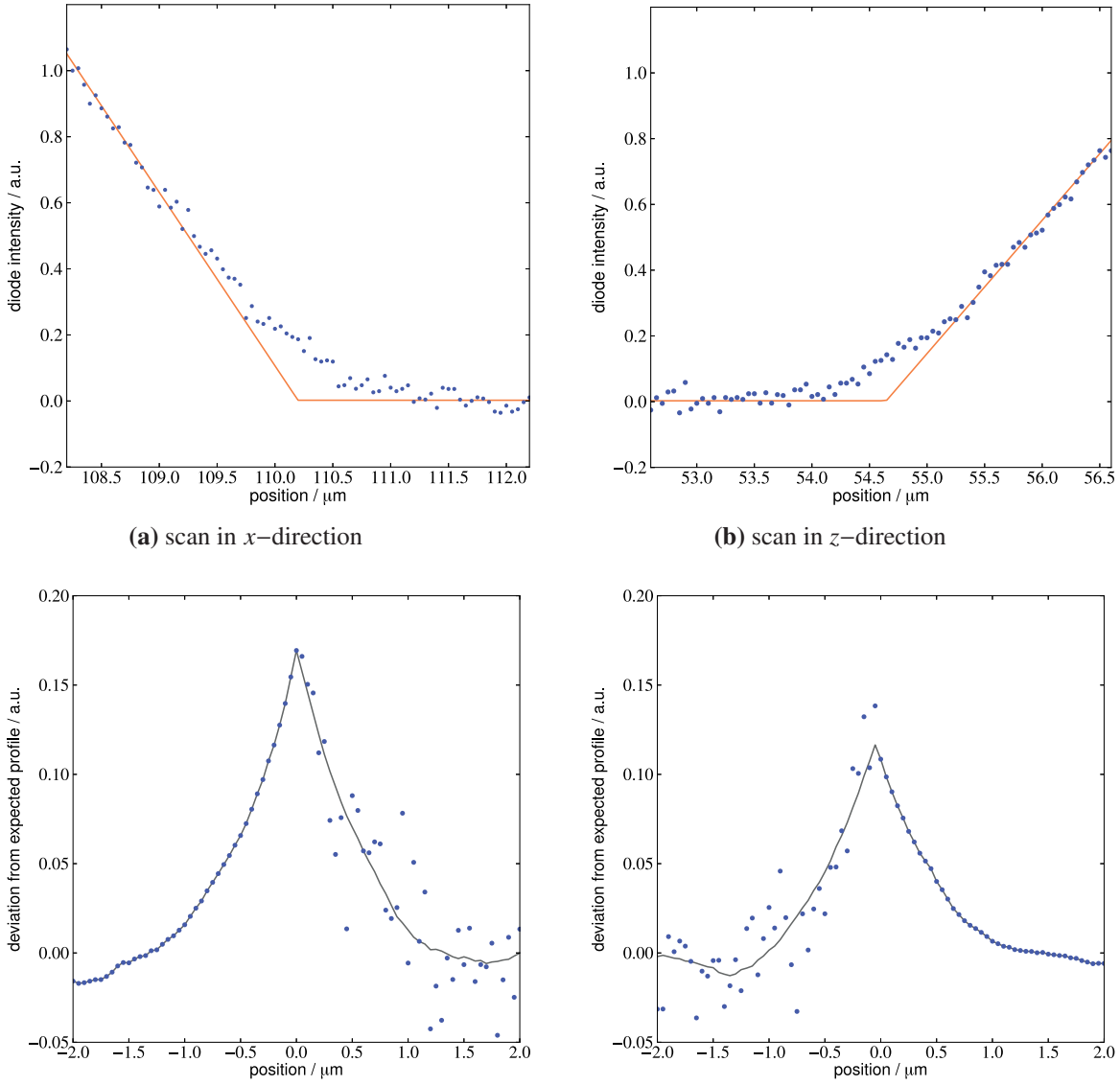

(a) scan in $x-$direction

(b) scan in $z-$direction

(c) deviation in $x-$direction

(d) deviation in $z-$direction

Figure 6.29: Plots of the measurement results for the gold edge gap measurements. The full scan shows two regions with a linear intensity decrease and the zero line. However, if looking closer at the intersection of these two regions ((**a**) and (**b**)), a discrepancy between the measured values and the expectations show. (**c**) and (**d**) show the deviations directly as well as a smoothed fitting curve which. Note that one side of the response function is very noisy as the signal is ideally zero and only the noise remains and dominates.

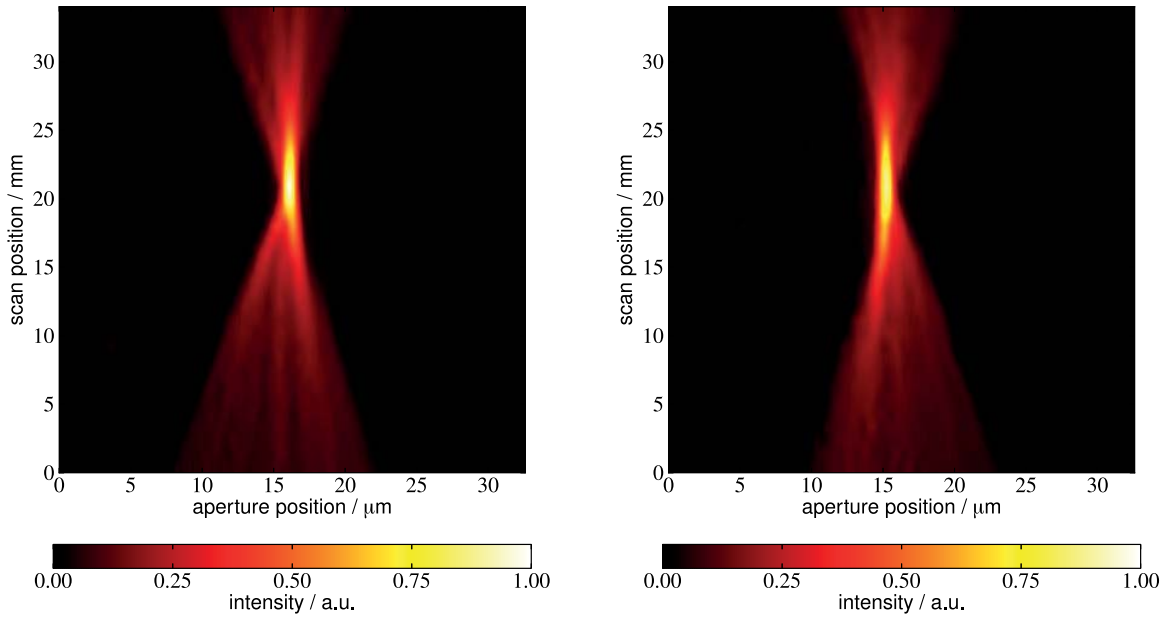

(a) scan in x−direction **(b)** scan in z−direction

Figure 6.30: Map of the derivative of the edge scans for different scan positions in beam direction. The position of the focus is obvious as the derivative is largest here and the width is smallest.

Considering that expected spot sizes are well below 1 µm, it is necessary to use this information to separate the real focal spot size from the measured value.

Finding the best focal distance is achieved by performing edge scans at different positions in beam direction. The resulting map shows the clear minimum in width in the focal spot and defines the working point. An example is given in Figure 6.30. The focal distance is given by the smallest width of the beam profile. The deconvolution of the system response kernel was performed in MatLab using the algebraic, iterative Lucy-Richardson method [77, 108] with 5 iterations. An exemplary result is shown in Figure 6.31. The deconvolution also pronounces the side maxima of the Airy disk, which are not clearly visible in the raw data. For this case, the focal spot size has been calculated to be $309.7 \times 316.6\,\mathrm{nm}^2$. This value is the smallest focus achieved for the cone–beam setup at P05 so far.

For estimating the accuracy of the measurement, a repeated measurement at the focal position has been performed for the lens 1231_02_L3 at $E = 20\,\mathrm{keV}$. The results yield the average FWHM and the standard deviation:

$$d_{x,\,FWHM} = 348.6 \pm 19.1\,\mathrm{nm}, \tag{6.14}$$

$$d_{z,\,FWHM} = 404.0 \pm 14.4\,\mathrm{nm}. \tag{6.15}$$

While there remains a variation in the measurements of the focal spot sizes, the measurement is well defined on the scale of the achieved focal spot sizes of larger than 300 nm.

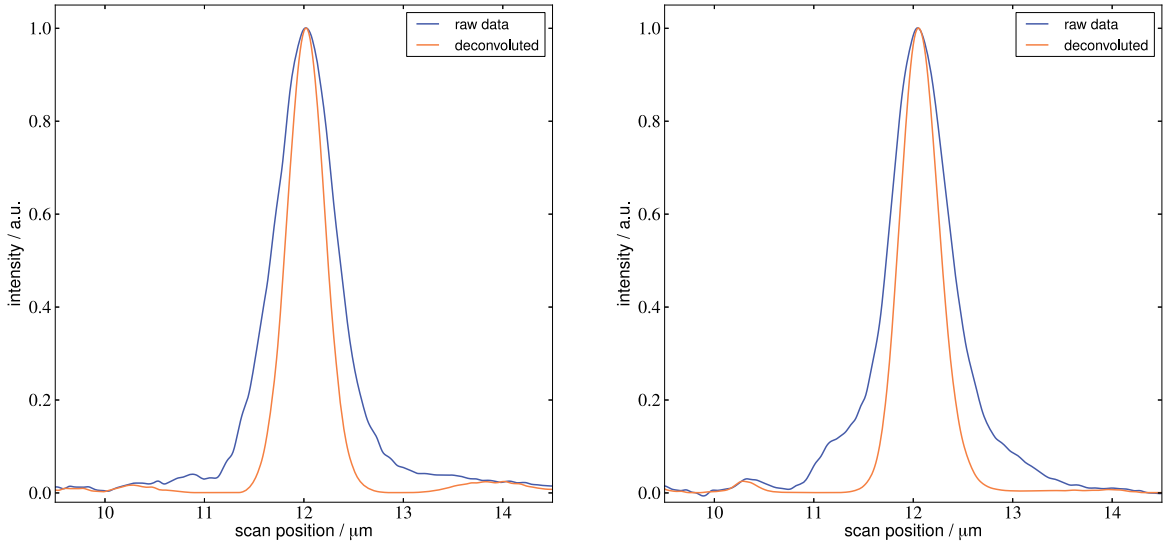

(a) horizontal **(b)** vertical

Figure 6.31: Result of the focus deconvolution (for lens design 08_762P, $E = 13\,\text{keV}$). Note that the side maxima expected in the Airy disk are visible and separate, an indication for the correctness of the deconvolution method and kernel.

As the expected resolution is limited by the focal spot size, a resolution between 300 nm and 400 nm seems reasonable from the optics point of view.

6.4.2 Phase effects

One of the problems using the cone beam setup at 3^{rd} generation sources are phase effects from the high degree of coherence. The long propagation distances are responsible for severe phase effects in the images. Figure 6.32 gives some exemplary images and Figure 6.33 shows the integrated profile of a line. Obviously, the phase effects dominate the image and the reconstruction based on the absorption signal is impossible.

Simple propagation based phase–retrieval algorithms assume that only the first maximum occurs. This corresponds to short propagation distances or large pixels. For stronger phase effects, more complex phase reconstruction techniques exist but implementing these would exceed the scope of this work. For more details, see for example the PhD thesis by M. Bartels [5].

6.4.3 Cone–beam: Conclusion and outlook

Further testing of the cone-beam setup has been postponed due to the limited amount of beamtime and the more promising results from the X–ray microscopy setup. As discussed in Section 5.1.1, the overall photon flux is significantly reduced compared to the X-ray microscopy setup, because no light–gathering optics like a condenser can be deployed. The installation of the new P05 double

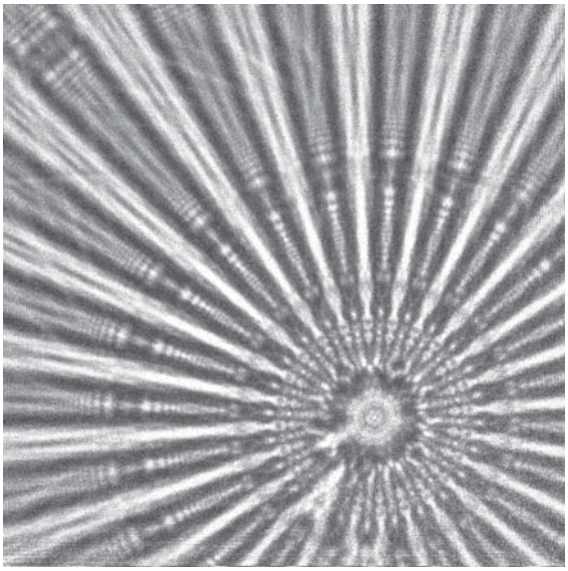

(a) cone–beam image of Siemens star

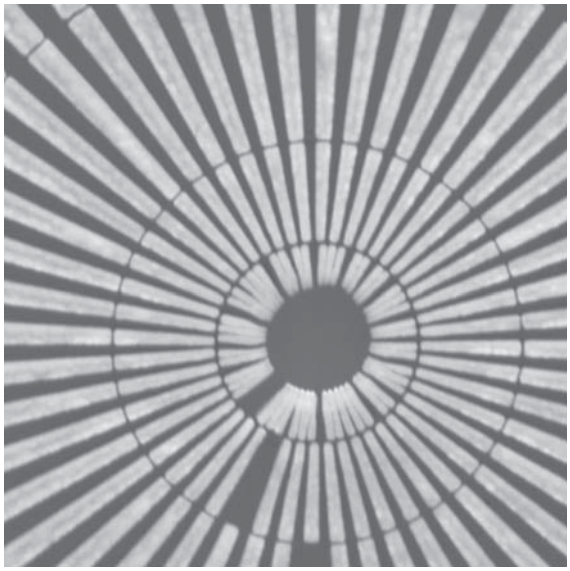

(b) SEM image of structure

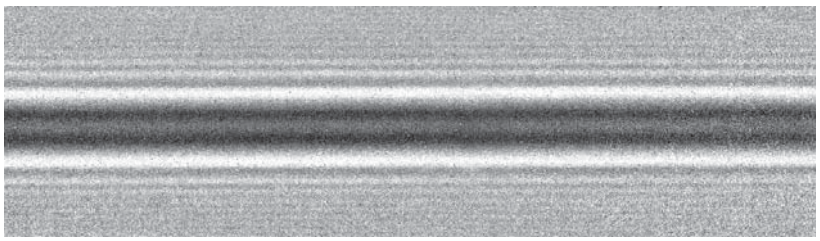

(c) cone–beam image of a line

Figure 6.32: Phase effects in the cone–beam setup. **(a)** and **(b)** show the center of the Siemens star measured with the cone–beam setup and the corresponding SEM image. The field of view is approximately $70 \times 70\,\mu m^2$. **(c)** shows the phase oscillations produced by a straight line.

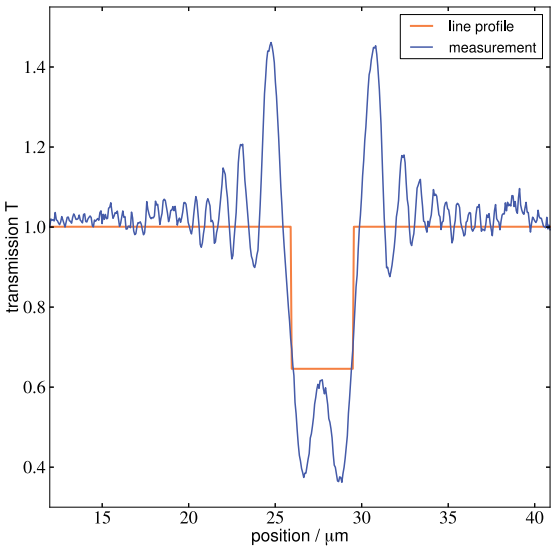

Figure 6.33: Plot of the measured absorption values for the line profile shown in Figure 6.32(c), horizontally integrated. The expected absorption profile is given for comparison. The phase effects dominate on a scale of several micrometer and prohibit absorption imaging with a resolution better than about 10 µm.

multilayer monochromator (DMM) with a broader bandwidth will increase the overall photon flux and the cone–beam setup can particularly profit from this development to reduce long exposure times.

As the lenses are chromatic, they suffer a focal distance shift if used with an energy bandwidth. The focal distance depends on the energy as follows:

$$f = \alpha E^2, \tag{6.16}$$

with all the constants merged in α. Using the derivative df/dE, substituting for α and rearranging the terms, the variation in the focal distance df as a function of the energy bandwidth dE is:

$$df = \frac{2f}{E} dE. \tag{6.17}$$

For example, consider a focal distance of $f = 150\,\text{mm}$. Using a typical depth of focus of $\Delta f \approx 300\,\mu\text{m}$, the acceptable relative energy bandwidth dE/E is given by

$$\frac{dE}{E} = \frac{df}{2f} = 1.0 \cdot 10^{-3}. \tag{6.18}$$

This value is about one order of magnitude above the value for the double crystal Bragg monochromator

$$\left(\frac{dE}{E}\right)_{DCM} = 1.35 \cdot 10^{-4}. \tag{6.19}$$

Increasing the relative energy bandwidth by a factor of 10 would also increase the flux by the same factor without any negative impact on the experimental performance. The new DMM has a bandwidth of $\Delta E/E = 10^{-2}$. Even though a cone–beam setup with refractive optics cannot use the complete energy bandwidth, it would still greatly benefit from a flux increase by a factor of 10. The transmitted bandwidth of the DMM can be limited by slightly detuning the double multilayers to match the experimental acceptance.

In this setup, the energy bandwidth is limited by the chromatic refractive optics. Installing achromatic optics would allow using the full energy bandwidth of the monochromator. A Kirkpatrick–Baez mirror system, for example, is completely achromatic and would fit the requirements of the cone–beam setup. These systems are capable of creating focal spots with sizes of below 200 nm at acceptable working distances. Installing a KB mirror could increase the photon flux by a factor of 100, compared to the current combination of Bragg double crystal monochromator and refractive optics.

A further boost in performance can be achieved by using photon counting detectors. These can greatly improve the statistics or reduce the counting times. Currently, the use of photon counting detectors in direct imaging applications is limited by their comparatively large pixel size (for ex-

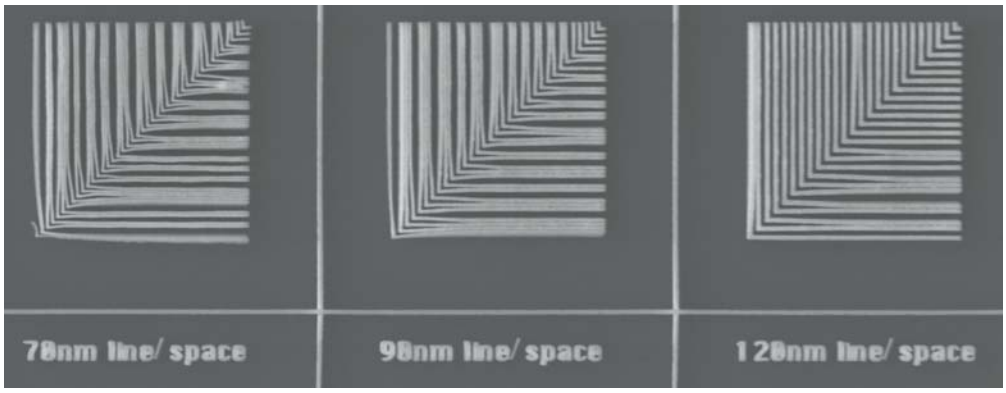

Figure 6.34: SEM image of the nano test pattern. Obviously, the periodic line and space structures are not as intended.

ample 75 µm for the Dectris Eiger) which requires a very high X–ray magnification. If the pixel sizes were to be further reduced, using this kind of detectors is an interesting option for cone–beam experiments.

6.5 X–ray microscopy resolution test

The majority of experiments have been performed with the X–ray microscopy geometry, i.e. with a condenser illumination and the magnifying X–ray optics installed behind the sample. The achieved resolutions and fields of view differ with energy and lens and will be discussed below. These measurements are amongst the latest that have been performed and new lenses for $E = 30\,\mathrm{keV}$ (layout 1231_A0_00) and $E = 17.4\,\mathrm{keV}$ (layout 400_18_13) have been used, each with a nominal working distance of $f = 100\,\mathrm{mm}$.

For resolution tests, an Xradia test pattern has been used. The test pattern features structures in the range from 50 nm to 800 nm. Unfortunately, the smaller structures often bundle and form thicker lines without a space in–between. Figure 6.34 shows an exemplary SEM image of line structures. Over the complete test pattern, the stability limit seems to be between 120 nm and 150 nm. Structures larger than the limit seem unaffected, whereas all smaller structures show some kind of damage. While an estimation of the resolution is difficult with unknown structure sizes, the resolution of lines with a spacing of 120 nm is possible. Tests have been performed at $E = 30\,\mathrm{keV}$ and $E = 17.4\,\mathrm{keV}$. Comparing the X–ray images with the SEM data show a good agreement between the two, as shown in Figure 6.35. Because the exact shape of the tilted structures is difficult to investigate with other means, a differentiation between real effects and image errors in the range below 100 nm is difficult.

In addition, the structures are well defined with smooth walls and are made of gold, which is a high–Z material. These facts are ideal for total reflection from the walls and can explain the X–ray transmission over 1 also visible in Figure 6.35(e) and (f). The maximum incidence angle—defined

(a) horizontal lines – X–ray microscopy data

(b) horizontal lines – SEM data

(c) vertical lines – X–ray microscopy data

(d) vertical lines – SEM data

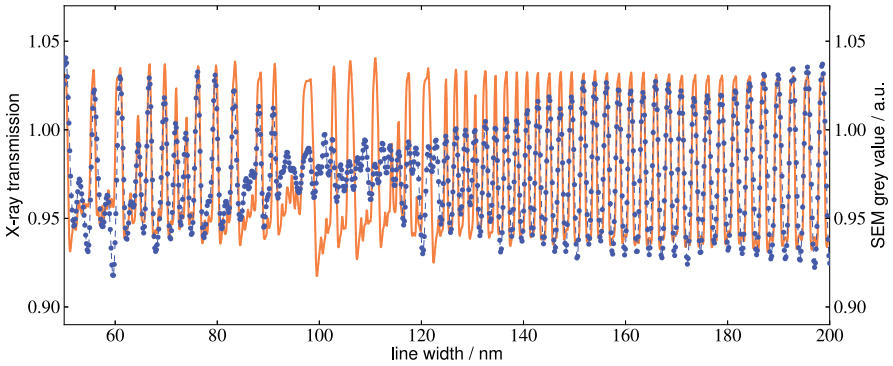

(e) vertical lines – X–ray data in blue, SEM gray value marked in orange

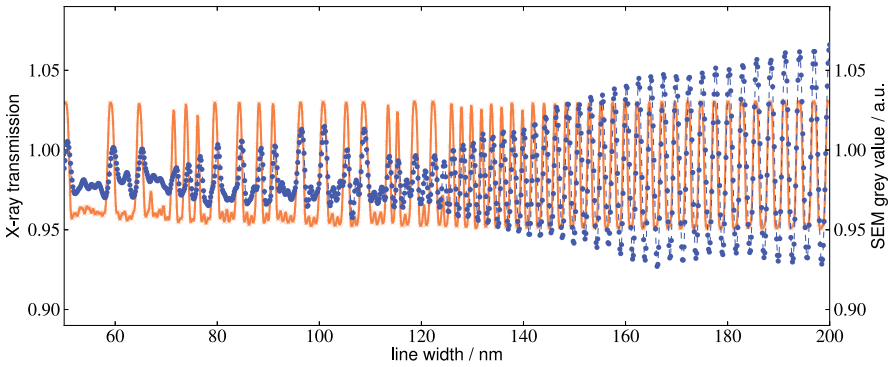

(f) horizontal lines – X–ray data in blue, SEM gray value marked in orange

Figure 6.35: X–ray microscopy images of line structures—measured at 30 keV—and SEM images for comparison for both horizontal and vertical lines. The nominal line width increases from 50 nm at the left to 200 nm at the right. The plots show that a good match is achieved between X–ray data and the SEM profile for the complete range down to 50 nm. Note that the SEM gray value does not give scaled data for height or thickness, but shows that the overall structure shape can be very well reproduced with the X–ray microscope.

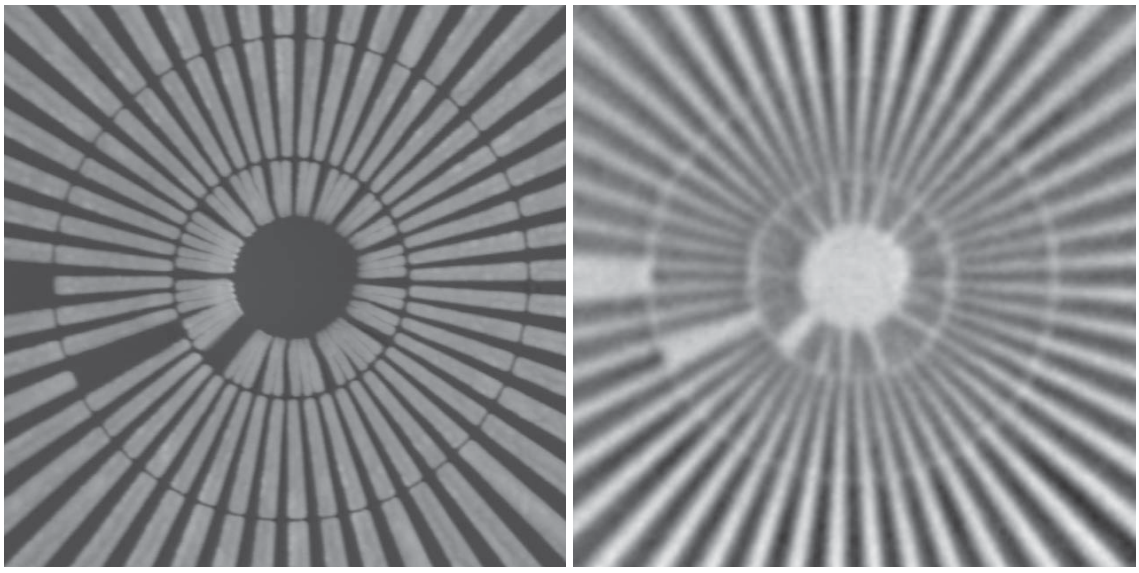

(a) SEM image of the Siemens star center **(b)** XRM image of Siemens star at $E = 17.4\,\text{keV}$

Figure 6.36: The center of the Siemens star on the test pattern. The line widths are $50 - 100\,\text{nm}$ in the innermost circle and $100 - 200\,\text{nm}$ in the second circle. The Siemens star also indicates a resolution of a little below 100 nm.

by the condenser geometry—is $\alpha = 400\,\mu\text{rad}$. At this α, the reflectivity of gold is still at $R = 0.93$ (calculated for $E = 30\,\text{keV}$, surface roughness 5 nm RMS) and increases to $R = 1$ with $\alpha \to 0$. This is a problem specific to the test pattern but explains the transmission values in Figure 6.35. Due to the high energy and low thickness ($t = 500\,\text{nm}$), absorption is very small with a theoretical transmission of $T = 0.97$ at $E = 30\,\text{keV}$ and $T = 0.90$ at $E = 17.4\,\text{keV}$ for the gold structures. Surface reflections on the structures explain both the intensity larger than 1 for the inter–line spaces and the reduced transmission of below $T = 0.97$ for the line structures. The average transmission if $T_{avg,\,hor} = 0.987$ and $T_{avg,\,vert} = 0.984$ for horizontal and vertical directions, respectively. This is in very good agreement with $T_{avg,\,theo} = 0.985$ for these line/space structures.

Even though the condenser should destroy most of the beam coherence, phase effects cannot be excluded either. Phase effects from edges would create oscillations, as shown in Figure 6.33 for the cone–beam setup. A strong indicator of these effects being phase effects is the fact that the amplitude of the oscillations increases with larger distances between the structures. In the case of pure wall reflections, the distance between the structures should make no difference whatsoever, because the structure spacing is sufficiently large if compared with the beam incidence angles.

As mentioned above, the thinner structures on the test pattern show some damage. Nonetheless, the structures as seem in the SEM can be seen in the X–ray microscopy setup as well, although with a limited resolution. Figure 6.37 shows images of line fields. The pattern structure, as seen in the SEM, can be well resolved with the X–ray microscope. The limit in resolution is around 90 nm, as these lines can be resolved—where separated. The Siemens star, shown in Figure 6.36,

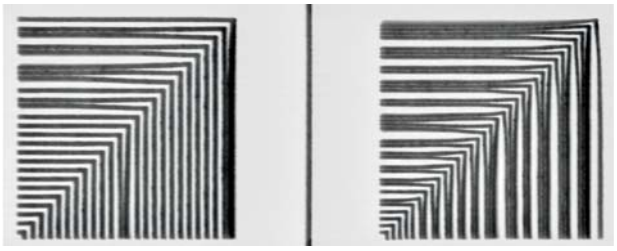

(a) SEM image of line fields

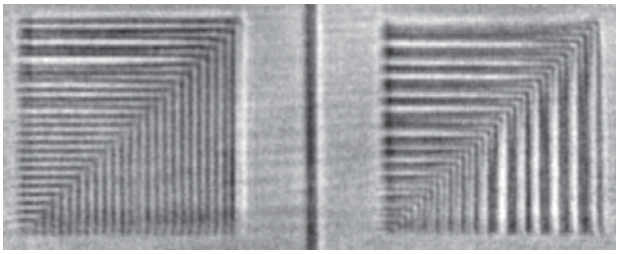

(b) XRM image of line fields at $E = 30\,\mathrm{keV}$

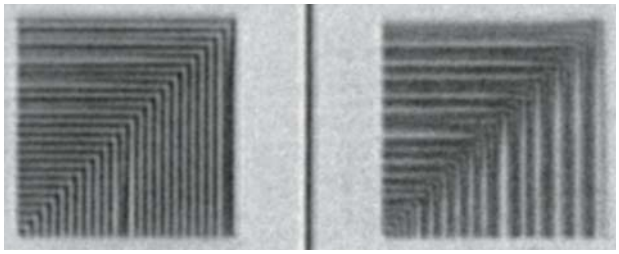

(c) XRM image of line fields at $E = 17.4\,\mathrm{keV}$

Figure 6.37: Images of line fields with 120 nm (left) and 90 nm (right) line and space structures. The SEM image is shown for comparison of the structures. The spacing of 120 nm is resolved very well and single structures in the 90 nm–field are visible at the 90–degree bend in the X–ray microscopy images.

confirms this resolution limit of below 100 nm.

The limit in resolution is still about a factor of two off the theoretical limit of the optics. Improving the resolution towards the theoretical limit of the optics is possible by optimizations in the mechanical stability of the experiment and in the mounting of the optics as well as improvements in the LIGA fabrication process.

6.6 Nanotomography

The first challenge for a successful nanotomography is the sample preparation. Because of the limited sample size with diameters below 100 µm, most mechanical preparation methods are not suitable. All samples which have been investigated at the P05 nanotomography endstation have been prepared with a Zeiss AURIGA Crossbeam FIB in Geesthacht, courtesy of Daniel Laipple [68]. Furthermore, these samples are mounted on the sample holder using a FIB as well. This is done by depositing platinum at the joining point. During the first measurements with such samples, a tipping of the sample over time showed up which prohibited the acquisition of a complete nanotomography measurement. Repeatedly moving the sample in and out of the beam, as required for reference images, strains the binding over the elastic limit and leads to plastic deformations and corresponding tilting of the sample. This problem could be solved by applying more platinum on the binding point and strengthening the bond.

Nanotomography using the X–ray microscopy setup has been successfully performed on two inorganic samples: A photonic glass sample which is made up of ceramic spherical particles and a

nanoporous gold sample infiltrated by polymer.

A robust sample holder and a strong sample mount are absolutely required for a nanotomography. However, due to the high flux on the sample, radiation stability of the sample is an important issue as well. So far, only the data of the ceramics sample could be reconstructed successfully.

6.6.1 Nanoporous gold sample – Radiation stability

Radiation damage is a well–known problem for many materials—especially soft matter—if X–ray measurements are performed on these materials. X–ray photons may break chemical bonds or produce free radicals that can diffuse in the sample and destroy the inner structure if they chemically react. Furthermore, gas can be produced within the material. These effects are typically non–linear and only occur above a material–specific threshold.

Even at the standard beamline flux at P05, many samples already show radiation damage effects in the micro tomography. In the microscopy setup with a condenser lens, the X-ray flux on the sample is increased by a factor of up to 30× compared to the normal flux without X–ray optics. Therefore, the radiation stability of each sample needs to be considered. While the limited amount of beamtime does not allow a systematic investigation of this effect, many problems can be attributed to radiation damage as the samples change during the measurement.

The nanoporous gold sample was infiltrated by a polymer for stabilizing the structure during preparation and transport. Figure 6.38 shows an SEM image of the sample after milling the sample in the FIB. The sample shape is a very well defined cylinder with straight walls. After several hours of X–ray illumination, the straight cylinder is bent. Figure 6.39 shows a radiograph of the deformed sample.

During all measurements, images at sample rotation settings of $\theta = 0°$ and $\theta = 90°$ have been acquired every forty angular steps, in addition to the sample images and references. For a static sample, these images should all be similar, except for noise. If a sample moves over time, the movement shows in these images as well. For the nanoporous gold sample, a strong movement could be observed. Because of the well–defined sidewalls of the sample, the sidewall orientation could be used to determine the sample orientation. The resulting time–dependent curves are given in Figure 6.40. The sample orientation changes by several degrees throughout one measurement. The condenser illumination is inhomogeneous over the field of view (compare Section 6.2.2) and the intensity is higher on the sample's left side. Furthermore, the sample has been rotated during the measurement by one half–circle. These two effects can qualitatively explain why the sample tilts over time. Because of the tilting effects, it was not possible to reconstruct this sample but the effect of radiation damage on a polymer–infiltrated sample could be observed and the information can be used in upcoming experiments.

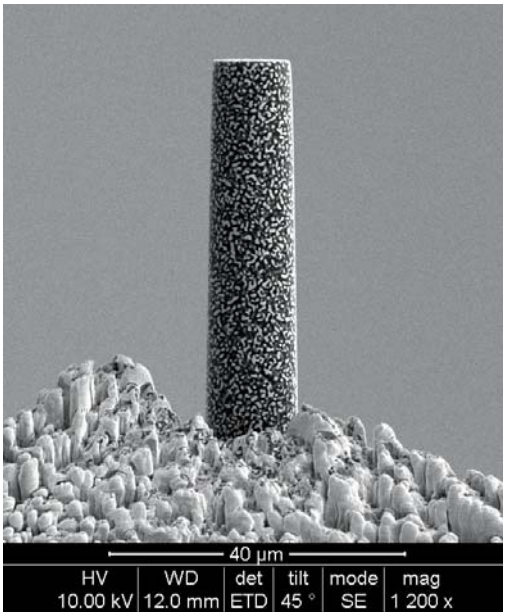

Figure 6.38: SEM image of the prepared pillar of nanoporous gold. The sample cylinder has a very high contrast in the SEM because the precursor material was infiltrated with a polymer for stabilization.

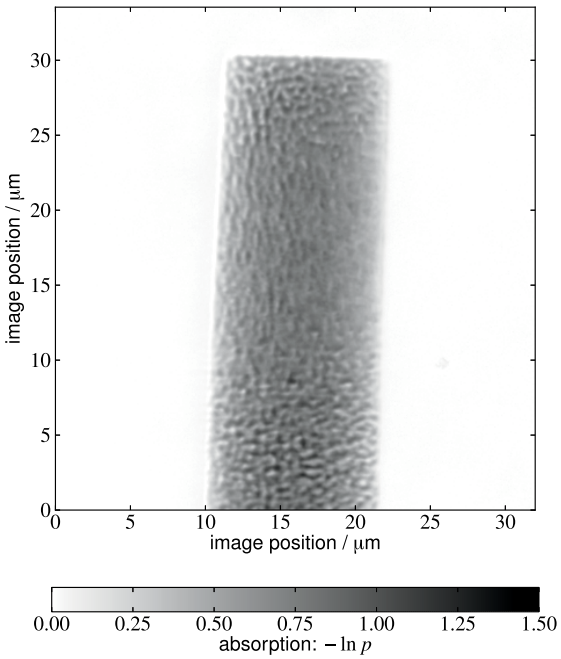

Figure 6.39: X–ray radiograph of the top of nanoporous gold sample. At the time of the image, the sample has been irradiated for several hours and a bending of the sample could be observed.

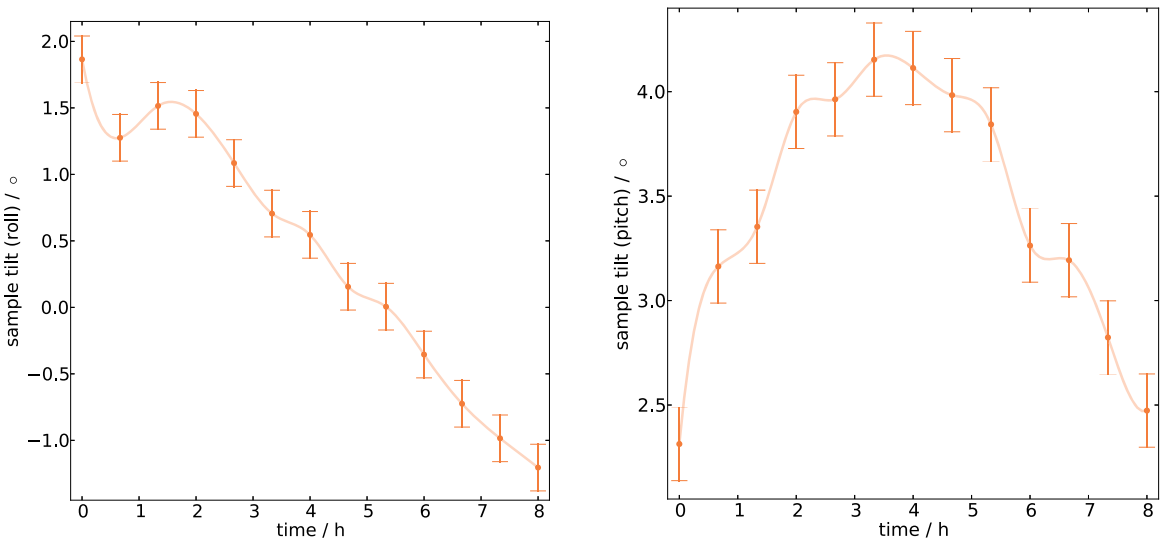

(a) sample roll **(b)** sample pitch

Figure 6.40: Measured sample orientation during a nano tomographic measurement. Orientation references have been acquired every 40^{th} image and the data points marked by the circles. A cubic spline interpolation is shown in light orange. The behavior in *Rx* and *Ry* directions is very different. Whereas the sample roll—shown in **(a)**—follows a very linear drift, the roll—shown in **(b)**—is highly nonlinear.

6.6.2 Photonic glass sample

The photonic glass sample which has been measured in the scope of this work originates from the SFB986 *Tailor–Made Multi–Scale Material Systems — M^3*. Photonic applications stable at high temperatures are one of the topics in the SFB986. Many technical applications require high temperatures, for example turbine and motor parts. The efficiency of gas turbines can be increased by raising the temperature. However, the temperature limit is defined by the materials used. Applying a thermal barrier coating which reflects thermal radiation (infrared), the working temperature can be increased without increasing the temperature of critical components.

Photonic glasses are a relatively novel material class for photonic applications [36, 37, 145]. Like photonic crystals, they consist of particles—in most cases spheres—with diameters of the order of the wavelength of light. Both direct and inverted structures work as photonic glasses: In direct structures, the ceramic particles themselves form the disordered photonic glass structures. In inverted structures, the matrix is created of polymer particles. The interstice is infiltrated by metals or oxides and the polymer particles are burned away, leaving only the inverted matrix.

One of the interesting properties of photonic glasses—which is also exploited in the use as thermal barrier coating—, is the broadband diffuse reflectivity: The absorption in the material is close to zero over a broad range of wavelengths and reflection is not directed but the reflected light is diffusely scattered in the hemisphere above the material [24, 65, 71].

Contrary to ordered photonic crystals, photonic glasses are disoriented structures in which the

particles are completely randomized in their position, except for the fact that they still form a connected network, i.e. the particles touch each other. The efficiency of the photonic structures is strongly dependent on their quality. Optical properties of photonic crystals suffer with increasing defect concentrations. For photonic glasses, local short–range ordering leads to increased absorption and hence reduced diffuse reflectivity. The effect on the photonic properties is stronger the larger the deviation from the perfect order, irrespective of the type of ordering (periodic or random). The fabrication of structures with a perfect disorder is as difficult as the fabrication of defect–free ordered systems. Photonic glasses are commonly assembled from colloidal suspensions and there are very few parameters which influence the assembly.

Concepts similar to the aforementioned photonic structures are also used in nature. Photonic crystals are used as iridescent colors [116, 140, 144] by butterflies, birds, and even some plants. Similarly, disordered photonic structures are used as broadband reflectors in the visible spectrum [78, 139], and the nanofibrillar structures with a thickness of only $d = 5\,\mu\text{m}$ give a whiteness and brightness impression similar to white paper.

Sample information

The sample consists of zirconium oxide spherical particles. These particles are synthesized from solution using a modified version of the Yan method [147] from a percursor solution supplied by Sigma–Aldrich. Primary ZrO_2 nanoparticles form in solution and these particles aggregate to microparticles. The size of the newly formed microparticles can be controlled by the ageing time in solution [147]. The solution was centrifuged for separating the particles. After filtering the solution and washing the particles, these were pre–calcinated in two steps at $T_1 = 120\,^\circ\text{C}$ and $T_2 = 450\,^\circ\text{C}$ for 3 hours each. The size of the resulting ZrO_2 particles used for this sample was $d = 2.05 \pm 0.11\,\mu\text{m}$ [23, 72].

For preparing the photonic glass, the pre-calcinated zirconia spheres were resuspended in an ethylene glycol solution. The solution was ultrasonicated for homogenizing the particle distribution in solution. A hydrophilic soda–lime glass was used as sample substrate and the side walls were defined by a silicon ring. The solution was drop–cast on the substrate and the sample has been heated to $T = 150\,^\circ\text{C}$ to evaporate the solvent from the solution. Varying the sample thickness is performed by changing the amount of solution cast into the area defined by the silicon ring. After evaporating the solvent, the layers were calcinated at $T = 600\,^\circ\text{C}$ for two hours.

The drop–casting resulted in a thin layer of randomly arranged particles with a thickness of $d \approx 35\,\mu\text{m}$. Because the contact area between the spheres is very small and no strong binding forces act between these, the overall stability of the coating is insufficient for handling and sample preparation. For stabilizing the coating, a low–viscosity epoxy glue has been used to infiltrate the sample and to fix the spheres in their respective positions. Using a FIB, a pillar of approximately

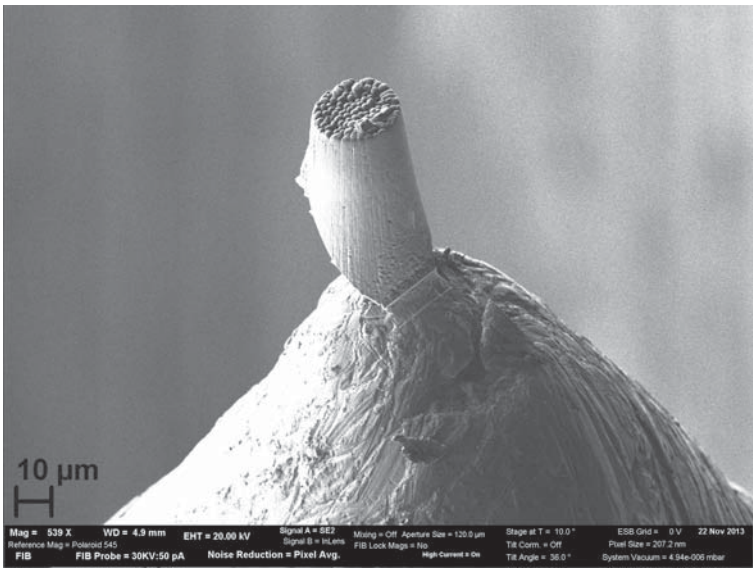

Figure 6.41: SEM image of the ZrO_2 sample after preparation with the FIB and mounted on the sample holder. [67]

30 µm diameter has been prepared from the sample [67]. Figure 6.41 shows an SEM image of the prepared sample. The sample has been attached on a standard P05 sample holder using the cold soldering option of the FIB workstation.

Measurement parameters

The nanotomography was performed at an X–ray energy of $E = 17.4\,\text{keV}$. The monochromator was optimized for highest flux without a pitch detune, because a condenser which blocks the direct beam has been used (compare Section 6.1.2). A rolled prism lens (design 10–866W–00B) with a working distance of 1.2 m and an illuminated field of view of $60 \times 60\,\mu\text{m}^2$ has been used as a condenser. With a diameter of $d = 1.8\,\text{mm}$ and the working distance of 1.2 m, the angular divergence in the illumination is

$$\alpha = \frac{0.9}{1200} = 7.5 \cdot 10^{-4},$$

thus slightly larger than the angular acceptance of the objective lens $\alpha_{obj} = 4.7 \cdot 10^{-4}$. This illumination is sufficiently divergent to use the full numerical aperture of the objective lens, i.e. to achieve the best possible resolution. Because the condenser optics creates a highly structured background, a diffuser has been installed in front of the sample position at a distance of $\Delta = 0.15\,\text{m}$ from the sample. The diffuser is a rotating piece of paper and the small angle scattering on the fibers smoothes the structured background [51]. Figure 6.42 shows the effect on the background illumination.

A lens from the design 1231_00_A0, #3 has been used as objective lens. The working distance was $b \approx 90\,\text{mm}$ and the lens–to–detector distance was $g \approx 2.20\,\text{m}$. A PCO 4000 detector with a

(a) direct image **(b)** diffuser installed

Figure 6.42: Effect of the diffuser on the background illumination: Both (a) and (b) are seen through the objective lens, in (b) the diffuser is installed. Using the diffuser, details in the illumination are completely removed and only a flat illumination remains. The images are grayscale with an arbitrary scaling.

pixel size of $d_{px} = 9.0\,\mu\text{m}$ has been used with a $M = 20\times$ infinity–corrected microscope objective and a $M = 1\times$ tube lens. These optics achieve an effective pixel size of 442 nm and a measured resolution of 1.6 µm could be achieved. A test structure has been used for determining the detector resolution. Note, however, that the structure had to be mounted around 50 mm in front of the scintillator, introducing strong phase effects. From previous experiments with the same scintillator, optics and detector, the resolution is expected to be below 1 µm. The measured effective magnification from the light optics is $M_{det} = 20.36$.

The scintillator used in this setup was a LSO (cerium–doped lutetium oxyorthosilicate) crystal with a thickness $t = 16\,\mu\text{m}$ mounted on a 100 µm thick glass substrate.

The effective pixel size and magnification in the X–ray microscopy setup could be determined by using a test structure. A measurement of the projected pixel size yields $d_{px} = 17.2\,\text{nm}$. The overall magnification is thus $M_{total} = 9.0/0.0172 = 523.3$. The magnification from the X–ray optics alone is correspondingly $M_{X-ray} = 523.3/20.36 = 25.7$.

A total of 900 angular projections have been acquired with an exposure time of $t = 30\,\text{s}$ each. A reference image has been taken every other image. In addition, projections at $\theta = 0°$ and $\theta = 90°$ have been taken every 40^{th} angular step to control the sample stability throughout the measurement. The overall measurement time for this sample was 17 hours.

Image correlation

The individual images of the measurement are corrected for the camera dark current by subtracting a dark image. The PETRA III beam current is logged and integration over the exposure time yields an average beam current value for each image—both for sample images and references. This beam intensity value has been used for intensity–normalization of all sample projections and reference images.

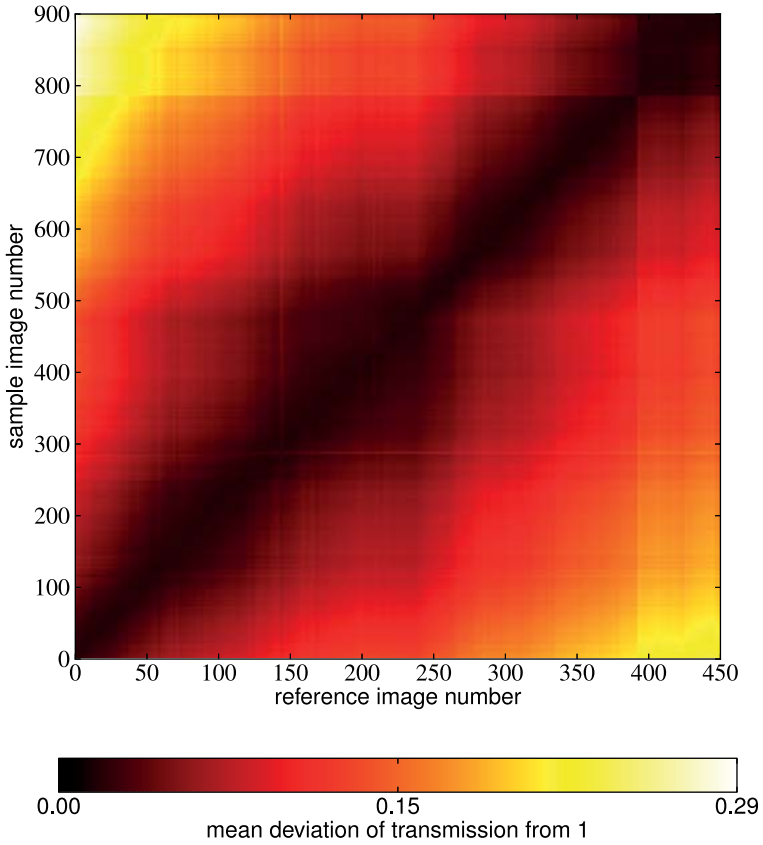

Figure 6.43: Map of reference and sample image correlation. The signal shows in the plot is the average deviation from 1 for the angular projection divided by the reference image. The general trend is strongly time–dependent with the best match very close to the diagonal.

For selecting the best–matching reference to each angular projection, the dark current corrected reference and sample images are compared. An image region which is never shadowed by the sample was chosen and the sample projection was divided by the reference image. Ideally, the resulting image has a uniform transmission of $T = 1$. Variations in the beam profile, beam position, and drift of components may change the beam position in the image over time. Comparing each reference image with each sample image allows selecting the best matching reference image for each sample projection. Figure 6.43 shows the resulting map of all image correlations. The time–dependence is the strongest influence, yielding a general trend of the best correlations being found at short times between images. This shows in the matching close to the diagonal. Figure 6.44 shows the indices of the best matches and confirms these findings.

Dividing each sample projection by the best–matching reference image yields attenuation images. The resulting image gives a measure of the attenuation according to Lambert–Beer's law (see Equations 2.9 and 2.10). For a tomographic reconstruction, the integral over the linear attenuation coefficient $\mu(x)$ is required as described in Section 3.3.1. The absorption image a, defined as

$$a = -\ln\left(\frac{i_{norm}}{r_{norm}}\right) \tag{6.20}$$

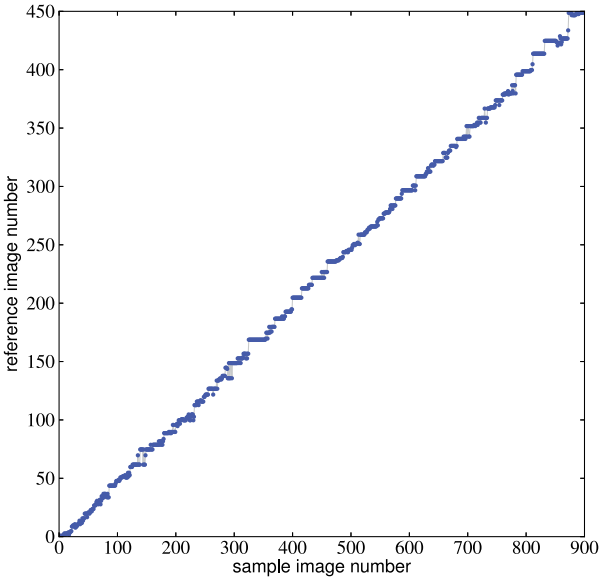

Figure 6.44: Indices of best matches in the correlation between sample and reference images.

with the normalized sample i_{norm} and absorption r_{norm} images, is equivalent to the projection $p_\theta(t)$, i.e. it corresponds to

$$a(x,z) = \int_0^d \mu\,(x,y,z))\,dy. \tag{6.21}$$

Figure 6.45 shows an absorption image of the sample. The effects of the sample preparation using a FIB are obvious by some platinum deposition on top and at the lower cut. The inner structures in the sample—spherical particles—can be seen as well.

As already discussed in the Sections about thermal drift (compare Section 5.2.6) and short–term stability (compare Section 6.1.3), the beam position and the mechanics are not completely stable over time. The sample position in the absorption images moves both in the horizontal and in the vertical directions. The effect is very severe and the most extreme variations are in the range of 1 µm. These movements need to be corrected before a reconstruction can be tested.

The correlation of the vertical position can performed using the definition of the projection $p_\theta(t,z)$. At any z_0, it is:

$$p_\theta(t,z_0) = \int_{-\infty}^{\infty}\int_{-\infty}^{\infty} \mu(x,y,z_0)\,\delta(x\cos\theta + y\sin\theta - t)\,dx\,dy. \tag{6.22}$$

We know that $\mu(x,y,z) \neq 0$ only for $x \in [-x_0, x_0],\ y \in [-y_0, y_0]$, with $x_0,\ y_0$ defined by the sample outer dimensions. Because of this fact, the integration in x and y can be limited to the intervals

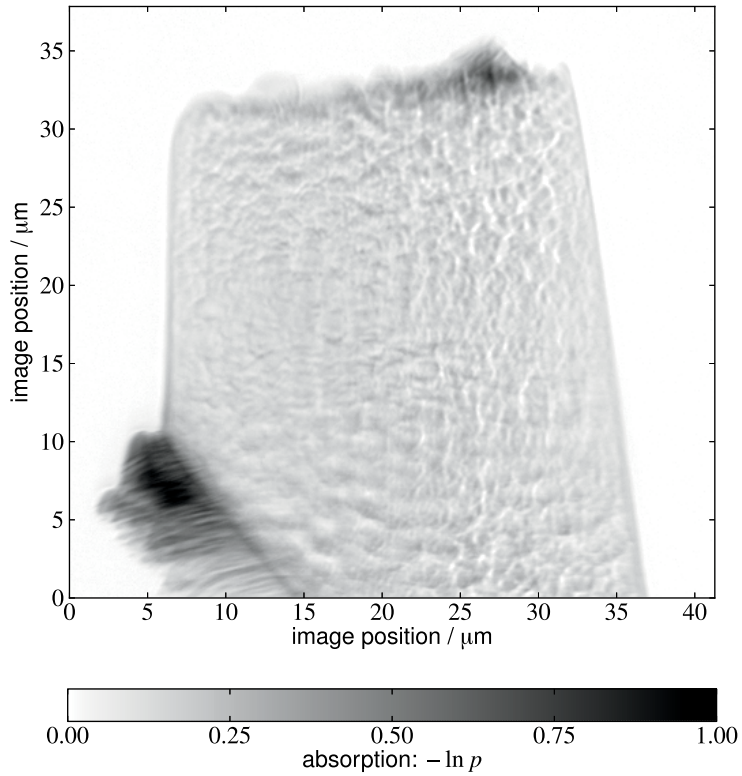

Figure 6.45: Projection of the ZrO_2 sample. The image is an absorption image, i.e. the image divided by the reference image and the scaling is logarithmic (compare Equation 6.20). Note the structures in the lower left corner which are an effect of the sample preparation with the FIB.

given above. Furthermore, consider an integration of $p_\theta(t, z_0)$ over t:

$$\begin{aligned} A(z_0,\, \theta) &= \int_{-\infty}^{\infty} p_\theta(t, z_0)\, dt \\ &= \int_{-\infty}^{\infty} \int_{-x_0}^{x_0} \int_{-y_0}^{y_0} \mu(x, y, z_0)\, \delta(x\cos\theta + y\sin\theta - t)\, dy\, dx\, dt \\ &= \int_{-x_0}^{x_0} \int_{-y_0}^{y_0} \mu(x, y, z_0) \int_{-\infty}^{\infty} \delta(x\cos\theta + y\sin\theta - t)\, dt\, dy\, dx \\ &= \int_{-x_0}^{x_0} \int_{-y_0}^{y_0} \mu(x, y, z_0)\, dy\, dx = A(z_0). \end{aligned} \tag{6.23}$$

The integral over $p_\theta(t, z_0)$ is a constant value $A(z_0)$ for all angular positions θ. For the case of discrete detector pixels, the sum of all absorption values in a detector row z_0 is constant. This relationship can be used to shift the images until their corresponding height profiles match. Figure 6.46 shows the result in the profiles obtained by an automatic height correction based on the $A(z_0)$ from Equation 6.23. Both the data shown in the figure and looking at the shifted projection images confirm that the height correction works. Because of the good statistics—all pixels in each row are summed up—, the result is very precise and no further processing is needed for the height correlation.

Correcting height drifts is also very important for the correction of horizontal movements. The

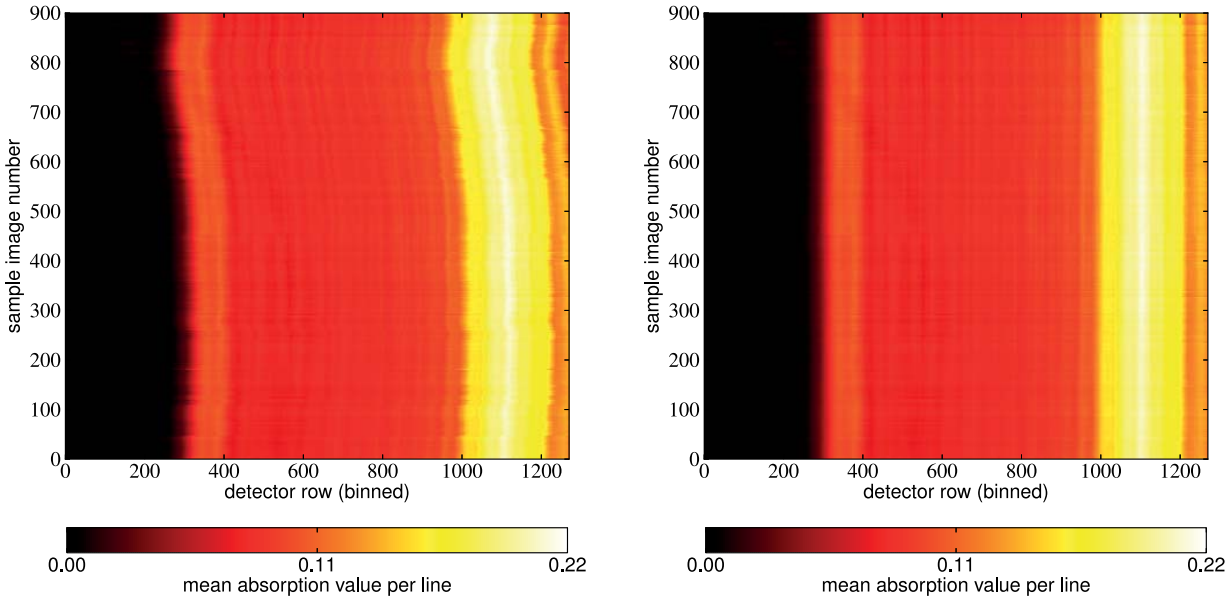

(a) raw data **(b)** correlated and shifted data

Figure 6.46: Correlation of height profiles to correct for vertical drifts of the sample. The x–axis in the image corresponds to the detector rows (i.e. heights z_i) and the different rotational steps are the different image numbers on the y–axis. The values $A(z_i)$ (compare Equation 6.23) are depicted by the color–coding. In a stable setup, each detector row shows a constant value. Because of the drift, the sample position varies over the rotation steps / image numbers (see **(a)**). By shifting the images in z–direction, the sample drift can be countered and constant values $A(z_i)$ for each row can be achieved.

center of mass of the sample is a fixed point in the sample. Using the absorption value $\mu(x, y, z)$ instead of the mass density $\rho(x, y, z)$, a similar value can be calculated and used. In most cases, this center of absorption is not directly centered on the axis of rotation, and it follows on a circular trajectory around the center of rotation. In the projection geometry of the detector, the center of absorption follows a sine curve. Using the detector coordinates (t, z), a center of absorption can be calculated for each detector row z_i. A comparison and position tracking is only viable if a sample slice at the same height is used in the calculation. Hence, a correction of height shifts is necessary. To further increase the statistics, a sum over several detector rows can be performed. The resulting value

$$C_{abs}(\theta) = \int_{z_0}^{z_1} \int_{0}^{n_{pix}} t\,\mu(t, z)\,dt\,dz, \tag{6.24}$$

with n_{pix} the number of horizontal detector pixels and z_0, z_1 the z–boundaries of the sample in detector coordinates. The function $C_{abs}(\theta)$ should follow a sine curve with the rotation angle:

$$C_{abs}(\theta) \propto \sin(\theta + \delta), \tag{6.25}$$

using a phase offset δ. Figure 6.47 shows the center of absorption values $C_{abs}(\theta)$ for the ZrO_2 sample. On a global scale, the curve can be well approximated by a sine function. On a small

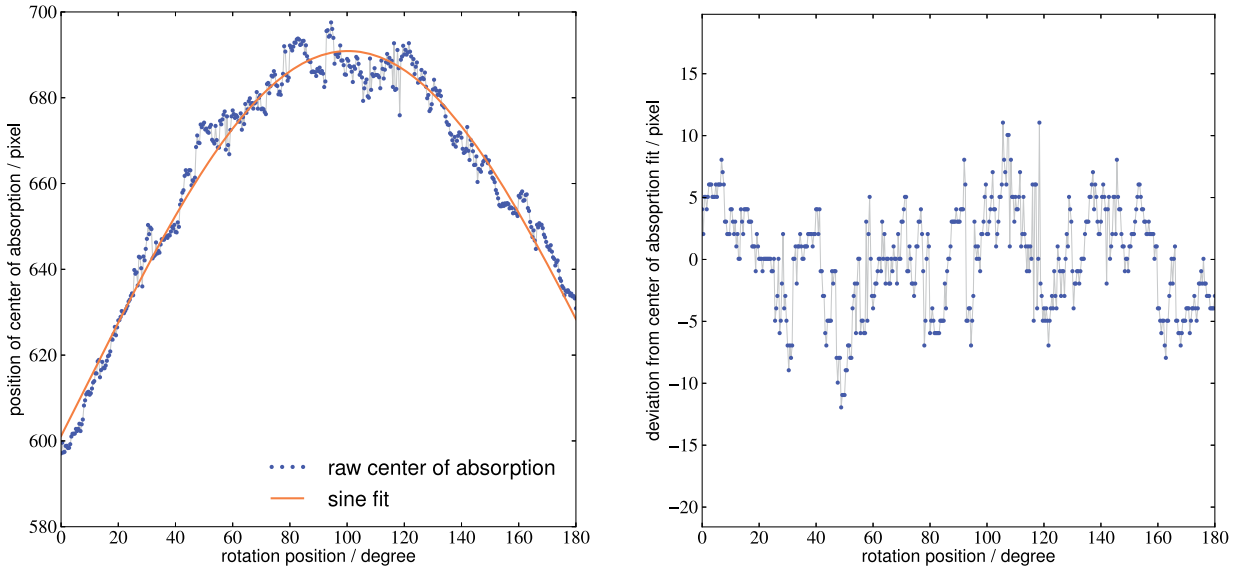

(a) center of absorption **(b)** deviation from sine fit

Figure 6.47: Horizontal sample position correction: Center of absorption calculations and sine fit. **(a)** shows that the center of mass roughly follows a sine curve, but there are still significant variations. **(b)** shows that the deviation from the fit is in the range of up to 10 pixels. The deviations from the sine curve can be used to correct the image position in the measurement.

scale, however, the deviations of $C_{abs}(\theta)$ from a smooth sine curve are as large as ten pixels and need to be corrected. Shifting the images according to the deviation of the data from the fit corrects for most of the horizontal positioning and drift errors. However, looking at consecutive, shifted absorption images, there are still horizontal jumps in the sample position. These need to be further corrected and the respective method will be discussed below.

If there are any deviations from a plain absorption image in the processed images—for example phase effects like edge enhancement—, the center of absorption will be influenced as well. While correcting for the center of absorption still significantly enhances the position stability, it is not yet sufficient in accuracy. Fine–tuning the position can be done by using the absorption profile of the sample. Figure 6.48 shows an exemplary horizontal absorption profile. Using the steep increase in the absorption value at the sides of the sample, it is possible to track the sample position.

For better statistics, it is necessary to average over several detector rows and accordingly, there is no hard boundary in the absorption values. Using thresholds at different absorption values of the curve, the positions of these thresholds can be tracked for each image.

While the sample shape should resemble a cylinder, the ion milling process also effects the sample shape: it is not ideally cylindrical but a truncated cone (compare Figures 6.41 and 6.45). Rotating this axially symmetric body, the projected shape is constant. Introducing an off–center mounting, the projected shape is still constant, but the position of the projection oscillates with a displacement amplitude which follows a sine curve. To allow for imperfections in sample shape

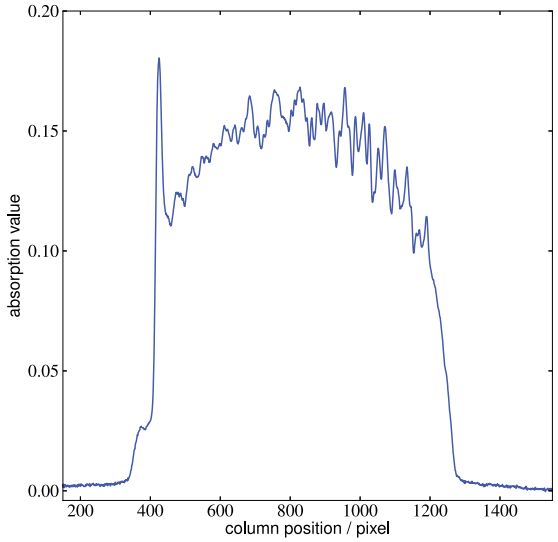

Figure 6.48: Horizontal absorption profile of the ZrO_2 sample, averaged over 500 detector rows. The outline of the sample is well defined by a strong increase in the local absorption. The small protrusion at the left is due to the strongly absorbing material deposited from the FIB sample preparation. Compare Figure 6.45, bottom left corner.

and anisotropies in the absorption, the sine should be replaced by a more general continuous function.

As mentioned above, the function which gives the threshold position against the rotation position should have a low curvature and follow the global movement of the threshold position. A low curvature is achieved by a low order–polynomial fit, whereas a low–order polynomial cannot generally approximate the global curve very well. The solution is a local fit: For each data point x_0, the data point interval of $[x_0 - 50,\ x_0 + 50]$ is used for fitting a 3rd–order polynomial function f_{x_0}. The function value at the position x_0,

$$y_{x_0} = f_{x_0}(x_0)$$

is used as the target position and the deviation of the threshold position from y_{x_0} is used as shift to correct the image position.

For enhanced statistics, a set of four threshold values has been used and the results have been averaged. Figure 6.49 shows the resulting shift from the threshold tracking. These shifts are a small correction to the overall position with a variance of $\sigma_{thresh} = 2.21$ pixels, whereas the center of absorption shift has a variance of $\sigma_{coa} = 4.13$ pixels. The center of absorption shift often seems to overestimate the necessary shifts, as the threshold shift mostly points in the opposite direction. This is backed by the fact that the overall correction, i.e. the sum of shifts from center of absorption and threshold fit has a smaller deviation from the original position than the center of absorption shift alone. The variance of the total shift is $\sigma_{total} = 3.44$ pixels.

Using the described corrections, the sample projections could be corrected to within an ac-

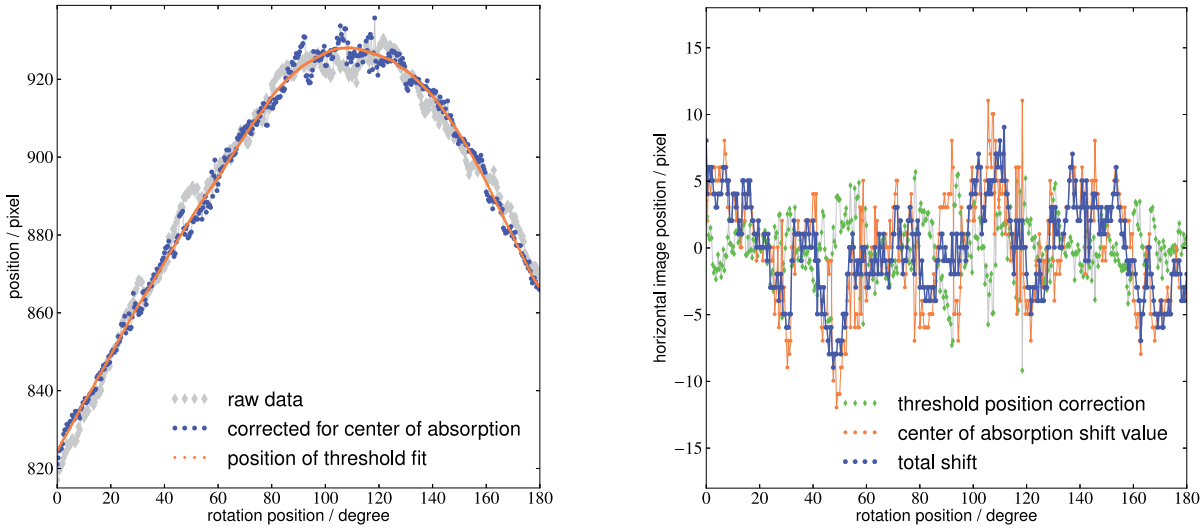

(a) threshold position **(b)** pixel shift

Figure 6.49: Results of thresholding used for horizontal image alignment. **(a)** shows a comparison of the sample position for raw data and corrected for center of absorption. The local fit of the threshold position follows a sine very closely, as expected, while the center of absorption fit still suffers from other effects that influence the result. **(b)** shows the necessary shift. The threshold position correction is smaller than the global shift introduced from the center of absorption.

curacy of 1 pixel. These corrected data could be used in the reconstruction pipeline to create a three–dimensional dataset. An overview of the complete correction routines is given in Figure 6.50.

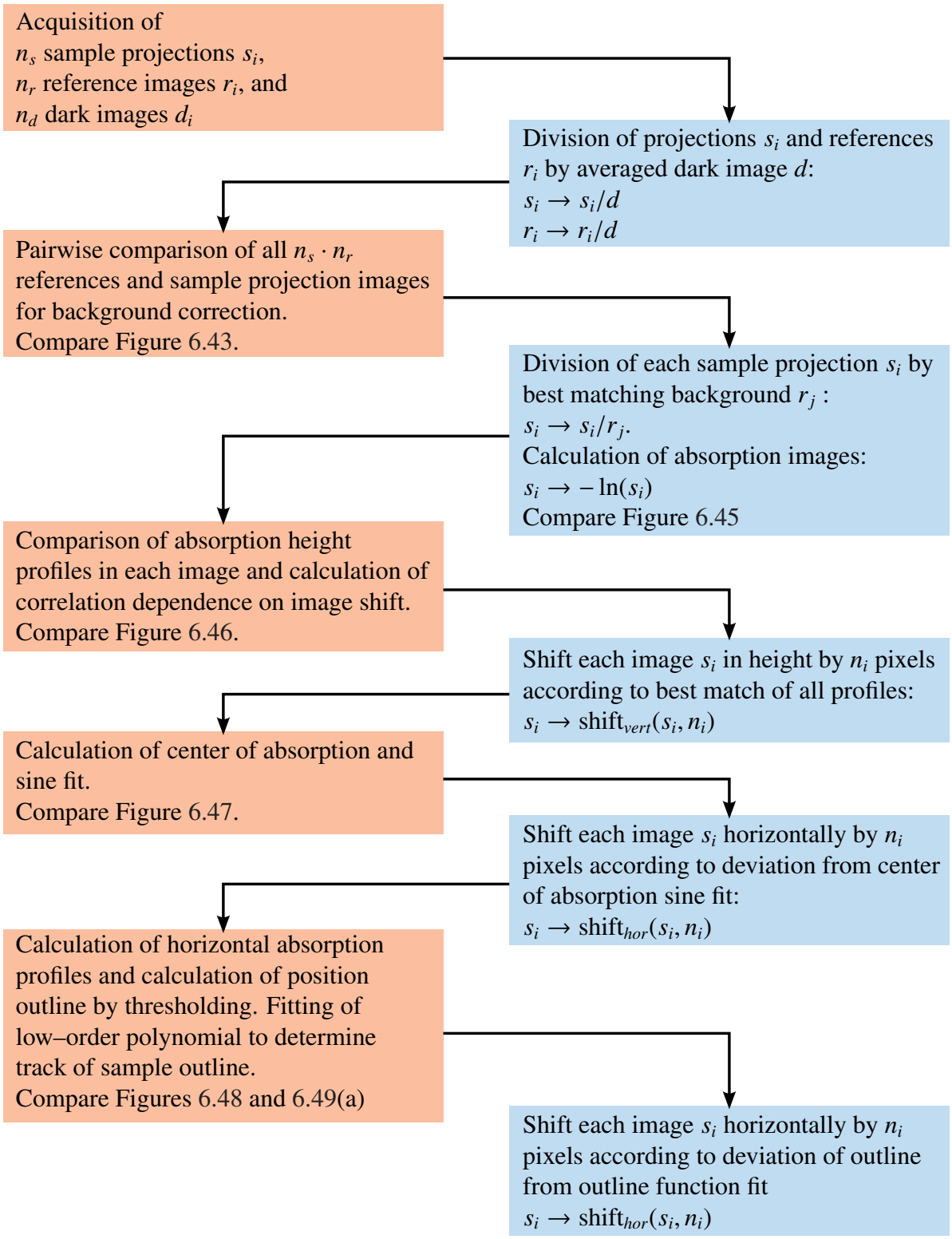

Figure 6.50: Flow diagram of the individual processing steps for the image position correction. General calculation and comparisons are shown on the left side with an orange underlay; image processing is shown right with a blue underlay.

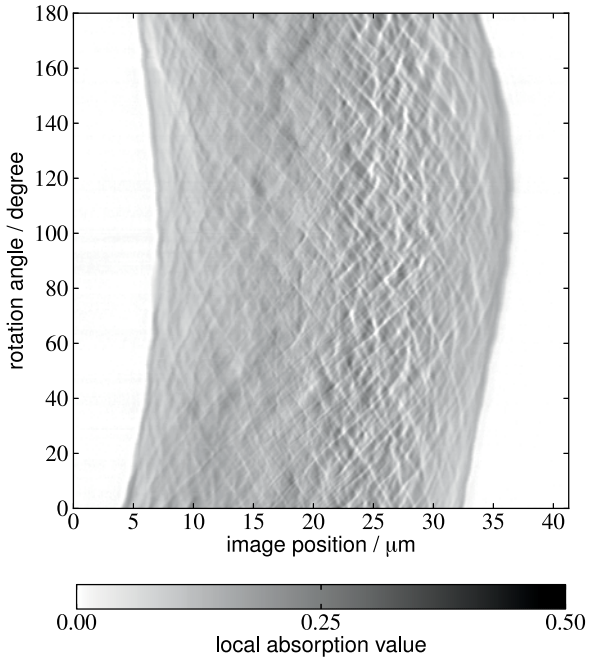

Figure 6.51: Exemplary sinogram from the ZrO_2 sample. The contrast in the left half of the image seems to be reduced. Because the position of the contrast reduction is stationary in the image, it can be pinned on the X–ray optics and is not a feature from the sample.

Reconstruction

The images shifted by the methods mentioned above can be rearranged to sinograms for a tomographic reconstruction. A sample slice is shown in Figure 6.51. The right side of the sinogram is very sharp and distinct features can be tracked in the sinogram, while the left side's contrast is significantly reduced. Although differences in the contrast can already be seen in individual projections, the systematic effect is only visible in the sinogram where the sample position varies but the optics position is stationary.

Using a filtered backprojection algorithm, the sample has been reconstructed from the sinograms. The contrast problems in the optics necessarily reduce the achievable resolution and density contrast, but still allow a reconstruction. Exemplary slices of the sample are shown in Figure 6.52. The general shape of the ZrO_2 spheres and their positions can be well resolved. There is some edge enhancement in the reconstructed data which is due to phase interference effects of the X–rays. This is a common problem for propagating coherent X–rays, but advances in the field of X–ray phase imaging will allow coping with these effects.
Using, for example, Paganin-like correction algorithms [101, 142], most phase effects can be suppressed or even completely eliminated. If phase effects are more severe, more complex algorithms based on transport of intensity need to be used [5]. Implementation of these algorithms goes beyond the scope of this work, but will be a necessity in the further development of the nanotomography experiment.

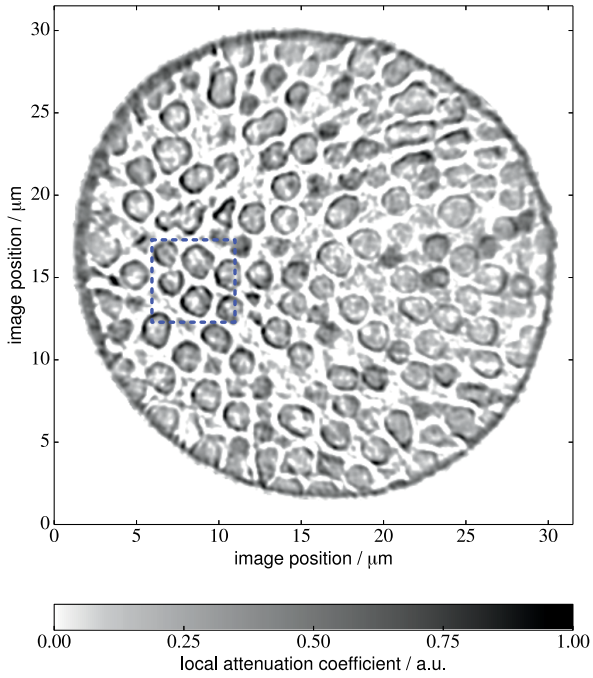

(a) *xy* slice of reconstructed volume

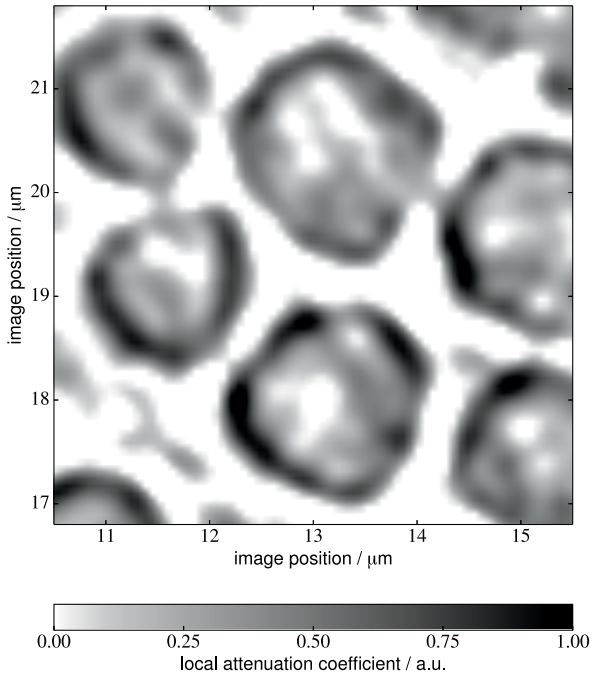

(b) zoom of marked region in **(a)**

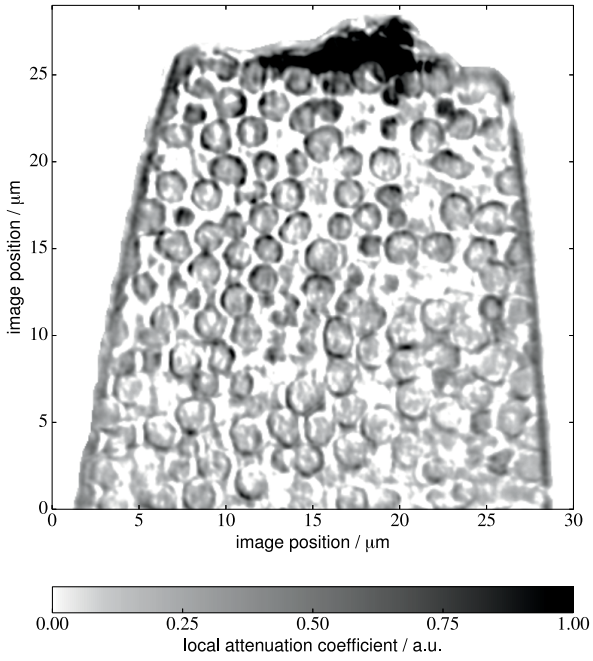

(c) *xz* slice of reconstructed volume

Figure 6.52: Reconstructed slices from the ZrO_2 sample. **(a)** shows a cut in the *xy*–plane, a zoom of the encircled region is shown in **(b)**. A slice in *xz*–direction is given in **(c)**. The cone–like shape of the sample and highly–absorbing platinum deposition on the top can be seen in this representation.

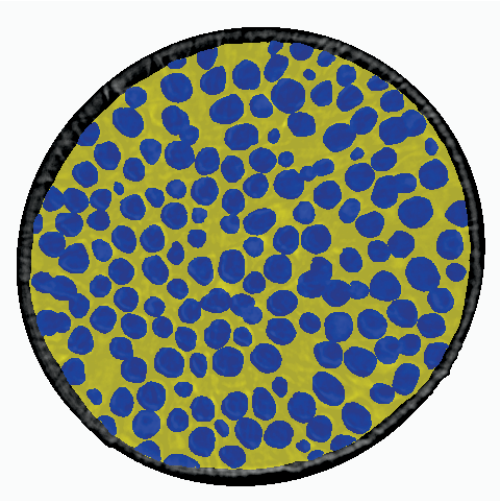

Figure 6.53: Example of a binarized slice. The particles are marked in blue and the voids are denoted in yellow. Because of the FIB redeposition at the sample outline (compare Figure 6.52), this area is ignored for the segmentation. The sample diameter is about 25 µm.

Analysis of packing fraction

The packing fraction η is defined as the ratio of particle volume to sampling volume. The scientific question for this photonic glass sample was the determination of the packing fraction η using the nanotomography reconstruction. In addition, the homogeneity of the sample and potential gradients in the packing density can be investigated.

The data quality of the reconstruction is not sufficient for an automatic segmentation. Therefore, several slices have been segmented manually. Figure 6.53 shows an exemplary binarized slice in which particles and voids have been separated.
Slices have been segmented at four different heights, with a distance of $\Delta h = 6.88\,\mu\text{m}$. At the upper three positions, three slices each have been segmented in a distance of $\Delta h_{local} = 206\,\text{nm}$. The bottommost position shows stronger fluctuations in η and seven slices have been segmented at this position with the same Δh_{local}. The segmented area values are given in Table 6.5 and the slice positions in the sample are shown in Figure 6.54. The uncertainty in the packing fraction is due to the manual segmentation. A test with repeated segmentations yielded a relative error of $\Delta \approx 1.5\,\%$.

At each height, the measurements of all slices have been used to determine an average packing fraction. Table 6.6 gives the resulting numbers. The packing fraction is very constant throughout the sample, but with a slight decrease at the top. Note, however, that the deviation from the global average of $\eta_{global} = 0.542$ is not significant.

For testing the feasibility of a FIB tomography on samples of this size, this sample has been sliced with a FIB after completing the nanotomography [67]. Figure 6.55 shows one of the resulting images. Cutting large cross–sections with a FIB is difficult and so–called curtaining artifact are visible in the lower part of the image. They show up as a rough, wavy surface. The position of

Slice number	packing fraction η	counting uncertainty
138	0.530	0.008
141	0.532	0.008
144	0.539	0.008
238	0.542	0.008
241	0.538	0.008
244	0.548	0.008
338	0.546	0.008
341	0.554	0.008
344	0.533	0.008
434	0.561	0.008
437	0.545	0.008
441	0.558	0.008
444	0.537	0.008
447	0.525	0.008
450	0.556	0.008
453	0.527	0.008

Table 6.5: Packing fraction of the spherical components at different segmentation positions.

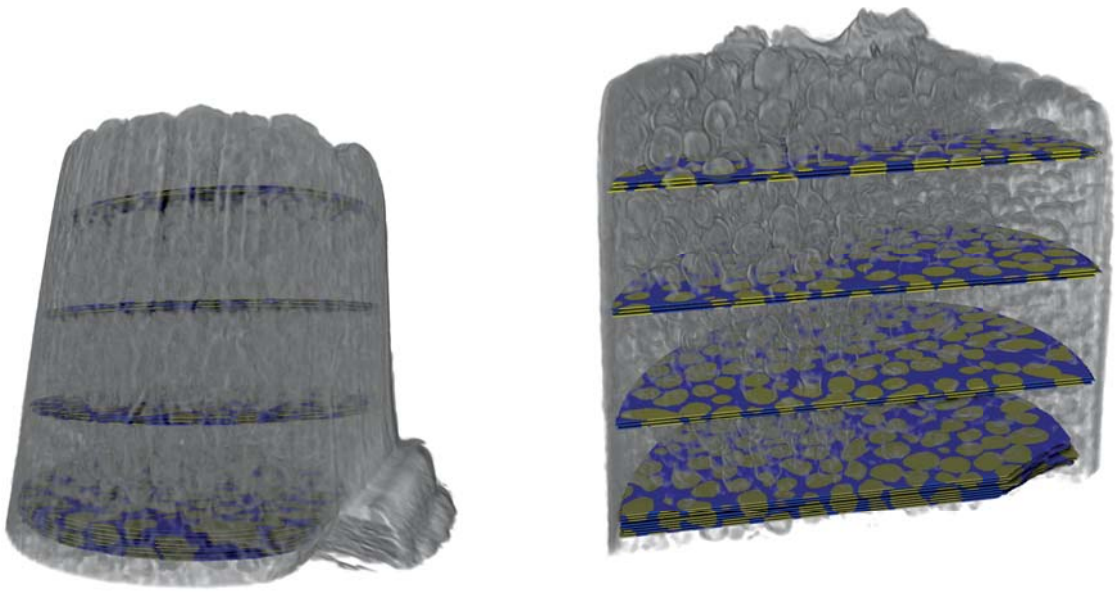

(a) **(b)**

Figure 6.54: 3D representations of the sample. The four segmented slices sets are shown in the 3D representation of the complete sample to estimate their positions. **(a)** shows the complete reconstructed volume, whereas **(b)** shows a representation with a cropping plane in the center of the sample. In both (a) and (b), the sample diameter is about 20 µm at the top and about 25 µm at the bottom.

position	average packing fraction η	uncertainty in packing fraction (95% confidence level)
140	0.534	0.009
240	0.542	0.009
340	0.544	0.009
440	0.544	0.006
global	0.542	0.005

Table 6.6: Average packing fractions at different sampling heights.

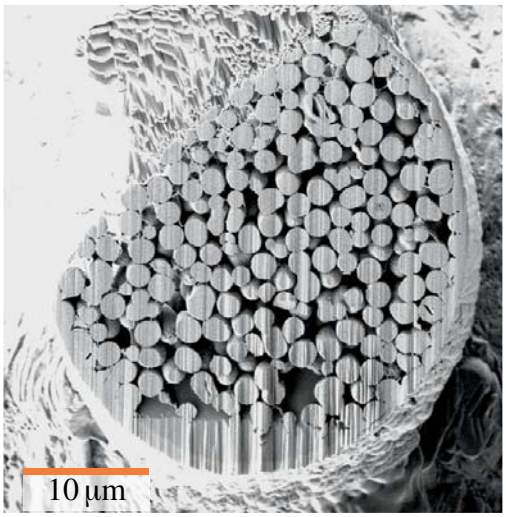

Figure 6.55: SEM image of the ZrO_2 photonic glass sample after FIB milling. The so–called curtaining effect of FIB milling is visible in the lower half of the image and leads to a wavy cutting surface [67].

the cut is slightly below the analyzed data around slice 500 in the sample system. The measured packing fraction $\eta_{FIB} = 0.562 \pm 0.008$ is slightly higher than the global average obtained from the nanotomography data. Note that the variation in η between individual slices is larger at the bottom of the sample and individual slices of the nanotomography measurement show values similar to η_{FIB}, giving a good agreement between the data.

A plot of the individual results for all slices and average values is given in Figure 6.56. While the overall packing fraction is constant throughout most of the sample and only drops towards the very top, the variations between individual slices become more pronounced at larger depths. It can be argued that this effect is be caused by the limited sample cross–section because averaging over several slices gives a very constant value for η. Nevertheless, the variations between individual slices become less pronounced towards the top of the sample. This is a hint of a more homogeneous particle distribution towards the sample top.

To achieve a stable structure without free particles, all particles need to keep a defined position. This state is called jammed and by definition, “a particle is jammed if it cannot be translated while fixing the positions of all of the other particles in the system” [135]. The investigated sample was mechanically stable, i.e. its particles have to be jammed. Therefore, the sample can only be compared to other jammed structures.

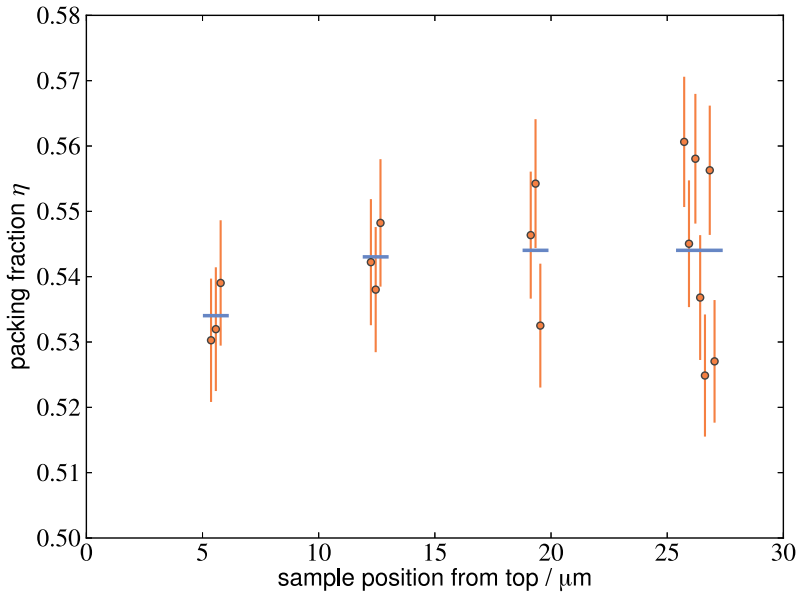

Figure 6.56: Plot of the packing fraction values η for the individual slices. The average for each position is marked in blue. The variations in individual slices become larger at a higher sample depth, whereas the average value stays constant. This can be an effect of the limited sampling volume in each slice, if a homogeneous packing is only achieved on larger scales with local variations.

The overall packing fraction $\eta_{global} = 0.542$ is significantly smaller than a random close packing (rcp) of $\eta_{rcp} \approx 0.64$ [33], which is the highest possible packing fraction for unordered spheres. In the literature, obtained values for random packing densities are dependent on the forces that act during packing [53, 135]. These forces are dominated by gravity, friction and elastic repulsion, but when particles in a solution are sedimenting, gravity is weakened by the buoyancy of the particles. Onoda and Liniger [100] experimentally found a connection between the packing density and acting forces, i.e. gravity, when sedimenting spheres from a solution. At ambient conditions ($g = g_0$), they found a packing fraction $\eta \approx 0.595$. In the limit of zero force, i.e. an equal mass density of particles and solution, an experimental limit of $\eta \approx 0.555 \pm 0.005$ was obtained. These numbers are in good agreement with the packing fraction obtained for the photonic glass sample obtained from a drop–cast solution.

Comparing the packing fraction of these random arrangements to ordered structures is of interest because the fabrication of photonic crystals and photonic glasses is very similar in its process. It is possible to create samples that show photonic crystalline behavior at one end and photonic glassy behavior at the other end of the sample [23]. Very small variations in the ordering and packing fraction can change the behavior from crystalline to glassy.

For example, a simple cubic organization gives a very similar packing fraction $\eta_{cubic} \approx 0.52$. Although it is possible to create ordered jammed arrangements with packing densities $\eta < 0.1$ [134], i.e. almost arbitrary low, these arrangements will not appear in self–organizing assembly. The densest ordered packing are hexagonal and face–centered cubic with $\eta_{fcc} \approx 0.740$. Starting

from a face–centered cubic packing and randomly removing individual spheres, the structure is stable until a critical packing fraction of $\eta \approx 0.52$ is reached. Such a structure could explain why ordered and disordered regions occur from the same starting conditions. Assume that an ordered first layer is formed onto which addition particles sediment. If the growth is too fast and leaves too many voids, the hexagonal structure will collapse and a random packing will occur. Otherwise, voids can be incorporated in a hexagonal packing and the sample behaves like a photonic crystal.

Conclusion

The X–ray microscopy setup at P05 has been successfully used to obtain a set of projection images from a photonic glass sample. Using image correlations and a–priori knowledge of the sample geometry, the X–ray microscopic projections could be normalized and aligned to allow a tomographic reconstruction using a filtered backprojection algorithm. While there are still artifacts like phase edge–enhancement in the reconstructed volume, the data could be used to successfully extract the volume packing fraction of the ZrO_2 particles.

Analyzing the sample at different heights, a very homogeneous packing fraction could be determined throughout the sample depth. The obtained packing fraction $\eta_{global} = 0.542 \pm 0.008$ is consistent with expected packing fraction for a force–free sedimentation of spherical particles. It is significantly smaller than a random close packing with $\eta_{rcp} \approx 0.64$ which has been assumed for this kind of sample. Using the corrected packing fraction, simulations of the photonic properties for this sample can be improved. If a sample with a higher packing fraction is required, the experimental procedure for the creation of these photonic glasses can be adapted, for example by using higher forces during sedimentation.

Chapter 7

Conclusion and outlook

Within the scope of this work, a successful nano tomography experiment was designed, implemented and performed. An optics concept for nano imaging at the PETRA III beamline P05 was developed—both for an X–ray microscopy and a cone–beam setup—, taking the framework of the beamline and the available space and distances into account. With a distance of only 65 m between source and experiment, the cone–beam setup requires a two–tiered setup to allow for a nanofocus at this relatively small distance to the source. The X–ray microscopy setup, however, is not strongly influenced by the comparably small source distance. The optics concept achieves resolutions of down to 100 nm using CRLs in both setups.

With the information on the required positions and accuracies from the optics, a concept for the mechanics was devised. This concept needed to be very flexible to be used for both setups and it had to comply with the spatial restraints in the experimental hutch. The resulting draft for the mechanics allows for a maximum of flexibility with the setup, including different magnification schemes, other X–ray optics, and potential new developments.

With the instrumentation installed, tests of all components were performed. The extent of higher harmonics in the beam was assessed and strategies for suppression were tested. It is critical for the cone–beam setup that no higher harmonics are present because these are focused at much larger distances. The geometrical setup—especially if using a two–tiered setup—enhances the relative contribution of higher harmonics and yields a net domination of these in the center of the field of view. In contrast, it is possible to eliminate the higher harmonics in the X–ray microscopy setup using a well–designed condenser and aperture slits in the experiment without requiring a suppression in the front–end: a central stop in the condenser absorbs all of the direct beam on the optical axis and off–axis points are masked by thick gold apertures.

Furthermore, the stability of the monochromator was investigated. While a long–term stability on the global level was achieved, the beam still suffers from high frequent vibrations. This problem could not be solved but is avoided by averaging over longer times. As typical exposure times for all

nano tomography experiments are in the range of at least several seconds, this constraint does not pose any severe limitations on the performance of the experiment. Installation of a large dedicated condenser is sufficient to eliminate these fluctuations.

In the framework of the VI–NXMM collaboration, the quality of the CRLs used as X–ray imaging optics were tested in detail. This information is crucial for the development of better X–ray optics at the Institute of Microstructure Technology (KIT). The problems which have been found are not systematically apparent in all lenses but only occur occasionally. The quality of the optics could be enhanced and newly developed aperture–optimized lenses [80] were successfully used. Tests of both the X–ray microscopy and cone–beam setup were conducted with these optical elements.

A proof–of–principle experiment was performed for the cone–beam setup. The focusing properties of some selected lenses were analyzed and the performance of the setup was tested. Focal spot sizes of approximately $300 \times 300\,\mathrm{nm}^2$ were achieved and radiograms of a test pattern could be successfully acquired. As expected from a third generation storage ring source, the high degree of coherence introduces strong phase effects in this imaging mode. The general structure of the test pattern was reproduced in detail, albeit the image was dominated by the aforementioned far–field phase effects and several phase oscillation periods are visible. Due to the image formation in the far–field, a simple a Paganin–like algorithm [101] cannot be used for the phase retrieval. The implementation of more refined algorithms [5] for correction was not performed in the scope of this work. Considering the uncertainty of the degree of coherence in the new PETRA III beam and with the focus on the X–ray microscopy setup, the expected strength and influence of phase effects was unclear. Analysis and correction of these phase effects was omitted and would go beyond the scope of the present thesis.

The X–ray microscopy setup was extensively tested at energies of $E = 17.4\,\mathrm{keV}$ and $E = 30\,\mathrm{keV}$ with different lenses. Using a test pattern, the achieved resolution in radiographies could be determined to be around 90 nm line and space for both energies.

Based on the working X–ray microscopy setup, nanotomography measurements of two samples originating from the SFB 986 M^3 – *Tailor–Made Multi–Scale Materials Systems* [115] was successfully performed. Radiation damage in the nanoporous gold sample led to a tilting of the sample during the measurement which prevented a reconstruction. The photonic glass sample was successfully measured and the data were further processed. Drifts in the experiment—which occurred during the measurement—led to variations of the sample position on the detector images. Both the vertical and horizontal position deviations of the sample were corrected for and a registered set of projections was used to reconstruct a 3D dataset of the sample.

The reconstructed photonic glass sample still shows artifacts from phase effects and minor errors in the X–ray optics. These artifacts prevented an automatic segmentation of the zirconia

particles from the void space. A manual segmentation was performed at several positions in the sample and the particle packing fraction could be extracted. The packing fraction η is significantly lower than the expected random close particle packing but is consistent with a force–free sedimentation of the particles. This result shows that it is necessary to further improve the sedimentation process to achieve a higher packing fraction. Furthermore, the currently achieved packing fraction can be used in updated simulation to compare the photonic properties of this material with theoretical expectations.

In the future, the stability of the setup has to be further improved. Interferometric tests showed that drifts correlate with variations in the thermal conditions in the hutch. The control parameters of the air conditioning system are one system that can be targeted. Installing thermal sensors close to the sample and optics might allow for using these values to control the air conditioning. In addition, tracking the detailed thermal conditions at as many components as possible, an automatic correction of thermal drifts can be contemplated.

The X–ray microscopy setup can be further improved by testing Fresnel zone plates as X–ray optics. These optics should yield higher resolutions at lower X–ray energies of around 10 keV. For imaging at higher X–ray energies, the refractive optics will be further improved in close collaboration with the IMT Karlsruhe.

The cone–beam setup could greatly benefit from significantly reduced measurement times by installing a high–flux option, for example the P05 multilayer monochromator in combination with a KB–mirror system. The phase effects occurring in the cone–beam setup are generally well understood. Implementing phase retrieval algorithms at the P05 beamline would allow for also using the phase signal which is more sensitive to small variations in the local electron density. Furthermore, sample sizes in the cone–beam setup are not limited by the optics acceptance so that sample with dimensions between 100 and 1000 µm can be investigated at a strongly improved resolution if compared to the micro tomography setup.

Appendix A

The PETRA III Storage Ring

DESY, the acronym for Deutsches Elektronen–Synchrotron, is located in Hamburg, Germany. While historically a high energy physics institution with the corresponding large rings for particle beams and collision experiments, all accelerators and rings are currently used for photon science experiments. Two storage rings (DORIS and PETRA) and a free electron laser (FLASH) deliver photons to many experiments.

A.1 Accelerators

To achieve the high energy of 6 GeV in the PETRA III storage rings, respectively, a cascade of accelerators is used. Electrons are generated in a high–power electron source and accelerated to 450 MeV in a linear accelerator. This electron beam is steered onto a tungsten target in which low energy electrons and positrons are generated, trapped and focused in a solenoid coil. The electrons and positrons are separated and the positron beam is again accelerated to 450 MeV in a linear accelerator.

The positrons are collected in the PIA ring (positron intensity accumulator) and a high–frequency system forms bunches with a defined time structure. These bunches are then inserted into the DESY ring, the only true synchrotron on the premises. Here, the positrons are accelerated until they reach their design energy, at which point they are transferred to the PETRA ring. Figure A.1 shows a schematic of the accelerator structure used to generate the high–energy positrons used in the PETRA storage ring.

A.2 PETRA III

While commonly called a synchrotron, the PETRA ring is actually only a storage ring, meaning that the particles do not increase their energy any more as they orbit. The most prominent ring

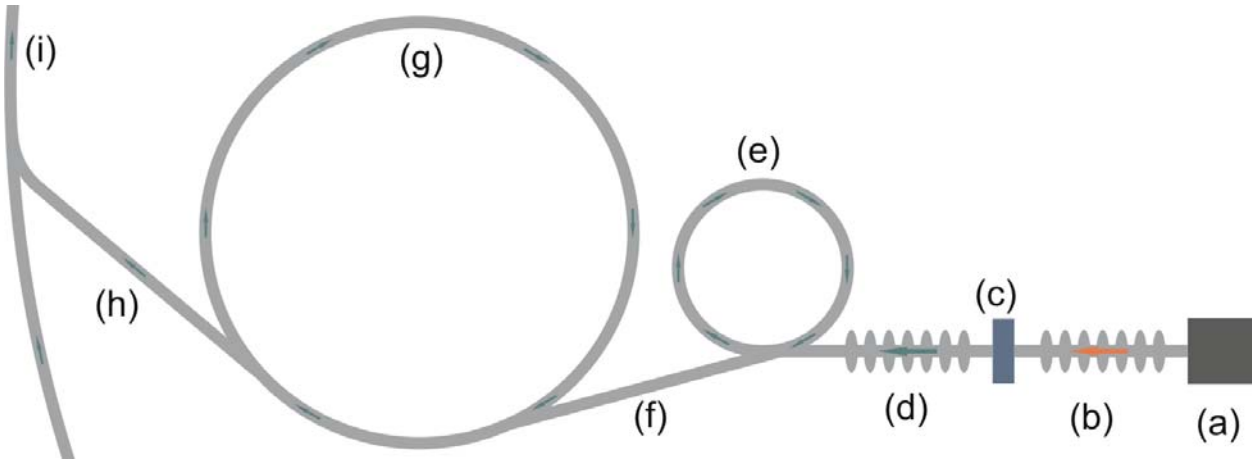

Figure A.1: Schematic of the accelerator structure for positrons to be used in the PETRA storage ring: (a) the electron gun, (b) linear electron accelerator, (c), conversion target for positron production, (d) linear positron accelerator, (e) positron accumulator, (f) transfer pipe, (g) DESY synchrotron to accelerate positrons to ring energy, (h) transfer pipe, and (i) PETRA storage ring.

parameters can be found in Table A.1. Of practical importance are the design energy which defines —in combination with the undulator parameters— the accessible energy range and especially the source sizes and divergences. As X–ray optics always generate a (demagnified) image of the source, a small source facilitates the creation of a nanofocused beam. The horizontal emittance ϵ_x, defined as

$$\epsilon_x = \sigma_x \cdot \sigma_{x'}$$

using the source size σ_x and the source divergence $\sigma_{x'}$ and similarly the vertical emittance ϵ_y are defined by the ring layout and constant. A smaller source size leads thus to a larger divergence. Due to the limited aperture of most X–ray optics, not all of the beam can be used for focusing, but a smaller focus can be achieved in return.

The 2304 m long ring has previously been used as a high energy physics ring for collision experiments and as such, already existed. 7/8 of the ring structure has been largely kept, except for

circumference	2304 m
design energy	6 GeV
design current	100 mA
horizontal source size* (RMS)	37 µm
horizontal divergence* (RMS)	27 µrad
vertical source size* (RMS)	5.7 µm
vertical divergence* (RMS)	5.4 µrad
horizontal emittance ϵ_x	1 nmrad
vertical emittance ϵ_y	0.01 nmrad

Table A.1: Key parameters of the PETRA III storage ring. All values marked with an asterisk are valid for a 2m undulator in low–β mode, as employed at the beamline IBL/P05. [4]

some upgrades and replacements. The last 1/8 of the ring has been completely refurbished and 14 beamlines have been installed. In addition, four damping wigglers have been installed in the ring to achieved the target emittance values.

While orbiting in the ring, the positrons lose energy as they generate synchrotron radiation, both as intended at the insertion devices and unintentionally at each turn during the orbit. This energy loss is compensated by radio frequency cavities which boost the particle energy by the amount lost during each orbit so that the particle energy stays roughly the same. In an average lifetime of 10 hours, each particle completes about 5 billion orbits with a position stability of about 10 micrometers.

Appendix B

Supplemental material on X–rays

B.1 Interaction processes

B.1.1 Scattering

The electromagnetic field can be scattered by single electrons in the atoms, atoms itself, molecules, and crystal structures. Here, I will only briefly describe the interaction with electrons as these are the dominating effects. Scattering by crystal structures (Bragg scattering) will not be described, but detailed descriptions can be found in the literature, e.g. Als–Nielsen and McMorrow [2].

Elastic scattering

The classical (non–quantum mechanical) description of the scattering tells that the EM field exerts a force on the electron, accelerating it in the process. The electron oscillates in the wave field as radiates like a dipole antenna. Necessarily, the emitted photon has the same momentum $\hbar\mathbf{k}$ as the incoming photon. This phenomenon is known as Thomson scattering. The scattering length r_0 is commonly also called the free electron radius:

$$r_0 = \left(\frac{e^2}{4\pi\epsilon_0 m_e c^2} \right) \tag{B.1}$$

and the corresponding interaction cross section is For atoms, the scattering is the sum of all electron scattering contributions and is called Rayleigh scattering. However, the correct phase has to be applied to superposition sum. If this calculation is performed, the result is the atomic form factor $f(\mathbf{Q}, \omega)$ with the wave vector transfer $\mathbf{Q}$ and the angular frequency $\omega = 2\pi\nu$ of the X-ray. In the case of forward scattering ($\mathbf{Q} = \mathbf{0}$) the form factor is often written as

$$f^0(\omega) = f_1^0(\omega) - i\, f_2^0(\omega). \tag{B.2}$$

Inelastic scattering

Of major importance is also the inelastic scattering, called Compton scattering. Assuming the electron is at rest and is hit by a X–ray photon which is scattered, the conservation of energy and momentum easily lead to the result (see for example Als-Nielsen and McMorrow [2]) that the X–ray wavelength changes by a factor proportional to

$$\lambda\!\!\!^{-}_c = \frac{\hbar}{m_e c}. \tag{B.3}$$

For higher photons energies, Compton scattering is the dominating interaction force between X–rays and matter. A comparison of interaction strengths can be seen in Figure 2.4 or Table 2.1.

B.1.2 Photoelectric absorption

Absorption of X–ray photons is a photoelectric effect: An electron absorbs the photon and is ejected from the atom, ionizing it in the process. The electron energy is then dissipated in the sample via inelastic collisions. The photo–electric absorption is the dominant interaction process for lower energies, but the interaction cross–section diminishes with increasing energies.

Pair production

For very high photon energies, the dominating interaction force is pair production. In pair production, a photon with a sufficiently high energy produces an electron–positron pair:

$$\nu \rightarrow e^+ + e^- \tag{B.4}$$

The minimum energy of the photon is 1.022 MeV, which is the rest mass for two electrons. Due to conservation of momentum, pair production cannot occur in vacuum but another particle is needed to allow the conservation of energy and momentum. The strongly bound and heavy nucleus can absorb uncompensated momentum.

B.2 Atomic form factors

For high photon energies (i.e. X–rays), the atomic form factors are:

$$f_1^0(\omega) = Z^* + \frac{1}{2\pi^2\, r_e\, c} \int_0^\infty \frac{\widetilde{\omega}^2 \sigma_a(\widetilde{\omega})}{\omega^2 - \widetilde{\omega}^2} d\widetilde{\omega} \tag{B.5}$$

$$f_2^0(\omega) = \frac{\omega\, \sigma_a(\omega)}{4\pi\, r_e\, c} \tag{B.6}$$

with the atomic number density n_a, the atomic photoabsorption cross section σ_a. Z^* is the relativistically corrected atomic number Z:

$$Z^* \approx Z - \left(\frac{Z}{82.5}\right)^{2.37} \tag{B.7}$$

If not in the energetic vicinity of absorption edges, the high photon–energy of f_1^0 simplifies to

$$f_1^0 \approx Z^*. \tag{B.8}$$

Appendix C

Publications related to this work

The progress of the nano tomography endstation has been presented in several publications and technical reports (DESY annual reports). The general experimental concept was first presented by Haibel et al. [43, 44] as part of the global beamline concept. However, only a general sketch of the optics concept existed at that point and the nano tomography is not discussed in much detail.

A test experiment at the DORIS III storage ring was performed to test the polymer CRL X–ray optics and the kinematics concept intended for the nano tomography endstation [95]. These results gave valuable feedback for the design of the P05 experiment.

The commissioning of the nano tomography experimental endstation was documented in two more experimental reports [94, 96] and a conference proceeding [97]. The development of the X–ray optics was performed by the Institute of Microstructure Technology (KIT), but many tests were performed in collaboration at the P05 nano tomography endstation. These tests advanced both the optics knowledge at the KIT and offered a chance for better understanding the experimental setup at P05. Results of the optics commissioning with focus on the quality of the optics resulted in two technical reports [118, 138] and a conference proceeding [81]. Experimental results of this optics commissioning is also part of the PhD thesis of H. Vogt [137] and F. Marschall [80] (both KIT).

The details of the optics and mechanics layout presented in Chapter 5 are not published. The results obtained from the stability measurements and front end commissioning were crucial for a successful experiment, but have not been published either. Scientific results from the first nano tomographies from the P05 station are being prepared for publication.

A complete list of the publications mentioned above is given below:

- Peer–reviewed papers

    1. A. Haibel, F. Beckmann, T. Dose, J. Herzen, M. Ogurreck, M. Müller, and A. Schreyer. Latest developments in microtomography and nanotomography at PETRA III. *Powder*

Diffraction, 25:161164, 2010.

2. A. Haibel, M. Ogurreck, F. Beckmann, T. Dose, F. Wilde, J. Herzen, M. Müller, A. Schreyer, V. Nazmov, M. Simon, A. Last, and J. Mohr. Micro- and nano-tomography at the GKSS Imaging Beamline at PETRA III. *Proceedings of SPIE*, 7804:78040B, 2010

3. M. Ogurreck, F. Wilde, J. Herzen, F. Beckmann, V. Nazmov, J. Mohr, A. Haibel, M. Müller, and A. Schreyer. The nanotomography endstation at the PETRA III Imaging Beamline. *Journal of Physics: Conference Series*, 425:182002, 2013

4. F. Marschall, A. Last, M. Simon, M. Kluge, V. Nazmov, H. Vogt, M. Ogurreck, I. Greving, and J. Mohr. Xray Full Field Microscopy at 30 keV. *Journal of Physics: Conference Series*, 499:012007, 2014

- PhD thesis

1. F. Marschall. *Entwicklung eines Röntgenmikroskops für Photonenenergien von 15 keV bis 30 keV*. PhD thesis, Karlsruher Institute of Technology (KIT), 2014.

2. H. Vogt. *Gerollte brechende Roentgenfolienlinsen*. PhD thesis, Karlsruher Institute of Technology (KIT), 2014

- Technical reports

1. M. Ogurreck, V. Nazmov, F. Beckmann, and A. Haibel. X-Ray Imaging Setup at Beamline BW2 for Testing of X-Ray Lenses and Kinematic Mounting Mechanics. HASYLAB Anuual Report, 2010.

2. M. Ogurreck, F.Wilde, T. Dose, I. Greving, J. Herzen, F. Beckmann, M. Müller, A. Schreyer, V. Nazmov, F. Marschall, A. Last, and J. Mohr. First commissioning results of the nano tomography endstation at P05. HASYLAB Anuual Report, 2012

3. M. Simon, F. Marschall, A. Last, M. Ogurreck, and F. Wilde. Component Evaluation for 30 keV-Full Field Microscope. HASYLAB Anuual Report, 2012.

4. M. Ogurreck, I. Greving, T. Dose, F. Beckmann, H. Vogt, F. Marschall, and A. Last. First results of the P05/IBL nano tomography endstation . HASYLAB Anuual Report, 2013

5. H. Vogt, A. Last, M. Kluge, F. Marschall, and M. Ogurreck. Rolled X-ray Prism lenses for microscopy illumination purposes. HASYLAB Anuual Report, 2013.

Bibliography

[1] L. Alianelli, K. J. S. Sawhney, R. Barrett, I. Pape, A. Malik, and M. C. Wilson. High efficiency nano-focusing kinoform optics for synchrotron radiation. *Optics Express*, 19:11120–11127, 2011.

[2] J. Als-Nielsen and D. McMorrow. *Elements of Modern X–ray Physics*. John Wiley & Sons, West Sussex, 2001.

[3] D. X. Balaic, K. A. Nugent, Z. Barnea, R. Garrett, and S. W. Wilkins. Focusing of X-rays by Total External reflection from a Paraboloidally Tapered Glass Capillary. *Journal of Synchrotron Radiation*, 2, 1995.

[4] K. Balewski, W. Brefeld, W. Decking, H. Franz, R. Röhlsberger, and E. Weckert. PETRA III: A Low Emittance Synchrotron Radiation Source. Technical report, DESY, 2004.

[5] M. Bartels. *Cone–beam x–ray phase contrast tomography of biological samples*. PhD thesis, Universität Göttingen, 2013.

[6] M. Bartels, M. Priebe, R. Wilke, S. Kruger, K. Giewekemeyer, S. Kalbfleisch, C. Olendrowitz, M. Sprung, and T. Salditt. Low–dose three–dimensional hard x–ray imaging of bacterial cells. *Optical Nanoscopy*, 1(1):10, 2012.

[7] F. Beckmann. *Entwicklung, Aufbau und Anwendung eines Verfahrens der Phasenkontrast–Mikrotomographie mit Röntgen–Synchrotronstrahlung*. PhD thesis, University of Dortmund, 1998.

[8] C. Bergemann, H. Keymeulen, and J. F. van der Veen. Focusing X-Ray Beams to Nanometer Dimensions. *Physical Review Letters*, 91:204801, 2003.

[9] D. H. Bilderback, D. J. Thiel, R. Pahl, and K. E. Brister. X-ray Applications with Glass-Capillary Optics. *Journal of Synchrotron Radiation*, 1:37–42, 1994.

[10] A. Bjeoumikhov, M. Erko, S. Bjeoumikhova, A. Erko, I. Snigireva, A. Snigirev, T. Wolffe, I. Mantouvaloue, W. Malzere, and B. Kanngiesser. Capillary μFocus X-ray lenses with

parabolic and elliptic profile. *Nuclear Instruments and Methods in Physics Research Section A: Accelerators, Spectrometers, Detectors and Associated Equipment*, 587:458–463, 2008.

[11] U. Bonse, Q. Johnson, M. Nichols, R. Nusshardt, S. Krasnicki, and J. Kinney. High resolution tomography with chemical specificity. *Nuclear Instruments and Methods in Physics Research Section A: Accelerators, Spectrometers, Detectors and Associated Equipment*, 246(13):644 – 648, 1986.

[12] W. Born and E. Wolf. *Principles of Optics*. Pergamon Press, Oxford, 1980.

[13] P. Boye, J. M. Feldkamp, J. Patommel, A. Schwab, S. Stephan, R. Hoppe, C. G. Schroer, M. Burghammer, C. Riekel, A. van der Hart, and M. Küchler. Nanofocusing refractive X-ray lenses: Fabrication and modeling . *Journal of Physics: Conference Series*, 186:012063, 2009.

[14] F. Busch. *Auflösungsvermögen einer Mikrotomographie–Kamera für Röntgen–Synchrotronstrahlung*. PhD thesis, University of Dortmund, 1994.

[15] L. De Caro and W. Jark. Diffraction theory applied to X-ray imaging with clessidra prism array lenses. *Journal of Synchrotron Radiation*, 15:176–184, 2008.

[16] A. M. Cormack. Representation of a Function by Its Line Integrals, with Some Radiological Applications. *Journal of Applied Physics*, 34:2722–2727, 1963.

[17] D. E. Cullen, J. H. Hubbell, and L. Kissel. EPDL97: the Evaluated Photon Data Library, '97 Version, 1997.

[18] R. J. Dejus and M. Sánchez del Río. XOP: A graphical user interface for spectral calculations and x-ray optics utilities. *Review of Sccientific Instruments*, 67:Proceedings of the conference on Synchrotron Radiation Instrumentation '95, 1996.

[19] M. Sánchez del Río and R. J. Dejus. XOP: a multiplatform graphical user interface for synchrotron radiation spectral and optics calculations. *Proceedings of SPIE*, 3152:Materials, Manufacturing, and Measurement for Synchrotron Radiation Mirrors, 148, 1997.

[20] M. Sánchez del Río and R. J. Dejus. XOP: recent developments. *Proceedings of SPIE*, 3448:Crystal and Multilayer Optics, 340, 1998.

[21] M. Sánchez del Río and R. J. Dejus. XOP 2.1: A new version of the X-ray optics software toolkit. In *Synchrotron Radiation Instrumentation: Eighth International Conference*, pages 784–787, 2004.

[22] M. Sánchez del Río, C. Ferrero, and V. Mocella. Computer simulations of bent perfect crystal diffraction profiles. *Proceedings of SPIE*, 3151:High Heat Flux and Synchrotron Radiation Beamlines, 312, 1997.

[23] J. J. do Rosario. Private communication. Technical University Hamburg–Harburg, 2013–2014.

[24] J. J. do Rosario, P. N. Dyachenko, R. Kubrin, R. M. Pasquarelli, A. Yu. Petrov, M. Eich, and G. A. Schneider. Facile Deposition of YSZ-Inverse Photonic Glass Films. *ACS Applied Materials & Interfaces*, 6(15):12335–12345, 2014.

[25] T. Donath. *Quantitative X-ray Microtomography with Synchrotron Radiation*. PhD thesis, University Hamburg, 2007.

[26] T. Donath, F. Beckmann, and A. Schreyer. Automated determination of the center of rotation in tomography data. *Journal of the Optical Society of America A*, 23:1048–1057, 2006.

[27] W. Ehrenberg. X–ray optics. *Nature*, 330:330–331, 1947.

[28] P. Elleaume. Optimization of compound refractive lenses for X-rays. *Nuclear Instruments and Methods in Physics Research Section A: Accelerators, Spectrometers, Detectors and Associated Equipment*, 412:483–506, 1998.

[29] P. Elleaume. Two-Plane Focusing of 30 keV Undulator Radiation. *Journal of Synchrotron Radiation*, 5:1–5, 1998.

[30] I. R. Entin and I. A. Smirnova. Double–Crystal Rocking Curve of the Forbidden Si 222 Reflection. *Acta Crystallographica Section A: Foundations of Crystallography*, 45:577–580, 1989.

[31] L. A. Feldkamp, L. C. Davis, and J. W. Kress. Practical cone-beam algorithm. *Journal of the Optical Society of America A*, 1:612–619, 1984.

[32] Y. P. Feng, S. K. Sinha, H. W. Deckman, J. B. Hastings, and D. P. Siddons. X-Ray Flux Enhancement in Thin-Film Waveguides Using Resonant Beam Couplers. *Physical Review Letters*, 71:537–540, 1993.

[33] J. L. Finney. Random Packings and the Structure of Simple Liquids. I. The Geometry of Random Close Packing. *Proceedings of the Royal Society of London. A. Mathematical and Physical Sciences*, 319(1539):479–493, 1970.

[34] B. P. Flannery, H. W. Deckman, W. G. Roberge, and K. L. D'Amico. Three-Dimensional X-ray Microtomography. *Science*, 237(4821):1439–1444, 1987.

[35] A. J. Fresnel. *Œvres Complètes d'Augustin Fresnel*, chapter Calcul de l'intensité de la lumière au centre de l'ombre d'un ecran et d'une ouverture circulaires eclairés par un point radieux. Imprimerie Impériale, Paris, 1866.

[36] P. D. García, R. Sapienza, and C. López. Photonic Glasses: A Step Beyond White Paint. *Advanced Materials*, 22(1):12–19, 2010.

[37] P.D. García, R. Sapienza, Á. Blanco, and C. López. Photonic Glass: A Novel Random Material for Light. *Advanced Materials*, 19(18):2597–2602, 2007.

[38] Physik Instrumente GmbH. Piezo nano positioning inspirationen 2009, 2009.

[39] T. Gomi. Volume Reconstruction of Cone–Beam Geometry. *Recent Patents on Medical Imaging*, 1:1–12, 2009.

[40] R. Gordon, R. Bender, and G. T. Herman. Algebraic reconstruction techniques (ART) for three-dimensional electron microscopy and X-ray photography. *Journal of Theoretical Biology*, 29:471, 1970.

[41] A. R. Greenleaf. *Photographic Optics*. The MacMillan Company, New York, 1950.

[42] L. Grodzins. Optimum energies for x–ray transmission tomography of small samples. *Nuclear Instruments and Methods in Physics Research*, 206:541–545, 1983.

[43] A. Haibel, F. Beckmann, T. Dose, J. Herzen, M. Ogurreck, M. Müller, and A. Schreyer. Latest developments in microtomography and nanotomography at PETRA III. *Powder Diffraction*, 25:161–164, 2010.

[44] A. Haibel, M. Ogurreck, F. Beckmann, T. Dose, F. Wilde, J. Herzen, M. Müller, A. Schreyer, V. Nazmov, M. Simon, A. Last, and J. Mohr. Micro- and nano-tomography at the GKSS Imaging Beamline at PETRA III. *Proceedings of SPIE*, 7804:78040B, 2010.

[45] B.L. Henke, E.M. Gullikson, and J.C. Davis. X-ray interactions: photoabsorption, scattering, transmission, and reflection at E=50-30000 eV, Z=1-92. *Atomic Data and Nuclear Data Tables*, 54:181–342, 1993.

[46] G. T. Herman. *Image Reconstruction from Projections*. Academic Press, New York, 1980.

[47] G. T. Herman, A. V. Lakshminarayanan, and A. Naparstek. Convolution reconstruction techniques for divergent beams. *Computers in Biology and Medicine*, 6:259–262, 1976.

[48] J. Herzen. *A grating interferometer for materials science imaging at a second-generation synchrotron radiation source*. PhD thesis, University of Hamburg, 2010.

[49] G. N. Hounsfield. Computerized transversial axial scanning (tomography): Part I. Description of system. *British Journal of Radiology*, 46:1016–1022, 1973.

[50] Saint-Gobain Ceramics & Plastics Inc. Cadmium tungstate scintillation material datasheet, 2013.

[51] S. C. Irvine, K. S. Morgan, Y. Suzuki, K. Uesugi, A. Takeuchi, D. M. Paganin, and K. K. W. Siu. Assessment of the use of a diffuser in propagation-based x-ray phase contrast imaging. *Optics Express*, 18:13478–13491, 2010.

[52] A. F. Isakovic, A. Stein, J. B. Warren, S. Narayanan, M. Sprung, A. R. Sandyd, and K. Evans-Lutterodt. Diamond kinoform hard X-ray refractive lenses: design, nanofabrication and testing. *Journal of Synchrotron Radiation*, 16:8–13, 2009.

[53] H. M. Jaeger and S. R. Nagel. Physics of the Granular State. *Science*, 255:1523–1531, 1992.

[54] W. Jark, F. Pérennès, and M. Matteucci. On the feasibility of large-aperture Fresnel lenses for the microfocusing of hard X-rays. *Journal of Synchrotron Radiation*, 13:239–252, 2006.

[55] W. Jark, F. Pérennès, M. Matteucci, L. Mancini, F. Montanari, L. Rigon, G. Tromba, A. Somogyi, R. Toucoulou, and S. Bohic. Focusing X-rays with simple arrays of prism-like structures. *Journal of Synchrotron Radiation*, 11:248–253, 2004.

[56] K. Jefimovs, J. Vila-Comamala, M. Stampanoni, B. Kaulich, and C. David. Beam-shaping condenser lenses for full-field transmission X-ray microscopy. *Journal of Synchrotron Radiation*, 15(1):106–108, 2008.

[57] A. C. Kak and M. Slaney. *Principles of Computerized Tomography*. IEEE Press, New York, 1987.

[58] B. Kaulich, S. Oestreich, M. Salome, R. Barrett, J. Susini, T. Wilhein, E. Di Fabrizio, M. Gentili, and P. Charalambous. Feasibility of transmission x-ray microscopy at 4 keV with spatial resolutions below 150 nm. *Applied Physics Letters*, 75:4061–4063, 1999.

[59] P. Kirkpatrick and A. V. Baez. Formation of Optical Images by X-Rays. *Journal of the Optical Society of America A*, 38:766–774, 1948.

[60] O. Klein and Y. Nishina. Über die Streuung von Strahlung durch freie Elektronen nach der neuen relativistischen Quantendynamik von Dirac. *Zeitschrift f¨ur Physik*, 52(11-12):853–868, 1929.

[61] A. Knochel, G. Gaul, and F. Lechtenberg, 1994. German Patent DE4444102C2.

[62] S. P. Krüger, K. Giewekemeyer, S. Kalbfleisch, M. Bartels, H. Neubauer, and T. Salditt. Sub-15 nm beam confinement by two crossed x-ray waveguides. *Optics Express*, 18:13492–13501, 2010.

[63] S. P. Krüger, H. Neubauer, M. Bartels, S. Kalbfleisch, K. Giewekemeyer, P. J. Wilbrandt, M. Sprung, and T. Salditt. Sub-10 nm beam confinement by X-ray waveguides: design, fabrication and characterization of optical properties. *Journal of Synchrotron Radiation*, 19:227–236, 2012.

[64] A. Kuba and G. T. Herman. Some mathematical concepts for tomographic reconstruction. In J. Banhart, editor, *Advanced Tomographic Methods in Materials Research and Engineering*, pages 19–36. Oxford University Press, 2008.

[65] R. Kubrin, H. S. Lee, R. Zierold, A. Yu. Petrov, R. Janssen, K. Nielsch, M. Eich, and G. A. Schneider. Stacking of Ceramic Inverse Opals with Different Lattice Constants. *Journal of the American Ceramic Society*, 95(7):2226–2235, 2012.

[66] O. Kurapova, B. Lengeler, C. G. Schroer, M. Küchler, T. Gessner, and A. van der Hart. Optimized fabrication of silicon nanofocusing x-ray lenses using deep reactive ion etching. *Journal of Vacuum Science and Technology B*, 25:1626–1629, 2007.

[67] D. Laipple. Private communication. Helmholtz–Zentrum Geesthacht, 2013–2014.

[68] D. Laipple. *Region of interest synchrotron nanotomography and FIB/SEM precharacterization on metallic engineering materials*. PhD thesis, University of Hamburg, to be submitted (2015).

[69] A. Last. *User manual - planar, refractive X–ray lenses with point focus, version 20.11.2008*, 2008.

[70] A. Last. private communication. Karlsruhe Institute of Technology, 2011–2014.

[71] H. S. Lee, R. Kubrin, R. Zierold, A. Yu. Petrov, K. Nielsch, G. A. Schneider, and M. Eich. Thermal radiation transmission and reflection properties of ceramic 3D photonic crystals. *Journal of the Optical Society of America B*, 29(3):450–457, Mar 2012.

[72] E. Leib. Private communication. University Hamburg, 2013–2014.

[73] B. Lengeler, C. Schroer, J. Tümmler, B. Benner, M. Richwin, A. Snigirev, I. Snigireva, and M. Drakopoulos. Imaging by parabolic refractive lenses in the hard X-ray range. *Journal of Synchrotron Radiation*, 6:1153–1167, 1999.

[74] B. Lengeler, C. G. Schroer, M. Kuhlmann, B. Benner, T. F. Günzler, O. Kurapova, F. Zontone, A. Snigirev, and I. Snigireva. Refractive x-ray lenses. *Journal of Physics D: Applied Physics*, 38:A218–A222, 2005.

[75] B. Lengeler, C. G. Schroer, M. Richwin, J. Tümmler, M. Drakopoulos, A. Snigirev, and I. Snigireva. A microscope for hard x rays based on parabolic compound refractive lenses. *Applied Physics Letters*, 74:3924–3926, 1999.

[76] A. Liénard. Champ électrique et magnétique, produit par une charge électrique concentrée en un point et animée d'un mouvement quelconque. *L'Éclairage Électrique*, 16:5–112, 1898.

[77] L. B. Lucy. An iterative technique for the rectification of observed distributions. *Astronomical Journal*, 79:745–754, 1974.

[78] S. M. Luke, B. T. Hallam, and P. Vukusic. Structural optimization for broadband scattering in several ultra-thin white beetle scales. *Applied Optics*, 49(22):4246–4254, Aug 2010.

[79] F. Marschall. private communication. Karlsruhe Institute of Technology, 2013–2014.

[80] F. Marschall. *Entwicklung eines Röntgenmikroskops für Photonenenergien von 15 keV bis 30 keV*. PhD thesis, Karlsruher Institute of Technology (KIT), 2014.

[81] F. Marschall, A. Last, M. Simon, M. Kluge, V. Nazmov, H. Vogt, M. Ogurreck, I. Greving, and J. Mohr. X–ray Full Field Microscopy at 30 keV. *Journal of Physics: Conference Series*, 499:012007, 2014.

[82] G. Martínez-Criado, R. Tucoulou, P. Cloetens, P. Bleuet, S. Bohic, J. Cauzid, I. Kieffer, E: Kosior, S. Labouré, S. Petitgirard, A. Rack, J. A. Sans, J. Segura-Ruiz, H. Suhonen, J. Susini, and J. Villanova. Status of the hard X-ray microprobe beamline ID22 of the European Synchrotron Radiation Facility. *Journal of Synchrotron Radiation*, 19(1):10–18, Jan 2012.

[83] A. G. Michette. No X-ray lens. *Nature*, 353:510, 1991.

[84] miCos GmbH. miCos Motion Control V10, 2012.

[85] H. Mimura, H. Yumoto, S. Matsuyama, Y. Sano, K. Yamamura, Y. Mori, M. Yabashi, Y. Nishino, K. Tamasaku, T. Ishikawa, and K. Yamauchi. Efficient focusing of hard x rays to 25 nm by a total reflection mirror. *Applied Physics Letters*, 90:051903, 2007.

[86] R. Mokso, P. Cloetens, E. Maire, W. Ludwig, and J.-Y. Buffière. Nanoscale zoom tomography with hard x rays using kirkpatrick-baez optics. *Applied Physics Letters*, 90:144104, 2007.

[87] K. Mueller. *Fast and accurate three–dimensional Reconstruction from Cone-Beam Projection Data using Algebraic Methods*. PhD thesis, Ohio State University, 1998.

[88] F. Natterer. *The Mathematics of Computerized Tomography*. Soc. for Industrial & Applied Math, 2001.

[89] V. Nazmov. private communication. Karlsruhe Institute of Technology, 2011–2014.

[90] V. Nazmov, E. Reznikova, A. Last, and V. Saile. Highly efficient 2-D nano focusing by an optical system of planar refractive lenses . *Journal of Physics: Conference Series*, 186:012069, 2009.

[91] V. Nazmov, E. Reznikova, J. Mohr, V. Saile, L. Vincze, B. Vekemans, S. Bohic, and A Somogyi. Parabolic crossed planar polymeric x-ray lenses. *Journal of Micromechanics and Microengineering*, 21:015020, 2011.

[92] V. Nazmov, E. Reznikova, J. Mohr, A. Snigirev, I. Snigireva, S. Achenbach, and V. Saile. Fabrication and preliminary testing of X-ray lenses in thick SU-8 resist layers. *Microsystem Technologies*, 10:716–721, 2004.

[93] V. Nazmov, E. Reznikova, A. Somogyi, J. Mohr, and V. Saile. Planar sets of cross X-ray refractive lenses from SU-8 polymer. *Proceedings of SPIE*, 5539:235–243, 2004.

[94] M. Ogurreck, I. Greving, T. Dose, F. Beckmann, H. Vogt, F. Marschall, and A. Last. First results of the P05/IBL nano tomography endstation . HASYLAB Anuual Report, 2013.

[95] M. Ogurreck, V. Nazmov, F. Beckmann, and A. Haibel. X-Ray Imaging Setup at Beamline BW2 for Testing of X-Ray Lenses and Kinematic Mounting Mechanics. HASYLAB Anuual Report, 2010.

[96] M. Ogurreck, F. Wilde, T. Dose, I. Greving, J. Herzen, F. Beckmann, M. Müller, A. Schreyer, V. Nazmov, F. Marschall, A. Last, and J. Mohr. First commissioning results of the nano tomography endstation at P05. HASYLAB Anuual Report, 2012.

[97] M. Ogurreck, F. Wilde, J. Herzen, F. Beckmann, V. Nazmov, J. Mohr, A. Haibel, M. Müller, and A. Schreyer. The nanotomography endstation at the PETRA III Imaging Beamline. *Journal of Physics: Conference Series*, 425:182002, 2013.

[98] W. H. Oldendorf. Isolated Flying Spot Detection of Radiodensity Discontinuities - Displaying the Internal Structure Pattern of a Complex Object. *IRE Transactions on Bio-Medical Electronics*, 8:68–72, 1961.

[99] C. Olendrowitz, M. Bartels, M. Krenkel, A. Beerlink, R. Mokso, M. Sprung, and T. Salditt. Phase-contrast x-ray imaging and tomography of the nematode Caenorhabditis elegans. *Physics in Medicine and Biology*, 57(16):5309, 2012.

[100] G. Y. Onoda and E. G. Liniger. Random loose packings of uniform spheres and the dilatancy onset. *Physical Review. Letters*, 64:2727–2730, May 1990.

[101] D. Paganin, S. C. Mayo, T. E. Gureyev, P. R. Miller, and S. W. Wilkins. Simultaneous phase and amplitude extraction from a single defocused image of a homogeneous object. *Journal of Microscopy*, 206(1):33–40, 2002.

[102] F. Pfeiffer, C. David, M. Burghammer, C. Riekel, and T. Salditt. Two-Dimensional X-ray Waveguides and Point Sources. *Science*, 297:230–234, 2002.

[103] John L. Provis, Volker Rose, Robert P. Winarski, and Jannie S.J. van Deventer. Hard x-ray nanotomography of amorphous aluminosilicate cements. *Scripta Materialia*, 65:316–319, 2011.

[104] J. Radon. Über die Bestimmung von Funktionen durch ihre Integralwerte längs gewisser Mannigfaltigkeiten. *Berichte über die Verhandlungen der Königlichen Sächsischen Akademie der Wissenschaften*, 69:262, 1917.

[105] J. Rehacek, Z. Hradil, M. Zawisky, W. Treiber, and M. Strobl. Maximum-likelihood absorption tomography. *Europhysics Letters*, 59:694, 2002.

[106] S. Rehbein, S. Heim, P. Guttmann, S. Werner, and G. Schneider. Ultrahigh-Resolution Soft-X-Ray Microscopy with Zone Plates in High Orders of Diffraction. *Physical Review Letters*, 103, 2009.

[107] E. Reznikova, T. Weitkamp, V. Nazmov, A. Last, M. Simon, and V. Saile. Investigation of phase contrast hard X-ray microscopy using planar sets of refractive crossed linear parabolic lenses made from SU-8 polymer. *Physica Status Solidi A*, 204:2811–2816, 2007.

[108] W. H. Richardson. Bayesian–Based Iterative Method of Image Restoration. *Journal of the Optical Society of America*, 62:55–59, 1972.

[109] V. Rose, T. Y. Chien, J. Hiller, D. Rosenmann, and R. P. Winarski. X-ray nanotomography of SiO2-coated Pt90Ir10 tips with sub-micron conducting apex. *Applied Physics Letters*, 99:173102, 2011.

[110] G.A. Schott. *Electromagnetic radation, and the mechanical reactions arising from it*. Cambridge University Press, Cambridge, 1912.

[111] C. G. Schroer, P. Boye, J. M. Feldkamp, J. Patommel, A. Schropp, D. Samberg, S. Stephan, M. Burghammer, S. Schöder, C. Reikel, B. Lengeler, G. Falkenberg, G. Wellenreuther, M. Kuhlmann, R. Frahm, D. Lützenkirchen-Hecht, and W. H. Schroeder. Hard X-ray Microscopy with Elemental, Chemical, and Structural Contrast. *Acta Physica Polonia A*, 117:357–368, 2010.

[112] C. G. Schroer, O. Kurapova, J. Patommel, P. Boye, J. Feldkamp B. Lengeler, M. Burghammer, C. Riekel, L. Vincze, A. van der Hart, and M. Küchler. Hard x-ray nanoprobe based on refractive x-ray lenses. *Applied Physics Letters*, 87:124103, 2005.

[113] C. G. Schroer and B. Lengeler. Focusing Hard X Rays to Nanometer Dimensions by Adiabatically Focusing Lenses. *Physical Review Letters*, 94:054802, 2005.

[114] C. G. Schroer, B. Lengeler, B. Benner, T. F. Gü nzler, M. Kuhlmann, A. Simionovici, S. Bohic, M. Drakopoulos, A. Snigirev, I. Snigireva, and W. Schröder. Microbeam Production Using Compound Refractive Lenses: Beam Characterization and Applications. *Proceedings of SPIE*, 4499, 2001.

[115] SFB 986. http://www.tuhh.de/sfb986/home.html, 2014 (accessed September 1, 2014).

[116] M. D. Shawkey, N. I. Morehouse, and P. Vukusic. A protean palette: colour materials and mixing in birds and butterflies. *Journal of The Royal Society Interface*, 6(Suppl. 2):S221–S231, 2009.

[117] M. Simon. *Röntgenlinsen mit großer Apertur*. PhD thesis, Karlsruher Institit für Technologie, 2010.

[118] M. Simon, F. Marschall, A. Last, M. Ogurreck, and F. Wilde. Component Evaluation for 30 keV-Full Field Microscope. HASYLAB Anuual Report, 2012.

[119] R. K. Smither, A. M. Khounsary, and S. Xu. Potential of a beryllium x-ray lens. *Proceedings of SPIE*, 3151:150–163, 1997.

[120] A. Snigirev, A. Bjeoumikhov, A. Erko, I. Snigireva, M. Grigoriev, V. Yunkin, M. Erkob, and S. Bjeoumikhova. Submicrometer hard X-ray focusing using a single-bounce ellipsoidal capillary combined with a Fresnel zone plate. *Journal of Synchrotron Radiation*, 14:227–228, 2007.

[121] A. Snigirev, A. Bjeoumikhov, A. Erko, I. Snigireva, M. Grigoriev, V. Yunkin, M. Erkob, and S. Bjeoumikhova. Two-step hard X-ray focusing combining Fresnel zone plate and single-bounce ellipsoidal capillary. *Journal of Synchrotron Radiation*, 14:326–330, 2007.

[122] A. Snigirev, B. Filseth, P. Elleaume, Th. Klocke, V. Kohn, B. Lengeler, I. Snigireva, A. Souvorow, and J. Tümmler. Refractive lenses for high energy X-ray focusing. *Proceedings of SPIE*, 3151:164–170, 1997.

[123] A. Snigirev, V. Kohn, I. Snigireva, and B. Lengeler. A compound refractive lens for focusing high-energy X-rays . *Nature*, 384:49–51, 1996.

[124] A. Snigirev, V. Kohn, I. Snigireva, A. Souvorov, and B. Lengeler. Focusing High-Energy X Rays by Compound Refractive Lenses. *Applied Optics*, 37:653–662, 1998.

[125] A. Snigirev, I. Snigireva, M. Grioriev, V. Yunkin, M. Di Michiel, S. Kuznetsov, and G. Vaughan. Silicon Planar Lenses for High Energy X-ray Nanofocusing. *Proceedings of SPIE*, 6705:670506–1 – 670506–11, 2007.

[126] I. Snigireva, A. Snigirev, S. Kuznetsov, C. Rau, T. Weitkamp, L. Shabelnikov, M. Grigoriev, V. Yunkin, M. Hoffmann, and E. Voges. Refractive and diffractive x-ray optical elements. *Proceedings of SPIE*, 4499, 2001.

[127] M. Stampanoni, F. Marone, J. Vila-Comamalaa, S. Gorelick, C. David, P. Trtik, K. Jefimovs, and R. Mokso. Hard X-ray Phase-Contrast Tomographic Nanoimaging. *AIP Conference Proceedings*, 1365:239–242, 2011.

[128] M. Stampanoni, R. Mokso, F. Marone, J. Vila-Comamala, S. Gorelick, P. Trtik, K. Jefimovs, and C. David. Phase-contrast tomography at the nanoscale using hard x rays. *Physical Review B*, 81:140105, 2010.

[129] M. Störmer, D. Häussler, W. Jäger, and R. Bormann. Large X-ray Optics: Fabrication and Characterization of Single and Multilayer Mirrors. *Optics and Precision Engineering*, 15:1869–1877, 2007.

[130] M. Störmer, C. Michaelsen, J. Wiesmann, P. Ricardo, and R. Bormann. Nanostructured Multi-Layers for Applications in X-ray Optics. In *The Dekker Encyclopedia of Nanoscience and Nanotechnology*, New York, 2006. Marcel Dekker Inc.

[131] S. Suehiro, H. Miyaji, and H. Hayashi. Refractive lens for X-ray focus. *Nature*, 352:385–386, 1991.

[132] Y. Sun and Y. Wang. Monitoring of Galvanic Replacement Reaction between Silver Nanowires and HAuCl4 by In Situ Transmission X-ray Microscopy. *Nano Letters*, 11:4386–4392, 2011.

[133] D. J. Thiel, D. H. Bilderback, and A. Lewis. Production of intensite micrometer-sized x-ray beams with tapered glass monocapillaries. *Review of Scientific Instruments*, 64:2872–2878, 1993.

[134] S. Torquato and F. H. Stillinger. Toward the jamming threshold of sphere packings: Tunneled crystals. *Journal of Applied Physics*, 102(9):–, 2007.

[135] S. Torquato, T. M. Truskett, and P. G. Debenedetti. Is Random Close Packing of Spheres Well Defined? *Physical Review Letters*, 84:2064–2067, 2000.

[136] H. Vogt. private communication. Karlsruhe Institute of Technology, 2012–2014.

[137] H. Vogt. *Gerollte brechende Roentgenfolienlinsen*. PhD thesis, Karlsruher Institute of Technology (KIT), 2014.

[138] H. Vogt, A. Last, M. Kluge, F. Marschall, and M. Ogurreck. Rolled X-ray Prism lenses for microscopy illumination purposes. HASYLAB Anuual Report, 2013.

[139] P. Vukusic, B. Hallam, and J. Noyes. Brilliant Whiteness in Ultrathin Beetle Scales. *Science*, 315(5810):348, 2007.

[140] P. Vukusic and J. R. Sambles. Photonic structures in biology. *Nature*, 424:852–855, 2003.

[141] G. Wang, T.-H. Lin, P.-C. Cheng, and D. M. Shinozaki. A General Cone-Beam Reconstruction Algorithm. *IEEE Transactions on Medical Imaging*, 12:486–496, 1993.

[142] T. Weitkamp, D. Haas, D. Wegrzynek, and A. Rack. ANKAphase: software for single-distance phase retrieval from inline X-ray phase-contrast radiographs. *Journal of Synchrotron Radiation*, 18:617–629, 2011.

[143] S. Werner. *Theoretische Untersuchungen und experimentelle Methoden zur Realisierung von Volumenzonenplatten für die Röntgenmikroskopie*. PhD thesis, Humboldt-Universität zu Berlin, 2010.

[144] H. M. Whitney, M. Kolle, P. Andrew, L. Chittka, U. Steiner, and B. J. Glover. Floral Iridescence, Produced by Diffractive Optics, Acts As a Cue for Animal Pollinators. *Science*, 323(5910):130–133, 2009.

[145] D. S. Wiersma. Disordered Photonics. *Nature Photonics*, 7:188–196, 2013.

[146] K. Wille. *Physik der Teilchenbeschleuniger und Synchrotronstrahlungsquellen*. Teubner, Stuttgart, 1996.

[147] B. Yan, C. V. McNeff, P. W. Carr, and A. V. McCormick. Synthesis and Characterization of Submicron-to-Micron Scale, Monodisperse, Spherical, and Nonporous Zirconia Particles. *Journal of the American Ceramic Society*, 88(3):707–713, 2005.

[148] B. X. Yang. Fresnel and refractive lenses for x-rays. *Nuclear Instruments and Methods in Physics Research Section A: Accelerators, Spectrometers, Detectors and Associated Equipment*, 328:578–587, 1993.

Acknowledgements

First of all, my thanks go to Prof. Martin Müller for giving me the opportunity to work on this interesting topic, for his support during this project, and for taking the time for discussions. Designing a new synchrotron experiment from scratch and accompanying it through the design and construction phase up to the first successful experiments was a very broad experience.

The HZG tomography group at the Hamburg outstation supported me in many ways and made for a very pleasant working atmosphere. I thank Astrid Haibel for introducing me into the topic and giving me technical support at the start. Felix Beckmann offered very helpful advice on many general tomography and reconstruction issues and almost convinced me of the advantages of using IDL as the primary script language. Fabian Wilde and Julia Herzen helped performing some of the many commissioning experiments necessary to get the experiment running. Thomas Dose, Hilmar Burmester, and Rene Kirchhof were a great help at all the technical issues around the experiment, like adapter plates, cables, design of sample holders etc. Imke Greving was most supportive during beamtimes and at discussing all the strange phenomena occurring at commissioning beamtimes. Thank you very much! I want to thank Julia, Imke and Felix again for proof–reading the manuscript and for giving constructive comments on it.

The X–ray optics used in this work were improved in cooperation with the IMT (KIT Karlsruhe). I want to thank Vladimir Nazmov, Felix Marschall, Harald Vogt, and Arndt Last for their help with the optics. Their support and help during shared beamtimes was essential at understanding the optics and getting the X–ray microscopy experiment to work.

The nanoporous gold sample investigated was kindly provided by Kaixiong Hu. I want to thank Elisabeth Leib for preparing the zirconia particles and Jefferson do Rosario for preparing the photonic glass. I want to especially thank Daniel Laipple for his dedication at preparing many slices and samples using the focused ion beam.

Last but not least, my thanks go to my girlfriend Selina, my parents and my brother Steffen for their support in all stages of this work.